Interaction ultrasons/os : de la caractérisation à la mécanotransduction

Cécile Baron

École doctorale nº 463 : Sciences du Mouvement Humain

Habilitation à Diriger des Recherches

Spécialité :"Biomécanique"

présentée et soutenue publiquement par

Cécile BARON

le 19 décembre 2017

Interaction ultrasons / os
De la caractérisation à la mécanotransduction

Jury

Mme Rachele Allena,	MCF HDR	Rapporteur
Mme Nadine Candoni,	Professeur	Rapporteur
M. Kay Raum,	Professeur	Rapporteur
M. Denis Aubry,	Professeur	Examinateur
M. Jean-François Aubry,	DR CNRS	Examinateur
M. Patrick Chabrand,	Professeur	Examinateur
Mme Hélène Follet,	CR INSERM HDR	Examinateur
M. Philippe Lasaygues,	IR CNRS	Invité

ISM - Etienne-Jules Marey
UMR CNRS 7287, Aix-Marseille Université, F-13009 Marseille, France

HDR

Table des matières

Liste des figures

Liste des tableaux

Chapitre 1

Activités de Recherche

« Il suivait son idée. C'était une idée fixe, et il était surpris de ne pas avancer. »

Jacques Prévert

Sommaire

Avant-propos

Ces phrases de Jacques Prévert citées à la page précédente me font sourire... Mon *idée fixe* à moi, ce sont les ultrasons ; et les ultrasons pour le vivant : des ultrasons pour diagnostiquer et des ultrasons pour soigner ; pour soigner tout au long de la vie, de la naissance à la vieillesse. Et même si mon idée est *fixe*, il me semble avoir avancé et cette idée évolue, navigue, se propage. Elle m'a fait faire de belles rencontres, poser beaucoup de questions. Elle continue à me faire *chercher* des réponses.
Ce sont ces chemins, ces pistes de réflexion et d'investigation que je vous propose de synthétiser dans ce manuscrit. Je vous en souhaite bonne lecture.

Introduction

À la suite de mes travaux de thèse sur la propagation d'ondes élastiques dans des milieux hétérogènes à propriétés continûment variables, j'ai choisi de m'intéresser à l'interaction des ultrasons avec le tissu osseux. Dans ce premier chapitre, nous commencerons pas décrire les travaux que j'ai menés pour caractériser la *qualité osseuse* de l'os adulte atteint de pathologies ostéofragilisantes telles que l'ostéoporose. L'os adulte sain est un matériau documenté et aujourd'hui bien connu. L'enjeu est donc dans la construction d'un outil d'évaluation de la qualité osseuse et de suivi de son évolution au cours de la vie : un outil de diagnostic.
Lorsqu'on envisage des modalités ultrasonores pour le vivant, on met en avant leur caractère non-invasif, non-irradiant, non-ionisant, la possibilité de développer des appareils peu coûteux et portables au lit du patient. Ces critères sont importants pour le patient et prennent une dimension supplémentaire dans le cas de patients pédiatriques pour lesquels les autres protocoles de diagnostic (Rayons X, IRM) sont lourds (sédation, anesthésie, dose). Par ailleurs, on sait aujourd'hui que l'os en croissance présente des pathologies spécifiques et que son comportement mécanique lui est propre. On ne peut pas se contenter de considérer l'os enfant comme un os adulte miniature. Cependant, pour diagnostiquer les pathologies, il faut définir un état *sain* de référence. Or l'os en croissance non-pathologique est un matériau mal connu. C'est pourquoi, j'ai trouvé très intéressant de contribuer à l'élaboration d'une base de données de référence sur l'os enfant en développant des outils d'imagerie haute résolution et des protocoles de caractérisation mécanique dédiés. L'idée est de faire un lien entre l'organisation du tissu et ses propriétés mécaniques à différentes échelles. L'enjeu est certes de caractériser le comportement mécanique de l'os enfant mais également de le mettre en relation avec des paramètres morphométriques accessibles par imagerie.
Mais les ultrasons sont plein de ressources et, **outil de diagnostic**, ils peuvent également être **vecteur thérapeutique**. C'est l'objet de la deuxième partie de ce premier chapitre. Cette deuxième partie débute par une étude où le tissu osseux apparaît au *second plan*. Il s'agissait d'étudier la propagation des ondes ultrasonores à l'intérieur du crâne pour analyser l'effet de l'apport des ultrasons dans la dissolution d'un caillot sanguin situé dans le cerveau. C'est à partir de là que l'enjeu *théranostique* des ultrasons est apparu dans ma recherche. C'est le déclic qui a provoqué mon intérêt pour la stimulation ultrasonore de la régénération osseuse, sujet qui alimente mes projets de recherche actuels.

1.1 Ultrasons & os : un outil de diagnostic

Après avoir travaillé sur la caractérisation ultrasonore de matériaux hétérogènes tels que le béton au cours de ma thèse, j'ai appliqué ces développements à l'évaluation ultrasonore de la résistance osseuse pour améliorer le diagnostic de l'ostéoporose. L'os humain peut être de 2 types (Figure 1.1) :

— l'os cortical ou os compact, os de faible porosité (entre 2 et 20 %) qui représente 80 % de la masse osseuse du squelette humain et qui constitue la partie centrale des os longs.

— l'os trabéculaire ou os spongieux, os très poreux (entre 25 et 95 %) présent dans les extrémités des os longs.

L'ensemble de mes recherches porte sur l'os cortical.

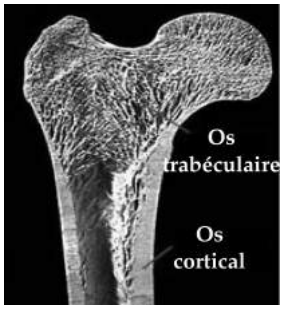

FIGURE 1.1 – Os cortical et os trabéculaire dans un os long.

1.1.1 Ultrasons et porosité corticale

Dès octobre 2005, au sein du Laboratoire d'Imagerie Biomédicale (UMR 7371) dirigé par Pascal Laugier (DR CNRS), j'ai mis en œuvre mes compétences en acoustique ultrasonore dans les matériaux hétérogènes tout en découvrant le domaine du biomédical. J'ai étudié l'impact de la porosité sur le comportement mécanique de l'os cortical *via* la propagation d'ondes ultrasonores en vue de construire un modèle numérique d'os le plus réaliste possible.

Caractérisation ultrasonore de l'os cortical

De façon générale, la pertinence du recours aux ultrasons pour évaluer l'os *in vivo* est désormais bien établie, en particulier dans le domaine de l'aide au diagnostic de l'ostéoporose, ostéopathie associée à un risque de fracture accru. Les dispositifs ultrasonores d'examen de l'os trabéculaire présentent ainsi de très bonnes performances en terme de prédiction du risque de fracture, performances d'ailleurs équivalentes à celles de la technique d'absorptiométrie des rayons X. Bien que plus récents et moins bien documentés, les systèmes ultrasonores d'examen de l'os cortical présentent aussi des capacités avérées à prédire la résistance osseuse et le risque de fracture ostéoporotique.

La perspective d'une évaluation de la qualité osseuse rompt avec la pratique actuelle, tout du moins dans le domaine de l'aide au diagnostic de l'ostéoporose. Actuellement, l'index ultrasonore utilisé pour prédire le risque de fracture est la vitesse des ondes élastiques ou la variation de l'atténuation de l'onde en fonction de la fréquence. L'os cortical a bénéficié d'études en amont qui, dans le cadre d'études expérimentales ou de modèles

académiques plus ou moins raffinés, ont établi que la vitesse des ondes élastiques observées résulte de l'effet combiné de plusieurs propriétés telles que l'épaisseur corticale, la porosité (rapport du volume occupé par les pores avec le volume total) et la minéralisation. Or l'os cortical autorise la propagation de plusieurs modes guidés dans une gamme de fréquences suffisamment élargie (type ondes de Lamb). Ces ondes sont, dans la pratique actuelle, observées en configuration de transmission axiale, émetteurs et récepteurs alignés selon la direction de l'axe de l'os. La vitesse de chacune de ces ondes a une dépendance spécifique aux propriétés osseuses. La richesse exceptionnelle de la réponse ultrasonore de l'os cortical laisse envisager la possibilité d'une caractérisation multiparamétrique de la qualité osseuse, mais cela nécessite de construire des modèles pertinents qui prennent en compte la complexité du tissu osseux : anisotropie, porosité multi-échelle, géométrie complexe. Améliorer la représentativité des modèles constitue un enjeu de première importance.

Simulation numérique de la propagation d'ondes ultrasonores au sein d'échantillons d'os reconstruits

Lors de mon post-doc, mon implication dans le projet coordonné par Maryline Talmant (CR CNRS), s'est essentiellement concentrée sur l'aspect numérique et la construction d'un modèle d'os virtuel. Le modèle d'os virtuel est construit en simulant numériquement des expériences physiques en transmission axiale réalisées sur des échantillons de radius humains *in vitro*. Ces simulations sont basées sur un code de calcul aux différences finies mis au point au laboratoire (www.simsonic.fr)[Bossy et al., 2004]. Les échantillons de tissu osseux sont obtenus à partir d'images de microtomographie (taille de pixel 10 microns) à une résolution suffisamment élevée pour reconstruire le réseau de pores vasculaires. Des blocs parallélépipédiques sont ensuite extraits de ces reconstructions pour être intégrés au code de calcul (Figure 1.2). Les propriétés mécaniques, cœfficients de rigidités et masse volumique, utilisées en données d'entrée sont elles-mêmes mesurées expérimentalement.

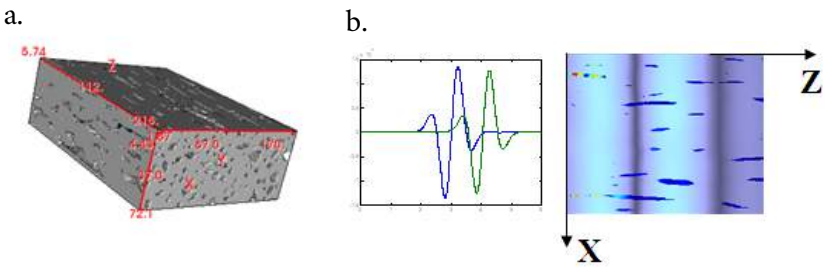

FIGURE 1.2 – Simulation de la propagation d'une onde plane (b) dans un bloc d'os reconstruit (a).

L'os cortical est modélisé, à cette échelle, par un milieu biphasique fluide/solide : des pores remplis d'un fluide supposé parfait et assimilé à de l'eau ; une matrice osseuse solide, élastique et anisotrope. Chacune des deux phases est caractérisée par ses propriétés mécaniques : cœfficients d'élasticité et masse volumique. En transmission axiale, pour des fréquences inférieures ou égales à 1 MHz, la longueur d'onde est de quelques millimètres et est supérieure à la dimension caractéristique des pores de quelques centaines de micromètres au maximum. L'onde plane ultrasonore propagée "voit" donc un milieu

homogène équivalent. Les échantillons reconstitués ayant des porosités couvrant le domaine de porosité de l'os cortical (jusqu'à 15 %), il est possible d'étudier l'impact de la porosité, en tant que fraction volumique, sur le comportement mécanique de l'os (cœfficients d'élasticité et anisotropie) *via* la simulation de propagation d'ondes de volume ultrasonores. La simulation d'un système de transmission axiale (émetteur/récepteurs) enregistre les signaux se propageant au sein des blocs-échantillons. Les vitesses de propagation sont ensuite calculées par détection d'un premier maximum. À partir des valeurs de vitesses de compression et de cisaillement ainsi obtenues selon les trois directions de l'espace, les cœfficients diagonaux de la matrice des rigidités ont été déduits en utilisant l'équation de Christoffel.

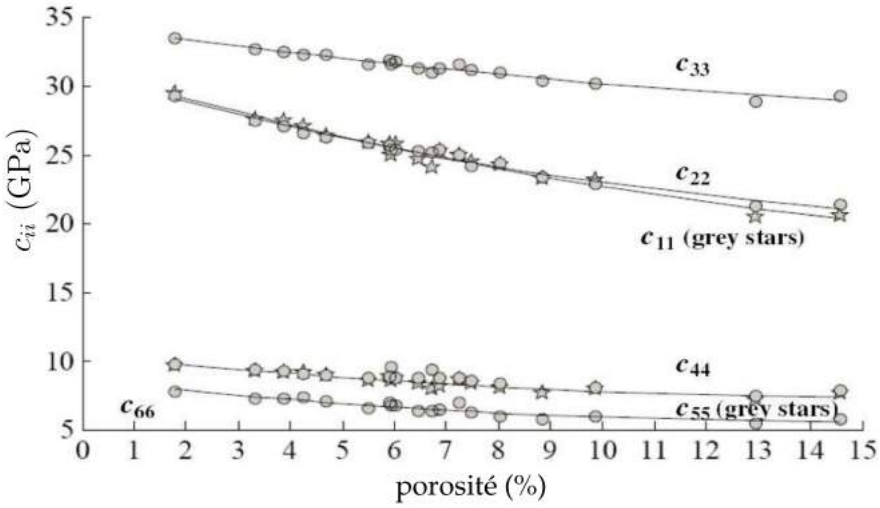

FIGURE 1.3 – Évolution des cœfficients de rigidités en fonction de la porosité corticale.

Ces résultats mettent en évidence la forte relation entre les mesures ultrasonores et la porosité ainsi que l'impact de la porosité sur l'anisotropie de l'os (Figure 1.3). La construction d'un modèle d'interaction des ultrasons avec l'os cortical doit donc intégrer ces facteurs pour une meilleure compréhension des phénomènes physiques induits.

Ces résultats (Figure 1.3) ont fait l'objet de plusieurs communications internationales et sont présentés dans un article publié au Journal of Acoustical Society of America [BARON et al., 2007] (cf. Chapitre 4 p.48).

1.1.2 L'os un milieu à gradient de propriétés

Les propriétés mécaniques de l'os cortical varient en fonction du site anatomique et des individus. L'un des enjeux majeurs de la caractérisation ultrasonore de la qualité osseuse est de déterminer des paramètres pertinents qui s'affranchiraient de ces variations inter-sites et inter-individus. Pour cela, j'ai proposé de considérer un nouveau paramètre pour caractériser la qualité mécanique de l'os cortical : la variation progressive (voire continue) des propriétés mécaniques (cœfficients d'élasticité) le long de l'épaisseur corticale. Le choix de ce paramètre s'est fait en observant les changements induits par l'ostéoporose. Dans le cas de cette pathologie, on observe en général un effet couplé : une *trabécularisation* de l'endoste qui entraîne un amincissement de la paroi. En d'autres termes la porosité augmente progressivement dans l'épaisseur corticale qui elle

diminue (Figure 1.4 a.). Dans la description même du processus on pressent qu'un paramètre qui intégrerait à la fois la microarchitecture (répartition des pores) et la géométrie de l'os (épaisseur corticale) serait un avantage dans l'évaluation de la qualité osseuse et surtout de son évolution. C'est le cas du gradient de propriétés mécaniques dans la direction radiale de l'os long.

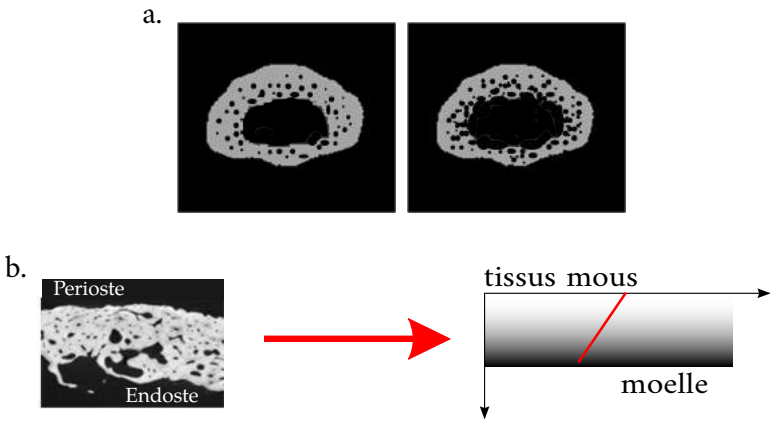

FIGURE 1.4 – a. Effet de l'ostéoporose : *trabécularisation* et amincissement de la corticale. b. Modélisation de l'os cortical comme un milieu à gradient de porosité unidirectionnel.

Formalisme de Stroh

Lors de mes travaux de thèse, j'ai developpé un outil numérique afin d'étudier la sensibilité des ondes élastiques à des profils continus de propriétés [BARON, 2005]. On considère un guide d'onde dont les propriétés mécaniques représentées par les cœfficients de rigidités C_{ij} et la masse volumique ρ varient dans une direction perpendiculaire à la direction de propagation d'ondes planes. La difficulté consiste à résoudre l'équation d'onde pour des cœfficients de rigidités et une masse volumique qui dépendent d'une variable de l'espace. Une des solutions les plus utilisées est la modélisation du milieu à gradient de propriétés par un milieu multicouche pour lequel les propriétés sont constantes par morceaux ce qui permet la résolution de l'équation d'onde de manière classique sur chacune des couches, ces solutions étant ensuite raccordées entre elles par les conditions aux limites. Cela fournit donc une solution exacte à un problème approché. L'objectif de mon travail de thèse était de fournir une solution approchée au problème exact et donc de formuler une solution analytique de l'équation d'onde en conservant des profils continus de variation des propriétés caractéristiques et d'évaluer cette solution numériquement. L'objectif a été atteint en utilisant le formalisme de Stroh [STROH, 1962] et les travaux d'A. Shuvalov [SHUVALOV, 2003; SHUVALOV et al., 2005].

Application à l'os cortical

L'idée a donc été de considérer l'os cortical comme un guide d'onde plan, dans une premier temps, dont les propriétés varient continûment dans la direction radiale de l'os, perpendiculaire à la direction de propagation des ondes dans le cas de la caractérisation par transmission axiale (Figure 1.4 b.) [BARON et NAILI, 2010] (cf. Chapitre 4 p.67). Ce modèle a ensuite été élargi au cas de guides d'ondes cylindriques plus représentatifs de la géométrie des os longs [BARON, 2011] (cf. Chapitre 4 p.79). Il restait à définir des variations de propriétés physiologiques et caractéristiques des changements du tissu osseux

liés à l'âge. En me basant sur les résultats obtenus par BOUSSON et al. [2001] et en mettant en œuvre les modèles d'homogénéisation (micromécaniques) définis par GRIMAL et al. [2011], j'ai déterminé des profils de propriétés réalistes pour différents âges. J'ai ainsi vérifié que les ondes ultrasonores étaient sensibles à ces variations de profils physiologiques dans une gamme de fréquences utilisée classiquement pour la caractérisation ultrasonore de l'os cortical [BOSSY et al., 2004; MOILANEN et al., 2007].
Cette étude confirme la pertinence des techniques de caractérisation ultrasonore pour l'évaluation de la qualité osseuse et a donné lieu à une pubication dans *Ultrasound in Medicine and Biology* [BARON, 2012] (cf. Chapitre 4 p.88).

Validation expérimentale

En parallèle, j'ai monté un protocole expérimental pour la caractérisation d'une plaque à gradient de propriétés. Le principe consiste à générer des ondes de compression à une incidence correspondant à la propagation de certains modes guidés. Les signaux temporels enregistrés sont ensuite traités par double transformée de Fourier afin de pouvoir identifier les courbes de dispersion (vitesse de phase en fonction du produit fréquence-épaisseur) des modes propagatifs. Le montage et le protocole ont été validés sur des plaques d'aluminium homogènes et isotropes de différentes épaisseurs (Figure 1.5).

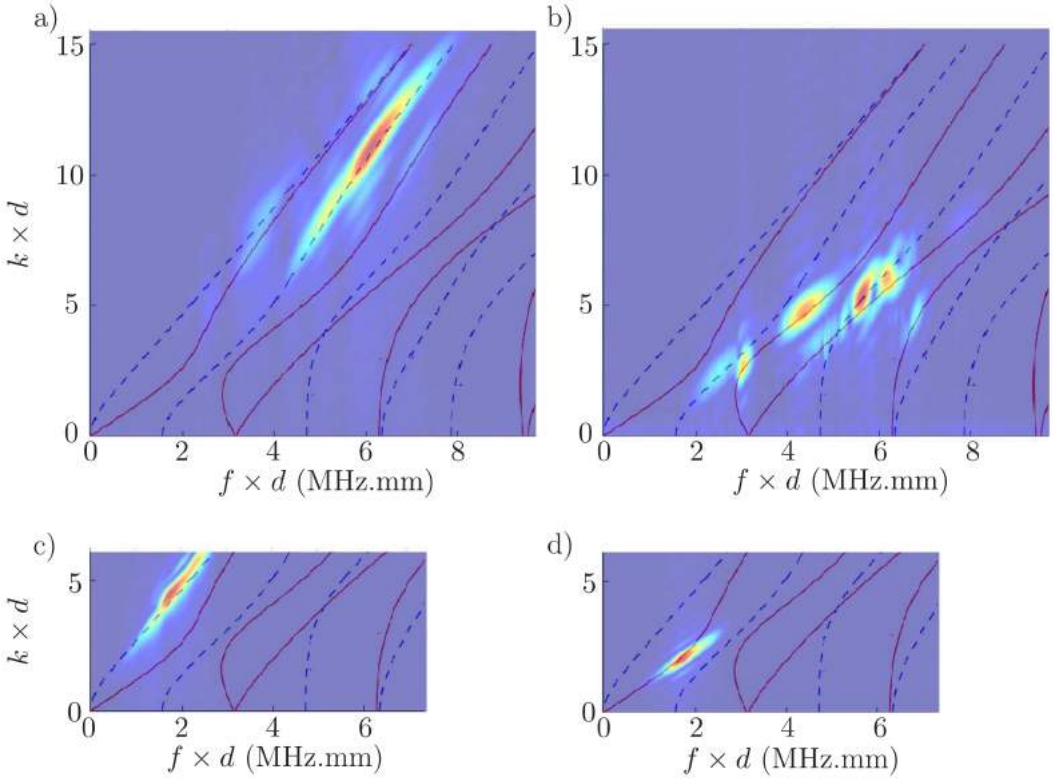

FIGURE 1.5 – Courbes de dispersion : produit nombre d'onde-épaisseur ($k \times d$) en fonction du produit fréquence-épaisseur ($f \times d$). a) Plaque d'aluminium de 5 mm d'épaisseur et un angle d'incidence de 28° : mode A_1. b) Plaque d'aluminium de 5 mm d'épaisseur et un angle d'incidence de 12° : modes S_1 et A_2. c) Plaque d'aluminium de 2 mm d'épaisseur et un angle d'incidence de 37° : mode A_0. d) Plaque d'aluminium de 2 mm d'épaisseur et un angle d'incidence de 12° : mode S_0.

Les mesures expérimentales ont été réalisées au LMA (UPR CNRS 7051) au mois d'août 2012 en collaboration avec le SERM (Service d'Études et de Réalisations Mécaniques). Le protocole et le montage ont donc été validés pour une plaque homogène et isotrope.

Reste à concevoir des matériaux à gradients de propriétés contrôlés et représentatifs des variations de propriétés mécaniques observées dans l'épaisseur de l'os cortical humain. Dans le cadre du DEFI CNRS REPOUSSE (cf. § 2.1.2 p.30), j'ai rencontré Laurent Malaquin du LAAS (UPR CNRS 8001, Toulouse) qui développe des protocoles de fabrication 3D susceptibles de fournir des matériaux à gradient de porosité contrôlé et morphologiquement proche de l'os cortical [MÉZIÈRE et al., 2016].

1.1.3 Caractérisation de l'os en croissance

Depuis 2009, je travaille sur la caractérisation de l'os enfant. L'os enfant est un matériau pour lequel les valeurs de référence des propriétés caractéristiques (mécanique, biochimie, structure) font cruellement défaut. La détermination de ces valeurs de référence est un enjeu crucial pour les cliniciens afin de développer des protocoles de diagnostic et de thérapie dédiés aux pathologies pédiatriques. Actuellement, le critère le plus utilisé pour diagnostiquer la fragilité osseuse est la mesure de la densité minérale osseuse (DMO), déterminée conventionnellement par rayons X à l'aide de scanner. Cependant, cette technique nécessite des protocoles particuliers adaptés à la pratique pédiatrique (anesthésie, dose de radiation). Par ailleurs, la mesure de la DMO donne accès exclusivement à la teneur en minéral de l'os (donnée quantitative) et ne fournit aucune information qalitative sur la microstructure ou les propriétés mécaniques de l'os. L'ambition est donc de fournir des valeurs de référence de la *qualité* de l'os en croissance : densité massique, modules d'élasticité, anisotropie, morphométrie, biochimie du collagène. Les différentes modalités de caractérisation de l'os enfant que j'ai utilisées ont été mises en œuvre sur des échantillons extraits de déchets chirurgicaux. La préparation des ces échantillons de faibles dimensions (découpe, état de surface) est délicate et nécessite des protocoles précis que nous avons développés spécifiquement.

Ces recherches ont été réalisées dans le cadre d'un contrat ANR (MALICE 2012-2016), d'un financement Carnot (CROISSANCE 2016) et de deux thèses que j'ai co-encadrées (Emmanuelle Lefèvre 2012-2015 et Marie Semaan 2015-2018). Ma contribution s'est concentrée sur 2 questions :

— imagerie haute résolution et étude morphométrique de l'os enfant ;

— anisotropie de l'os enfant par caractérisation US.

Morphométrie de l'os cortical enfant

Il est aujourd'hui clairement établi que l'architecture de l'os et son organisation multi-échelle sont des déterminants de la qualité osseuse. Un des enjeux est donc l'évaluation de paramètres morphométriques de l'os en tant que matériau poreux. Il est important de préciser que l'os est un matériau à plusieurs niveaux de porosité à différentes échelles de mésoscopique à nanoscopique. On considère ici la porosité mésoscopique qui est la porosité vasculaire constituée des canaux de Havers et de Volkmann.
On cherche, d'une part à reconstituer fidèlement le réseau poral 3D, ceci afin de respecter les orientations privilégiées et la géométrie des pores et en déduire la contribution de la microstructure dans l'anisotropie générale du tissu osseux (Figure 1.6) ; d'autre part à définir le tenseur d'élasticité de la matrice osseuse supposée anisotrope. J'ai initié des travaux concernant l'étude de la morphométrie de l'os en croissance à partir d'analyses d'images des échantillons collectés dans le cadre du projet MALICE. L'objectif est de dé-

terminer les paramètres caractéristiques susceptibles de réfléter la qualité de l'os chez l'enfant.

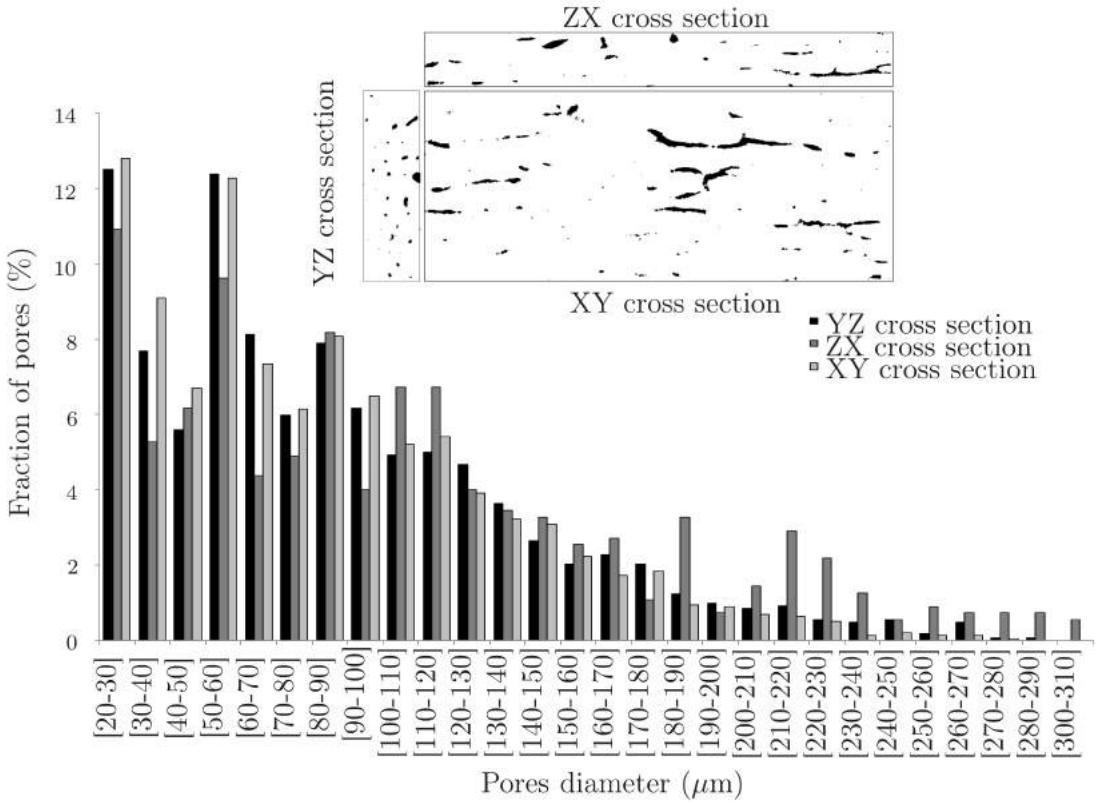

FIGURE 1.6 – Répartition des diamètres de pores selon les 3 directions de l'espace pour un échantillon paralellépipédique de radius humain adulte.

En collaboration avec Yohann Bala (post-doc ANR MALICE), nous avons reconstruit 54 échantillons cubiques d'os enfants et adultes à partir d'images RX obtenues par micro-CT (Skyscan 1174, Skyscan NV, Kontich, Belgium)(Figure 1.7). La taille de voxel a été fixée à 8,14 µm. Les analyses morphométriques ont été effectuées en utilisant une méthode semi-automatique (CTAnalyser Software V 1.14.4, Skyscan NV, Kontich, Belgium).

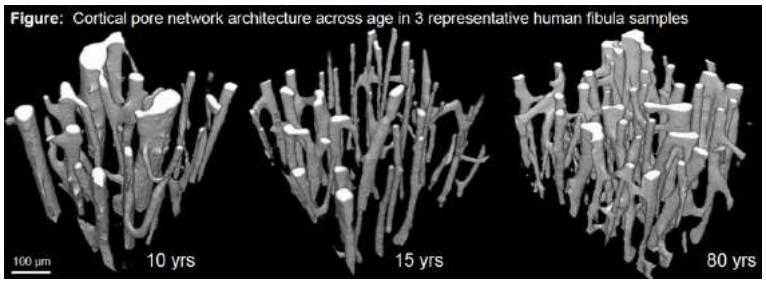

FIGURE 1.7 – Reconstruction 3D du réseau de pores vasculaires sur 3 échantillons.

Nous avons ainsi évalué l'évolution de la structure porale en fonction de l'âge : les pores peu nombreux mais de diamètres importants dans l'enfance laissent place à une structure plus compacte (pores nombreux mais de petit diamètre) à l'adolescence pour aboutir à une structure plus poreuse (pores nombreux et diamètre important) avec le

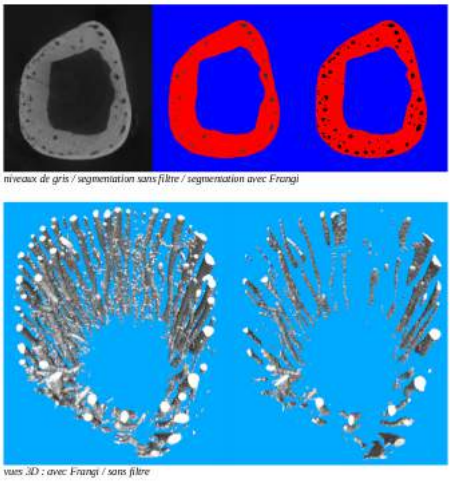

FIGURE 1.8 – Effet du filtre sur la détection des petits canaux de porosité sur des images d'os enfant (voxel de 19 µm). Porosité avec et sans filtre estimée à respectivement 7,2% et 2,8%.

vieillissement. Notre étude ne couvre malheureusement pas la tranche d'âge 20-50 ans.

Pour aller plus loin dans la maîtrise de l'évaluation de ces paramètres, j'ai contacté Jérôme Vicente développeur du logiciel libre iMorph (http ://imorph.sourceforge.net/). Le projet CROISSANCE financé par l'institut Carnot a permis le recrutement de Pierric Mora (post-doc 1 an) qui a développé des outils spécifiques de traitement d'images pour l'analyse morphométrique du réseau poral de l'os cortical en croissance. Ces avancées repose sur l'utilisation d'un filtre mis au point dans la cadre de la reconstruction de réseau vasculaire [FRANGI et al., 1998] et implémenté par Pierric dans le logiciel iMorph (Figure 1.8). Les résultats ont montré l'importance de l'utilisation de ce filtre pour obtenir une estimation correcte de la porosité dans le cas d'images de résolution inférieure à 10 µm et en présence de petits canaux. Dans le cas d'images d'os enfants à 19 µm par exemple, l'écart relatif dans l'estimation de la porosité avec et sans filtre peut atteindre plus de 150% (Figure 1.8) !

On a ainsi amélioré l'estimation de la porosité volumique ainsi que les paramètres géométriques des pores vasculaires. Ces travaux ont été présentés au congrès de l'European Society of Biomechanics (ESB) en juillet 2017 à Séville et font l'objet d'une publication en fin de rédaction qui sera soumise à Calcified Tissue International prochainement. Ces analyses ont été menées à la fois sur les pièces anatomiques récoltées en sortie de blocs opératoires ou sur cadavres (pièces tubulaires Figure 1.8) et sur les parallélépipèdes extraits de ces mêmes pièces sur lesquels seront effectués les tests de caractérisation mécanique (cf. §1.1.3). Cela nous permettra :

— d'estimer la représentativité des blocs extraits et l'hétérogénéité spatiale du réseau poral ;
— de mettre en corrélation les propriétés morphométriques et mécaniques du tissu.

Anisotropie de l'os cortical enfant

L'un des défis lancés par le projet MALICE est la caractérisation de l'anisotropie de l'os en croissance à l'échelle mésoscopique (du matériau). La caractérisation mécanique par méthodes ultrasonores ou par tests mécaniques s'avère délicate du fait de la petitesse des échantillons récoltés, échantillons provenant de déchets chirurgicaux.
Nous avons choisi de travailler sur des échantillons parallélépipédiques qui sont testés :

— par ultrasons en transmission selon les 3 axes ;
— par spectroscopie à résonance ultrasonore ;
— par nanoindentation.

La préparation des échantillons (découpe et conservation) est un enjeu de premier plan. Au cours des thèses d'Emmanuelle Lefèvre et de Marie Semaan et en collaboration avec Vincent Long du SERM (LMA - UPR CNRS 7051), nous avons conçu et développé un porte-échantillon pour la scie à lame diamantée et vitesse lente (Isomet 4000 - Buelher) que nous utilisons pour la découpe des échantillons. Ce porte-échantillon assure le parallélisme des faces opposées et la perpendicularité des faces adjacentes. Une grande précision dans la géométrie est indispensable pour les tests mécaniques prévus.

Caractérisation ultrasonore par transmission - Lors du stage de Marine Loubet réalisé au LMA (avril-juin 2014), nous avons conçu et testé un protocole de caractérisation ultrasonore de petits échantillons en utilisant des pinducers (Figure 1.9). Les échantillons d'os cortical étaient issus d'un même fémur bovin obtenu en boucherie. Des parallélépipèdes de différentes tailles (entre 2 et 10 mm de côté) ont été découpés à l'aide de l'ISOMET 4000. Le dispositif ultrasonore est en immersion dans une cuve remplie d'eau. Les mesures sont réalisées en transmission. Différentes techniques de traitement du signal ont été programmées sous Matlab afin d'évaluer les temps de vol et d'en déduire les vitesses de propagation des ondes longitudinales.

La caractérisation a été réalisée selon les 3 axes et les résultats obtenus sur les échantillons d'os bovin sont en parfait accord avec les données de la littérature et mettent en évidence le caractère orthotrope de l'os cortical bovin. Un deuxième protocole a été mis en place pour mesurer la vitesse de propagation des ondes de cisaillement selon les 3 axes à l'aide de transducteurs au contact (Figure 1.9). On a ainsi accès aux 6 coefficients diagonaux du tenseur d'élasticité.

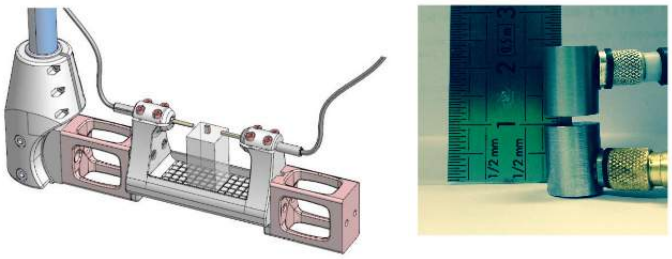

FIGURE 1.9 – Montages expérimentaux pour la caractérisation ultrasonore de petits échantillons.

Cette étude préliminaire sur os bovin a servi de validation de protocole expérimental afin de le mettre en oeuvre sur les échantillons d'os humains adultes et enfants étudiés par Emmanuelle Lefèvre au cours de sa thèse. On a ainsi déterminé les 6 coefficients diagonaux de la matrice de rigidité (Table 1.1) et conclut à l'isotropie transverse des échantillons étudiés avec $C_{33} > C_{11} = C_{22}$ et $C_{44} = C_{55} > C_{66}$ (1 = radial, 2 = circonférentiel et 3 = axial).

Ce travail a fait l'objet d'une publication dans une revue internationale à comité de lecture [LEFÈVRE et al., 2015] (cf. Chapitre 4 p.99).
Les résultats ainsi obtenus ont été mis en relation avec l'étude morphométrique pilotée par Yohann Bala (cf § précédent), travail qui a donné lieu à plusieurs communications dans des congrès internationaux et à une publication dans une revue internationale à comité de lecture [BALA et al., 2016] (cf. Chapitre 4 p.108).

	Enfants (n=13) 6-18 ans (13 ± 4) Moyenne (écart-type)	Adultes (n=16) 50-95 ans (75 ± 13) Moyenne (écart-type)	p-values
C_{11}	16,1 (2,5)	17,7 (3,6)	0,021
C_{22}	15,3 (2,5)	17,7 (6,1)	0,045
C_{33}	23,6 (4,4)	28,0 (5,1)	0,011
C_{44}	4,1 (0,8)	4,8 (0,6)	0,017
C_{55}	4,0 (0,9)	4,9 (1,1)	0,019
C_{66}	3,0 (0,4)	3,6 (1,0)	0,017

TABLEAU 1.1 – Valeurs des cœfficients de rigidité obtenues sur des fibulae. Les p-values pour la comparaison entre les groupes sont obtenues *via* le test de Mann-Whitney.

Caractérisation par spectroscopie à résonance ultrasonore - Dans le cadre de la thèse de Marie Semaan, nous avons cherché à compléter les résultats obtenus par Emmanuelle Lefèvre et à déterminer l'intégralité de la matrice des rigidités. Pour cela nous avons mis au point un protocole expérimental de spectroscopie à résonance ultrasonore (RUS) en nous basant sur les travaux de Simon Bernard [BERNARD et al., 2013, 2015, 2016]. Le montage expérimental a été réalisé au LMA en collaboration avec Cédric Payan et Philippe Lasaygues. Il a été validé sur des matériaux de référence et des échantillons d'os bovin de géométrie (paralellépipède) et de taille (qq mm de côté) similaires aux échantillons d'os enfants par Clémentine Boullai, stagiaire que j'ai co-encadrée au LMA (UPR CNRS 7051) d'avril à juin 2016. Dans un premier temps, nous avons utilisé le logiciel RITA développé par Pierre-Yves Lebas à Los Alamos sur la base théorique de MIGLIORI et al. [1993]. A partir des caractéristiques de l'échantillon (dimensions et masse) et en faisant une hypothèse sur les valeurs de la matrice de rigidité, on calcule les fréquences propres, puis on effectue une acquisition (Figure 1.10) avec des transducteurs de cisaillement à 250 kHz.

FIGURE 1.10 – Dispositif de spectroscopie à résonance ultrasonore.

Le signal est analysé pour déterminer les fréquences des modes enregistrés. Le problème inverse pour l'obtention du tenseur complet des cœfficients de rigidités (C_{ij}) est ensuite résolu sur la base d'un schéma de Levenberg-Marquardt [LEBEDEV, 2002]. L'os cortical est un matériau fortement hétérogène, ce qui rend ses modes de résonance difficiles à mesurer et à identifier, les résultats obtenus avec RITA se sont révélés très dépendants des valeurs de (C_{ij}) utilisées pour initialiser la résolution du problème inverse. Ces valeurs sont issues de la littérature pour l'os adulte [BERNARD et al., 2013] et l'os enfant [LEFÈVRE et al., 2015] et pose une hypothèse sur l'anisotropie présumée de l'os : ortho-

trope pour l'os adulte et isotrope transverse pour l'os enfant.
Lors de son post-doctorat, Pierric Mora a développé sous Python un module d'inversion des données de résonance ultrasonore intégrant l'approche bayésienne d'identification des modes décrite dans [BERNARD et al., 2015]. Cette approche probabiliste est bien adaptée aux petits nombres et aux faibles occurences comme c'est le cas pour notre étude. Appelée également *probabilité subjective*, elle est basée sur la prise en compte de connaissances *a priori*. L'approche bayésienne a montré que malgré un manque d'information, des données incomplètes, elle permet de résoudre de nombreux problèmes inverses. Elle se différencie de l'approche statistique standard car elle permet de déduire des résultats avec peu d'informations, au prix d'une complexité accrue de calculs.
Les résultats obtenus sur l'os adulte sont en parfait accord avec la littérature et ont fait l'objet d'une communication orale au congrès de l'ESB (European Society of Biomechanics) en 2017. Le protocole ainsi validé a été appliqué pour la caractérisation de l'os enfant. A ma connaissance, c'est la première fois que l'on obtient le tenseur des rigidités complet sur des échantillons d'os enfants non-pathologiques, ce qui constitue une avancée considérable dans la connaissance de la qualité mécanique de l'os en croissance.

$$\begin{pmatrix} 16,6(0,8) & 10,3(0,8) & 10,8(0,9) & 0 & 0 & 0 \\ 10,3(0,8) & 16,6(0,8) & 10,8(0,9) & 0 & 0 & 0 \\ 10,8(0,9) & 10,3(0,8) & 24,2(0,7) & 0 & 0 & 0 \\ 0 & 0 & 0 & 4,4(0,4) & 0 & 0 \\ 0 & 0 & 0 & 0 & 4,4(0,4) & 0 \\ 0 & 0 & 0 & 0 & 0 & 3,13(0,07) \end{pmatrix} \text{(GPa)}$$

Cette étude confirme la caractéristique isotropie transverse de l'os enfant (plan d'isotropie perpendiculaire à l'axe de l'os). Ces résultats ont été soumis au Journal of Biomechanics pour une Short Communication.

Nanoindentation - L'anisotropie de l'os cortical est le résultat de l'orientation du réseau poral et de l'anisotropie de la matrice osseuse. La contribution de chacun des 2 facteurs est intéressante à étudier dans la perspective de développer des modèles d'homogénéisation pertinents.
Dans le cadre de la thèse de Marie Semaan, nous avons fait l'acquisition d'un appareil de nanoindentation instrumentée (NHT^2 Anton Parr) afin de caractériser l'os en croissance à l'échelle micrométrique. À l'aide d'une pointe de géométrie connue, on indente le matériau en appliquant une force donnée, la profondeur d'enfoncement induite permet de déduire le module d'Young dans la direction d'application de la force en utilisant le modèle développé par OLIVER et PHARR [1992]. En testant les 3 directions de l'espace on peut avoir des informations sur l'anisotropie de la matrice solide indépendamment de l'organisation du réseau poreux. À cette échelle, le tissu osseux est composé de tissus ostéonal et interstitiel (Figure 1.11). L'idée est de relier les paramètres mécaniques ainsi mesurés aux propriétés mécaniques évaluées à l'échelle mésoscopique par méthodes ultrasonores. Ces mesures nécessitent une préparation des échantillons minutieuse et précise, pour cela nous avons conçu et développé un système de polissage qui assure à la fois le parallélisme des faces opposées et une qualité de surface suffisante pour mener les mesures de nanoindentation.

Nous avons validé le protocole expérimental sur de l'os bovin. Les tests sur les os adultes et enfants ont été réalisés. L'évaluation du module d'indentation nécessite une

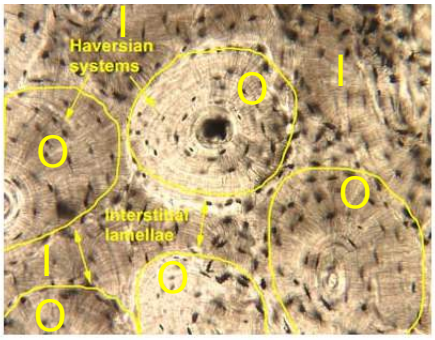

FIGURE 1.11 – Structure haversienne du tissu cortical humain. O : tissu osteonal ; I : tissu interstitiel.

analyse statistique sur une grand nombre de points, la caractérisation par nanoindentation de l'ensemble des échantillons récoltés a pris plusieurs mois. Une publication est en cours de rédaction et devrait être soumise début 2018.

Les ultrasons apparaissent donc comme des outils pertinents pour le diagnostic de pathologies osseuses. Leur caractère non-invasif, non-irradiant et non-ionisant sont des critères stratégiques en particulier en pédiatrie. Par ailleurs, ce sont des dispositifs peu coûteux et portables ce qui permet d'envisager une utilisation rapide et au lit du patient.
Ces avantages peuvent également être mis en œuvre en thérapie car les ondes ultrasonores peuvent aussi participer au traitement des tissus biologiques.

1.2 Ultrasons & tissus biologiques : vecteur thérapeutique

On aborde ici deux expériences : la première concerne la propagation d'ondes ultrasonores à l'intérieur du crâne et la deuxième l'interaction des ultrasons avec l'os en cours de régénération.

1.2.1 Sonothrombolyse

Du 1er novembre 2006 au 31 août 2007, j'ai occupé un poste d'Attachée Temporaire d'Enseignement et de Recherche à l'université Paris 7. J'ai effectué ma recherche à l'institut Langevin en collaboration avec Jean-François Aubry (DR CNRS).

Mon étude portait sur le contrôle de l'innocuité de pratiques thérapeutiques utilisant la sonothrombolyse dans le traitement d'Accidents Vasculaires Cérébraux (AVC) ischémiques.

Il existe deux types d'Accidents Vasculaires Cérébraux :

— 20% sont hémorragiques. L'hémorragie se produit lorsqu'une artère cérébrale éclate et laisse le sang s'écouler dans le cerveau, l'artère pouvant être fragilisée par une hypertension artérielle ou une malformation de naissance.

— 80% sont ischémiques. L'ischémie (thrombose) se produit lorsqu'une artère cérébrale est obstruée, il y a formation d'un caillot sanguin (thrombus) qui empêche l'irrigation du cerveau. Les diabétiques et les hypertendus en sont les principaux sujets puisque ces maladies concourt à l'épaississement de la paroi des artérioles cérébrales, parfois jusqu'à l'occlusion.

Traitement des AVC par sonothrombolyse

La thrombolyse est utilisée pour soigner le deuxième type d'AVC. Elle consiste à désagréger les caillots sanguins chimiquement, en injectant par voie intra artérielle un médicament anticoagulant (un activateur tissulaire de plasminogène ou tPA).

Des études expérimentales ont montré qu'émettre des ultrasons à travers la boite crânienne pouvait augmenter l'efficacité de la thrombolyse, c'est-à-dire accélérer l'effet du médicament injecté et donc l'efficacité du traitement administré au patient atteint d'une ischémie. C'est ce que l'on appelle la sonothrombolyse. Pour confirmer ces résultats et évaluer le risque et la praticabilité chez l'être humain de la sonothrombolyse, une étude clinique a été entreprise sur des patients victimes d'AVC ischémiques sévères [DAFFERTSHOFER et al., 2005]. Malgré des premiers résultats encourageants, la survenue d'hémorragies cérébrales secondaires chez la quasi-totalité (13 sur 14) des patients traités avec le tPA associé aux ultrasons basse fréquence (300 kHz) suscite encore aujourd'hui des doutes et soulève des interrogations quant au protocole expérimental à adopter (taille des transducteurs, fréquence d'émission, durée d'émission etc.).

Le recours à un outil numérique de simulation de la propagation d'ondes ultrasonores à travers le cerveau permet de comprendre quel phénomène provoque ces hémorragies cérébrales secondaires et d'explorer les solutions alternatives à envisager pour les éviter à l'avenir.

La simulation numérique pour le contrôle de l'innocuité de la sonothrombolyse

La modélisation des propriétés acoustiques du crâne, vitesse de phase, masse volumique et absorption acoustique, utilise les données de densité fournies par des images de coupes transversales de crâne obtenues par rayons X à partir desquelles on peut reconstruire un modèle de crâne réaliste en 3D.

Afin de réaliser des simulations numériques de la propagation d'ondes ultrasonores à travers le crâne, un schéma aux différences finies est utilisé pour implémenter l'équation d'onde dans un fluide en tenant compte de l'absorption. Pour vérifier la validité de la modélisation, la propagation d'une onde plane émise par le réseau de transducteurs a été simulée et comparée à des signaux expérimentaux avec succès [AUBRY et al., 2003].

L'étude s'est basée sur la comparaison de deux études cliniques menées sur des patients dans le cadre de traitement d'AVC sévères : la première nommée CLOTBUST associait un anticoagulant à l'apport d'ultrasons à une fréquence de 2 MHz par le biais d'un scanner-doppler [ALEXANDROV et al., 2004], la seconde, TRUMBI, accélérait l'action de l'anticoagulant par l'apport d'ultrasons basses fréquences (300 kHz) [DAFFERTSHOFER et al., 2005]. Dans le premier cas, les résultats ont montré une action bénéfique des ultrasons dans la dissolution du caillot alors que le second cas a dû être interrompu pour cause d'effets secondaires néfastes (hémorragies atypiques). À l'aide de l'outil numérique présenté brièvement ci-dessus, nous avons cherché à comprendre les phénomènes mis en jeu dans ce traitement par sonothrombolyse. Une fois les cartes d'absorption, de masse volumique et de vitesse reconstruites pour générer le modèle 3D du crâne, on utilise le code aux différences finies évoqué au paragraphe précédent pour résoudre l'équation d'onde en milieu absorbant. Les conditions expérimentales sont reproduites au plus proche de la réalité : position et taille des émetteurs, distance focale, fréquence et durée d'émission. En simulant les deux dispositifs cliniques, nous avons mis en évidence des phénomènes de cavitation acoustique (formation de bulles de gaz dans les zones de dépression du fluide) dans le cerveau pouvant être à l'origine des hémorragies cérébrales secondaires observées dans le protocole TRUMBI. Ces zones de cavitation acoustique

n'apparaissent pas dans le cadre de l'étude CLOTBUST, à 2 MHz l'énergie des ultrasons est fortement absorbée lors de la traversée du crâne. Les simulations numériques ont mis en évidence le rôle prépondérant de la forme du crâne dans l'apparition d'ondes stationnaires et la formation de *hot spot* (pic de pression). Il semble donc qu'il faille rester en des-

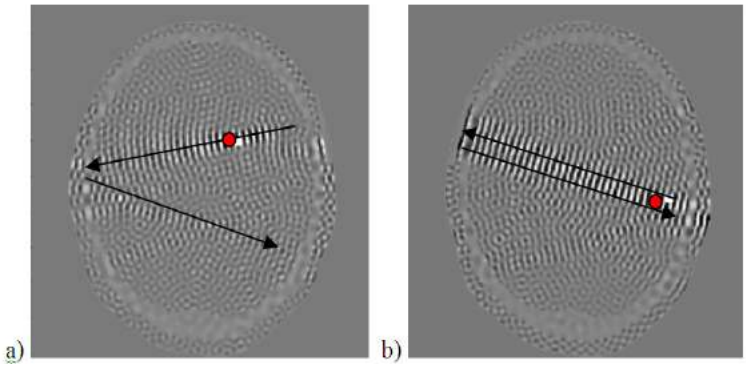

FIGURE 1.12 – Position du pic de pression négative (point rouge) et répartition du champ ultrasonore au travers des fenêtres temporales a) droite et b) gauche.

sous du seuil de cavitation mais il faut connaître quel en serait l'impact sur le phénomène de sonothrombolyse. Après une exploration bibliographique poussée et des discussions avec des cliniciens ayant participé à la campagne d'essais, il est apparu des contradictions concernant les niveaux de pression générés et les paramètres d'émission. Les conclusions de l'analyse que j'ai menée sur ce sujet font l'objet d'un article publié dans Ultrasound in Medicine and Biology en 2009 [BARON et al., 2009] (cf. Chapitre 4 p.57).

1.2.2 Stimulation ultrasonore de la régénération osseuse

En 2012, j'ai décidé de mener un travail nouveau que j'avais évoqué dans mon projet de recrutement CNRS. Il s'agit de comprendre les mécanismes en jeu dans la stimulation utrasonore de la cicatrisation osseuse. L'essentiel de mes travaux portent sur les ultrasons en tant que vecteur de diagnostic (caractérisation mécanique), j'avais envie d'explorer le potentiel des ultrasons comme vecteur thérapeutique, révélé par l'étude sur la sonothrombolyse (cf. § précédent).
Lorsqu'on évoque les ultrasons dans le milieu biomédical, on pense immédiatement à l'échographie comme outil d'imagerie. Les ultrasons sont également utilisés focalisés et à haute intensité (High Intensity Focused Ultrasound HIFU) en routine clinique pour détruire les calculs rénaux ou des tissus tumoraux. Il existe un phénomène observé cliniquement qui demeure mal compris : la stimulation ultrasonore de la cicatrisation osseuse. Les ultrasons impliqués sont des ultrasons pulsés de faible intensité (Low Intensity Pulsed UltraSound : LIPUS). L'effet des ultrasons sur la régénération du tissu a été mis en évidence dans les années 50. À partir des années 80, plusieurs publications ont étudié ce phénomène dans différents processus d'adaptation de l'os à son environnement : croissance [DUARTE, 1983] ; remodelage ciblé [CHAN et al., 2006] ; cicatrisation [SCHORTINGHUIS et al., 2003]. En 1994, la FDA donne son accord pour l'utilisation de cette modalité en application clinique. Un appareil de traitement à domicile est aujourd'hui commercialisé Exogen (Bioventus). Pour autant, bien qu'observée cliniquement et sur modèle animal [HECKMAN et al., 1994; MAYR et al., 2000] et étudiée depuis plus de 30 ans, la stimulation ultrasonore de la cicatrisation osseuse reste mal comprise et les mécanismes physiques

sous-jacents demeurent mal définis. C'est dans l'intention de combler ce manque que j'ai initié un projet en collaboration avec Carine Guivier-Curien (MCF, IRPHE UMR 7342 CNRS Aix-Marseille Université) pour développer un modèle numérique pertinent susceptible d'amener des éléments de réponse sur cette thématique.

L'os est un matériau vivant qui possède la capacité de s'adapter aux contraintes environnementales et de se réparer en cas de fracture grâce au processus de remodelage osseux : savant équilibre entre les actions des ostéoclastes (qui détruisent l'os) et des ostéoblastes (qui construisent l'os), le tout piloté par les ostéocytes (Figure 1.13).

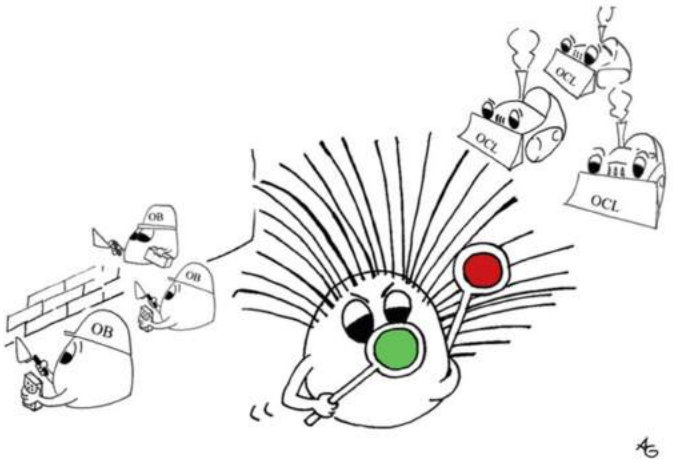

Fig. 3. A schematic sketch representing the central role of osteocytes in bone remodelling. Osteocytes sense the mechanical load and subsequently produce signaling molecules like nitric oxide and prostaglandins that can regulate the activity of the effector cells, the osteoclasts and the osteoblasts, which subsequently leads to adequate bone mass and architecture. OB, osteoblast; OCL, osteoclast.

FIGURE 1.13 – From [KLEIN-NULEND et al., 2013]

On se place dans le cas de fracture dans la partie centrale (diaphyse) des os longs (fémur, tibia, radius etc.). On se concentre donc toujours sur l'os cortical. Cependant, alors que dans mes travaux précédents, j'ai considéré la porosité vasculaire et sa contribution à la mécanique de l'os, la question du remodelage osseux nécessite de prendre en compte également un deuxième niveau de porosité. L'os sera donc considéré comme un milieu à double porosité (Figure 1.14) :

— porosité vasculaire : Ø100 µm contient les vaisseaux sanguins et les nerfs ;

— porosité lacuno-canaliculaire : Ø10 µm contient les ostéocytes cellules osseuses pierre angulaire de la mécanotransduction.

Le réseau lacuno-canaliculaire est au coeur de notre problématique. En effet, parmi les hypothèses fortes formulées dans la littérature, le principe de stimulation ultrasonore de la cicatrisation osseuse reposerait sur la génération de contraintes de cisaillement fluide, au sein du fluide interstitiel qui baigne les osteocytes, qui déclencheraient la réponse ostéocytaire et l'activation du remodelage osseux.

L'objectif que je me suis fixé est d'identifier le *message mécanique* que les ostéocytes perçoivent à la suite d'une stimulation ultrasonore de type LIPUS. Pour cela, un modèle numérique à deux échelles a été dévéloppé avec la collaboration de Vu-Hieu Nguyen et Salah Naili (MSME UMR 8208 CNRS UPEC UPEM, Créteil) sous le logiciel commercial Comsol Multiphysics. L'enjeu est de prendre en compte un phénomène multiphysique et multi-échelle.

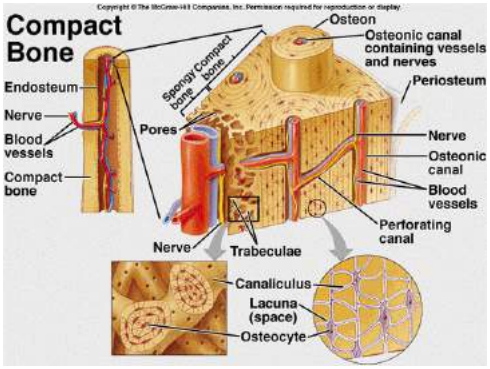

FIGURE 1.14 – L'os cortical vu comme un milieu à double porosité.

Deux modèles numériques sont implémentés :

— le premier est 2D et représente l'échelle du tissu (Figure 1.15 gauche),

— le second est 3D et représente une lacune ostéocytaire et ses canalicules idéalisées au sein de la matrice extracellulaire. (Figure 1.15 droite)

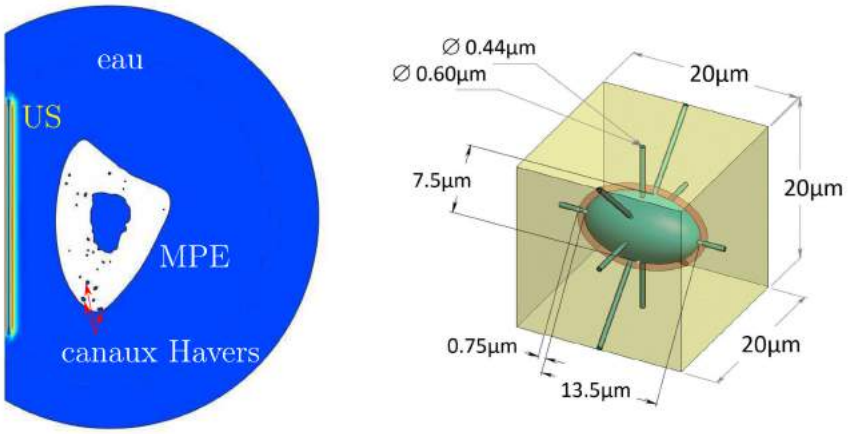

FIGURE 1.15 – Modèles aux échelles méscopique (à gauche) et microscopique (à droite). MPE : matrice poroélastique.

À l'échelle du tissu ou échelle mésoscopique - On considère tout d'abord un modèle 2D permettant de simuler une stimulation ultrasonore équivalente à celle induite par Exogen (f = 1 MHz, pression = 67 kPa, duty cycle = 20 %, durée du pulse = 1 ms, Øtransducteur = 10 mm) sur un seul cycle de 1 ms et de mesurer les effets de l'interaction des ultrasons avec le tissu osseux (Figure 1.15 gauche). Le tissu osseux est ici représenté par un milieu biphasique : un fluide (assimilé à de l'eau) dans la porosité vasculaire (canaux de Havers) reconstruite à partir d'images RX et une matrice poroélastique (MPE) intégrant la contribution de la porosité lacuno-canaliculaire. Les caractéristiques de ce matériau anisotrope et poroélastique sont empruntées à la littérature [COWIN et al., 2009; NGUYEN et NAILI, 2012; SCHEINER et al., 2015]. La propagation des ultrasons à travers cette matrice poroélastique est représentée par un modèle de Biot. La propagation d'ondes en milieux poreux dans le domaine temporel a été implémentée dans Comsol en formulation faible par Vu-Hieu Nguyen. Les tissus mous environnants sont modélisés par un domaine fluide

entourant l'os.
On mesure en sortie de simulation un gradient de pression dans le fluide interstitiel du réseau lacuno-canaliculaire entre l'endoste (interface entre l'os et le canal médulaire) et le périoste (interface entre l'os et les tissus mous environnants), dans l'axe du transducteur émetteur (Figure 1.16). Cette valeur sera utilisée comme donnée d'entrée dans le modèle d'ostéocyte.

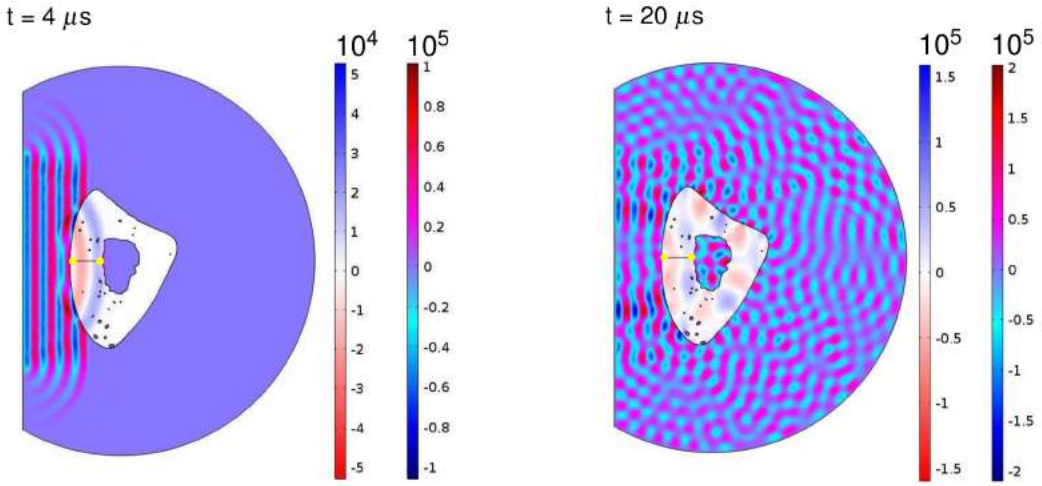

FIGURE 1.16 – Pression acoutique et pression du fluide interstitiel (Pa). Le gradient de pression du fluide interstitiel est évalué entre les 2 points jaunes.

À l'échelle de l'osteocyte ou échelle microscopique - On considère un modèle 3D représentant un ostéocyte unique inclus dans la matrice extracellulaire. On distingue trois milieux (Figure 1.15 droite) :

— en bleu, l'osteocyte composé d'un corps cellulaire ellipsoidal et de ramifications tentaculaires cylindriques modélisé par un solide élastique (module d'Young E = 4,47 kPa, rapport de Poisson ν = 0,3)

— en jaune, la matrice extracellulaire supposée solide élastique linéaire et isotrope (E = 16,6 GPa, ν = 0,38)

— en orange, le fluide interstititiel qui remplit l'espace entre l'ostéocyte et la matrice supposé newtonien (masse volumique $\rho = 997\ kg/m^3$, viscosité $\mu = 885 \times 10^{-4}\ kg.m^{-1}.s^{-1}$).

Le modèle mésoscopique fournit une évaluation du gradient de pression induit par la stimulation ultrasonore dans le fluide interstitiel. Le modèle microscopique donne une estimation des contraintes de cisaillement générées par ce gradient de pression et de leur répartition au sein du fluide interstitiel.

Modèle multi-échelle et multiphysique - Le gradient de pression dans le fluide interstitiel induit par la stimulation ultrasonore a été évalué à 30 Pa/µm. Ce gradient de pression induirait une contrainte de cisaillement fluide maximale de 6 Pa, valeur en cohérence avec de récentes publications [ANDERSON et al., 2005; VERBRUGGEN et al., 2016]. Cependant plusieurs facteurs doivent être encore analysés :

— la simulation a été réalisée sur un cycle d'excitation de 1 ms, or le traitement est d'ordinaire de 15 minutes soit 900 000 cycles ! on peut donc s'attendre à observer un effet cumulatif de la répétition des cycles ;

— les propriétés de la matrice osseuse sont celles d'un os mature, or le protocole intervient à différents stades de cicatrisation et les ultrasons interagissent donc avec des tissus dont les propriétés varient au cours du temps ;

— la géométrie de l'ostéocyte est ici représentée par un ellipsoïde de section circulaire, or des études récentes sur de l'os humain montrent une forme plus aplatie selon une direction [VARGA et al., 2015] ;

— le comportement du fluide interstitiel a été supposé newtonien.

— etc.

Ces limitations seront explorées dans les années à venir (cf. § 2.1 p.27).

Ce travail a donné lieu à une présentation dans un congrès international en juillet 2016 (European Society of Biomechanics Congress 2016, Lyon, France). Les avancées de ce projet ont été présentées dans 2 congrès internationaux Interpore 2017 et ESUCB 2017 (European Symposium on Ultrasonic Characterization of Bone 2017).

1.3 Références

ALEXANDROV, A., C. MOLINA, J. GROTTA, Z. GARAMI, S. FORD, J. ALVAREZ-SABIN, M. J., M. SAQQUR, A. DEMCHUK, L. MOYE, M. HILL et A. WOJNER. 2004, «Ultrasound-Enhanced Systemic Thrombolysis for Acute Ischemic Stroke.», *New England Journal of Medecine*, vol. 351, p. 2170–2178. 16

ANDERSON, E. J., S. KALIYAMOORTHY, J. IWAN, D. ALEXANDER et M. L. KNOTHE TATE. 2005, «Nano-microscale models of periosteocytic flow show differences in stresses imparted to cell body and processes», *Annals of Biomedical Engineering*, vol. 33, p. 52–62. 20

AUBRY, J.-F., M. TANTER, M. PERNOT, J.-L. THOMAS et M. FINK. 2003, «Experimental demonstration of noninvasive transskull adaptative focusing based on prior computed tomography scans.», *Journal of the Acoustical Society of America*, vol. 113, p. 84–93. 16

BALA, Y., E. LEFÈVRE, J.-P. ROUX, C. BARON, P. LASAYGUES, M. PITHIOUX, V. KAFTANDJIAN et H. FOLLET. 2016, «Pore network microarchitecture influences human cortical bone elasticity during growth and aging», *Journal of the Mechanical Behavior of Biomedical Materials*, vol. 63, p. 164–173. 12

BARON, C. 2005, *Le développement en série de Peano du matricant pour l'étude de la propagation d'ondes en milieux continûment variables - Peano expansion of the matricant to study elastic wave propagation in continuously heterogeneous media*, thèse de doctorat, Universite Bordeaux 1, France. 7

BARON, C. 2011, «Propagation of elastic waves in an anisotropic functionally graded hollow cylinder in vacuum», *Ultrasonics*, vol. 51, p. 123–130. 7

BARON, C. 2012, « Using the gradient of human cortical bone properties to determine age-related bone changes via ultrasonic guided waves», *Ultrasound in Medicine and Biology*, vol. 38, p. 972–981. 8

BARON, C., J. AUBRY, M. TANTER, S. MEAIRS et M. FINK. 2009, «Simulation of intracranial acoustic fields in clinical trials of sonothrombolysis», *Ultrasound in Medicine & Biology*, vol. 35, p. 1148–1158. 17

BARON, C. et S. NAILI. 2010, «Propagation of elastic waves in a fluid-loaded anisotropic functionally graded waveguide : Application to ultrasound characterization», *Journal of Acoustical Society of America*, vol. 127, p. 1307–1317. 7

BARON, C., M. TALMANT et P. LAUGIER. 2007, «Effect of porosity on effective diagonal stiffness coefficients (c_{ii}) and anisotropy of cortical at 1 MHz : A finite-difference time domain study», *Journal of the Acoustical Society of America*, vol. 122, p. 1810–1817. 6

BERNARD, S., Q. GRIMAL et P. LAUGIER. 2013, «Accurate measurement of cortical bone elasticity tensor with resonant ultrasound spectroscopy», *Journal of the Mechanical Behavior of Biomedical Materials*, vol. 18, p. 12–19. 13

BERNARD, S., G. MARRELEC, P. LAUGIER et Q. GRIMAL. 2015, «Bayesian normal modes identification and estimation of elastic coefficients in resonant ultrasound spectroscopy», *Inverse Problems*, vol. 31, n° 6, p. 065 010. 13, 14

BERNARD, S., J. SCHNEIDER, P. VARGA, P. LAUGIER, K. RAUM et Q. GRIMAL. 2016, «Elasticity–density and viscoelasticity–density relationships at the tibia mid-diaphysis assessed from resonant ultrasound spectroscopy measurements», *Biomechanics and modeling in mechanobiology*, vol. 15, n° 1, p. 97–109. 13

BOSSY, E., M. TALMANT et P. LAUGIER. 2004, «Three-dimensional simulations of ultrasonic axial transmission velocity measurement on cortical models», *Journal of Acoustical Society of America*, vol. 115, p. 2314–2324. 5, 8

BOUSSON, V., A. MEUNIER, C. BERGOT, E. VICAUT, M. A. ROCHA, M. H. MORAIS, A.-M. LAVAL-JEANTET et J.-D. LAREDO. 2001, «Distribution of intracortical porosity in human midfemoral cortex by age and gender», *Journal of Bone and Mineral Reasearch*, vol. 16, p. 1308–1317. 8

CHAN, C. W., L. QIN, K. M. LEE, M. ZHANG, J. C. Y. CHENG et K. S. LEUNG. 2006, «Low intensity pulsed ultrasound accelerated bone remodeling during consolidation stage of distraction osteogenesis», *Journal of Orthopaedic Research : Official Publication of the Orthopaedic Research Society*, vol. 24, n° 2, p. 263–270. 17

COWIN, S. C., G. GAILANI et M. BENALLA. 2009, «Hierarchical poroelasticity : movement of interstitial fluid between porosity levels in bones», *Philosophical Transactions of the Royal Society of London A : Mathematical, Physical and Engineering Sciences*, vol. 367, n° 1902, p. 3401–3444. 19

DAFFERTSHOFER, M., A. GASS, P. RINGLEB, M. SITZER, U. SLIWKA, T. ELS, O. SEDLACZEK, W. J. KOROSHETZ et G. HENNERICI. 2005, «Transcranial low-frequency ultrasound-mediated thrombolysis in brain ischemia : increased risk of hemorrhage with combined ultrasound and tissue plasminogen activator : results of a phase II clinical trial», *Stroke*, vol. 36, p. 1441–1446. 16

DUARTE, L. R. 1983, «The stimulation of bone growth by ultrasound», *Archives of orthopaedic and traumatic surgery*, vol. 101, n° 3, p. 153–159. 17

FRANGI, A. F., W. J. NIESSEN, K. L. VINCKEN et M. A. VIERGEVER. 1998, «Multiscale vessel enhancement filtering», dans *Medical Image Computing and Computer-Assisted Intervention — MICCAI'98*, édité par W. M. Wells, A. Colchester et S. Delp, Lecture Notes in Computer Science, Springer Berlin Heidelberg, p. 130–137. 11

GRIMAL, G., K. RAUM, A. GERISCH et P. LAUGIER. 2011, «A determination of the minimum sizes of representative volume elements for the prediction of cortical bone elastic properties.», *Biomechanics and Modeling in Mechanobiology*, vol. OnLineFirst^{TM}, p. 1–13. 8

HECKMAN, J. D., J. P. RYABY, J. MCCABE, J. J. FREY et R. F. KILCOYNE. 1994, «Acceleration of tibial fracture-healing by non-invasive, low-intensity pulsed ultrasound», *The Journal of Bone and Joint Surgery. American Volume*, vol. 76, nº 1, p. 26–34. 17

KLEIN-NULEND, J., A. D. BAKKER, R. G. BACABAC, A. VATSA et S. WEINBAUM. 2013, «Mechanosensation and transduction in osteocytes», *Bone*, vol. 54, nº 2, p. 182–190. v, 18

LEBEDEV, A. V. 2002, «Method of linear prediction in the ultrasonic spectroscopy of rock», *Acoustical Physics*, vol. 48, nº 3, p. 339–346. 13

LEFÈVRE, E., P. LASAYGUES, C. BARON, C. PAYAN, F. LAUNAY, H. FOLLET et M. PITHIOUX. 2015, «Analyzing the anisotropic Hooke's law for children's cortical bone», *Journal of the Mechanical Behavior of Biomedical Materials*, vol. 49, p. 370–377. 12, 13

MAYR, E., V. FRANKEL et A. RÜTER. 2000, «Ultrasound – an alternative healing method for nonunions ?», *Archives of Orthopaedic and Trauma Surgery*, vol. 120, nº 1-2, p. 1–8. 17

MIGLIORI, A., J. SARRAO, W. M. VISSCHER, T. BELL, M. LEI, Z. FISK et R. LEISURE. 1993, «Resonant ultrasound spectroscopic techniques for measurement of the elastic moduli of solids», *Physica B : Condensed Matter*, vol. 183, nº 1–2, p. 1–24. 13

MOILANEN, P., M. TALMANT, P. NICHOLSON, S. CHENG, J. TIMONEN et P. LAUGIER. 2007, «Ultrasonically determined thickness of long cortical bones : Three-dimensionnal simulations of in vitro experiments.», *Journal of Acoustical Society of America*, vol. 122, p. 2439–2445. 8

MÉZIÈRE, F., P. JUSKOVA, J. WOITTEQUAND, M. MULLER, E. BOSSY, R. BOISTEL, L. MALAQUIN et A. DERODE. 2016, «Experimental observation of ultrasound fast and slow waves through three-dimensional printed trabecular bone phantoms», *The Journal of the Acoustical Society of America*, vol. 139, nº 2, p. EL13–18. 9

NGUYEN, V.-H. et S. NAILI. 2012, «Simulation of ultrasonic wave propagation in anisotropic poroelastic bone plate using hybrid spectral/finite element method», *International Journal for Numerical Methods in Biomedical Engineering*, vol. 28, nº 8, p. 861–876. 19

OLIVER, W. et G. PHARR. 1992, «An improved technique for determining hardness and elastic modulus using load and displacement sensing indentation experiments», *Journal of Materials Research*, vol. 7, nº 06, p. 1564–1583. 14

SCHEINER, S., P. PIVONKA et C. HELLMICH. 2015, «Poromicromechanics reveals that physiological bone strains induce osteocyte-stimulating lacunar pressure», *Biomechanics and Modeling in Mechanobiology*. 19

SCHORTINGHUIS, J., B. STEGENGA, G. M. RAGHOEBAR et L. G. M. D. BONT. 2003, «Ultrasound Stimulation of Maxillofacial Bone Healing», *Critical Reviews in Oral Biology & Medicine*, vol. 14, nº 1, p. 63–74. 17

SHUVALOV, A. 2003, «A sextic formalism for three-dimensional elastodynamics of cylindrically anisotropic radially inhomogeneous materials», *Proceedings of the Royal Society of London A.*, vol. 459, p. 1611–1639. 7

SHUVALOV, A., O. PONCELET, M. DESCHAMPS et C. BARON. 2005, «Long-wavelength dispersion of acoustic waves in transversely inhomogeneous anisotropic plates», *Wave Motion*, vol. 42, p. 367–382. 7

STROH, A. N. 1962, «Steady state problems in anisotropic elasticity», *Journal of Mathematics and Physics*, vol. 41, p. 77–103. 7

VARGA, P., B. HESSE, M. LANGER, S. SCHROF, N. MÄNNICKE, H. SUHONEN, A. PACUREANU, D. PAHR, F. PEYRIN et K. RAUM. 2015, «Synchrotron X-ray phase nano-tomography-based analysis of the lacunar-canalicular network morphology and its relation to the strains experienced by osteocytes in situ as predicted by case-specific finite element analysis», *Biomechanics and Modeling in Mechanobiology*, vol. 14, n° 2, p. 267–282. 21

VERBRUGGEN, S. W., T. J. VAUGHAN et L. M. MCNAMARA. 2016, «Mechanisms of osteocyte stimulation in osteoporosis», *Journal of the Mechanical Behavior of Biomedical Materials*, vol. 62, p. 158–168. 20

Chapitre 2

Projet de Recherche

« Ce n'est qu'un combat, il faut continuer le début »

Coluche

Sommaire

Introduction

Les travaux de ces 5 dernières années ont abouti à la caractérisation multi-échelle de l'os enfant non-pathologique. L'objectif de cette recherche était de fournir une base de données de référence pour améliorer le diagnostic des pathologies osseuses et adapter les traitements thérapeutiques. L'idée était de donner un point de comparaison entre un os sain et un os atteint d'une pathologie. Il reste bien sûr bien des choses à explorer, cependant on peut considérer que nous avons fourni les premières valeurs caractéristiques définissant la *qualité* de l'os enfant. Ces résultats peuvent maintenant être utilisés pour traiter des problématiques cliniques liées au remodelage osseux telles que la fracture, la distraction osseuse ou encore les métastases osseuses.
Comme évoqué dans le chapitre précédent, les ultrasons peuvent être utilisés comme vecteur de diagnostic mais également comme vecteur thérapeutique : les modalités ultrasonores ont donc un potentiel *théranostique*.
Bien qu'observés cliniquement, les effets des ultrasons sur le processus de régénération osseuse, lors d'une fracture par exemple, demeurent mal compris. Il n'existe aucun modèle capable d'expliquer les mécanismes physiques qui régissent l'activation du remodelage osseux par une stimulation ultrasonore. L'objectif de ce projet est de comprendre ces mécanismes pour adapter le dispositif thérapeutique et à terme le coupler à un système d'évaluation ultrasonore de la qualité mécanique de l'os régénéré. L'utilisation des ultrasons est particuièrement stratégique en pédiatrie de part leurs caractéristiques non-vasives, non-irradiantes et non-ionisantes. Par ailleurs, les dispositifs ultrasonores sont portables et de faible coût. On peut donc envisager, comme c'est le cas de l'Exogen (cf. § 1.2.2), un traitement au lit du patient ou encore à domicile, ce qui pour de jeunes patients peut s'avérer particulièrement recommandé.
Concevoir un dispositif ultrasonore théranostique adapté à la pratique pédiatrique et capable d'individualiser le traitement et le suivi diagnostic en temps réel : voilà le défi auquel j'ai décidé de contribuer.

Dans ce chapitre, nous abordons l'interaction des ultrasons avec les tissus biologiques **vivants** : c'est-à-dire que les ultrasons modifient les processus cellulaires des tissus ciblés. C'est un changement de paradigme important. Après avoir étudié comment les ultrasons **ré-agissent** avec le tissu osseux, dans ce cas la question et la réponse sont ultrasonores et l'os est *inerte* ; je propose d'analyser comment les ultrasons **agissent** sur le tissu osseux, dans ce cas la question est ultrasonore et la réponse est cellulaire, l'os est *vivant*. **La pierre angulaire de ce projet est la compréhension de la *mécanotransduction ultrasonore* des cellules osseuses**. Sur ce principe, on peut aborder plusieurs problématiques sur des lésions localisées : stimulation de cicatrisation fracturaire, stimulation de régénération de gros volume avec biomatériau (hydrogel), traitement des métastases osseuses. Dans tous les cas il s'agit de stimuler ou de ré-équilibrer le processus de remodelage osseux par une sollicitation mécanique ultrasonore.

2.1 Mécanotransduction ultrasonore de la régénération osseuse

2.1.1 Modèle numérique de stimulation ultrasonore de la cicatrisation osseuse

Amélioration du modèle numérique

Comme souligné précédemment le travail débuté sur la stimulation ultrasonore de la cicatrisation osseuse est un travail préliminaire qui a mis en évidence la pertinence du développement d'un modèle numérique.

Objectifs : Mieux comprendre les interactions des ondes ultrasonores avec le tissu osseux en cours de cicatrisation. Modélisation numérique (Comsol Multiphysics) et expérimentation (mécanique et ultrasonore).

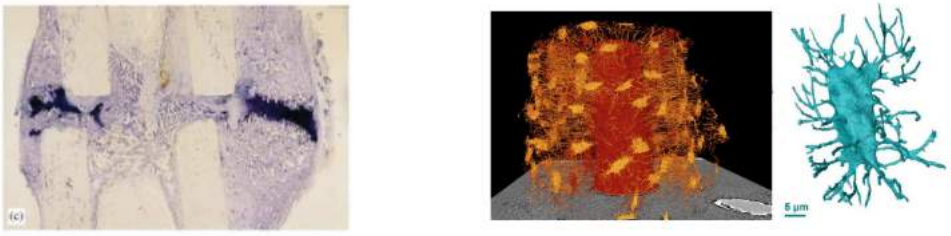

FIGURE 2.1 – Histologie d'un cal osseux [CLAES et HEIGELE, 1999] et images Synchrotron du réseau lacuno-canaliculaire (Creatis Lyon).

De nombreux points sont à l'étude, en voici quelques uns :

À l'échelle mésoscopique

- Géométrie et matériaux - Le premier modèle 2D développé considère une section d'os long dans un plan perpendiculaire à l'axe de l'os. On associe à cette géométrie un matériau dont les propriétés correspondent à de l'os sain et mature. Afin de considérer une géométrie de cal osseux plus réaliste (Figure 2.1 gauche), je me suis inspirée du modèle idéalisé décrit par BAILÓN-PLAZA et VAN DER MEULEN [2001]; CLAES et HEIGELE [1999]. Il s'agit d'un modèle 2D dans un plan contenant l'axe de l'os qui prend en compte la présence d'un cal osseux et distingue différents tissus en son sein (Figure 2.2).

  La répartition de ces différents tissus représente l'évolution de la cicatrisation. Une des hypothèses formulées dans la littérature est que la stimulation ultrasonore intervient préférentiellement au début du processus de cicatrisation et peu en phase de consolidation. Pour explorer cette hypothèse, je considèrerai différentes répartitions des tissus cicatriciels représentatives de différentes phases de cicatrisation. On pourra ainsi étudier l'interaction des ondes ultrasonores de type LIPUS sur ces configurations évolutives et déterminer à quel stade les effets de la stimulation ultrasonore sont les plus marqués. Par la suite, je me baserai sur des coupes histologiques ou de l'imagerie haute résolution sur modèle animal (proposée par Kay Raum, Charité – Universitätsmedizin Berlin) pour reconstruire la géométrie et la

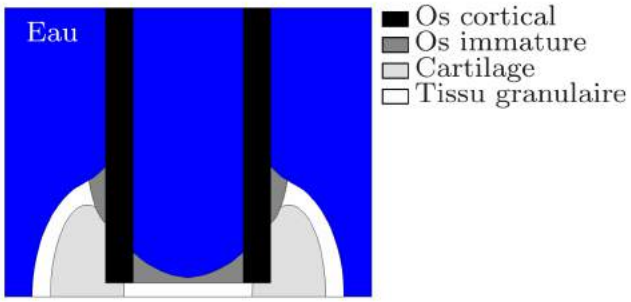

FIGURE 2.2 – Géométrie et composition du cal osseux.

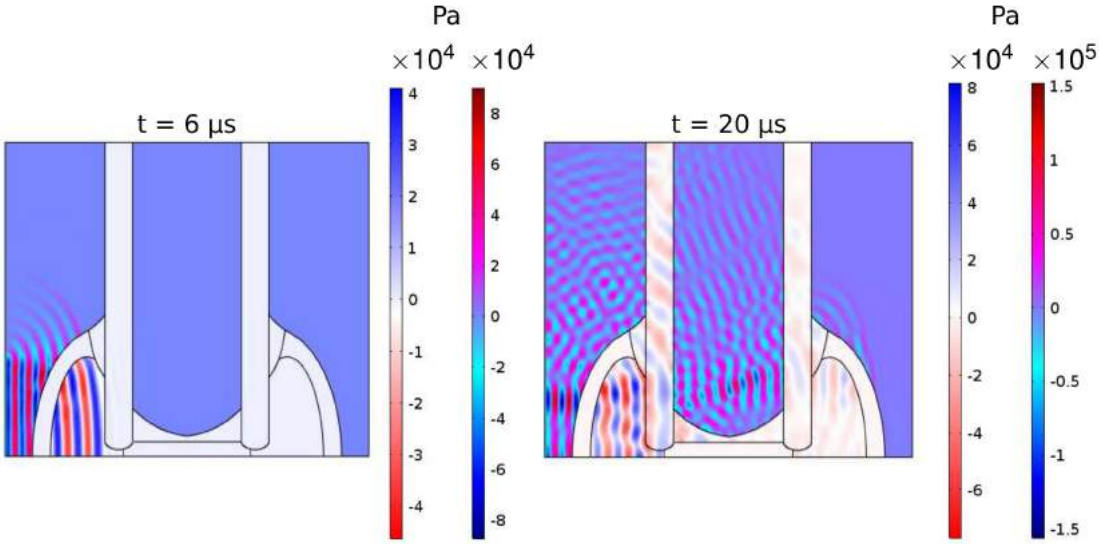

FIGURE 2.3 – Propagation des ondes US dans le cal osseux.

composition du cal osseux. D'autres propriétés caractéristiques des tissus biologiques peuvent également être intégrées pour enriichir le modèle et explorer d'autres mécanismes. L'absorption des tissux cicatriciels, de l'os et des tissus mous environnants ainsi que la piezoélectricité de l'os seront prises en compte très prochainement.

- Ondes pulsées - Un autre aspect important et qui nécessite des développements numériques est la prise en compte de la durée de traitement de 15 minutes, soit la répétition de 900 000 cycles et l'éventualité d'un effet cumulatif.
- Dynamique cellulaire - Il peut également être envisagé de coupler ce modèle avec des modèles de différenciation cellulaire [GONZÁLEZ-TORRES et al., 2010; ISAKSSON et al., 2007; PRENDERGAST et al., 1997]. Cependant, les échelles de temps sont différentes, 15 minutes pour la traitement par ultrasons contre plusieurs semaines pour la dynamique cellulaire. Il faut donc repenser le modèle numérique dans ce sens. C'est l'objet d'une reflexion menée avec Jean-Louis Milan, maître de conférences dans mon équipe et spécialiste de la modélisation de la mécanique cellulaire.

À l'échelle microscopique

- Géométrie et mécanique de l'ostéocyte - Le modèle d'ostéocyte que j'ai développé avec Carine Guivier-Curien (IRPHE UMR 7342 CNRS Aix-Marseille Université) est

très simplifié (cf. § 1.2.2). Pour l'améliorer, on peut par exemple s'inspirer des études morphométriques récentes réalisées sur de l'os humain, qui définissent plus précisément les dimensions de la lacune ostéocytaire [VARGA et al., 2015]. Pour autant, ces études n'ont pas été menées sur de l'os enfant. Il serait intéressant de le faire. Pour cela je me suis mise en relation avec Felix Ricoh (U1006 INSERM / Aix-Marseille Université) spécialiste de la microscopie à force atomique (AFM) sur les cellules. En s'inspirant des travaux de LIN et XU [2011] nous avons prévu de faire des images AFM du réseau lacuno-canaliculaire de l'os enfant et également d'évaluer les propriétés mécaniques (modules d'Young) de l'ostéocyte et de la matrice extracellulaire selon les 3 directions de l'espace.

- Morphométrie du réseau lacuno-canaliculaire - Un autre aspect à prendre en compte est bien évidemment l'effet du réseau lacuno-canaliculaire (Figure 2.1 droite), l'ostéocyte n'est pas isolé dans la matrice extracellulaire mais connecté à plusieurs dizaines d'autres ostéocytes. Lors de la présentation de mes travaux à congrès de l'IBDW/ESUCB (International Bone Densitometry Workshop et European Symposium on Ultrasonic Characterization of Bone) en juin 2017, Françoise Peyrin (CREATIS INSA Lyon) m'a proposé de me fournir des images haute résolution du réseau lacuno-canaliculaire. Nous avosn reçu ces images et sommes en train de les exploiter. Cela offre la possibilité de faire une étude morphométrique à l'aide du logiciel iMorph et des outils développés par Pierric Mora (cf. § 1.1.3.a.) et d'étudier le comportement du fluide dans ce réseau à l'aide du logiciel Comsol Multiphysics.
- Évaluation de la perméabilité du réseau lacuno-canaliculaire - La valeur de la perméabilité de ce réseau poreux reste sujet à polémique et un enjeu majeur pour la modélisation que je développe. La perméabilité est un paramètre clé pour comprendre la mécanotransduction, en effet il reflète à la fois la structure du milieu et les mécanismes du vivant. Une méthode traditionnelle de mesure expérimentale de la perméabilité est basée sur la loi de Darcy. Il s'agit de mesurer le volume de fluide traversant une unité de surface par unité de temps à travers une couche poreuse et de le diviser par le gradient de pression généré à travers la couche. À ce jour, cette mesure est inaccessible dans le réseau lacuno-canaliculaire. La perméabilité est donc estimée par des approches théoriques ou expérimentales couplées à des modèles numériques/analytiques et varie entre 10^{-17} et 10^{-25} m^2 [CARDOSO et al., 2013]. Les avancées récentes en imagerie RX fournissent une meilleure estimation de la morphométrie du réseau lacuno-canaliculaire en 3D et permettent ainsi d'améliorer la modélisation des flux. Le logiciel iMorph développé par Jérôme Vicente est déjà utilisé pour l'estimation de la perméabilité dans des mousses et des argiles et pourrait être adapté à l'estimation de la perméabilité du réseau lacuno-canaliculaire.
  Par ailleurs, je suis en contact avec Jean-Philippe Berteau en poste à la City University of New York dans le département du Professeur Stephen Cowin décédé cette année. L'équipe du Professeur Cowin compte parmi les spécialistes de la poroélasticité de l'os et de l'évaluation de sa perméabilité. J'ai participé au symposium organisé à sa mémoire à Rotterdam en mai dernier (Interpore 2017). J'y ai rencontré Luis Cardoso, professeur au City College of New York et responsable du Department of Biomedical Engineering proche collaborateur de Stephen Cowin. Collaborer avec eux sur la stimulation ultrasonore de la cicatrisation osseuse représenterait une opportunité à saisir.

Lorsque le modèle sera validé, nous pourrons alors procéder à une optimisation des paramètres ultrasonores. En effet les paramètres utilisés par Exogen sont des paramètres

historiques qui ont fait la preuve de leur innocuité et sont repris de publications en publications. Quelques études *in vitro* ou *in silico* ont exploré l'influence de la fréquence d'excitation ou de l'intensité délivrée mais à ce jour l'optimisation des paramètres de stimulation ultrasonore de la cicatrisation osseuse *in vivo* reste à effectuer.
Pour poursuivre ces travaux, j'ai l'intention de proposer très prochainement un sujet de thèse en co-encadrement avec Vu-Hieu Nguyen (MCF-HDR). Je suis également en relation avec Guillaume Haiat qui s'intéresse à la stimulation ultrasonore pour l'intégration d'implants dentaires.

2.1.2 Stimulation ultrasonore de la régénération osseuse de l'os distracté en présence d'un hydrogel

Ce projet a également trouvé une place dans le DEFI CNRS REPOUSSE porté par Martine Pithioux (ISM UMR 7287 CNRS Aix-Marseille Université) depuis janvier 2016 sur la régénération de gros volume osseux soutenue par l'implantation d'un hydrogel biomimétique du périoste (membrane osteoprogénitrice entourant l'os) et la stimulation ultrasonore du processus de réparation. Dans ce projet, les ultrasons n'interagissent plus uniquement avec le tissu osseux en régénération mais également avec le matériau biomimétique. Il s'agit d'une part d'optimiser la structure du biomatériau pour le rendre sensible à la stimulation ultrasonore et ainsi guider les processus cellulaires : colonisation, prolifération, différenciation et d'autre part d'adapter les paramètres ultrasonores pour favoriser la régénération osseuse. Sur la base du réseau de collaborations initié par ce projet, une demande de financement a été déposée pour la campagne ANR 2018.

Modèle numérique

Le modèle numérique sera fortement inspiré par celui développé pour étudier l'interaction des ultrasons avec une fracture osseuse sans biomatériau (cf. § 2.1.1). Il reste à définir les propriétés mécaniques et de structure du biomatériau afin de les intégrer de façon pertinente. Concernant la conception de l'hydrogel biomimétique, il est envisagé de concevoir une structure poreuse à gradient controlé, je pourrai ainsi utiliser les modèles que j'ai developpés sur la propagation des ondes ultrasonores dans des milieux à gradient de propriétés (cf. § 1.1.2).

Modèle expérimental *in-vitro*

Un premier modèle microfluidique simple sera conçu en collaboration avec Laurent Malaquin du LAAS (UPR 8001 CNRS Toulouse) pour avoir une idée des phénomènes induits par l'interaction des ondes ultrasonores de longueur d'onde millimétrique avec des canaux fluides micrométriques. La littérature sur le sujet est peu fournie.
Par la suite, un modèle de lacune ostéocytaire idéalisé devrait être réalisé par fabrication 3D (LiPhy UMR 5588 CNRS Université Grenoble Alpes et INSA Lyon).
L'enjeu est de coupler une résolution submicrométrique et une matrice de module d'Young comparable à celui de la matrice extracellulaire (15-20 GPa). Pour cela, nous envisageons de procéder en 2 étapes, un premier moule sera réalisé au LiPhy (UMR 5588 CNRS Université Grenoble Alpes) afin de reproduire la lacune ostéocytaire ellipsoidale et les canaliculi cylindriques, puis ce moule sera enrobé dans une matrice céramique puis dissous pour créer une cavité ostéo-canaliculaire. Une première étape a déjà été explorée au LiPhy (Figure 2.4).

FIGURE 2.4 – Fabrication 3D d'ostéocytes idéalisés par Olivier Stefan (LiPhy UMR 5588 CNRS Université Grenoble Alpes).

Dans un premier temps, cette cavité sera remplie de fluide (eau) et soumise à une excitation ultrasonore de type LIPUS. Les mesures seraient réalisées en externe. En parallèle, en collaboration avec Thierry Leïchle du LAAS (UPR 8001 CNRS Toulouse), nous réfléchissons à des dispositifs miniaturisés implantables dans la cavité.
Un autre aspect que nous souhaitons explorer avec Laurent Malaquin et Thierry Leïchlé est la caractéristique piezo-électrique de l'os qui pourrait être utilisée pour en faire un élément actif de la mesure et de l'excitation.
Par la suite, nous explorerons également, les interactions des ultrasons de type LIPUS avec l'hydrogel développé par Romain Debret et Jérôme Sohier au LBTI (UMR 5305 CNRS Université Claude Bernard Lyon 1) au sein d'un bioréacteur.

Modèle animal

Comme cela a été rapporté à plusieurs reprises dans la littérature, [PADILLA et al., 2014], les phénomènes induits par une stimulation ultrasonore *in vitro* sont très différents des phénomènes *in vivo*. C'est pourquoi il est particulièrement intéressant de confronter les résultats numériques à un modèle animal pour validation et optimisation. Comme mentionné précédemment, notre équipe développe un modèle animal (rat Sprague-Dawley) pour comprendre le processus de cicatrisation osseuse lors d'une distraction (=allongement). Nous sommes en contact avec la société Bioventus qui commercialise le système Exogen afin qu'ils nous fournissent un dispositif que nous pourrions tester sur les rats distractés et ainsi étudier les effets de la stimulation ultrasonore sur la cicatrisation *in-vivo*. Lorsque cette étape aura été validée, j'envisage de démarrer une étude sur patients en collaboration avec les chirurgiens orthopédistes de l'APHM (Assistance Publique des Hôpitaux de Marseille) membres de notre équipe (Pr Franck Launay).

2.1.3 Dispositif ultrasonore théranostique

L'étape suivante est de coupler un dispositif de diagnostic capable d'estimer le stade de réparation de la lésion osseuse (fracture, distraction, métastase). C'est l'objet d'un projet sur lequel je collabore avec Philippe Lasaygues (LMA UPR 7051 CNRS Marseille) sur la tomographie ultrasonore appliquée à l'os enfant. Sur ce sujet, nous avons encadré ensemble le stage de fin d'études de Jules Plisson (élève ingénieur de l'ENSIM, Le Mans) d'avril à août 2017. Je développe un modèle numérique (Comsol Multiphysics) reprenant les caractéristiques de son protocole expérimental d'antenne de tomographie US mis au

point au LMA. L'idée est d'optimiser la configuration expérimentale et de coupler la méthode d'acquisition à une méthode d'inversion issue de la géophysique développée par Dimitri Komatitsch (LMA UPR 7051 CNRS Marseille). Ceci améliorera la détection des lésions mais permettra également de les caractériser. On obtiendra ainsi un diagnostic plus quantitatif de la qualité osseuse et il deviendra alors possible d'adapter le traitement au mieux.
Après une validation *in vitro*, le modèle permettra de prendre en compte toute la complexité de la configuration *in vivo* (présence de tissus mous, os en paire, osteosarcome). Le couplage de cette modalité d'imagerie avec la stimulation ultrasonore de la régénération osseuse fait l'objet d'une lettre d'intention adressée à l'ANR.

2.2 Mécanotransduction ultrasonore des métastases osseuses

L'amélioration de la cicatrisation osseuse lors de fractures est une des illustrations des phénomènes de **mécanotransduction** induite par la sollicitation ultrasonore. Ce principe peut être appliqué dans le cas de la régénération de gros volumes osseux en présence de biomatériaux (cf. § 2.1.2) mais également pour traiter d'autres pathologies entrainant des lésions locales liées à des dysfonctionnements du remodelage osseux.

C'est sur la base de cette réflexion que j'ai proposé un projet qui a obtenu un financement de la Mission pour l'Interdisciplinarité du CNRS : SUBITO pour **S**timulation **U**ltrasonore **B**asse **I**ntensité pour la **T**hérapie **O**sseuse : application au traitement des tumeurs.

> Objectifs : Caractériser les interactions des ondes ultrasonores avec l'os métastasé : du tissu à la cellule. Modélisation numérique (Comsol Multiphysics) et expérimentation sur cultures cellulaires (mécanique et ultrasonore).

Ce projet, translationnel et interdisciplinaire, se focalisera sur le traitement de tumeurs osseuses par stimulation ultrasonore basse intensité (SUBI) appliquée avant et/ou après résection. Pour cela, il nous faut comprendre les mécanismes multiphysiques et multiéchelles qui sous-tendent les réponses tissulaire et cellulaire de l'os aux ultrasons pour les maîtriser et concevoir un outil thérapeutique innovant utilisable aussi bien en oncologie adulte que pédiatrique. Le projet regroupe des acousticiens (Philippe Lasaygues, LMA UPR 7051 CNRS), des physiciens (Felix Rico et Nicolas Buzhinsky, BioAFMLab, U1006 INSERM Aix-Marseille Université), des biomécaniciens (Carine Guivier-Curien, IRPHE UMR 7342 CNRS Aix-Marseille Université) et des biologistes (Jean-Claude Scimeca et David Momier, iBV UMR 7277 CNRS Inserm Université Côte d'Azur). Il comporte un volet numérique et un volet expérimental *in vitro*.

2.2.1 Métastases et remodelage osseux

Les tumeurs osseuses perturbent le (re)modelage osseux et provoquent une importante fragilisation de l'os entraînant des événements squelettiques graves (fractures, compression spinale, aplasie médullaire). Lutter contre l'affaiblissement de la résistance osseuse et favoriser la reconstruction de l'os après résection représentent des enjeux primordiaux dans le traitement du cancer. L'effet des ultrasons sur les métastases osseuses en tant que vecteur thérapeutique est mal connu et mérite d'être exploré. Un article récent analyse les effets de sollicitation ultrasonore de type LIPUS sur les cellules cancéreuses et conclut sur le potentiel bénéfique des ultrasons dans cette configuration [SAWAI

et al., 2012]. Cette tendance semble également confirmée par les travaux de thèse de Sophie Tardoski (Universté Claude Bernard - Lyon 1) [TARDOSKI, 2015].

2.2.2 Mécanotransduction ultrasonore : du tissu à la cellule

Le modèle que je développe pour la stimulation ultrasonore de la cicatrisation osseuse peut être adapté pour étudier l'interaction ultrasons/métastases osseuses. Ce modèle intégrera (i) la propagation d'ondes dans l'os, matériau poroélastique ; dans les tissus mous, fluides visqueux et dans les fluides biologiques (moelle et sang) ; (ii) les interactions fluides/structures à l'échelle de la cellule. Il fournira une évaluation du stimulus mécanique appliqué aux cellules osseuses en fonction des paramètres ultrasonores (fréquence, intensité, cycle, durée). La réaction biologique ainsi stimulée sera étudiée *in-vitro* sur culture cellulaire. Le projet explorera l'adaptation du protocole de SUBI de la régénération osseuse au traitement des tumeurs osseuses. Des protocoles originaux associant l'émission d'US et la co-culture de cellules osseuses avec des cellules tumorales seront mis en œuvre. La culture cellulaire sera réalisée sur des cellules humaines de différents types : - des ostéoclastes et ostéoblastes : cellules responsables respectivement de la résorption et de l'apposition osseuse ; - une lignée de carcinome mammaire (MDA-MB-231) et son sous-clone à tropisme osseux (MD-231BO). L'objectif est d'établir un lien entre les paramètres ultrasonores et la réponse des cellules osseuses et tumorales. Nous mesurerons la viabilité/prolifération (comptage, MTT/XTT) ainsi que le génotype/phénotype des cellules (quantification transcriptome/protéome, marquages immuno-histochimiques). En parallèle, nous procéderons à une caractérisation mécanique des conditions d'adhésion des cellules tumorales soumises à une SUBI par microscopie à force atomique. On envisage également d'étudier l'effet des US en complément d'un traitement aux bisphosphonates (Bps), traitement pratiqué dans le cas de patientes atteintes de cancer du sein (le partenaire iBV dispose déjà de biomatériaux chargés en BPs utilisables comme support de culture). L'enjeu est double : relier les paramètres de la SUBI imposée à l'échelle du tissu avec les contraintes perçues par les cellules osseuses à l'échelle microscopique et optimiser les paramètres ultrasonores pour favoriser la reconstruction osseuse sans provoquer la prolifération des cellules cancéreuses.

2.3 Références

BAILÓN-PLAZA, A. et M. C. VAN DER MEULEN. 2001, «A mathematical framework to study the effects of growth factor influences on fracture healing», *Journal of Theoretical Biology*, vol. 212, nº 2, p. 191–209. 27

CARDOSO, L., S. P. FRITTON, G. GAILANI, M. BENALLA et S. C. COWIN. 2013, «A review of recent advances in the assessment of bone porosity, permeability, and interstitial fluid flow», *Journal of biomechanics*, vol. 46, nº 2, p. 253–265. 29

CLAES, L. E. et C. A. HEIGELE. 1999, «Magnitudes of local stress and strain along bony surfaces predict the course and type of fracture healing», *Journal of Biomechanics*, vol. 32, nº 3, p. 255–266. v, 27

GONZÁLEZ-TORRES, L. A., M. J. GÓMEZ-BENITO, M. DOBLARÉ et J. M. GARCÍA-AZNAR. 2010, «Influence of the frequency of the external mechanical stimulus on bone healing : a computational study», *Medical Engineering & Physics*, vol. 32, nº 4, p. 363–371. 28

ISAKSSON, H., O. COMAS, C. C. VAN DONKELAAR, J. MEDIAVILLA, W. WILSON, R. HUISKES et K. ITO. 2007, «Bone regeneration during distraction osteogenesis : Mechano-regulation by shear strain and fluid velocity», *Journal of Biomechanics*, vol. 40, nº 9, p. 2002–2011. 28

LIN, Y. et S. XU. 2011, «AFM analysis of the lacunar-canalicular network in demineralized compact bone», *Journal of Microscopy*, vol. 241, nº 3, p. 291–302. 29

PADILLA, F., R. PUTS, L. VICO et K. RAUM. 2014, «Stimulation of bone repair with ultrasound : a review of the possible mechanic effects», *Ultrasonics*, vol. 54, nº 5, p. 1125–1145. 31

PRENDERGAST, P. J., R. HUISKES et K. SØBALLE. 1997, «Biophysical stimuli on cells during tissue differentiation at implant interfaces», *Journal of Biomechanics*, vol. 30, nº 6, p. 539–548. 28

SAWAI, Y., H. MURATA, K. KOTO, T. MATSUI, N. HORIE, E. ASHIHARA, T. MAEKAWA, S. FUSHIKI et T. KUBO. 2012, «Effects of low-intensity pulsed ultrasound on osteosarcoma and cancer cells», *Oncology Reports*, vol. 28, nº 2, p. 481–486. 32

TARDOSKI, S. 2015, *Traitement des métastases osseuses par association d'un bisphosphonate avec des ultrasons de faible intensité*, thèse de doctorat, Lyon 1. 33

VARGA, P., B. HESSE, M. LANGER, S. SCHROF, N. MÄNNICKE, H. SUHONEN, A. PACUREANU, D. PAHR, F. PEYRIN et K. RAUM. 2015, «Synchrotron X-ray phase nano-tomography-based analysis of the lacunar-canalicular network morphology and its relation to the strains experienced by osteocytes in situ as predicted by case-specific finite element analysis», *Biomechanics and Modeling in Mechanobiology*, vol. 14, nº 2, p. 267–282. 29

Conclusion

Douze ans après ma thèse, l'*idée* est plus *fixe* que jamais (cf. p.2) ! Je veux utiliser les ultrasons pour le vivant et contribuer au développement d'une application clinique théranostique. Ces quelques pages décrivent des interactions d'ondes ultrasonores avec le tissu osseux, matériau complexe, hétérogène, anisotrope, multi-échelle et **vivant**. On y aborde les ultrasons en tant qu'outil de diagnostic à l'échelle du tissu (caractérisation) et les ultrasons en tant que vecteur thérapeutique, déclencheur de réactions cellulaires (mécanotransduction). Les expériences résumées ici, du diagnostic de l'ostéoporose à la mécanotransduction ultrasonore de l'os en passant par la caractérisation de l'os en croissance, ont amené un changement de paradigme en introduisant la finalité d'une application clinique et en bousculant les priorités. Pour le praticien hospitalier, la priorité est de soigner. Pour le chercheur, la priorité est de comprendre. Peut-on soigner sans comprendre ? Bien sûr ! mais l'ambition est de comprendre pour **mieux** soigner : une meilleure caractérisation des lésions osseuses permettra une meilleure prise en charge thérapeutique, plus adaptée au patient ; une description éclairée de la mécanotransduction ultrasonore assurera un dosage pertinent de la stimulation par ultrasons ; la maîtrise de ces éléments ouvrira alors le champs des possibles et on pourra envisager d'autres applications. Au fil de ces années, j'ai collaboré avec des cliniciens, des biologistes, des physiciens, des biomécaniciens, des acousticiens dont les disciplines, lorsqu'elles se rencontrent, font avancer la connaissance.
Comprendre pour mieux soigner tel est l'enjeu de ma recherche aujourd'hui.

Chapitre 3

Curriculum Vitae

Sommaire

3.1 Curriculum Vitae

CNRS

2010 - **Chargée de Recherche**
Groupe Interdisciplinaire de Biomécanique des systèmes Ostéoarticulaire et Cardiovasculaire (GIBoc) Institut des Sciences du Mouvement - Etienne-Jules Marey (UMR 7287) - CNRS/Aix-Marseille Université.

Recherche : caractérisation mécanique de l'os en croissance. Interaction des ondes élastiques ultrasonores avec des milieux hétérogènes et en particulier les tissus biologiques : theragnostic.
Mots-clés : biomécanique, propagation d'ondes, milieux hétérogènes, multi-échelles, tissus biologiques, simulation numérique.

Congé parental du 19 janvier au 19 juillet 2013 (6 mois).

Université

2008 - 2010 **Maître de conférences en mécanique à l'Université Pierre et Marie Curie (Paris 6)**
Equipe Modélisation, Propagation et Imagerie Acoustique - Institut Jean le Rond d'Alembert (UMR 7190) - CNRS/UPMC Paris 6.

Propagation d'ondes élastiques guidées dans un tube anisotrope et hétérogène : application à la caractérisation de la fragilité osseuse.

PostDoctorat

2007 - 2008 **Attachée Temporaire d'Enseignement et de Recherche**
Laboratoire de Modélisation et Simulation Multi échelle (UMR 8208) - CNRS/Paris Est.
Réponse d'une plaque continûment variable immergée dans un fluide : application à la caractérisation ultrasonore de l'os cortical.
Collaboration : Salah Naili.

2006 - 2007 **Attachée Temporaire d'Enseignement et de Recherche**
Institut Langevin - Ondes et Images (UMR 7587) - CNRS/Paris 7.
Contrôle de l'innocuité de la sonothrombolyse dans le traitement des accidents vasculaires cérébraux ischémiques par simulation numérique.
Collaboration : Jean-François Aubry, Mickael Tanter.

2005 - 2006 **Post-doc CNRS**
Laboratoire d'Imagerie Biomedicale (UMR 7371) - CNRS/UPMC.
Etude de l'impact de la porosité sur le comportement élastique de l'os cortical en vue de l'évaluation de la fragilité osseuse. Elaboration d'un modèle numérique de l'os cortical : étude de l'interaction de l'os et des ondes ultrasonores.
Collaboration : Maryline Talmant, Quentin Grimal, Pascal Laugier.

Doctorat

2002 - 2005	**Thèse en mécanique université Bordeaux 1.** Institut de Mécanique et d'Ingénierie (UMR 5295) - CNRS/Bordeaux 1. *Le développement en série de Peano du matricant pour l'étude de la propagation des ondes élastiques en milieux à propriétés continûment variables* Directeur : Marc Deschamps ; encadrants : MM. O. Poncelet et A. L. Shuvalov. http ://tel.archives-ouvertes.fr/docs/00/11/39/51/PDF/These.pdf

Formation

2002	Diplôme d'ingénieur en Mécanique du CESTI SupMeca (Centre d'Etudes Supérieures des Techniques Industrielles) de Paris devenu ISMeP (Institut Supérieur de Mécanique de Paris). Diplôme d'Etudes Approfondies de Mécanique (option fluides) de Paris 6 (mention Bien).
1997 - 1999	Classes préparatoires MPSI-MP au lycée M. Montaigne à Bordeaux (33).

Enseignement

2015 - 2016	**Vacation** (30h/an) Polytech - Aix-Marseille université - TP Ondes electromagnétiques (1ère année). - TD Programmation Matlab (4ème année).
2011 - 2012	**Vacation** (20h/an) Polytech - Aix-Marseille université - TD Ondes electromagnétiques (1ère année).
2010 - 2012	**Vacation** (20h/an) IUT Saint Jérôme - Aix-Marseille université - Cours et TP Résistance des matériaux : application aux tissus biologiques et biomatériaux (L2).
2008 - 2010	**MCF** (192h/an) UPMC Paris 6 - Cours Méthodologie appliquée à la mécanique et à l'ingénierie (L1) ; - TD Mécanique du solide rigide (L2) ; - TD Mécanique des milieux continus (fluides et solides) (L3) ; - Cours et TP Initiation à MatLab et Comsol Multiphysics (M1) ; - Cours Acoustique dans les fluides (M2) ; - TP Atelier logiciel : modélisation éléments finis sous Comsol Multiphysics (M2) ; - Cours - TD Ondes et Vibrations 3ème ème année de l'Ecole Polytechnique Universtaire ; - Encadrement de projets (M1) : *Caractérisation ultrasonore de la paroi d'un anévrisme.*
2007 - 2008	**ATER** (96 h) Université Paris 12 - Val de Marne : - TD et TP Mécanique Générale (L2) ; - TD Probabilités, théorie des distributions (L3) ; - TD Ondes Mécanique (M1).
2006 - 2007	**ATER** (96 h) Université Paris 7 : - TD Ondes et Acoustique (L2) ;

	- TP Optique Ondulatoire (L3) ; - TP Traitement des signaux aléatoires (M1).
2003 - 2005	**Monitorat** de Mécanique (128h) Université Bordeaux 1 : - TD Mécanique (L1) ; - TP CAO (Pro Engineer, modélisation 3D) et TP «Statique» ; - Cours Mathématique pour la Physique.

Encadrement

3 thèses	Jean-Philippe BERTEAU *Caractérisation multimodale des propriétés biomécaniques de l'os cortical de l'enfant au cours de la croissance* Emmanuelle LEFEVRE *Evaluation multi-échelle et multimodale de l'os en croissance* Marie SEMAAN *Reference values for the quality of non-pathological child bone*
1 post-doc	Pierric MORA *Analyse morphométrique de l'os cortical sous IMorph*
10 Stages	2 IUT Mesures Physiques 2 Licence Pro Maintenance et Technologie Biomédicales 6 Master 2/Ingénieur

Collaborations

ANR *MALICE*	LMA UPR 7051 CNRS, France Lyos U1033 INSERM Université de Lyon, France LVA INSA Lyon, France IUSTI UMR 6595 CNRS Aix-Marseille Université, France
DEFI CNRS *REPOUSSE*	LBTI UMR 5305 CNRS Université Claude Bernard Lyon 1, France LAAS CNRS, Toulouse, France MATEIS INSA Lyon, France. LiPhy UMR 5588 CNRS Université Grenoble Alpes, France
MI CNRS *SUBITO*	Carine Guivier-Curien de l'IRPHE (UMR 7342 CNRS Aix-Marseille Université) Philippe Lasaygues du LMA (UPR 7051 CNRS Marseille) Felix Rico et Nicolas Buzhinsky du BioAFMLab (U1006 INSERM Aix-Marseille Université) Jean-Claude Scimeca et David Momier de l'iBV (UMR 7277 CNRS INSERM Université Côte d'Azur, Nice)

GDR	MécaBio : *Mécanique des matériaux et fluides biologiques* (GDR 3570) animé par Gwennou Coupier (LiPhy UMR 5588 CNRS Université Grenoble Alpes) et Anne-Virginie Salsac (BMBI, UMR 7338 CNRS UTC Sorbonne Universités, Compiègne, France)
Autres	Vu-Hieu Nguyen et Salah Naili du laboratoire MSME (UMR 8208 CNRS UPEC UPEM, Créteil) sur le projet de stimulation ultrasonore de la cicatrisation osseuse Kay Raum du Julius Wolff Institute for Biomechanics and Musculoskeletal Regeneration, Université de Médecine Berlin, Allemagne Jean-Philippe Berteau de la City University of New York, Department of Biomedical Engineering, USA

Animations scientifiques

Congrès	Membre du comité d'organisation du 38ème congrès de la Société de Biomécanique les 4, 5 et 6 septembre 2013 à Marseille Membre du comité d'organisation 16th Anglo-French Physical Acoustics Conference (AFPAC) les 23, 24 et 25 janvier 2017 à Marseille
Vulgarisation	Fête de la Science 2011

Expertises scientifiques

Reviewer	Journal of the Acoustical Society of America Ultrasonics Journal of Composites
Jury	Thèse de Xiaodong DENG *Nondestructive evaluation of thermal sprayed coating by acoustic microscopy and eddy current testing* soutenue le 25 mars 2014 à l'INSA Lyon. Thèse de Antoisse ABDULATUF *Modélisation et simulation de la propagation d'ondes guidées dans des milieux élastiques en présence d'incertitudes. Application à la caractérisation ultrasonore.* soutenue le 11 juillet 2017 à l'UPEC Créteil.

3.2 Publications

1. Revues à comité de lecture
   - Y. Bala, E. Lefèvre, J-P. Roux, C. Baron, P. Lasaygues, M. Pithioux, V.Kaftandjian, H. Follet, 2016. *Pore Network Microarchitecture Influences Human Cortical Bone Elasticity During Growth and Aging.* Journal of the Mechanical Behavior of Biomedical Materials 63, 164-173.
   - K. Metwally, E. Lefèvre, C. Baron, R. Zheng, M. Pithioux, P. Lasaygues, 2016. *Measuring mass density and ultrasonic wave velocity : A wavelet-based method applied in ultrasonic reflection mode.* Ultrasonics 65, 10-17.
   - J-Ph. Berteau, E. Gineyts, M. Pithioux, C. Baron, G. Boivin, P. Lasaygues, P. Chabrand and H. Follet, 2015. *Ratio between mature and immature enzymatic cross-links impacts post-yiels cortical bone behavior : an insight into greenstick fractures of the child fibula.* Bone 79, 190-195.

— J-Ph. Berteau, C. Baron, M. Pithioux, F. Launay, P. Chabrand and P. Lasaygues, 2014. *In vitro ultrasonic and mechanic characterization of the modulus of elasticity of children cortical bone.* Ultrasonics 54, 1270-1276.

— E. Lefèvre, P. Lasaygues, C. Baron, C. Payan, F. Launay, H. Follet, M. Pithioux, 2015. *Analyzing the anisotropic Hooke's law for children's cortical bone.* Journal of the Mechanical Behavior of Biomedical Materials 49, 370-377.

— C. Baron, 2012. *Using the gradient of human cortical bone properties to determine age-related bone changes via ultrasonic guided waves.* Ultrasound in Medicine and Biology 38, 972-981.

— C. Baron, 2011. *Propagation of elastic waves in an anisotropic functionally graded hollow cylinder in vacuum.* Ultrasonics 51, 123-130.

— C. Baron, S. Naili, 2010. *Propagation of elastic waves in a fluid-loaded anisotropic functionally graded waveguide : Application to ultrasound characterization.* Journal of Acoustical Society of America 127, 1307-1317.

— C. Baron, J.-F. Aubry, M. Tanter, S. Meairs, M. Fink, 2009. *Simulation of intracranial acoustic fields in clinical trials of Sonothrombolysis.* Ultrasound in Medicine & Biology 35, 1148-1158.

— C. Baron, S. Naili, 2008, *Propagation d'ondes élastiques au sein d'un guide d'ondes élastiques anisotrope à gradient unidirectionnel sous chargement fluid.*, Comptes Rendus de Mécanique 336, 722-730.

— C. Baron, M. Talmant, P. Laugier, 2007. *Effect of porosity on effective diagonal stiffness cœfficients (c_{ii}) and elastic anisotropy of cortical bone at 1 MHz : a finite-difference time domain study.* Journal of Acoustical Society of America 122(3), 1810-1817.

— C. Baron, A.L. Shuvalov, O. Poncelet, M. Deschamps, 2007. *Impact of localized inhomogeneity on the surface-wave velocity and bulk-wave reflection in solids.* Ultrasonics 46, 1-12.

— A.L. Shuvalov, O. Poncelet, M. Deschamps, C. Baron, 2005. *Long-wavelength dispersion of acoustic waves in transversely inhomogeneous anisotropic plates.* Wave Motion, 42(4), 367-382.

2. Conférences invitées dans des congrès

— C. Baron, C. Guivier-Curien, V-H. Nguyen, S. Naili, 2017. *Bone repair and ultrasound stimulation : an insight into the interaction of LIPUS with the bone callus through a multiscale computational study.* 174th Meeting of the Acoustical Society of America 2017, La Nouvelle Orléans (USA).

3. Actes de colloque à comité de lecture

— M. Semaan, P. Mora, F. Launay, C. Baron, J. Vicente, M. Pithioux, 2017, *Cortical bone porosity enhancement by multiscale vessel filtering* in Proceedings of the 23^{rd} Congress of the ESB 2017.

— M. Semaan, P. Mora, P. Lasaygues, C. Payan, F. Launay, C. Baron, M. Pithioux, 2017, *Characterising small bone samples using RUS : Validation on adult bone towards children bone characterisation* in Proceedings of the 23^{rd} Congress of the ESB 2017.

— C. Baron, C. Guivier-Curien, V-H. Nguyen, S. Naili, 2016, *How to understand the effects of LIPUS on bone healing ? A multiscale computational investigation* in Proceedings of the 22^{nd} Congress of the ESB 2016, [hal-01345763 - version 1]

— Y. Bala, E. Lefèvre, J.-P. Roux, C. Baron, P. Lasaygues, M. Pithioux, V. Kaftandjian, H. Follet, 2016. *Pore Network architecture determines cortical bone elasticity during growth and aging*. ESB 2016, Osteoporosis International 27, S170.

— E. Lefèvre, P. Lasaygues, C. Baron, C. Payan, H. Follet, M. Pithioux, 2015. *Ultrasonic assessment of diagonal stiffness coefficients in children cortical bone*. 40^{th} Congress of the Société de Biomécanique Computer methods in biomechanics and biomedical engineering 18 (Suppl 1), 1978-1979.

— E. Lefèvre, C. Baron, M. Pithioux, 2014. *Structural and Behavioral Analysis of the Children Cortical Bone*. 39^{th} Congress of the Societe de Biomecanique, Computer methods in biomechanics and biomedical engineering 17 (Suppl 1), 60-61.

— S. Le Cann, T. Cachon, E. Viguier, C. Baron, L. Miladi, T. Odent, J.M. Rossi, P. Chabrand, 2014. *The influence of age and localization on pedicle fixation in immature porcine spines*. 39^{th} Congress of the Societe de Biomecanique, Computer methods in biomechanics and biomedical engineering 17 (Suppl 1), 66-67.

— E. Lefèvre, F. Duboeuf, C. Baron, M. Pithioux, H. Follet, 2014. *Mineral Density and Microhardness of Children Cortical Bone*. in Proceedings of the 7^{th} World Congress of Biomechanics.

— R. Zheng, E. Lefèvre, C. Baron, Ph. Lasaygues, 2013. *Thin bone sample assessment using ultrasonic transmitted signals based on wavelet processing method*. in Proceedings of the International Congress on Ultrasonics, 576-580.

— E. Lefèvre, C. Baron, M. Pithioux, 2013. *Evaluation of the elastic modulus of cortical bone : adaptation of experimental protocols to small samples*. 38^{th} Congress of the Société de Biomécanique, Computer methods in biomechanics and biomedical engineering 16 (Suppl 1), 328-329.

— J.-Ph. Berteau, M. Pithioux, C. Baron, E. Gineyts, H. Follet, Ph. Lasaygues, P. Chabrand, 2012. *Characterisation of the difference in fracture mechanics between children and adult cortical bone*. 37^{th} Congress of the Société de Biomécanique, Computer methods in biomechanics and biomedical engineering 15 (Suppl 1), 281-282.

— J.-Ph. Berteau, C. Baron, M. Pithioux, P. Chabrand, Ph. Lasaygues, 2012. *Children cortical bone characterisation : the ultrasonic issue.* Acoustics 2012, France [hal-00810619 - version 1].

— C. Baron, 2012. *Ultrasonic guided waves in cortical bone modeled as a functionally graded anisotropic tube.* Acoustics 2012, France [hal-00810617 - version 1].

4. Communications à des congrès, symposium

— C. Baron, C. Guivier-Curien, V-H. Nguyen, S. Naili, 2017. *Ultrasonic waves in anisotropic porous media : concrete and bone*. IBDW/ESUCB 2017, Bad Staffelstein (Allemagne).

— C. Baron, C. Guivier-Curien, V-H. Nguyen, S. Naili, 2017. *Bone repair and ultrasound stimulation : an insight into the interaction of LIPUS with the lacuno-canalicular network of cortical bone through a multiscale computational study*. Interpore 2017, Rotterdam (Pays Bas).

— C. Baron, 2016. *Ultrasonic waves in anisotropic porous media : concrete and bone*. Congrés Français d'Acoustique 2016, Le Mans (France).

— E. Lefèvre, C. Baron, C. Payan, P. Lasaygues, M. Pithioux, H. Follet, 2015. *Ultrasonic assessment of children's cortical bone anisotropy*. Congrès Français de Mécanique 2015, Lyon (France).

— E. Lefèvre, C. Baron, M. Pithioux, 2014. *Structural and Behavioral Analysis of the Children Cortical Bone.* 39^{th} Congress of the Societe de Biomecanique, Computer methods in biomechanics and biomedical engineering 17 (Suppl 1), 60-61.

— S. Le Cann, T. Cachon, E. Viguier, C. Baron, L. Miladi, T. Odent, J.M. Rossi, P. Chabrand, 2014. *The influence of age and localization on pedicle fixation in immature porcine spines.* 39^{th} Congress of the Société de Biomécanique, Computer methods in biomechanics and biomedical engineering 17 (Suppl 1), 66-67.

— E. Lefèvre, F. Duboeuf, C. Baron, M. Pithioux, H. Follet, 2014. *Mineral Density and Microhardness of Children Cortical Bone.* in Proceedings of the 7^{th} World Congress of Biomechanics.

— R. Zheng, E. Lefèvre, C. Baron, Ph. Lasaygues, 2013. *Thin bone sample assessment using ultrasonic transmitted signals based on wavelet processing method.* in Proceedings of the International Congress on Ultrasonics, 576-580.

— E. Lefèvre, C. Baron, M. Pithioux, 2013. *Evaluation of the elastic modulus of cortical bone : adaptation of experimental protocols to small samples.* 38^{th} Congress of the Société de Biomécanique, Computer methods in biomechanics and biomedical engineering 16 (Suppl 1), 328-329.

— J.-Ph. Berteau, M. Pithioux, C. Baron, E. Gineyts, H. Follet, Ph. Lasaygues, P. Chabrand, 2012. *Characterisation of the difference in fracture mechanics between children and adult cortical bone.* 37^{th} Congress of the Société de Biomécanique (SB) Computer methods in biomechanics and biomedical engineering 15 (Suppl 1), 281-282.

— J.-Ph. Berteau, C. Baron, M. Pithioux, P. Chabrand, Ph. Lasaygues, 2012. *Children cortical bone characterisation : the ultrasonic issue.* Acoustics 2012, France [hal-00810619 - version 1].

— C. Baron, 2012. *Ultrasonic guided waves in cortical bone modeled as a functionally graded anisotropic tube.* Acoustics 2012, France [hal-00810617 - version 1].

— C. Baron, M. Talmant, P. Laugier, 2006. *Impact of Microstructure on Elastic Behavior of Cortical Bone.* in IEEE Ultrasonics Symposium, 2116-2119.

— C. Baron, O. Poncelet, A. Shuvalov, M. Deschamps, 2003. *Calculation of the velocity spectrum of the vertically inhomogeneous plates by using series expansion of the matricant.* in Proceedings of the World Congress on Ultrasonics, 605-608.

5. Chapitres d'ouvrage

— Recherche
C. Baron, O. Poncelet, A.L. Shuvalov, M. Deschamps, 2013. Part I, Chapter 4 : Propagation in Continuously Stratified Media, in Materials and Acoustics Handbook, Wiley Editor.
C. Baron, O. Poncelet, A.L. Shuvalov, M. Deschamps, 2006. Chapitre 4 : Propagation en milieux à stratification continue, in Matériaux et Acoustique, Hermes, Editor.

— Enseignement
Y. Berthaud, C. Baron, F. Bouchelaghem, J-L. Le Carrou, B. Daunay, E. Sultan 2014 Mini manuel de Mécanique des solides - Cours et exercices corrigés ($2^{ème}$ édition Ed. Dunod).
Y. Berthaud, C. Baron, F. Bouchelaghem, J-L. Le Carrou, B. Daunay, E. Sultan 2009 Mini manuel de Mécanique des solides - Cours et exercices corrigés (Ed. Dunod).

3.3 Transfert technologique, relations industrielles et valorisation

Participation à un contrat de recherche ANR : MALICE (2012 - 2016)
Analyse multiéchelle de la croissance osseuse chez l'enfant : une approche conjointe par imagerie ultrasonore et modélisation biomécanique.
Co-encadrement de la thèse d'Emmanuelle Lefèvre. Responsable de la tâche *Numerical simulation of ultrasounds in children bone.*
Partenaires scientifiques : LMA (UPR CNRS 7051), ISM (UMR CNRS 7287), Lyos (UMR INSERM 1033), LVA (INSA Lyon).
Partenaires institutionnels : CNRS, INSERM, Aix-Marseille Université, Université Claude Bernard Lyon 1, Institut National des Sciences Appliquées de Lyon.

Participation à un projet de l'Institut Carnot Star : CROISSANCE (2016)
Amélioration du diagnostic lors d'une distraction osseuse.
Co-encadrement du post-doctorat de Pierric Mora.
Partenaires scientifiques : LMA (UPR CNRS 7051), ISM (UMR CNRS 7287), IUSTI (UMR CNRS 7343).
Partenaires institutionnels : Institut Carnot STAR, SATT Sud Est.

Participation au DHU - Imaging, projet financé par la fondation universitaire A*MIDEX et porté par le Professeur Eric Guedj. Ce projet allie la recherche en imagerie moléculaire à l'imagerie interventionnelle et regroupe l'ensemble des plateformes et modalités d'imagerie du site d'Aix-Marseille afin de favoriser les interactions diagnostiques et thérapeutiques au bénéfice des patients.
Financement d'un stage de M2 en co-encadrement avec Philippe Lasaygues sur la tomographie ultrasonore.

Chapitre 4

Morceaux choisis

Sommaire

4.1 JASA 2007

Journal of the Acoustical Society of America, 2007

Effect of porosity on effective diagonal stiffness cœfficients (c_{ii}) and elastic anisotropy of cortical bone at 1 MHz : a finite-difference time domain study.
C. Baron, M. Talmant, P. Laugier.
JASA 122(3), 1810-1817.

Effect of porosity on effective diagonal stiffness coefficients (c_{ii}) and elastic anisotropy of cortical bone at 1 MHz: A finite-difference time domain study

Cécile Baron,[a] Maryline Talmant, and Pascal Laugier
Université Pierre et Marie Curie-Paris 6, Laboratoire d'Imagerie Paramétrique, Paris F-75005, France and CNRS, LIP, Paris F- 75006, France

(Received 16 March 2007; revised 12 June 2007; accepted 21 June 2007)

Finite-difference time domain (FDTD) numerical simulations coupled to real experimental data were used to investigate the propagation of 1 MHz pure bulk wave propagation through models of cortical bone microstructures. Bone microstructures were reconstructed from three-dimensional high resolution synchrotron radiation microcomputed tomography (SR-μCT) data sets. Because the bone matrix elastic properties were incompletely documented, several assumptions were made. Four built-in bone matrix models characterized by four different anisotropy ratios but the same Poisson's ratios were tested. Combining them with the reconstructed microstructures in the FDTD computations, effective stiffness coefficients were derived from simulated bulk-wave velocity measurements. For all the models, all the effective compression and shear bulk wave velocities were found to decrease when porosity increases. However, the trend was weaker in the axial direction compared to the transverse directions, contributing to the increase of the effective anisotropy. On the other hand, it was shown that the initial Poisson's ratio value may substantially affect the variations of the effective stiffness coefficients. The present study can be used to elaborate sophisticated macroscopic computational bone models incorporating realistic CT-based macroscopic bone structures and effective elastic properties derived from μCT-based FDTD simulations including the cortical porosity effect. © *2007 Acoustical Society of America.* [DOI: 10.1121/1.2759165]

PACS number(s): 43.80.Ev, 43.80.Qf, 43.80.Jz, 43.80.Vj [FD] Pages: 1810–1817

I. INTRODUCTION

Quantitative ultrasound has received considerable interest in recent years for its potential to assess different bone properties that are relevant to predict bone fragility.

Axial transmission is a generic term to designate a variety of techniques devised to assess cortical bone using a linear arrangement of ultrasound emitters and receivers placed on top of the overlying soft tissue. A part of the ultrasonic energy is guided along the cortex and can be radiated at the interface between soft tissue and bone. Various technical implementations of the technique have been proposed at different frequencies in the range 250 kHz–1.25 MHz.[1–4]

Several wave types contribute to the total pressure field sensed by the receivers. The first arriving signal (FAS) is of special interest for *in vivo* assessment of cortical bone because it arrives prior to all other contributions, and therefore, can be easily determined from time-of-flight measurements of the signals received at different positions parallel to the interface.[5] The nature of the wave associated with the first arriving signal was found to change with increasing cortical thickness to wavelength ratio (Cort.Th/λ) from an S_0 Lamb mode for Cort.Th/$\lambda \ll 1$ to a lateral wave for Cort.Th/$\lambda \gg 1$.[6]

Recently, axial transmission approaches have been described that work in a low frequency range and exploit a later arriving signal, a slow guided wave mode, in addition to the FAS.[4,7,8] This guided wave mode is well described by the theory for guided waves in plate [fundamental antisymmetric (or flexural) guided wave].[2]

Clinical trials revealed the ability of these techniques in discriminating normal and osteoporotic subjects.[1,8,9] Clinical performances were enlightened by *in vitro* experiments. Experimental studies on excised human radii demonstrate the sensitivity of FAS velocity to porosity and degree of mineralization[5] and also to intrinsic elastic properties.[10] In addition, the velocity of the fundamental antisymmetric guided wave shows an exquisite sensitivity to cortical thickness.[11,12]

Another approach used to give insight into clinical performances is the modeling of ultrasound propagation in axial transmission configuration. Bone finite-difference time domain (FDTD) studies, using either a generic model of the structure (plate or tube models)[6,12] or bone structures reconstructed from three-dimensional x-ray tomography data, provided valuable insights into the relationships between ultrasound propagation characteristics (e.g., velocity of FAS or flexural mode) and bone properties such as cortical thickness and porosity. However, in these previous works, the models ignore the true local material properties, generic values were used instead.

We assume that the prediction capabilities of the computed tomography (CT) based finite-difference simulations may be enhanced with further refinements such as incorporating in the model individualized material properties.

[a]Electronic mail: norabelic@yahoo.fr

Bone is a poroelastic medium with a porous network filled with a fluid-like medium (marrow) embedded in an elastic tissue matrix. Cortical porosity mainly consists in an oriented network of Haversian canals of typically 50 μm diameter approximately aligned with the long axis of the bone and of resorption cavities around 50–200 μm in diameter. At a smaller scale, small transverse canaliculi and osteocytes lacunae (typically less than 10 μm diameter) also contribute to cortical porosity. Each Haversian canal is surrounded by a layered cylindrical structure, called osteon, of typically 200 μm diameter and between the osteons is the highly mineralized interstitial tissue. The wavelength in axial transmission is much longer than the typical size of these structures and the material properties required as input into the bone computational models are effective properties, the values of which are determined by the anisotropic elastic properties of the bone tissue matrix and by the oriented cortical porosity. First, the presence of pores inside the cortex induces a decrease of whole bone stiffness and density compared to stiffness and density of the bone matrix.[13] Second, due to its preferential orientation, the porous network contributes to the mechanical anisotropy of bone.[14] Progress in CT-based FDTD models requires knowing the effective individual material properties in which the effects of both cortical porosity and anisotropic elasticity are properly taken into account.

Scarce data on porosity-related anisotropic stiffness can be found in literature. Several experimental studies have investigated the impact of porosity on the longitudinal Young's modulus.[15–18] As these studies were reduced to axial direction, they did not provide any information on the contribution of porosity to the anisotropy. A few studies, based on experiments or micromechanics models have examined the dependence of effective anisotropic stiffness coefficients on tissue properties and especially on porosity. Dependence on porosity of four elastic moduli of cortical bone assumed to be transversally isotropic has been reported in a single experimental study.[13] Micromechanics provided comprehensive models of effective elastic properties of bone using various hypotheses to describe elastic properties of the bone matrix and the pore network.[14,19] In particular, Sevostianov *et al.*[14] have depicted the effect of porous network on overall stiffness coefficients of cortical bone assuming an isotropic bone matrix and identifying the effect of pore distribution. In the related field of composite media with unidirectional pores, a similar analysis was performed by Ichitsubo *et al.*[20] with an anisotropic matrix.

In this study, we report on microcomputed tomography (μCT) based FDTD simulations whereby the effective elastic properties are directly computed for individualized porous network of 19 cortical bone microstructures reconstructed from high resolution synchrotron radiation microtomography (SR-μCT). The bone matrix was modeled as a homogeneous anisotropic medium. As the elastic properties of the bone matrix were only partially documented in our samples, four built-in models were used for each specimen. The computational bone model for ultrasonic propagation in bone and the basis of the SR-μCT-based FDTD simulations are described in Sec. II. In Sec. III the results of the effective elastic properties are examined as a function of porosity for the different bone models. We close with a discussion of the limitations and potential extension of the current study.

II. MATERIALS AND METHODS

A. Samples

In this study we use a subset of 19 samples from a collection of human radii with soft tissue removed and previously assessed by different experimental techniques such as SR-μCT and scanning acoustic microscopy (SAM), which provided accurate data for cortical bone microstructure and estimates of material properties (density, stiffness) that were used to build the cortical bone models developed in the present paper.

Assessment of the microstructure was reported in Ref. 5. Small portions were cut in the postero-lateral zone of the distal radius. The dimensions were typically 10 mm long in the direction parallel to the bone axis and 8 mm long in the circumferential direction. These volumes were imaged by SR-μCT[21] at the European Synchrotron Radiation Facility (ESRF, Grenoble, France). The radiographs [two-dimensional (2D) projections] were recorded on a 1024×1024 charge-coupled device-based 2D detector and the voxel size was set to $10 \times 10 \times 10$ μm^3. From sets of 2D projections under different angles of view, three-dimensional reconstructions of the microstructure were obtained by tomography algorithm. The amount of mineral was 1082 ± 16 mg/cm^3 in the whole collection of samples.

Among the 19 samples considered in this study, 10 were previously studied by scanning acoustic microscopy at 50 MHz with a spatial resolution of 23 μm and a spatial sampling rate of 20 μm $\times$ 20 μm.[22] The section adjacent to the samples investigated by SR-μCT was scanned and a mapping of the acoustic impedance was provided. It was shown that the setup resolved Haversian canals larger than 25 μm. As a consequence, these measurements were representative of the impedance of the bone matrix at a scale of 20 μm. The acoustical impedance averaged over the whole set of specimens was found to be 8.1 ± 0.5 MRa.

B. Configuration of the simulation

Propagation of transient 1 MHz plane waves in the 3D reconstructed bone microstructures was computed using a FDTD code, SIMSONIC, developed in the laboratory and detailed elsewhere,[6,23] which computes a numerical solution to the 3D linear elastic wave propagation. The algorithm is based on Virieux scheme,[24] and uses first-order derivative in space and time.

The code requires the simulation box to be defined as right angle volume. Therefore, parallelepipedic volumes were extracted from the 3D SR-μCT reconstructed volumes (Fig. 1). The volume of the blocks analyzed in simulation with a spatial step of 20 μm varies from 9 to 36 mm^3, depending on the thickness of the sample.

A combination of symmetric boundary conditions (tangential velocities equal on both sides of the boundary and normal velocities null on the boundary) and/or antisymmetric boundary conditions (tangential velocities null on the bound-

FIG. 1. Three-dimensional porous network (pores are in grey) in a parallel-epipedic block extracted from the μCT reconstructed bone structure. On the right-hand side are shown a transverse and longitudinal cross section through the three-dimensional porous network. The preferential orientation of the pores is along the bone axis.

ary and normal velocities equal on both sides of the boundary) on the simulation domain was applied to ensure the propagation of compression and/or shear plane bulk waves. Perfectly matched layers (PML) on sides and edges of the simulation domain were used to avoid unphysical reflections.[25]

SimSonic provides the transient signals associated with transmission of 1 MHz bulk compression or shear waves through the reconstructed volumes. Typical signals are shown in Fig. 2. Plane bulk waves velocities were deduced from time of flight measurements by detection of first signal maximum.

C. Derivation of effective stiffness

Effective stiffness coefficients were derived from velocities of simulated pure bulk wave propagating in principal directions and from effective mass density. For cortical bone the general degree of anisotropy is that of orthotropic material symmetry,[26] which is characterized by nine independent stiffness coefficients. The stiffness matrix can expressed as follows using the abbreviated subscript notation:[27]

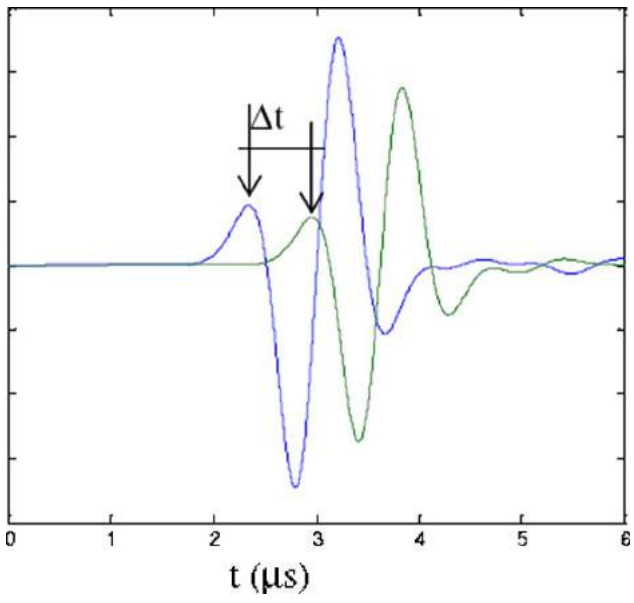

FIG. 2. (Color online) Velocity evaluation from the first maximum signal detection.

$$C = \begin{pmatrix} c_{11} & c_{12} & c_{13} & 0 & 0 & 0 \\ c_{12} & c_{22} & c_{23} & 0 & 0 & 0 \\ c_{13} & c_{23} & c_{33} & 0 & 0 & 0 \\ 0 & 0 & 0 & c_{44} & 0 & 0 \\ 0 & 0 & 0 & 0 & c_{55} & 0 \\ 0 & 0 & 0 & 0 & 0 & c_{66} \end{pmatrix} \quad \begin{matrix} \mathrm{X} \leftrightarrow 1 \\ \text{with } \mathrm{Y} \leftrightarrow 2\,, \\ \mathrm{Z} \leftrightarrow 3 \end{matrix} \quad (1)$$

where the X direction corresponds to the radial direction (i.e. thickness direction), the Y direction is the circumferential direction, and the Z direction is along the bone axis. But, as described by Katz,[28] the Haversian cortical bone is transverse isotropic in nature because of the locally uniaxial architecture of osteons. Consequently, numerous studies[29–31] assumed the cortical bone as a transverse isotropic elastic solid medium, which reduces the number of independent coefficients of the stiffness matrix to five. Considering transverse isotropy with (XY) as the isotropic plane,[32–34] the stiffness coefficients of $\mathbf{C}$ verify $c_{13}=c_{23}$, $c_{22}=c_{11}$, $c_{44}=c_{55}$, and $c_{66}=(c_{11}-c_{12})/2$.

When the waves propagate along principal directions of symmetry, the diagonal terms of the stiffness matrix c_{11}, c_{12}, and c_{33} are related to the phase velocity of compression-bulk wave which propagates along the X, Y, and Z direction, respectively, with

$$V_x = \sqrt{\frac{c_{11}}{\rho}}, \quad V_y = \sqrt{\frac{c_{22}}{\rho}}, \quad V_z = \sqrt{\frac{c_{33}}{\rho}}. \quad (2)$$

The stiffness coefficients c_{44} and c_{55} are related to the phase velocity of shear wave which propagate in Z direction and c_{66} in the transverse plane according to

$$V_{yz} = \sqrt{\frac{c_{44}}{\rho}}, \quad V_{xz} = \sqrt{\frac{c_{55}}{\rho}}, \quad V_{xy} = \sqrt{\frac{c_{66}}{\rho}}. \quad (3)$$

The effective stiffness coefficients were deduced from Eqs. (2) and (3) calculating the effective mass density ρ with the following rule of mixture:

$$\rho = \rho^0(1-p) + p\rho_w, \quad (4)$$

where ρ^0 is the mass density of the tissue matrix, ρ_w is the mass density of the fluid filling the pores (water), and p is the porosity.

D. Numerical bone models

Maps of the mass density and of the stiffness coefficients were used as input data in the software. The cortical bone was modeled as a two-phase medium constituted by the bone matrix and the fluid filling the pores. Each phase was supposed to be homogeneous within and between the samples. The spatial variation of density and stiffness in the simulation volume (spatial step of 20 μm) relies on the presence of the pores. Both components were clearly delineated by segmentation of the original reconstructed SR-μCT data and were defined by fixed mass density and stiffness coefficients.

TABLE I. Four bone matrix models.

	c_{33}^0 (GPa)	c_{11}^0 (GPa)	c_{33}^0/c_{11}^0	c_{13}^0/c_{11}^0	c_{55}^0/c_{11}^0	c_{66}^0/c_{11}^0
Model 1	34.3	34.3	1	0.43	0.29	0.29
Model 2	34.3	30.6	1.12	0.42	0.34	0.29
Model 3	34.3	27.3	1.26	0.42	0.38	0.31
Model 4	34.3	22.9	1.5	0.41	0.45	0.30

Ideal nonviscous fluid (water) was assumed to fill the pores. The mass density was (ρ_f=1 g/cm^3), and the stiffness coefficients were calculated from the following Lame's constants values (λ=2.25 GPa, μ=0 GPa).

Simulations in each bone sample microstructure were conducted with four different models of bone matrix shown in Table I. For the isotropic case (model 1), two independent stiffness coefficients are required (c_{33}^0, c_{13}^0) to define the elasticity of the bone matrix, and in the three transversely isotropic models (models 2–4), five independent stiffness coefficients are needed (c_{11}^0, c_{33}^0, c_{55}^0, c_{13}^0, and c_{12}^0). Here, the subscript zero is used to denote the intrinsic stiffness of the tissue matrix.

In all the models, the axial stiffness c_{33}^0 was taken close to 34 GPa, the overall mass density ρ^0 of the bone matrix mass 1.91 g/cm^3. These values were derived from SR-μCT and SAM data averaged over the samples that were investigated with these techniques. In Ref. 22, the mass density of the solid matrix was related by a second-order polynomial fit to the mineral amount. According to this, the mass density in our study was approximated to a value of 1.91 mg/cm^3, considering the mean value of mineralization previously measured and neglecting the intersample variations. The axial stiffness c_{33}^0=34.3 GPa was derived from acoustic impedance (Z=8.1 MRa) values measured at 50 MHz, with a resolution of 23 μm well adapted to spatial grid of the simulation (20 μm). The axial stiffness was derived using the relation

$$c_{33}^0 = \frac{Z^2}{\rho^0} \tag{5}$$

between acoustical impedance and density, with ρ^0 =1.91 g/cm^3. Because the standard deviation of the acoustic impedance over the samples was small and the variations of the mean value of the acoustic impedance were weak between the different regions investigated, a fixed value of c_{33}^0 was adopted within and between specimens. We choose to couple the numerical simulations to experimental data obtained on the same set of specimens investigated by both scanning acoustic microscopy and μCT. This might have resulted in stiffness values slightly higher than values reported in the literature.[13,35] We do not expect the trends reported here to be accurate in an absolute sense. However, since our main conclusion is based on the comparative performance of the models, the general trends reported here are expected to hold in a relative sense. All four models are built around the same value of c_{33}^0. It would be interesting to carry out a parametric study on the influence of this absolute value.

With models 2–4, transversely isotropic bone matrices with various degrees of anisotropy were explored. The value of the anisotropy ratio $AR_0=c_{33}^0/c_{11}^0$ was chosen in the range 1–1.5. The value of c_{11}^0 was therefore determined from the selected anisotropy ratio value. Moreover, for the three transversely isotropic matrix (models 2–4), the shear stiffness coefficient c_{55}^0 was fixed to 10.4 GPa.[36]

The other stiffness coefficients, c_{13}^0 and c_{12}^0, were derived from the relationship between Poisson's ratio and stiffness, assuming the bone matrix to be either isotropic (model 1) or transversely isotropic (models 2–4), with the following relationships:

$$\nu_L^0 = \frac{c_{13}^0}{c_{11}^0 + c_{12}^0}, \quad \nu_T^0 = \frac{c_{33}^0 c_{12}^0 - (c_{13}^0)^2}{c_{33}^0 c_{11}^0 - (c_{13}^0)^2}. \tag{6}$$

The longitudinal ν_L^0 and the transverse ν_T^0 Poisson's ratios were equal and set to a value of 0.3, a commonly used value in the literature.[37–39] Model 2 was build with AR^0=1.12, a value reported in Hofmann *et al.*[36] In model 3, a ratio of anisotropy c_{33}^0/c_{11}^0=1.26 was adopted, according to Turner's report.[37] In addition, we kept in this model the value of the longitudinal shear modulus given in Ref. 36 providing c_{55}^0.

Model 4 was used to enlarge the range of anisotropy ratio and AR^0 reaches the value of 1.5, the value of c_{33}^0 and c_{55}^0 remaining the same as in models 2 and 3.

E. Pore size and porosity

Figure 2 shows a typical 3D reconstruction of the porous network. To perform numerical simulation, the original grey scale reconstructions were segmented to yield binary mappings of the porous network. The segmentation threshold laid between the two well-separated distributions of pixel values

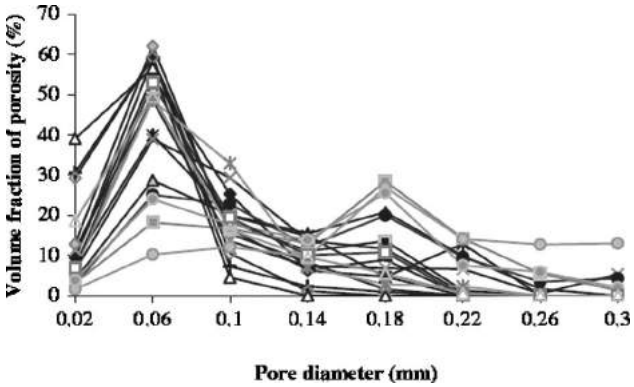

FIG. 3. Distribution of pores diameter through the 19 samples.

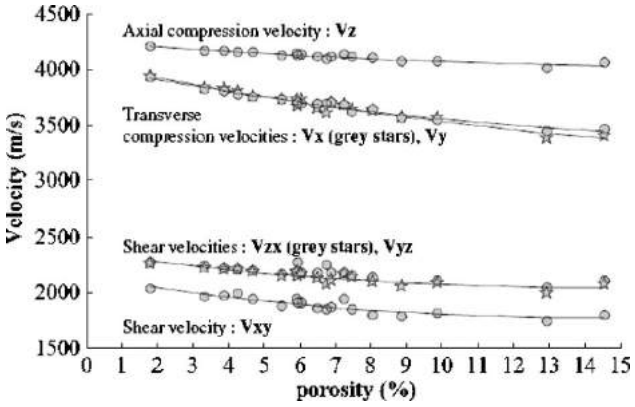

FIG. 4. Effective compression and shear bulk wave velocities deduced from FDTD simulations as a function of cortical porosity (model 2). The grey stars represent V_x and V_{zx}.

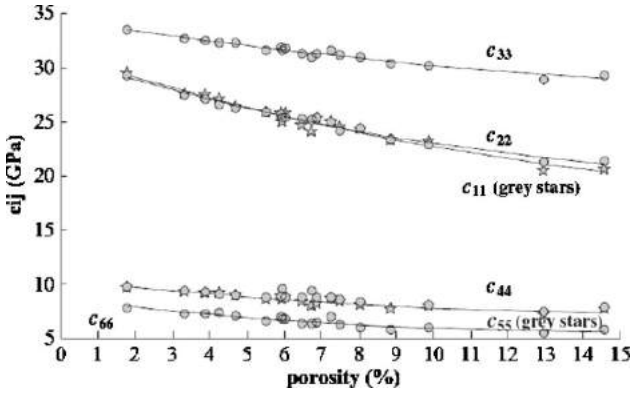

FIG. 5. Effective diagonal stiffness coefficients as a function of porosity (model 2).

corresponding to the bone tissue and to the empty pores. The porosity was defined for each specimen as the ratio of the volume of pores to the total bone volume. The pore area related to different pore diameters was estimated in each reconstructed tomographic cross section, and then the pore areas were summed over the cross sections and multiplied by the spatial step increment between two consecutive slices to obtain the porosity. The distribution of the porosity as function of pore diameters was deduced from the morphological analysis of the 19 reconstructed microstructures. In addition, structural parameters such as mean pore density (number of detected pores per mm^2) and mean pore diameter (the equivalent diameter was determined from the area of the individual canals) were extracted.

III. RESULTS

A. Pore size and porosity

Each of the 19 samples had a porosity falling in the range 2%–15%. The distribution of diameters for the 19 specimens illustrated in Fig. 3 shows a bimodal distribution with two pore classes, the 60- and the 180-μm-diam groups, as contributors to the porosity (Fig. 3). The spatial resolution of SR-μCT was not sufficient to resolve the smallest pores (osteocytes lacunae, canaliculi) of a few microns in diameter. A higher resolution (<10 μm) is needed to consistently visualize all cortical pores in human bone.[40]

The average porosity in these samples was about 7%, the average pore number density was 15 mm^{-2}, and the mean pore diameter was about 80 μm. These results are consistent with previous morphological studies on human cortical bone.[22,41]

B. Effective velocities and stiffness coefficients as a function of cortical porosity

Velocities of compression and shear bulk plane waves along the three principal axes of symmetry were computed for the 19 bone specimens and the 4 models. Figure 4 presents results for model 2. All the effective compression and shear bulk wave velocities decrease when porosity increases. However, the decrease was less pronounced for propagation along the long axis of the bone compared to the transverse directions. For a 10% increase in porosity, waves that propagate in the transverse plane undergo a decrease of 12% (470 m/s) for compression waves and 17% (370 m/s) for shear waves, while waves that propagate in the Z direction are reduced by 4% (160 m/s) for compression waves and 11% (260 m/s) for shear waves.

Similar trends of velocity variation versus porosity were observed for the four bone matrix models (Table II).

As a consequence of the decrease of both the effective mass density [Eq. (4)] and bulk wave velocities (Fig. 4) with the porosity, all the effective diagonal stiffness coefficients decline with the porosity as illustrated for model 2 in Fig. 5.

In all the bone models, a quadratic law between stiffness coefficients and porosity (ap^2+bp+c) was a better fit than a linear regression, although the first coefficient of the polynomial was small (see Table III).

TABLE II. Absolute (relative variation) of compression and shear waves velocities for a 10% increase of porosity (from 0 to 10%).

(m/s)	Compression waves in the transverse plane V_x and V_y	Compression wave in the axial direction V_z	Shear wave in the transverse plane V_{xy}	Shear waves in the axial direction V_{zx} and V_{yz}
Model 1	530 (12%)	190 (4.5%)	380 (17%)	250 (11%)
Model 2	470 (12%)	160 (4%)	370 (17%)	260 (11%)
Model 3	420 (11%)	150 (3.5%)	355 (17%)	200 (9%)
Model 4	350 (10%)	130 (3%)	320 (11%)	270 (11%)

TABLE III. Quadratic law variations of the diagonal stiffness coefficients vs porosity $c_{ii}=a(p\%)^2+bp\%+c$.

$AR^0=1.12$	c_{11}	c_{22}	c_{33}	c_{44}	c_{55}	c_{66}
a	0.024	0.026	0.011	0.004	0.013	0.014
b	−1.088	−1.047	−0.527	−0.232	−0.398	−0.412
c	31.15	30.82	34.37	10.14	10.47	80.60
R^2	0.97	0.98	0.96	0.80	0.88	0.88

C. Porosity contribution to effective anisotropy

The influence of porosity on effective stiffness is weaker in the axial direction (i.e., for c_{33} and for c_{44} and c_{55}) compared to the transverse directions (i.e., for c_{11} and c_{22} and for c_{66}), a result that contributes to the increase of the effective anisotropy as a function of porosity compared to the original elastic anisotropy of the bone matrix.

The effective anisotropy ratio ($AR=c_{33}/c_{11}$) normalized by the intrinsic anisotropy ratio of the bone matrix ($AR^0=c_{33}^0/c_{11}^0$) is plotted as a function of porosity for the four different bone models in Fig. 6. Normalized anisotropy ratios are consistently found to be greater than one and increasing with the porosity. The data indicate that the porosity contributes to the overall effective elastic anisotropy of bone structure. The higher the porosity, the higher its contribution to the bone elastic anisotropy. A 10% increase of porosity (from 0 to 10%) results in a relative increase of anisotropy ranging between 16% (for $AR^0=1.5$) and 20% (for the isotropic case) for the four bone matrix models studied.

Furthermore, the effective shear anisotropy ratio ($AR'=c_{55}/c_{66}$) increases with the porosity: For a 10% increase of porosity, the AR' is 16% greater for the isotropic case (model 1), 14% greater for models 2 and 3, and 12% greater for model 4.

The relative contribution of porosity to structural anisotropy of cortical bone is all the more important because the bone matrix is weakly anisotropic.

On the other hand, the other anisotropy ratios assessed by FDTD simulations (c_{ii}/c_{11}) were found to remain almost unchanged with the porosity.

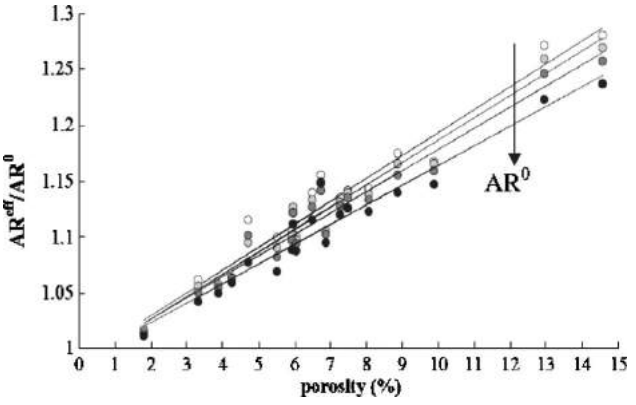

FIG. 6. Normalized effective anisotropy ratio (AR/AR_0) as a function of porosity for the different bone matrix models. Open circles correspond to the isotropic case (model 1), the light grey circles to model 2 ($AR^0=1.12$), the dark grey circles to model 3 ($AR^0=1.26$), and the closed circles to model 4 ($AR^0=1.5$).

IV. DISCUSSION

Our results suggest that the porous network introduces or reinforces transverse isotropy, as expected owing to its preferential orientation parallel to the bone axis. Indeed, it is noteworthy that the effect of porosity is similar for c_{11} and c_{22}, and for c_{44} and c_{55}. As pictured by Fig. 5, the differences between c_{11} and c_{22} and between c_{44} and c_{55} induced by the porous network were subtle: for example, $(c_{11}-c_{22})/c_{11}\leqslant 2\times10^{-4}$ for $p\leqslant 10\%$ and $(c_{11}-c_{22})/c_{11}\approx 4\times10^{-2}$ for $p\geqslant 10\%$. Therefore, if either isotropic (model 1) or transversely isotropic symmetry (models 2–4) is assumed for the tissue matrix, the introduction in the bone model of the oriented porous network resulted in a structure with effective transversely isotropic elastic properties. The result is consistent with the well-known effective macroscopic transverse isotropy of human cortical bone.[34,42–44]

However, two additional conditions, $c_{13}=c_{23}$ and $c_{66}=(c_{11}-c_{12})/2$, required by this symmetry could not be checked here because mixed-indices stiffness coefficients were not evaluated. The evaluation of the mixed-indices stiffness coefficients c_{12}, c_{13}, and c_{23} requires one either to rotate the sample or to record angular variation of transmitted bulk wave. In the first case, it would be necessary to modify the software to implement capabilities of working with material of more general anisotropy than orthotropy, and in the second case it would be necessary to implement a more sophisticated signal processing. As these tasks were not under the scope of this study, the stiffness coefficients c_{12}, c_{13}, and c_{23} were not evaluated. However, note that under the reasonable assumption of a macroscopic transverse anisotropy, c_{12} can be simply derived from the knowledge of c_{11} and c_{66} with $c_{66}=(c_{11}-c_{12})/2$.

Coupling μCT-based models of bone microstructure with FDTD simulations is a powerful means to compute the effect of porosity on effective stiffness and elastic anisotropy of bone. The high spatial resolution reached by SR-μCT allows an accurate determination of the porous network. However, the bone computational model also requires input data for the stiffness of the bone tissue matrix. Because the complete set of real data (five stiffness coefficients and mass density) for the bone matrix was not known, some hypotheses were made. The Poisson's ratios are not easy to determine experimentally and therefore are not known with accuracy, and an *a priori* value of 0.3 for the Poisson's ratios was assumed, following a commonly adopted assumption in many studies, especially finite element analyses,[45] despite the rather wide range of values, between 0.12 and 0.63, reported in literature.[31,42] Thus, one limitation of our study is related to the assumption adopted regarding the values of the

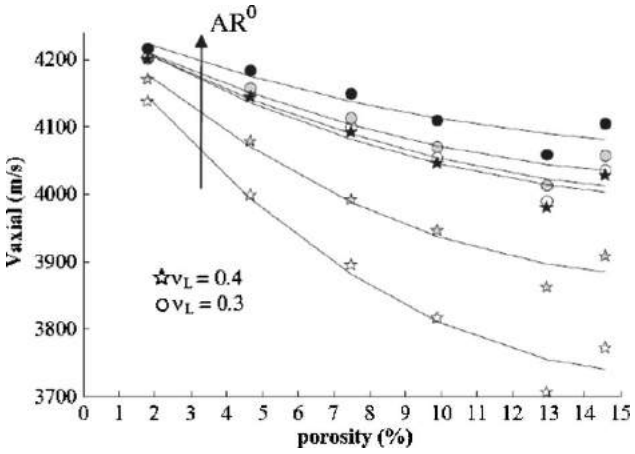

FIG. 7. Influence of the longitudinal Poisson's ratio on the dependence of the axial velocity on the cortical porosity. The stars represent the data obtained for ν_L=0.4 and the circles represent the data related to ν_L=0.3. The colors from white to black correspond to increasing AR^0 (model 1, model 2, and model 4).

Poisson's ratios, as mentioned in Raum *et al.*[22] Here, in a first step we have investigated the influence of the longitudinal Poisson's ratio value on the axial velocity as a function of porosity for model 1 (model 1 is isotropic, the longitudinal and transverse Poisson's ratios are equal), model 2, and model 4. For these bone models, the computations have been run with an input Poisson's ratio value of 0.4 instead of 0.3. The new Poisson's ratio value was properly taken into account by modifying the value of the stiffness coefficients c_{12}^0 and c_{13}^0 according to Eq. (6).

The influence of the Poisson's ratio value on the axial velocity is presented in Fig. 7. The increase of Poisson's ratio from 0.3 to 0.4 induces a stronger impact of porosity on axial velocity and a better differentiation of the behavior between the different anisotropy models. For a longitudinal Poisson's ratio of 0.3 and a 10% increase of porosity, the axial velocity decreases by 190 m/s (4%) for model 1, 165 m/s (4%) for model 2, and 130 m/s (3%) for model 4. When the longitudinal Poisson's ratio is fixed to 0.4, the impact of a 10% increase of porosity on the axial velocity is of 430 m/s (10%) for model 1, 300 m/s (7%) for model 2, and 200 m/s (5%) for model 4. Consequently, an accurate estimation of the Poisson's ratios or of the related stiffness coefficients, especially the mixed-indices ones, at the matrix level is critical for a reliable prediction of relative variation of ultrasound velocities as function of porosity. Advances in this field have been published recently.[31,45]

The present study permits a direct assessment of the effect of porosity on the stiffness coefficients of cortical bone. However, the morphology of the porous network is complex and requires several parameters to be fully characterized, including the size of the pores, pore density (number of pores per unit of area), spatial distribution of the pores, and shape of the pores.[46] The question arises as to whether these properties are determinant factors of the effective stiffness and the elastic anisotropy of cortical bone. Simplified models of porous networks were numerically built in order to better understand these effects for fixed values of porosity. Preliminary results (not shown here) suggest that the influence of morphological parameters is small. For example, with a simplified model with a periodic spatial distribution of cylindrical inclusions embedded in the bone matrix, with their axis parallel to the axis of the bone, only subtle difference of 2% in the axial compression velocity could be observed. However, more work is required to explore the consequences of morphological variations in the cortical porosity on effective elastic properties.

The results of the present study can be used to elaborate sophisticated macroscopic computational bone models incorporating realistic CT-based macroscopic bone structures and effective elastic properties derived from μCT-based FDTD simulations taking into account the effect of cortical porosity. These macroscopic computational bone models are of considerable interest as they can be used in order to evaluate the effect of porosity and of macroscopic bone structure on measured velocities in axial transmission. The frequency bandwidth (around 1 MHz) in this study is in the range of that typically used in some of the clinical settings. However, as mentioned in Sec. I, other devices are working at lower frequencies (around 250 kHz). Work on velocity frequency dispersion in cortical bone is sparse. Studying the frequency dependence of stiffness coefficients is potentially important. Therefore, specific attention must be paid in future works to the determination of phase velocity and amplitude in different frequency ranges.

V. CONCLUSION

The effect of oriented cortical bone porosity on ultrasound plane bulk wave velocities and elastic stiffness coefficients was investigated using transient numerical simulation of ultrasound plane bulk waves in 3D reconstructed microstructure of cortical bone samples. The effective stiffness coefficients were found to decrease with increasing porosity. The preferential orientation of the pore network along the bone axis induced an additional anisotropy (16%–20%) of the effective medium compared to the initial anisotropy of the bone tissue matrix. With initial Poisson's ratios values of 0.3, the variation of the effective anisotropy ratio was found to be fairly the same whatever the original anisotropy of the bone matrix was. However, the Poisson's ratio of the elastic bone matrix was found to be a critical determinant of the evaluation of relative variation of effective velocities and in turn of effective stiffness coefficients as a function of porosity.

[1]D. Hans, S. K. Srivastav, C. Singal, R. Barkmann, C. F. Njeh, E. Kantorovitch, C. C. Gluer, and H. K. Genant, "Does combining the results from multiple bone sites measured by a new quantitative ultrasound device improve discrimination of hip fracture?," J. Bone Miner. Res. **14**, 644–651 (1999).
[2]P. Moilanen, P. H. F. Nicholson, T. Kärkkäinen, Q. Wang, J. Timonen, and S. Cheng, "Assessment of the tibia using ultrasonic guided waves in pubertal girls," Osteoporosis Int. **14**, 1020–1027 (2003).
[3]E. Bossy, M. Talmant, M. Defontaine, F. Patat, and P. Laugier, "Bidirectional axial transmission can improve accuracy and precision of ultrasonic velocity measurement in cortical bone: A validation on test materials," IEEE Trans. Ultrason. Ferroelectr. Freq. Control **51**, 71–79 (2004).
[4]A. Tatarinov, N. Sarvazyan, and A. Sarvazyan, "Use of multiple acoustic wave modes for assessment of long bones: Model study," Ultrasonics **43**, 672–680 (2005).

[5]E. Bossy, M. Talmant, F. Peyrin, L. Akrout, P. Cloetens, and P. Laugier, "An in vitro study of the ultrasonic axial transmission technique at the radius: 1-MHz velocity measurements are sensitive to both mineralization and intracortical porosity," J. Bone Miner. Res. **19**, 1548–1556 (2004).
[6]E. Bossy, M. Talmant, and P. Laugier, "Three-dimensional simulations of ultrasonic axial transmission velocity measurement on cortical bone models," J. Acoust. Soc. Am. **115**, 2314–2324 (2004).
[7]F. Lefebvre, Y. Deblock, P. Campistron, D. Ahite, and J. J. Fabre, "Development of a new ultrasonic technique for bone and biomaterials in vitro characterization," Biomedical Materials Res. Part B, (Applied Biomaterials) **63**, 441–446 (2002).
[8]P. H. F. Nicholson, P. Moilanen, T. Kärkkäinen, J. Timonen, and S. Cheng, "Guided ultrasonic waves in long bone: Modelling, experiment and in vivo application," Physiol. Meas **23**, 755–768 (2002).
[9]R. Barkmann, E. Kantorovich, C. Singal, D. Hans, H. K. Genant, M. Heller, and C. C. Glüer, "A new method for quantitative ultrasound measurements at multiple skeletal sites: First results of precision and fracture discrimination," Clinical Densitometry **3**, 1–7 (2000).
[10]K. Raum, I. Leguerney, F. Chandelier, E. Bossy, M. Talmant, A. Saied, F. Peyrin, and P. Laugier, "Bone microstructure and elastic tissue properties are reflected in QUS axial transmission measurements," Ultrasound Med. Biol. **31**, 1225–1235 (2005).
[11]M. Muller, P. Moilanen, E. Bossy, P. H. F. Nicholson, V. Kilappa, J. Timonen, M. Talmant, S. Cheng, and P. Laugier, "Comparison of three ultrasonic axial transmission methods for bone assessment," Ultrasound Med. Biol. **31**, 633–642 (2005).
[12]P. Moilanen, V. Kilappa, P. Nicholson, J. Timonen, and S. Cheng, "Thickness sensitivity of ultrasound velocity in long bone phantoms," Ultrasound Med. Biol. **30**, 1517–1521 (2004).
[13]X. N. Dong and X. E. Guo, "The dependence of transverse elasticity of human femoral cortical bone on porosity," J. Biomech. **37**, 1281–1287 (2004).
[14]I. Sevostianov and M. Kachanov, "Impact of the porous microstructure on the overall elastic properties of the osteonal cortical bone," J. Biomech. **33**, 881–888 (2000).
[15]D. R. Carter and W. C. Hayes, "The compressive behaviour of bone as a two phase porous material," J. Bone Jt. Surg., Am. Vol. **59**, 954–962 (1977).
[16]J. D. Currey, "The effect of porosity and mineral content on the Young's modulus of elasticity of compact bone," J. Biomech. **21**, 131–139 (1988).
[17]T. S. Keller, Z. Mao, and D. M. Spengler, "Young's modulus, bending strength, and tissue physical properties of human compact bone," J. Orthop. Res. **8**, 592–603 (1990).
[18]S. Bensamoun, J.-M. Gherbezza, J.-F. de Belleval, and M.-C. Ho Ba Tho, "Transmission scanning acoustic imaging of human cortical bone and relation with the microstructure," Clin. Biomech. (Los Angel. Calif.) **19**, 639–647 (2004).
[19]X. N. Dong and X. E. Guo, "Prediction of cortical bone elastic constants by a two-level micromechanical model using generalized self-consistent method," J. Biomech. Eng. **128**, 309–316 (2006).
[20]T. Ichitsubo, M. Tane, O. Hirotsugu, M. Hirao, T. Ikeda, and H. Nakajima, "Anisotropic elastic constants of lotus-type porous copper: Measurements and micromechanics modeling," Acta Mater. **50**, 4105–4115 (2002).
[21]M. Salome, F. Peyrin, P. Cloetens, C. Odet, A.-M. Laval-Jeantet, J. Baruchel, and P. Spanne, "A synchrotron radiation microtomography system for the analysis of trabecular bone samples," Med. Phys. **26**, 2194–2204 (1999).
[22]K. Raum, R. O. Cleveland, F. Peyrin, and P. Laugier, "Derivation of elastic stiffness from site-matched mineral density and acoustic impedance maps," Phys. Med. Biol. **51**, 747–758 (2006).
[23]E. Bossy, F. Padilla, F. Peyrin, and P. Laugier, "Three-dimensional simulation of ultrasound propagation through trabecular bone structures measured by Synchrotron tomography," Phys. Med. Biol. **50**, 5545–5556 (2005).
[24]J. Virieux, "P-SV wave propagation in heterogeneous media: Velocity-stress finite-difference method," Geophysics **51**, 889–901 (1986).
[25]F. Collino and C. Tsogka, "Application of the PML absorbing layer model to the linear elastodynamic problem in anisotropic heterogeneous media," Geophysics **66**, 294–307 (2001).
[26]R. B. Ashman, S. C. Cowin, W. C. Van Burskirk, and J. C. Rice, "A continuous wave technique for the measurement of the elastic properties of cortical bone," J. Biomech. **17**, 349–361 (1984).
[27]B. A. Auld, *Acoustic Fields and Waves in Solids*, Rob E. Krieger Publishing Company (Malabar, FL 1973).
[28]J. L. Katz and K. Ukraincik, "On the anisotropic elastic properties of hydroxyapatite," J. Biomech. **4**, 221–227 (1971).
[29]H. S. Yoon and J. L. Katz, "Ultrasonic wave propagation in human cortical bone. II. Measurement of elastic properties and microhardness," J. Biomech. **9**, 459–462 (1976).
[30]J. L. Katz, "Anisotropy of Young's modulus of bone," Nature (London) **283**, 106–107 (1980).
[31]M. Pithioux, P. Lasaygues, and P. Chabrand, "An alternative ultrasonic method for measuring the elastic properties of cortical bone," J. Biomech. **35**, 961–968 (2002).
[32]W. C. Van Burskirk, S. C. Cowin, and R. N. Ward, "Ultrasonic measurements of orthotropic elastic constants of bovine femoral bone," J. Biomech. Eng. **103**, 67–71 (1981).
[33]J. L. Katz, H. S. Yoon, S. Lipson, R. Maharidge, A. Meunier, and P. Christel, "The effects of remodeling on the elastic properties of Bone," Calcif. Tissue Int. **36**, S31–S36 (1984).
[34]J. Y. Rho, "An ultrasonic method for measuring the elastic properties of human tibial cortical and cancellous bone," Ultrasonics **34**, 717–783 (1996).
[35]K. Hasegawa, C. H. Turner, and D. B. Burr, "Contribution of collagen and mineral to the elastic anisotropy of bone," Calcif. Tissue Int. **55**, 381–386 (1994).
[36]T. Hofmann, F. Heyroth, H. Meinhard, W. Fränzel, and K. Raum, "Assessment of composition and anisotropic elastic properties of secondary osteon lamellae," J. Biomech. **39**, 2282–2294 (2006).
[37]C. H. Turner, J. Y. Rho, Y. Takano, T. Y. Tsui, and G. M. Pharr, "The elastic properties of trabecular and cortical bone tissues are similar: Results from two microscopic measurement techniques," J. Biomech. **32**, 437–441 (1999).
[38]J. Y. Rho, P. Zioupos, J. D. Currey, and G. M. Pharr, "Microstructural elasticity and regional heterogeneity in human femoral bone of various age examined by nano-indentation," J. Biomech. **35**, 189–198 (2002).
[39]C. E. Hoffler, X. E. Guo, P. K. Zysset, and S. A. Goldstein, "An application of nano-indentation technique to measure bone tissue lamellae properties," J. Biomech. Eng. **127**, 1046–1053 (2005).
[40]D. M. L. Cooper, J. R. Matyas, M. A. Katzenberg, and B. Hallgrimson, "Comparison of microcomputed tomographic and microradiographic measurements of cortical bone porosity," Calcif. Tissue Int. **74**, 437–447 (2004).
[41]D. M. L. Cooper, A. L. Turinsky, C. W. Sensen, and B. Hallgrimsson, "Quantitative 3D analysis of the canal network in cortical bone by microcomputed tomography," Anat. Rec. **274B**, 169–179 (2003).
[42]D. T. Reilly and A. H. Burstein, "The elastic and ultimate properties of compact bone tissue," J. Biomech. **8**, 393–405 (1975).
[43]A. Ambardar and C. D. Ferris, "Compact anisotropic bone: Elastic constants, in vitro aging effects and numerical results of a mathematical model," Acta Biol. Acad. Sci. Hung. **29**, 81–94(1978).
[44]S. Lipson and J. L. Katz, "The relationship between elastic and microstructure of bovine cortical bone," J. Biomech. **17**, 231–240 (1984).
[45]R. Shahar, P. Zaslansky, A. A. Fiesem, J. D. Currey, and S. Weiner, "Anisotropic Poisson's ratio and compression modulus of cortical bone determined by speckle interferometry," J. Biomech. **40**, 252–264 (2007).
[46]D. M. L. Cooper, A. L. Turinsky, C. W. Sensen, and B. Hallgrimson, "Effect of voxel size on 3D micro-CT analysis of cortical bone porosity," Calcified Tissue Int. **80**, 211–219 (2007).

4.2 UMB 2009

Ultrasound in Medicine and Biology, 2009

Simulation of intracranial acoustic fields in clinical trials of Sonothrombolysis.
C. Baron, J.-F. Aubry, M. Tanter, S. Meairs, M. Fink.
UMB 35, 1148-1158.

Ultrasound in Med. & Biol., Vol. 35, No. 7, pp. 1148–1158, 2009

0301-5629/09/$–see front matter

doi:10.1016/j.ultrasmedbio.2008.11.014

● *Original Contribution*

SIMULATION OF INTRACRANIAL ACOUSTIC FIELDS IN CLINICAL TRIALS OF SONOTHROMBOLYSIS

CECILE BARON,* JEAN-FRANÇOIS AUBRY,* MICKAEL TANTER,* STEPHEN MEAIRS,† and MATHIAS FINK*

*Laboratoire Ondes et Acoustique, University Paris 7, Paris, France; and †Department of Neurology, Universitätsklinikum Mannheim, University of Heidelberg, Mannheim, Germany

(*Received* 13 *March* 2008, *revised* 5 *November* 2008, *in final form* 14 *November* 2008)

Abstract—Two clinical trials have used ultrasound to improve tPA thrombolysis in patients with acute ischemic stroke. The Combined Lysis of Thrombus in Brain Ischemia Using Transcranial Ultrasound and Systemic tPA (CLOTBUST) trial reported accelerated recanalisation of the middle cerebral artery (MCA) in patients with symptoms of MCA infarction, which were monitored with 2-MHz transcranial Doppler. In CLOTBUST, there was no increased bleeding as evidenced by cranial computed tomography. The Transcranial Low-Frequency Ultrasound-Mediated Thrombolysis in Brain Ischemia (TRUMBI) trial, which employed magnetic resonance imaging (MRI) before and after tPA thrombolysis, was discontinued prematurely because of an increased number of secondary hemorrhages, possibly related to the use of low frequency 300-kHz ultrasound. The purpose of our work is to help identify possible mechanisms of intracerebral hemorrhage resulting from sonothrombolysis by applying a simulation tool that estimates the pressure levels in the human brain that are produced with different sonothrombolysis devices. A simulation software based on a finite difference time domain (FDTD) three-dimensional (3D) scheme was developed to predict acoustic pressures in the brain. This tool numerically models the wave propagation through the skull and reproduces both ultrasound protocols of CLOTBUST and TRUMBI for analysis of the distribution of acoustic pressure in the brain during stroke treatment. For the simulated TRUMBI trial, we analyzed both a "high" and "low" hypothesis according to published parameters (for high and low amplitude excitations). For these hypotheses, the mean peak rarefactional pressures in the brain were 0.26 ± 0.2 MPa (high hypothesis) and 0.06 ± 0.05 MPa (low hypothesis), with maximal local values as high as 1.2 MPa (high hypothesis) and 0.27 MPa (low hypothesis) for configurations modelled in this study. The peak rarefactional pressure was thus higher than the inertial acoustic cavitation threshold in the presence of a standing wave in large areas of the brain, even outside the targeted clot. For the simulated CLOTBUST trial, the maximum peak negative pressure was less than 0.07 MPa. This simulated pressure is below the threshold for both inertial and stable acoustic cavitation but likewise lower than any acoustic pressure that has been reported as sufficient for effective sonothrombolysis. Simulating the pressure field of ultrasound protocols for clinical trials of sonothrombolysis may help explain mechanisms of adverse effects. Such simulations could prove useful in the initial design and optimization of future protocols for this promising therapy of ischemic stroke. (E-mail: norabelic@yahoo.fr) **© 2009 World Federation for Ultrasound in Medicine & Biology.**

Key Words: **Stroke, Ultrasound, Sonothrombolysis, Numerical simulation, Safety.**

INTRODUCTION

Stroke is now the second leading cause of death in industrialized countries. The great majority of strokes are ischemic (85%). This is generally due to a blood clot, which occludes a cerebral artery and causes brain necrosis in the territory of the supplying vessel. The key point in the treatment of ischemic stroke is the rapidity of the reperfusion to avoid irreversible damage of brain tissue and sequelae for the patient (Caplan 1999). So far, intravenous recombinant tissue plasminogen activator (tPA) is the only effective and approved treatment available for acute ischemic stroke, despite controversial results concerning the balance between its established beneficial thrombolytic effect and its potential neurotoxicity (Benchenane et al. 2004).

Several *in vitro* and *in vivo* (animal models) studies have revealed that ultrasonic exposure of clots (with $I_{SPTA.3}$ ranging from 700 to 1750 mW/cm^2) accelerates the effect of fibrinolytic agents over a wide range of frequencies (from 20 kHz to 2 MHz) (Kudo 1989; Lauer et al. 1992; Kornowski et al. 1994; Francis et al. 1995;

Address correspondence to: Cecile Baron, Laboratoire Ondes et Acoustique, CNRS, ESPCI, University Paris 7, INSERM, 10, rue Vauquelin, 75005 Paris, France. E-mail: norabelic@yahoo.fr

Behrens et al. 1999; Alexandrov et al. 2004; Daffertshofer et al. 2004). Mechanisms of ultrasound-accelerated tPA thrombolysis include reversible disaggregation of cross-linked fibrin fibers (Braaten et al. 1997), microcavity formation in the shallow layer of thrombus (Kondo et al. 1999) and increased uptake and penetration of tPA into clots (Francis et al. 1995). Cavitation, bubble formation in the rarefactional pressure zones, plays an important role in the production of such bioeffects (Blinc et al. 1993; Everbach and Francis 2000; Behrens et al. 2001; Meunier et al. 2007). Thermal effects may also contribute to ultrasound-assisted thrombolysis (Shaw et al. 2006)

Two clinical trials of sonothrombolysis for treatment of ischemic stroke have been reported. CLOTBUST (Combined Lysis of Thrombus in Brain Ischemia Using Transcranial Ultrasound and Systemic tPA) (Alexandrov et al. 2004) was a multicenter randomized clinical trial on 126 patients who had acute ischemic stroke due to occlusion of the middle cerebral artery (MCA). All patients were treated with intravenous tPA within 3 h after the onset of symptoms. Target patients received along with tPA, 2-MHz, pulsed wave transcranial Doppler monitoring for a duration of 2 h. A complete reperfusion or dramatic clinical recovery was observed for 49% of the patients in the target group (tPA + US) and for only 30% of the control group. No secondary effects linked with ultrasound exposure were identified.

Another clinical trial on sonothrombolysis, the TRUMBI trial (Transcranial Low-Frequency Ultrasound-Mediated Thrombolysis in Brain Ischemia), was stopped prematurely because of the occurrence of a higher number of intracerebral hemorrhages after tPA treatment combined with transcranial sonication at 300 kHz (Daffertshofer et al. 2005). Unlike the CLOTBUST study, rigorous MRI monitoring was performed in all patients and not just in those where control imaging after thrombolysis was warranted clinically. This led to detection of MRI evidence of hemorrhage in 93% of the target patients and 42% of the control patients in TRUMBI. Among these hemorrhages, all were classified as hemorrhagic transformation in the tPA only group versus 61% in the tPA plus ultrasound group. Five hemorrhages in the target group were symptomatic hemorrhages, possibly linked to ultrasound exposure.

The reasons for the different outcomes in these two clinical trials of sonothrombolysis are unclear. Indeed, experimental studies using animal models (Daffertshofer et al. 2004) were unable to demonstrate harmful secondary effects of ultrasound insonification using TRUMBI parameters. One report has suggested that hemorrhages in TRUMBI were related to abnormal permeability of the human blood-brain barrier that was induced by wide-field low-frequency insonation (Reinhard et al. 2006). Wang and coworkers (Wang et al. 2008) hypothesize that in TRUMBI a pulse length of 765 mm combined with a very wide beam can cause overlap many times as the wave runs its course back and forth across the brain, reflecting off the skull. Therefore, the instantaneous intensity of ultrasound in the brain tissue may multiply constructively at some localized sites of brain tissue, resulting in MIs that are larger than the maximum limit set by the Food and Drug Administration (FDA).

The purpose of our work is to better understand the brain pressure amplitude distribution involved in these studies through numerical simulations. This approach may allow localization of potential areas of acoustic cavitation and, thus, help explain mechanisms of adverse effects of sonothrombolysis.

MATERIALS AND METHODS

Ultrasound parameters from clinical studies of sonothrombolysis

All the pressure levels involved in the clinical studies (CLOTBUST or TRUMBI) have been deduced from data collected in various publications. Namely, peak negative pressure had to be deduced from the derated $I_{SPTA.3}$.

$$I_{SPTA.3} = P_{-}^2 / 2\rho c \quad (1)$$

ρ is the mass density and c is the ultrasound wave's velocity. The derating factor is fixed to 0.3 dB/cm-MHz and the derated intensities are noted with the index ''.3'' (AIUM/NEMA 1992). Due to the frequencies used in the clinical studies, the derated $I_{SPTA.3}$ has to be taken into account carefully in the CLOTBUST study whereas the value of $I_{SPTA.3}$ is very close to that of $I_{SPTA.3}$ in the TRUMBI protocol.

Assuming that the nonlinear effects are negligible in this configuration, we considered

$$P_{p2p} = 2P_{-} \quad (2)$$

P_{p2p} is the peak-to-peak acoustic pressure.

CLOTBUST study. The emitter was a 10 mm-diameter single element delivering a 2-MHz pulsed wave with duty cycle of 15% and short emission duration of 15 μs. The focusing was set in the ipsilateral hemisphere. The focal length depends on the targeted region: proximal (between 30 mm and 45 mm) or distal (more than 45 mm). At 45 mm away from the transducer, the derated spatial-peak time-averaged intensity, $I_{SPTA.3}$ was measured at 739 mW/cm^2 (Moehring et al. 2000) and a $I_{SPPA.3}$ of 4.9 W/cm^2. The corresponding pressure in water is, thus, equal to 0.385 MPa.

TRUMBI study. The diamond pattern transducer (50 mm diameter) emitted an unfocused pulsed ultrasound wave at 300 kHz modulated in frequency ($\pm$1.5 kHz) to

limit standing waves. The targeted zone was the contralateral brain hemisphere corresponding to a distance around 100 mm.

The emission parameters reported in (Daffertshofer et al. 2005) include a 5% duty cycle (corresponding to an emission duration of 500 μs) and a spatial-peak time-average intensity ($I_{SPTA.3}$) of 700 mW/cm^2 in water with a pulse repetition frequency of 100 Hz.

Taking into account the duty cycle, the spatial-peak pulse-average intensity ($I_{SPPA.3}$) was 14 W/cm^2, corresponding to a mechanical index (MI) in water of 1.18. However, the authors claim that the mechanical index was less than 0.2. Wang (2008) recently estimated the MI used in the TRUMBI study and concluded that the value given in (Daffertshofer et al. 2005) was wrong: the MI was 1.18 and the pressure was higher than the one expected by the authors of the TRUMBI study. However, a closer look at the description of the emission parameters given in (Daffertshofer et al. 2005) could be interpreted in another way: the 5% duty cycle has been added in order to ''further reduce thermal effects'' and was, thus, not taken into account in the evaluation of the 700 mW/cm^2 $I_{SPTA.3}$ in water, so that technically speaking, it corresponds to an $I_{SPPA.3}$ of 0.7 W/cm^2. This corresponds to the back-calculation of a mechanical index of 0.25.

To summarize, data given in (Daffertshofer et al. 2005) are not coherent: either the given MI is equal to 1.18 or it is equal to 0.2. Since it is unclear which interpretation of the published data is correct, both parameters will be evaluated in this study, according to two separated hypothesis.

High hypothesis. The MI is equal to 1.18. It corresponds to an $I_{SPPA.3}$ of 14 W/cm^2 . This hypothesis is supported by Wang et al (2008) and corresponds to the published $I_{SPTA.3}$ (Daffertshofer et al 2005). The corresponding pressure in water is, thus, equal to 0.65 MPa.

Low hypothesis. The MI is equal to 0.2. It corresponds to an $I_{SPPA.3}$ of 0.7 W/cm^2. This hypothesis is supported by the designers of the TRUMBI device and corresponds to the published MI value (Daffertshofer et al 2005). The corresponding pressure in water is, thus, equal to 0.15 MPa.

A frequency modulation was used in the TRUMBI study to avoid standing waves: 300 $\pm$ 1.5 kHz but no reference to the exact frequency modulation was given. Different frequency modulation options have, thus, been tested: ramp or sinusoidal modulation. Furthermore, in order to study the influence of the frequency modulation, various frequency ranges have been modelled (300 kHz; 300 $\pm$ 1.5 kHz; 300 $\pm$ 15 kHz; 300 $\pm$ 150 kHz).

Ultrasonic parameters of both CLOTBUST and TRUMBI studies are summarized in Table 1.

The mechanical index (MI)

In order to evaluate the likelihood of cavitation-related biological effects, the most relevant indicator was established to be the mechanical index (MI) (Apfel and Holland 1991). Indeed acoustic cavitation activity occurs in areas of rarefactional pressure and depends on the ultrasound frequency. The MI is defined as follows:

$$\mathrm{MI}=\frac{P_-}{\sqrt{f}} \tag{3}$$

with P_- the in situ peak rarefactional pressure in megapascal and f the ultrasound center frequency in megahertz.

In this study, as the simulation is taking into account the absorption in the tissues, the computed pressure corresponds to the in situ peak rarefactional pressure P_-. Equation 3, thus, enables to directly calculate the simulated MI.

To avoid adverse biologic effects related to acoustic cavitation, the FDA (FDA–510K) imposes the diagnostic devices to ensure a MI less than 1.9 (Dalecki 2004).

No adverse biologic effect induced by ultrasound alone on mammals has been recorded for MI $<$ 0.3 (AIUM/NEMA 1992). Nevertheless, this threshold may be lowered in the presence of tPA and clot and in a standing wave field.

Importantly, this definition of MI is only valid for single cycle pulses. As in previous publications (Daffertshofer et al. 2005; Wang et al. 2008), the MI will be used later in this article to analyse previous results. Significant work has been done on the influence of pulse duration and pulse repetition frequency on the safety of ultrasound-induced lung hemorrhage (O'Brien Jr 2007). Church and O'Brien Jr. introduced recently a modified MI taking into account the pulse length (Church and O'Brien Jr 2007). Basically, the threshold for cavitation decreases with pulse length and reaches a plateau for 10 cycles: the modified MI is three times higher than the classical one in water. All the MIs given in this article refer to conventional calculations (for one cycle pulses). As all pulses have much more than 10 cycles, such MIs do not reflect the exact biologic effects of ultrasound but only serve as reference for the readers in addition to the pressure levels.

The skull acoustical model

From high resolution computed tomography (CT) images, a three-dimensional (3D) portion of the skull is reconstructed. CT images were acquired with a GE Genesis CT scanner (GENESIS Medical Imaging, Inc., Huntley, Illinois, USA) (3 mm slice thickness, 1 mm between slices, slice resolution: 0.69 mm $\times$ 0.69 mm) at the Curie Institute Hospital (Paris, France). The Curie Institute institutional review board approved the imaging protocol and data was anonymized before transmission

Table 1. Parameters for the two trials

	CLOTBUST	TRUMBI
Number of patients	126	26
Transducer diameter (mm)	10	50
Focused/unfocused	yes	no
Distance of the target (mm)	Proximal (30-45) Distal (>45)	100
Frequency (MHz)	2	0.3
Emission duration (μs)	15	500
Pulse repetition frequency (MHz)	0.1	0.0001
I_{SPPA} (W/cm^2)	4.9	14 (high hypothesis) 0.7 (low hypothesis)
Peak negative pressure in water	0.385	0.65 (high hypothesis) 0.15 (low hypothesis)

CLOTBUST = Combined Lysis of Thrombus in Brain Ischemia Using Transcranial Ultrasound and Systemic tPA; TRUMBI = Transcranial Low-Frequency Ultrasound-Mediated Thrombolysis in Brain Ischemia.

to the Laboratoire Ondes et Acoustique. All measurements and simulations were performed on one female skull. Patient data protection regulations for this study do not allow disclosure of ethnic group or age. As previously described in (Aubry et al. 2003), the acoustical properties of the skull are then deduced from the raw CT data.

The brain acoustical model

The brain is considered as soft tissue with an acoustical behavior close to that of water (Wells 1977):

$$\rho_{\text{brain}} = 1000\text{kg/m}^3;\ c_{\text{brain}} = 1500\text{m/s} \tag{4}$$

The brain is an absorbing medium, the absorption coefficient depends on the ultrasound frequency and was set to (Goss et al. 1978).

$$\text{abs}_{\text{brain}} = 0.5\text{dB/cm/MHz} \tag{5}$$

Thus, in our simulations the brain is modelled by a homogeneous absorbing medium.

Simulation code

Three-dimensional (3D) finite simulations have been performed in order to evaluate pressure field distributions and pressure levels in the brain. Simulations were performed with a C++ finite differences program developed at the Laboratoire Ondes et Acoustique (UMR CNRS 7587, Paris, France). The scalar heterogeneous wave equation with loss absorption (eqn 6) was discretized with a second order in space and second-order centered in time scheme. A fourth order approximation Higdon absorption boundary (Higdon 1991) condition was used on computation volume borders to avoid unphysical reflections (reflections are typically 40 dB lower than the incident wave field over a wide range of incidence angles).

$$\left(1+\tau(\vec{r})\frac{\partial}{\partial t}\bullet\right)\left[\rho(\vec{r})\,\nabla\bullet\left(\frac{1}{\rho(\vec{r})}\nabla\, p\,(\vec{r},t)\right)\right] - \frac{1}{c(\vec{r})^2}\frac{\partial^2 p\,(\vec{r},t)}{\partial\, t^2} = S(\vec{r},t) \tag{6}$$

where $c(\vec{r})$is the speed of sound, $\rho(\vec{r})$ the density and $\tau(\vec{r})$ the absorption coefficient in the medium either in the skull bone or in the brain. The pressure field p and the source term S depend on both space and time.

Simulations were conducted at 2-MHz and 300-kHz central frequency. The simulation grid was set to one tenth of a wavelength. In order to meet the Von Neumann stability criteria (Press et al. 1992), the temporal step is given by $\Delta t < \frac{\Delta x}{\max_{\vec{r}}(c_0(\vec{r}))\sqrt{3}}$, where Δx is the spatial step of the grid. An example of the 3D pressure field in the region of interest located in front of the transducer is given on Fig. 1. One can see the appearance of vibration nodes and antinodes in the 3D wave field distribution. For sake of clarity, only two-dimensional (2D) views will be displayed in the results. In both studies, we assumed that the clinicians located the transducers optimally, perpendicularly to the temporal window. Such a configuration was reproduced at best in the simulation process.

Definition of the targeted area

Each clinical study had its own procedure to target the clot once it was located.

Trumbi. The transducer was positioned on the temporal bone window on the contralateral side of the head with a clot-probe distance around 100 mm (Daffertshofer et al. 2005).

Clotbust. The transducer was positioned on the temporal bone window ipsilateral to the clot. Typically, the clot-probe distance was around 45 mm (Alexandrov et al. 2004).

According to each set-up, the location of the targeted region has been estimated in respect to the location of the probe. Even though no model of clot has been introduced in the simulations, pressure levels obtained in the expected location of a clot were analyzed for each study. Such regions-of-interest (1 cm × 1 cm × 1 cm) will be later referred to as ''expected location of the clot''. Parameters described in this section are summarized in Table 1.

Cavitation threshold

In order to determine in which areas of the brain inertial cavitation might occur, the pressure field simulated in the brain has been mapped. The areas where the pressure

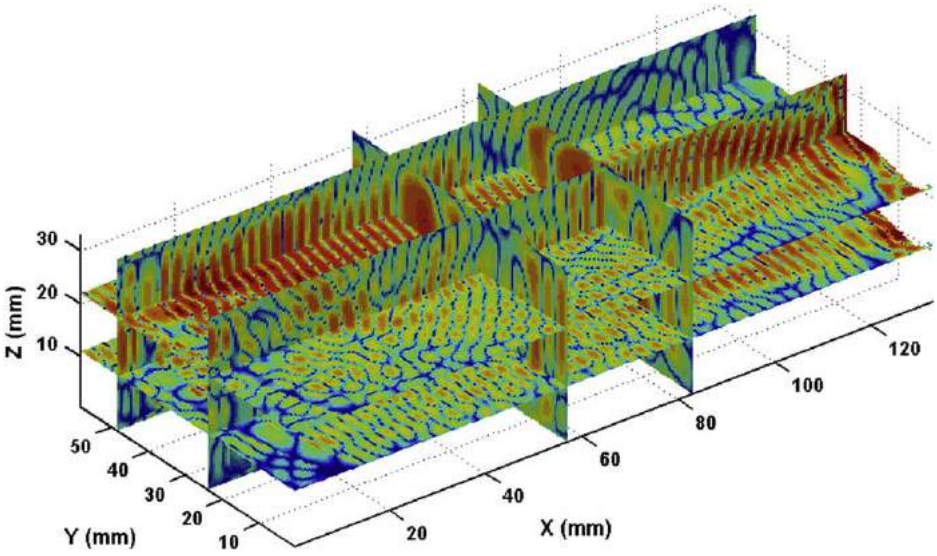

Fig. 1. Three-dimensional simulation of the acoustic field after propagation through the skull bone (in a dB scale with a 60 dB dynamic). The transducer is located on the right side of the image.

went beyond the threshold for inertial acoustic cavitation in a standing wave field have been plotted. The inertial acoustic cavitation threshold applied to our analysis was derived from (Azuma et al. 2005). In Azuma's study the acoustic cavitation threshold was measured in degassed water, in a standing wave field established inside a human skull, at 617-kHz frequency. The back-calculated peak rarefactional pressure was 0.27 MPa. By considering that the cavitation threshold increases as the square root of the frequency, the corresponding threshold at 300 kHz is equal to 0.19 MPa. It is important to note here that the cavitation threshold in a standing wave field is much smaller than the threshold in a progressive wave field. This is mainly due to the fact that nanobubbles can be trapped in antinodes and create bigger bubbles by coalescing (Azuma et al. 2005). Those microbubbles inertially collapse as soon as they reach their resonant size.

RESULTS

The TRUMBI study

Several points are crucial in analyzing the interaction between the biologic medium and the ultrasound field: the location and the amplitude of the peak rarefactional pressure and the possibility of standing waves formation.

Peak rarefactional pressure. In the whole area of the brain in front of the transducer, the mean peak rarefactional pressure is equal to 0.26 ± 0.2 MPa in the case of the high hypothesis and 0.06 ± 0.05 MPa in the case of the low hypothesis.

Table 2 summarizes the simulated pressure levels at the expected location of the clot and the maximum pressure levels achieved in the brain (on the so-called ''hot spot'') with the corresponding MI: the maximum peak rarefactional pressure in the brain is equal to 1.2 MPa for the high hypothesis and 0.27 MPa for the low hypothesis. At the expected location of the clot, the maximum peak rarefactional pressure is equal to 1 MPa for the high hypothesis and 0.22 MPa for the low hypothesis.

The location of the corresponding maximum pressure levels achieved in the brain can be seen in Fig. 2 (black dots). The location of these ''hot spots'' is highly dependent on the skull shape and on the position of the probe. The pressure field distribution in the brain for two different locations of the probe has been represented:

Table 2. Simulation results for the TRUMBI set-up

	Left temporal window (parallel to the skull)	Right temporal window (parallel to the skull)
Maximum peak rarefactional pressure (MPa) High hypothesis/low hypothesis	1.2/0.27	1.1/0.25
MI_{max} High hypothesis/low hypothesis	2.2/0.49	2/0.45
Pressure at the expected location of the clot (MPa) High hypothesis/low hypothesis	1/0.22	0.8/0.18
MI_{clot} High hypothesis/low hypothesis	1.8/0.40	1.5/0.33

TRUMBI = Transcranial Low-Frequency Ultrasound-Mediated Thrombolysis in Brain Ischemia; MI = Mechanical Index.

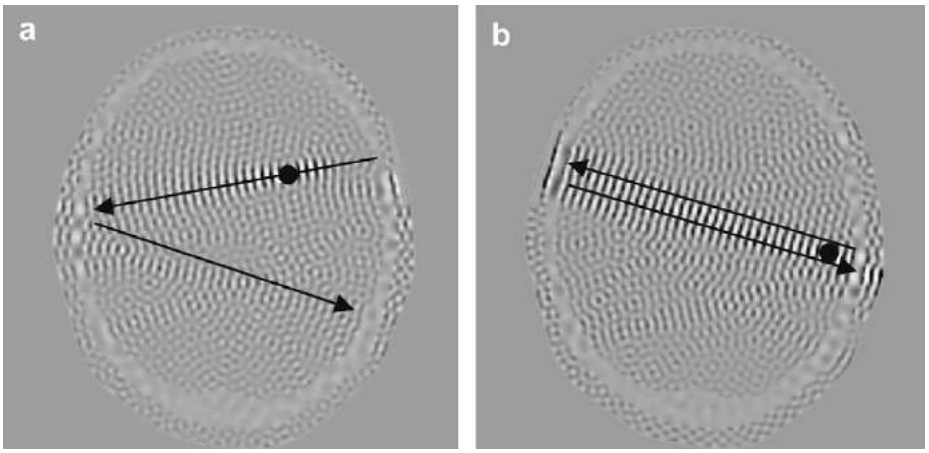

Fig. 2. Maximum peak rarefactional pressure (black spot) location and shape of the ultrasound field through (a) the right and (b) the left temporal windows.

probe located on the right temporal window (Fig. 2a) and on the left temporal window (Fig. 2b). The maximum peak rarefactional pressure is not located in the same area: between the emitter and the clot for the right window configuration and near the bone at the opposite side from the emitter for the left window configuration. Moreover, in Fig. 2a, the acoustic beam is reflected with an angle whereas in Fig. 2b the reflected wave travels parallel to the incident wave yielding to completely different pressure field distribution in the brain. In the latter case, a standing wave is likely to occur all the way in front of the transducer.

Standing waves. In order to have a closer look at potential standing wave formation, the acoustic pressure is presented as a function of time in Fig. 3 for our high hypothesis. In the case of the low hypothesis, the patterns are identical and only the pressure amplitudes differ. It corresponds to the configuration with the transducer located on the right temporal window. Each plot represents the pressure recorded at the location of the maximum pressure amplitude observed in the brain (a,''hot spot'') and at the expected location of the clot (b,''clot''). The distance of the ''hot spot'' from the emitter surface is 65 mm. The distance of the clot (targeted region) from the emitter surface is equal to 100 mm. One can see that the amplitude is varying with time, indicating interferences between direct waves and waves reflected on the contralateral skull.

Cavitation. Figure 4 represents in grey the areas where the pressure went beyond the threshold for inertial cavitation in a standing wave. The inertial acoustic cavitation threshold applied to our analysis was set to 0.19 MPa (derived from [Azuma et al. 2005]). During sonication, each time the simulated pressure levels went beyond the cavitation threshold, the corresponding pixel was definitely turned to from a black pixel to a grey one.

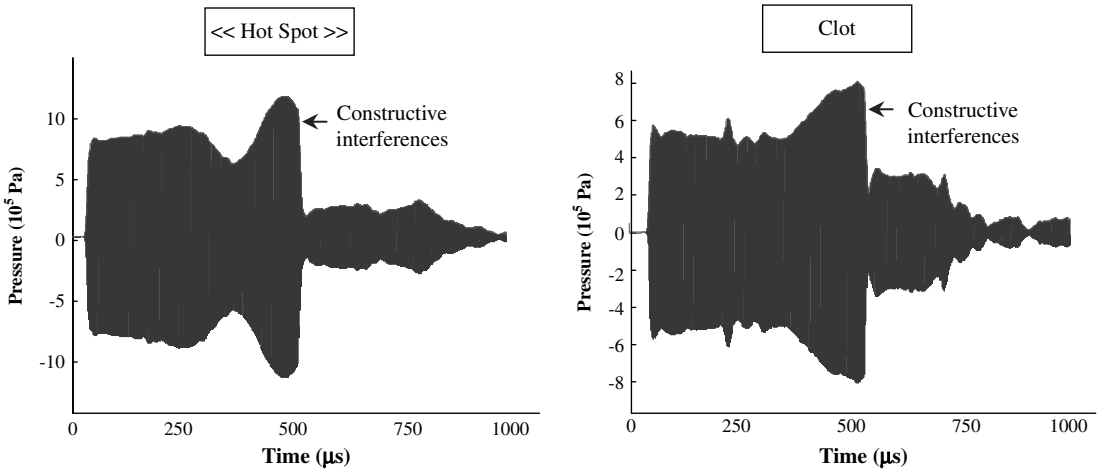

Fig. 3. Evolution of the acoustic pressure waveform as a function of time for one emission burst of 500 μs for two locations: at the maximum pressure amplitude location (left) and at the expected location of the clot (right).

The zone where the acoustic cavitation is liable to take place is not confined to the clot for both the low hypothesis (Fig. 4a) and the high hypothesis (Fig. 4b): such areas exist in tissues located in front of the transducer all along the brain. This observation may be related to the occurrence of atypical hemorrhages outside the targeted region.

Frequency modulation. Different frequency modulation options have been tested (Fig. 5) in order to take into account the frequency modulation used in the TRUMBI study. Areas where the acoustic pressure is higher than 0.19 MPa (Azuma et al. 2005) are displayed in grey color. Figure 5a is the reference, without modulation. Different frequency modulation options have been tested: ramp (left: Fig 5b, d and f) or sinusoidal modulation (right: Fig. 5c, e and g). Furthermore, in order to study the influence of the frequency modulation, various frequency ranges have been modelled (300 ± 1.5 kHz [Fig. 5b and c]; 300 ± 15 kHz [Fig. 5d and e]; 300 ± 150 kHz [Fig. 5f and 5g]). One can see that whatever the modulation, when frequency is shifted, the locations of the maximum pressure amplitude are shifted: nanobubbles are not trapped at the same location for a long time anymore but the pressure levels remains higher than 0.19 MPa in all cases.

The CLOTBUST study

The maximum peak negative pressure recorded in the simulation is equal to 0.07 MPa in the whole brain. The MI in the brain is thus less than 0.05. At the location of the maximum peak negative pressure (hot spot), the pressure is not affected by standing waves: the pressure reaches a plateau at 0.07 MPa during all the duration of the burst and vanishes at the end of the burst.

At the expected location of the clot, the peak negative pressure is 0.05 MPa, without any standing wave pattern. Standing waves are confined in the vicinity of the contralateral skull, within a 1 cm band. Nevertheless, in the standing wave area, the pressure field is one order of magnitude smaller than the hot spot. The main values of maximum peak negative pressure concerning both studies are summarized in Table 3.

DISCUSSION

For the CLOTBUST study, the simulated maximum negative peak pressure is 0.07 MPa: the simulated MI in the brain is less than 0.05. In fact, the pressure is so low after attenuation of the skull bone that it has been questioned whether any thrombolytic effect at all can be expected (Pfaffenberger et al. 2005). According to several *in vitro* studies (Blinc et al. 1993; Everbach and Francis 2000; Behrens et al. 2001; Meunier et al. 2007), stable acoustic cavitation seems to be the key process of low-frequency sonothrombolysis. As underlined by Vykhodtseva and colleagues (Vykhodtseva et al. 1995), it is very difficult to measure the stable and inertial cavitation thresholds in living tissues because they depend on numerous parameters: propagation medium, ultrasound frequency, duty cycle, pulse duration and standing wave. In a recent paper (Datta et al. 2006), Datta and colleagues demonstrated the sensitivity of cavitation thresholds to the medium. The likelihood of cavitational effects is higher when the ultrasound field is applied to plasma containing tPA and a clot, than when it is applied to plasma alone (Table 4). According to all experimental measurements of cavitation thresholds in tissues published in the literature, our simulations show that stable cavitation is not likely to occur in the brain with the CLOTBUST acoustical setup. Stable cavitation cannot explain the efficiency of the CLOTBUST approach. Nevertheless, there is little evidence that cavitation plays

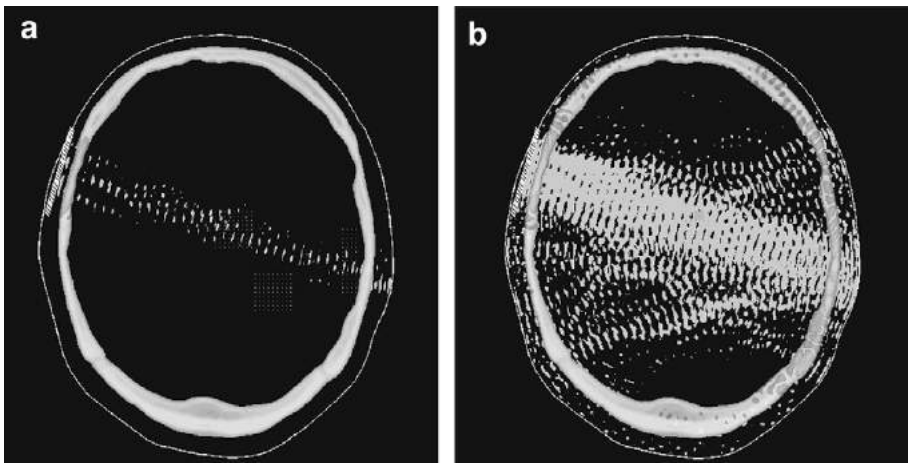

Fig. 4. Two-dimensional representation of the cavitation area (in grey) through one insonation for a 50 mm-emitter and with frequency modulation of the signal (ramp ± 1.5 kHz). (a) Low hypothesis. (b) High hypothesis.

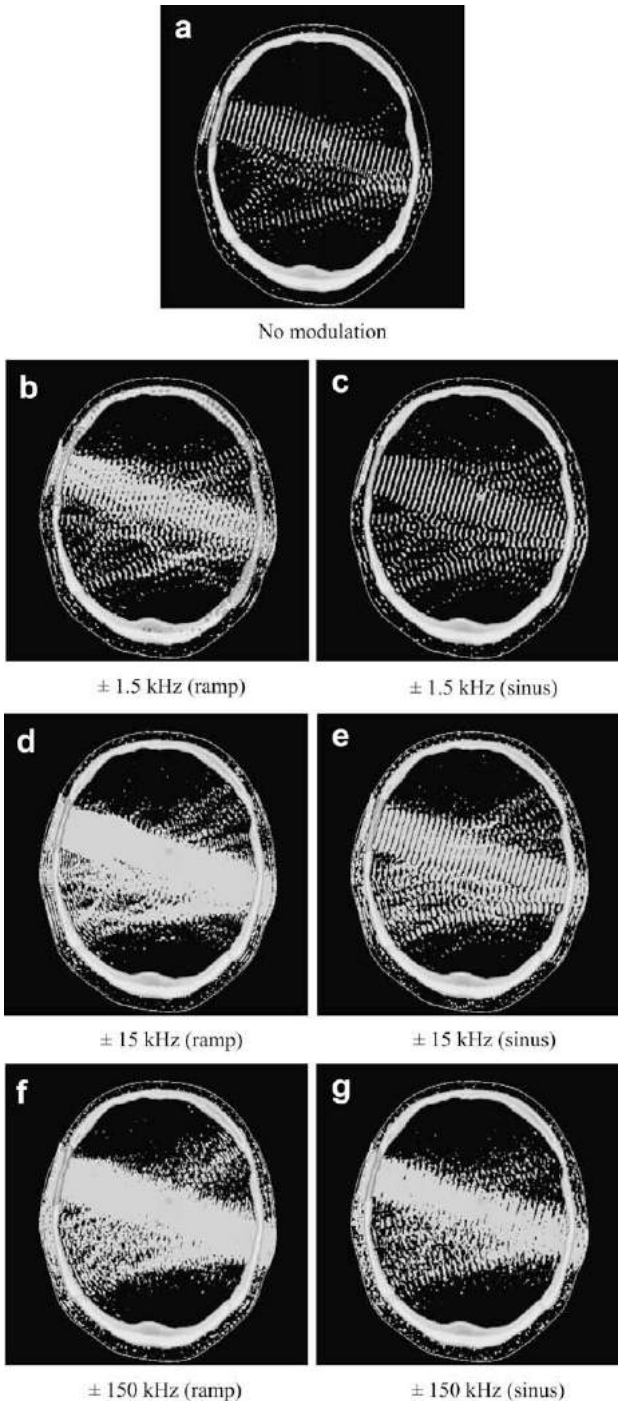

Fig. 5. Comparison of pressure repartition in different cases of frequency modulation.

such an important role *in vivo* and one should be cautious when extrapolating *in vitro* results to the clinical situation.

Several reports have hypothesized that high pressure amplitudes were used in the TRUMBI study (Azuma et al. 2005; Wang et al. 2008). Such reasoning was correct regarding the TRUMBI acoustical data available: MI and I_{SPTA} given in (Daffertshofer et al. 2005) were not compatible. Considering that the MI was not equal to 0.2 but that $I_{SPTA.3}$ was truly equal to 700 mW/cm^2 yielded high pressure levels generated in water (high hypothesis). In this article, a new analysis of the TRUMBI acoustical data has been proposed. We hypothesized a mix-up between the Spatial Peak-Temporal Average intensity and the Spatial Peak-Pulse Average intensity: $I_{SPTA.3}$ is not equal to 700 mW/cm^2 but $I_{SPPA.3}$ is. In that case, the MI meets 0.2. Such a low hypothesis is highly plausible.

Whatever the pressure level, as first highlighted by Azuma (2005) the simulations performed in this article confirmed the possibility of standing wave formation when using the TRUMBI set-up on a human skull. Moreover, pressure field distributions in the brain could be plotted (Fig. 2). Standing waves are likely to occur not only near the bone (Fig. 2.a) (Azuma et al. 2005) but also all along the way in front of the transducer (Fig. 2b). As the emission duration in the TRUMBI protocol (500 μs) corresponds to several crossings of the brain, the ultrasound wave is reflected more than four times in the brain so that complex pressure fields can be obtained in the brain (Fig. 2). These pressure fields are highly dependent on the position of the transducer: the transducer was positioned at best perpendicularly to the bone for both left and right bone window configurations (Fig. 2a and b), as was performed clinically by the physician for each study. Even though human skulls are almost symmetrical, the pressure fields differ significantly, most probably due to slightly different angles between the probe and the skull. Interestingly, these figures highlight two remarkable different phenomena that are likely to occur in the brain during TRUMBI sonication.

Figure 2a. The plane wave emitted by the transducer has been focused towards the hot spot because of a lens effect induced by the shape of the skull: right after crossing the skull, the wave front is no longer planar, but cylindrical. Figure 6 highlights that in this configuration the maximum peak rarefactional pressure is precisely in the area where the atypical secondary hemorrhage occurred for the pathologic case reported in (Daffertshofer et al. 2005)

Figure 2b. The wave is reflected perpendicularly to the skull interface located at the opposite side of the transducer, yielding to a standing wave pattern all the way in front of the transducer.

The skull bone is usually considered as a barrier for ultrasonic waves. Simulating the pressure fields generated by the TRUMBI set-up highlights a particular property of the skull: at low frequency, absorption is weak in the bone and in the brain, so that the skull potentially acts as a sur-pressure generator by either creating an acoustical lens (Fig. 2a) or acting as a resonator (Fig. 2b). These two examples are not exhaustive and other ways to generate

Table 3. Simulation results for CLOTBUST and TRUMBI set-ups

	CLOTBUST	TRUMBI (high hypothesis)	TRUMBI (low hypothesis)
Frequency	2 MHz	300 kHz	300 kHz
$I_{SPTA.3}$	700 mW/cm^2	700 mW/cm^2	35 mW/cm^2
Expected pressure in water	0.385 MPa	0.65 MPa	0.15 MP
Simulated maximum pressure in the brain	0.07 MPa	1.2 MPa	0.27 MPa

CLOTBUST = Combined Lysis of Thrombus in Brain Ischemia Using Transcranial Ultrasound and Systemic tPA; TRUMBI = Transcranial Low-Frequency Ultrasound-Mediated Thrombolysis in Brain Ischemia.

hot spots in the brain can be envisioned: any constructive interference due to reflections on any part of the skull bone, like the orbital shelf or the anterior clinoid. The curvature of the skull plays an important role and may explain the discrepancy between the results of this study and the previous ones carried out *in vitro* or on animal models (Daffertshoffer et al. 2004).

Simulations demonstrate that due to the complex skull geometry and due to the length of the emission (500 μs), standing waves are likely to occur at the targeted location and outside the targeted location with pressure levels higher than 0.27 MPa (low hypothesis). On the contrary CLOTBUST simulations show that standing waves are confined to a 1cm band close to the contralateral skull with pressure levels 10 times lower than in the targeted location.

The simulations could thus, explain the atypical secondary hemorrhages observed in the TRUMBI study for two reasons: the possibility of inertial cavitation in a large area of the brain is demonstrated in Fig. 4 but possible tPA extravasation might also occur. A recent paper (Reinhard et al. 2006) points out the abnormal permeability of the human blood-brain barrier (BBB) which can be induced by wide-field low-frequency insonation. The observed excessive bleeding rate with low-frequency sonothrombolysis might thus be attributable to primary BBB disruption by ultrasound. (Hynynen et al. 2006) evaluated the threshold for BBB disruption to 0.4 MPa, using 260-kHz focused ultrasound bursts and ultrasound contrast agent. This threshold is far below the maximum peak pressure amplitude simulated in the brain for the TRUMBI set-up with the high hypothesis and on the order of magnitude of the one simulated with the low hypothesis. Ultrasound could, thus, induce BBB opening in areas remote from the brain infarction so that tPA could diffuse in the brain parenchyma. As tPA is a known neurotoxic agent which can induce hemorrhages (Benchenane et al. 2004; Kaur et al. 2004), this might also explain the occurrence of secondary hemorrhages in TRUMBI.

Table 4. Acoustic cavitation thresholds from (Azuma et al. 2005) and (Datta et al. 2006)

	Frequency (MHz)	Peak rarefactional pressure for cavitation (MPa)	MI
(Azuma et al. 2005, inertial cavitation)			
Degassed water and skull	0.617	0.275	0.35
(Datta et al. 2006, inertial cavitation)			
Degassed water	0.12	>0.65	>1.88
Plasma alone	0.12	0.50	1.44
Plasma + tPA	0.12	0.47	1.36
Plasma + tPA + clot	0.12	0.27	0.78
(Datta et al. 2006, stable cavitation)			
Degassed water	0.12	>0.65	>1.88
Plasma alone	0.12	0.39	1.13
Plasma + tPA	0.12	0.34	0.98
Plasma + tPA + clot	0.12	0.2	0.58

MI = Mechanical Index.

One of the main differences between the clinical trials studied in this article is the ultrasound frequency. In the CLOTBUST trial, the frequency is seven times higher than in the TRUMBI trial, thus, the attenuation through the skull is much higher and explains mostly the difference in the pressure level. Sonothrombolysis devices are often characterized by the value of their I_{SPTA} in the absence of skull bone. Nevertheless, even though both studies claimed to have the same $I_{SPTA.3}$ (739 mW/cm^2 for CLOTBUST and 700 mW/cm^2 for TRUMBI), the simulated maximum pressure levels in the brain are significantly different: 0.07 MPa for CLOTBUST and 1.2 MPa (high hypothesis) or 0.27 MPa (low hypothesis). Basically, the skull attenuation is eight times lower in TRUMBI compared with CLOTBUST. In order to evaluate the safety and the efficiency of sonothrombolysis systems, the mean $I_{SPTA.3}$ (or mean peak negative pressure) expected in the brain appears to be more relevant than $I_{SPTA.3}$ value (or mean peak negative pressure) in water. We have shown that such pressure levels can be estimated with finite differences simulations. Moreover, simulation could be of value for optimizing the efficacy and the safety of new sonothrombolytic devices. For example, in order to reduce standing waves Daffertshoffer et al. (2005) proposed to apply a 0.5% frequency modulation. Our simulations have shown, however, that this approach was not sufficient to significantly

4.3 JASA 2010

Journal of the Acoustical Society of America, 2010

Propagation of elastic waves in a fluid-loaded anisotropic functionally graded waveguide : Application to ultrasound characterization.
C. Baron, S. Naili.
JASA 127, 1307-1317.

Propagation of elastic waves in a fluid-loaded anisotropic functionally graded waveguide: Application to ultrasound characterization

Cécile Baron and Salah Naili[a)]
Laboratoire de Mécanique Physique, Faculté des Sciences et Technologie, Université Paris 12–Val de Marne, 61 Avenue du Général de Gaulle, 94010 Créteil Cedex, France

(Received 27 June 2008; revised 19 August 2009; accepted 22 December 2009)

Non-destructive evaluation of heterogeneous materials is of major interest not only in industrial but also in biomedical fields. In this work, the studied structure is a three-layered one: A laterally heterogeneous anisotropic solid layer is sandwiched between two acoustic fluids. An original method is proposed to solve the wave equation in such a structure without using a multilayered model for the plate. This method is based on an analytical solution, the matricant, explicitly expressed under the Peano series expansion form. This approach is validated for the study of a fluid-loaded anisotropic and homogeneous plane waveguide with two different fluids on each side. Then, original results are given on the propagation of elastic waves in an asymmetrically fluid-loaded waveguide with laterally varying properties. This configuration notably corresponds to the axial transmission technique to the ultrasound characterization of cortical bone *in vivo*.
 [DOI: 10.1121/1.3292949]

PACS number(s): 43.40.Dx, 43.20.Mv [ADP] Pages: 1307–1317

I. INTRODUCTION

A lot of natural media have unidirectional varying elastic properties. The mantel crust, the oceans, and cortical bone are some of these functionally graded media. Scientists focused on the advantages presented by this type of materials in terms of mechanical behavior, and since the 1980s, they developed industrial functionally graded materials (FGMs) particularly exploited in high-technology and biomedical applications. Consequently, the non-destructive evaluation of these materials is a key issue. Surface and guided waves play a major role in non-destructive testing and evaluation of complex structures. Several studies are dedicated to the leaky Lamb wave propagation in fluid-loaded plates (Chimenti and Nayfeh, 1990; Chimenti and Rokhlin, 1990; Deschamps and Poncelet, 2000). In all these studies, the media are homogeneous or multilayered. In this work, we introduce a general method to take into account the continuity of the property variation in an anisotropic waveguide. This method is based on the knowledge of an analytical solution of the wave equation, the matricant, explicitly expressed via the Peano series (Peano, 1888). The accuracy of the numerical evaluation of this solution and its validity domain are perfectly managed (Baron, 2005; Youssef and El-Arabawi, 2007). Because it deals with an analytical solution, all the wave propagation parameters are controlled. This represents an advantage with respect to numerical methods such as finite-element and finite-difference methods for which the problem treated is a global one, making difficult to analyze and interpret the experimental data, which result from the interaction and coupling of numerous physical phenomena. To the best of our knowledge, this is the first method to evaluate the mechanical behavior of a fluid-loaded anisotropic waveguide with continuously varying properties without modeling the FGM plate by a multilayered plate. Consequently, in the context of real materials with continuously varying properties (such as bone, bamboo, or manufactured FGM), this method could allow assessing the solution to a more realistic model with a controlled accuracy and without an increase in the computation-time.

In this work, we first present the method and its setup with fluid-structure interaction; then we proceed to the validation of the method by comparing our results to the dispersion curves obtained from classical schemes on homogeneous waveguides (isotropic and anisotropic). Two advantages of the method are underlined: (i) An asymmetric fluid-loading may be taken into account without modifying the scheme for the numerical solution, and (ii) the influence of the property gradient on the ultrasonic response of the waveguide may be investigated via the frequency spectrum of the reflection coefficient modulus. Finally, we get onto the relevancy of this model applied to the ultrasound characterization of cortical bone by the axial transmission technique.

II. BACKGROUND

Contemporary work efforts over the last 2 decades illustrate some of the technology interest on guided waves to non-destructive evaluation. Namely, Rose (2002) gave a review of ultrasonic guided wave inspection potential. A lot of papers deal with the interaction between guided waves and a solid plate immersed in a fluid or embedded between two different fluids. Guided modes in an infinite elastic isotropic plate in vacuum were first treated by Rayleigh (1885) then by Lamb (1917). The Lamb wave problem is reserved, strictly speaking, for wave propagation in a traction-free homogeneous isotropic plate. To deal with guided modes in a fluid-loaded plate, we use the term "leaky Lamb waves" as the energy is partly radiated in the fluids on both sides of the plate. For the basic Lamb problem—plate in vacuum—the

[a)]Author to whom correspondence should be addressed. Electronic mail: naili@univ-paris12.fr

solutions of the dispersion equation are real whereas in the case of a plate bounded by media on both sides, the dispersion equation has complex solutions. In 1961, Worlton (1961) gave an experimental confirmation of the theoretical work of Lamb (1917), by obtaining experimentally the dispersion curves of aluminum and zirconium plates, asserting that water loading has little effect on the behavior of waves in plates. In 1976, Pitts *et al.* (1976) presented some numerical test results on the relationship between real part of the reflection coefficient poles and the phase velocity of leaky Lamb modes in a homogeneous isotropic brass plate in water. Folds and Loggins (1977) proposed analytical expressions of the reflection and transmission coefficients for plane waves at oblique incidence on a multilayered isotropic plate immersed in water based on Brekhovskikh's (1980) analysis. They found good agreement with their theoretical results and experimental data. Few years later, Fiorito *et al.* (1979) developed a resonance formalism for the fluid-loaded elastic plate and gave some theoretical and numerical results for an isotropic steel plate immersed in the water. This formalism was generalized to the interactions of acoustic plane waves with an asymmetrically fluid-loaded elastic plate by Franklin *et al.* (2001). Nayfeh, Chimenti, and Rokhlin produced a lot of works on wave propagation in anisotropic media and particularly in fiber composite plates immersed in a fluid (Chimenti and Nayfeh, 1986, 1990; Chimenti and Rokhlin, 1990; Nayfeh and Chimenti, 1988, 1989; Rokhlin and Wang, 2002). Based on their formalism, Deschamps and Poncelet (2000) placed the emphasis on the difference between what they called transient Lamb wave-solutions of the characteristic equation of the plate for complex frequency and real slowness (time attenuation), and heterogeneous Lamb waves for which the slowness is complex and the frequency is real (spatial attenuation). These two ways of resolution of the dispersion equation have two different physical meanings—space or time attenuation—and consequences of this difference are developed in their paper (Deschamps and Poncelet, 2000). A critical point is the validity of the Cremer's coincidence hypothesis: The real couples (angular frequency ω and phase velocity v_φ), such that the reflection coefficient is minimum, may be identified as velocity dispersion of plate waves. Experimentally checked in a lot of configurations, it appears to be not well satisfied in several cases (for instance, graphite-epoxy plates when the ratio between fluid and plate mass densities is not "small") (Chimenti and Nayfeh, 1986; Nayfeh and Chimenti, 1988). The results obtained by Deschamps and Poncelet (2000) on fluid-loaded plate show a good correlation between dispersion curves obtained in complex frequency and the minima of the reflection coefficient, which suggests that the Cremer's coincidence principle is still valid considering time attenuation. All these studies show the evidence that the wave propagation in fluid-loaded elastic plate emerges as a very delicate problem, which needs cautious treatment.

III. GENERAL FORMULATION OF THE PROBLEM

We consider a three-dimensional multilayer system composed of one elastic solid layer sandwiched between two acoustic fluid layers. Let $\mathbf{R}(\mathrm{O},\mathbf{x}_1,\mathbf{x}_2,\mathbf{x}_3)$ be the Cartesian frame of reference where O is the origin of the space and $(\mathrm{x}_1,\mathrm{x}_2,\mathrm{x}_3)$ is an orthonormal basis for this space. The coordinate of the generic point $\mathbf{x}$ in $\mathbf{R}$ is specified by (x_1,x_2,x_3). The acoustic fluid layers occupy an open unbounded domain. Both fluids f_1 and f_2 are supposed perfect, of respective mass densities ρ_{f_1} and ρ_{f_2}; the constant speeds of sound in each fluid are c_{f_1} and c_{f_2}, respectively. The thickness of the solid layer is denoted by d and its mass density by ρ. The interfaces between the fluids and the solid layer are infinite planes parallel to the $(\mathbf{x}_1,\mathbf{x}_2)$-plane. The $\mathbf{x}_3$-axis is oriented downward and the origin O is located at the interface between the upper fluid f_1 and the solid layer. Therefore, we assume that the structure is a two-dimensional one and that the guided waves travel in the plane $x_2=0$; in the following parts, this coordinate is implicit and is omitted in the mathematical expressions. Moreover, the solid layer will be so-called plate.

The elastic plate is supposed to be anisotropic and is liable to present continuously varying properties along its thickness ($\mathbf{x}_3$-axis). These mechanical properties are represented by the stiffness fourth-order tensor $\mathbb{C}=\mathbb{C}(x_3)$ and the mass density $\rho=\rho(x_3)$.

A. System equations

1. The wave equation in the fluid f_n (for n=1 or 2)

In the fluid f_n and the context of the linear acoustic theory, the linearized Euler's equation and the constitutive equations are written as

$$-\frac{\partial p^{(n)}}{\partial x_j}=\rho_{f_n}\frac{\partial^2 u_j^{(n)}}{\partial t^2},$$

$$p^{(n)}=K_{f_n}\,\mathrm{div}\,\mathbf{u}^{(\mathbf{n})}, \tag{1}$$

where $\mathbf{u}^{(n)}$ and $p^{(n)}$, respectively, represent the displacement vector and the pressure in the fluid f_n; its compressibility and the speed of sound in the fluid at equilibrium are, respectively, K_{f_n} and $c_{f_n}=\sqrt{K_{f_n}/\rho_{f_n}}$. The operator div is the divergence.

The solutions of system (1) for the fluid f_n are sought under the form

$$\mathbf{f}_n(x_1,x_2;t)=\mathbf{A}_n(x_3)\exp\,\imath(k_1x_1+k_3^{(n)}x_3-\omega t), \tag{2}$$

where k_1 and $k_3^{(n)}$ are the wavenumbers, respectively, along the $\mathbf{x}_1$-axis and $\mathbf{x}_3$-axis in the fluid f_n; the angular frequency is noted ω and $\imath$ is the imaginary unit.

We consider an incident wave reaching the plate at an angle θ_1 from the $\mathbf{x}_3$-axis in the fluid f_1. The incident displacement-field is defined in the following form, assuming that its amplitude is normalized:

$$\mathbf{u}_I^{(1)}=\begin{pmatrix}\sin\,\theta_1\\0\\\cos\,\theta_1\end{pmatrix}\exp\,\imath(k_1x_1+k_3^{(1)}x_3-\omega t), \tag{3}$$

with $k_1=(\omega/c_{f_1})\sin\,\theta_1$ and $k_3^{(1)}=(\omega/c_{f_1})\cos\,\theta_1$. From this, the expressions of the reflected displacement-field $\mathbf{u}_R^{(1)}$ in f_1 and of the transmitted displacement-field $\mathbf{u}_T^{(2)}$ in f_2 are deduced as follows:

$$\mathbf{u}_R^{(1)} = R\begin{pmatrix} \sin\theta_1 \\ 0 \\ -\cos\theta_1 \end{pmatrix} \exp \imath(k_1 x_1 - k_3^{(1)} x_3 - \omega t),$$

$$\mathbf{u}_T^{(2)} = T\frac{\rho_{f_2}}{\rho_{f_1}}\begin{pmatrix} \sin\theta_1 \\ 0 \\ \cos\theta_1 \end{pmatrix} \exp \imath(k_1 x_1 + k_3^{(2)} x_3 - \omega t). \quad (4)$$

where $R=R(x_1,x_3;t)$ and $T=T(x_1,x_3;t)$, respectively, represent the reflection and transmission coefficients, which will be expressed explicitly in the sequel. The incident, reflected, and transmitted pressure fields, respectively, noted $p_I^{(1)}$, $p_R^{(1)}$, and $p_T^{(2)}$, are deduced from expressions (3) and (4), and the second equation of the system (1)

$$p_I^{(1)} = -\imath\omega \times \rho_{f_1} c_{f_1} \times \exp \imath(k_1 x_1 - k_3^{(1)} x_3 - \omega t),$$

$$p_R^{(1)} = -\imath\omega \times \rho_{f_1} c_{f_1} \times R \times \exp \imath(k_1 x_1 - k_3^{(1)} x_3 - \omega t),$$

$$p_T^{(2)} = -\imath\omega \times \rho_{f_2} c_{f_2} \times T \times \exp \imath(k_1 x_1 + k_3^{(2)} x_3 - \omega t). \quad (5)$$

B. The wave equation in the plate waveguide

The body forces in the solid plate are neglected. The balance equation of linear momentum associated with the constitutive law of linear elasticity (Hooke's law) gives the following equations:

$$\frac{\partial \sigma_{ij}}{\partial x_j} = \rho \frac{\partial^2 u_i}{\partial t^2},$$

$$\sigma_{ij} = \frac{1}{2} C_{ijk\ell}\left(\frac{\partial u_k}{\partial x_\ell} + \frac{\partial u_\ell}{\partial x_k}\right), \quad (6)$$

where u_i (for $i=1,\ldots,3$) and σ_{ij} (for $i,j=1,\ldots,3$), respectively, represent the components of the displacement-field $\mathbf{u}$ and of the stress $\boldsymbol{\sigma}$. In system (6), Einstein's convention of summation on repeated indices is used. The solutions are sought for the vectors of displacement $\mathbf{u}$ and traction σ_{i3} (for $i=1,\ldots,3$) (assumed to be harmonic in time t and space along the $\mathbf{x}_1$-axis) under the form

$$\mathbf{f}(x_1,x_3;t) = \mathbf{A}(x_3)\exp \imath(k_1 x_1 - \omega t). \quad (7)$$

C. Fluid-loading interface conditions

The conditions at both interfaces $x_3=0$ and $x_3=d$ are the continuity of the normal displacement and the continuity of the normal stress. We consider that the fluids f_1 and f_2 are perfect; consequently, the shear stresses are zero at the interfaces [$\sigma_{13}(x_1,0;t)=\sigma_{13}(x_1,d;t)=0$ and $\sigma_{23}(x_1,0;t)=\sigma_{23}(x_1,d;t)=0$]. The following relations are obtained:

$$u_3(x_1,0;t) = u_3^{(1)}(x_1,0;t), \quad u_3(x_1,d;t) = u_3^{(2)}(x_1,d;t),$$

$$\sigma_{33}(x_1,0;t) = -p^{(1)}(x_1,0;t), \quad \sigma_{33}(x_1,d;t) = -p^{(2)}(x_1,d;t), \quad (8)$$

with

$$u_3^{(1)} = \mathbf{u}_I^{(1)} \cdot \mathbf{x}_3 + \mathbf{u}_R^{(1)} \cdot \mathbf{x}_3, \quad u_3^{(2)} = \mathbf{u}_T^{(2)} \cdot \mathbf{x}_3 \quad \text{and}$$

$$p^{(1)} = p_I^{(1)} + p_R^{(1)}, \quad p^{(2)} = p_T^{(1)}. \quad (9)$$

D. A closed-form solution: The matricant

Introducing expression (7) in Eq. (6), we obtain the wave equation under the form of a second-order differential equation with non-constant coefficients. For particular forms of profiles, this equation has analytical solutions expressed with special functions (Bessel or Hankel functions) (Vlasie and Rousseau, 2004). But, in the general case, there is no analytical solution to the problem thus formulated. The most current methods to solve the wave equation in unidirectionally heterogeneous media are derived from the Thomson–Haskell method (Haskell, 1953; Thomson, 1950). These methods are appropriate for multilayered media (Hosten and Castaings, 2003; Kenneth, 1982; Lévesque and Piché, 1992; Wang and Rokhlin, 2001). But, for continuously varying media, these techniques mean to replace the continuous profiles of properties with step-wise functions. Thereby, the studied problem becomes an approximate one, even before the resolution step; the accuracy of the solution as its validity domain is hard to evaluate. Moreover, the multilayered model of the waveguide creates some "virtual" interfaces likely to induce artifacts. In order to deal with the exact problem, that is to keep the continuity of the properties' variation, the wave equation is re-written under the form of an ordinary differential equation system with non-constant coefficients for which an analytical solution exists: the matricant (Baron, 2005).

1. Hamiltonian form of the wave equation

We consider that the plate presents material symmetries that allow decoupling the pressure–shear vertical (P-SV) waves, polarized in the propagation plane $(\mathbf{x}_1,\mathbf{x}_3)$ and the shear horizontal (SH) waves polarized along $\mathbf{x}_2$-axis. The incident medium f_1 is a perfect fluid; only the P-SV waves travel in the plate. Applying a spatio-temporal Fourier transform on (x_1,t) of the displacement-field [noted $\hat{\mathbf{u}}(k_1,x_3;\omega)$ after Fourier transform] and on the traction field [noted $\hat{\sigma}_{i3}(k_1,x_3;\omega)$ for $i=1,\ldots,3$] and using the Voigt notation ($C_{ijk\ell}$ for $i,j,k,\ell=1,\ldots,3$ is replaced with c_{IJ} for $I,J=1,\ldots,6$), Eq. (6) leads to Stroh's (1962) sextic plate formalism (Hamiltonian formulation of the wave equation)

$$\frac{\partial \hat{\sigma}_{13}}{\partial x_3} = \rho(\imath\omega)^2 \hat{u}_1 - \imath k_1 \hat{\sigma}_{11}, \quad \frac{\partial \hat{\sigma}_{33}}{\partial x_3} = \rho(\imath\omega)^2 \hat{u}_3 - \imath k_1 \hat{\sigma}_{13}, \quad (10)$$

$$\hat{\sigma}_{11} = \imath k_1 c_{11} \hat{u}_1 + c_{33}\frac{\partial \hat{u}_3}{\partial x_3}, \quad \hat{\sigma}_{13} = c_{55}\left(\frac{\partial \hat{u}_1}{\partial x_3} + \imath k_1 \hat{u}_3\right),$$

$$\hat{\sigma}_{33} = \imath k_1 c_{13} \hat{u}_1 + c_{33}\frac{\partial \hat{u}_3}{\partial x_3}. \quad (11)$$

According to Eqs. (10) and (11), $\hat{\sigma}_{11}$ is function of $\hat{u}_1$ and $\hat{\sigma}_{33}$. The wave equation becomes a matrix system expressed using the Thomson–Haskell parametrization of Stroh's (1962) sextic plate formalism

$$\frac{d}{dx_3}\eta(x_3) = \iota\omega\mathbf{Q}(x_3)\,\eta(x_3), \tag{12}$$

that is,

$$\frac{d}{dx_3}\begin{pmatrix} \iota\omega\hat{u}_1 \\ \iota\omega\hat{u}_3 \\ \hat{\sigma}_{13} \\ \hat{\sigma}_{33} \end{pmatrix} = \iota\omega\begin{pmatrix} 0 & s_1 & 1/c_{55}(x_3) & 0 \\ -s_1c_{13}(x_3)/c_{33}(x_3) & 0 & 0 & 1/c_{33}(x_3) \\ \rho(x_3)-s_1^2\zeta(x_3) & 0 & 0 & -s_1c_{13}(x_3)/c_{33}(x_3) \\ 0 & \rho(x_3) & -s_1 & 0 \end{pmatrix}\begin{pmatrix} \iota\omega\hat{u}_1 \\ \iota\omega\hat{u}_3 \\ \hat{\sigma}_{13} \\ \hat{\sigma}_{33} \end{pmatrix}, \tag{13}$$

with the relations

$$\zeta(x_3) = c_{11}(x_3) - \frac{c_{13}^2(x_3)}{c_{33}(x_3)}, \quad k_1 = \omega s_1, \tag{14}$$

where s_1 is the x_1-component of the slowness. The matrix $\mathbf{Q}$ includes all the information about the heterogeneity of the waveguide because it is expressed from the plate mechanical properties $(\rho(x_3),\mathbb{C}(x_3))$ and from two acoustical parameters (s_1,ω).

2. Explicit solution: The Peano expansion of the matricant

The wave equation thus formulated has an analytical solution expressed between a reference point $(x_1,0,x_3^0)$ and some point of the plate $(x_1,0,x_3)$ in the propagation plane. This solution is called the matricant and is explicitly written under the form of the Peano series expansion (Gantmacher, 1959; Peano, 1888; Pease, 1965):

$$\mathbf{M}(x_3,x_3^0) = \mathbf{I} + (\iota\omega)\int_{x_3^0}^{x_3}\mathbf{Q}(\xi)d\xi + (\iota\omega)^2 \times \int_{x_3^0}^{x_3}\mathbf{Q}(\xi)\left(\int_{x_3^0}^{\xi}\mathbf{Q}(\xi_1)d\xi_1\right)d\xi + \ldots, \tag{15}$$

where $\mathbf{I}$ is the identity matrix of dimension (4,4). If the matrix components $\mathbf{Q}(x_3)$ are bounded in the study interval, these series are always convergent (Baron, 2005). The components of the matrix $\mathbf{Q}$ are continuous in x_3 and the study interval is bounded (thickness of the waveguide); consequently the hypothesis is always verified. We underline that the $\iota\omega$-factorization leads up to a polynomial form of the matricant. The $\iota\omega$-polynomial coefficients are matrices independent of ω.

3. Boundary conditions: Fluid-structure interaction

Using the propagator property of the matricant through the plate thickness, the state-vector [defined in Eq. (13)] at the second interface $\eta(d)$ is evaluated from the state-vector at the first interface $\eta(0)$ as follows:

$$\eta(d) = \mathbf{M}(d,0)\,\eta(0). \tag{16}$$

The fluid-structure interaction sets the conditions of zero shear stresses (see Sec. III C), used after a spatio-temporal Fourier transform on (x_1,t). Equation (16) becomes

$$\begin{pmatrix} \iota\omega\hat{u}_1(k_1,d;\omega) \\ \iota\omega\hat{u}_3(k_1,d;\omega) \\ 0 \\ \hat{\sigma}_{33}(k_1,d;\omega) \end{pmatrix} = \begin{pmatrix} M_{11} & M_{12} & M_{13} & M_{14} \\ M_{12} & M_{22} & M_{23} & M_{24} \\ M_{13} & M_{23} & M_{33} & M_{34} \\ M_{14} & M_{24} & M_{34} & M_{44} \end{pmatrix} \times \begin{pmatrix} \iota\omega\hat{u}_1(k_1,0;\omega) \\ \iota\omega\hat{u}_3(k_1,0;\omega) \\ 0 \\ \hat{\sigma}_{33}(k_1,0;\omega) \end{pmatrix}. \tag{17}$$

The condition to obtain a nontrivial solution to Eq. (17) leads to the following relation:

$$\iota\omega\hat{u}_1(k_1,0;\omega)\times M_{13} + \iota\omega\hat{u}_3(k_1,0;\omega)\times M_{32} + \hat{\sigma}_{33}(k_1,0;\omega)\times M_{34} = 0, \tag{18}$$

where M_{ij} (for $i,j=1,\ldots,4$) represent the components of the matrix $\mathbf{M}$. The displacement component $\hat{u}_1(k_1,0;\omega)$ can be expressed as a linear combination of $\hat{u}_3(k_1,0;\omega)$ and $\hat{\sigma}_{33}(k_1,0;\omega)$; thus system (16) of dimension 4 is reduced to a matrix system of dimension 2

$$\eta(d) = \begin{pmatrix} P_1 & P_2 \\ P_3 & P_4 \end{pmatrix}\eta(0) \quad \text{where} \quad \eta(x_3) = \begin{pmatrix} \iota\omega\hat{u}_3 \\ \hat{\sigma}_{33} \end{pmatrix}, \tag{19}$$

with the relations

$$P_1 = M_{22} - M_{21}\frac{M_{32}}{M_{31}}, \quad P_2 = M_{24} - M_{21}\frac{M_{34}}{M_{31}},$$

$$P_3 = M_{42} - M_{41}\frac{M_{32}}{M_{31}}, \quad P_4 = M_{44} - M_{11}\frac{M_{34}}{M_{31}}. \tag{20}$$

Interface conditions (8) are transformed in the Fourier domain (k_1,ω). The expressions of the displacement and the pressure in the fluids [see Eqs. (3)–(5)], so that the one of the displacement and traction fields in the solid plate [see Eq. (19)], are substituted in the transformed interface conditions.

Setting $\eta(0)=(\alpha_1,\alpha_2)^T \exp \imath(k_1x_1-\omega t)$, where the superscript ^{T} designates the transpose operator, we obtain the following matrix equation:

$$\begin{pmatrix} \imath\omega s_3^{(1)} c_{f_1} & 1 & 0 & 0 \\ -\imath\omega\rho_{f_1} c_{f_1} & 0 & 1 & 0 \\ 0 & P_1 & P_2 & -\imath\omega s_3^{(2)} c_{f_2} \exp(\imath\omega s_3^{(2)} d) \\ 0 & P_3 & P_4 & -\imath\omega\rho_{f_2} c_{f_2} \exp(\imath\omega s_3^{(2)} d) \end{pmatrix} \begin{pmatrix} \hat{R} \\ \alpha_1 \\ \alpha_2 \\ \hat{T} \end{pmatrix} = \begin{pmatrix} \imath\omega s_3^{(1)} c_{f_1} \\ \imath\omega\rho_{f_1} c_{f_1} \\ 0 \\ 0 \end{pmatrix}, \tag{21}$$

where $\mathbf{s}^{(n)}=\mathbf{k}^{(n)}/\omega$ is the slowness-vector in the fluid f_n ($n=1$ or 2). The quantities $\hat{R}$ and $\hat{T}$ are, respectively, the reflection and transmission coefficients expressed in the Fourier domain: $\hat{R}=\hat{R}(k_1,x_3;\omega)$ and $\hat{T}=\hat{T}(k_1,x_3;\omega)$. The two first lines of system (21) express the boundary conditions at the first interface ($x_3=0$) and the two last lines those at the second interface ($x_3=d$) introducing the Fourier transform of expressions (3)–(5) in the following relations:

$$\eta(0) - \begin{pmatrix} \imath\omega\hat{u}_{3_R}^{(1)} \\ -\hat{p}_R \end{pmatrix}_{x_3=0} = \begin{pmatrix} \imath\omega\hat{u}_{3_I}^{(1)} \\ -\hat{p}_I \end{pmatrix}_{x_3=0},$$

$$\begin{pmatrix} P_1 & P_2 \\ P_3 & P_4 \end{pmatrix} \eta(0) - \begin{pmatrix} \imath\omega\hat{u}_{3_T}^{(2)} \\ -\hat{p}_T \end{pmatrix}_{x_3=d} = \begin{pmatrix} 0 \\ 0 \end{pmatrix}, \tag{22}$$

where $\hat{u}_{3_R}^{(1)}$, $\hat{u}_{3_I}^{(1)}$, and $\hat{u}_{3_T}^{(2)}$ are the components along $\mathbf{x}_3$-axis of $\hat{\mathbf{u}}_R^{(1)}$, $\hat{\mathbf{u}}_I^{(1)}$, and $\hat{\mathbf{u}}_T^{(2)}$ vectors, respectively. Note the equality between the quantities $u_{3_T}^{(2)}$ and $u_3^{(2)}$ where this last is defined in Eq. (9).

4. Expression of the reflection and transmission coefficients

From Eq. (21), we deduce the analytical expressions of the reflection and transmission complex coefficients

$$\hat{R}(s_1,x_3;\omega) = \frac{(P_3 - P_1Z_2 + P_4Z_1 - P_2Z_1Z_2)}{(P_3 - P_1Z_2 - P_4Z_1 + P_2Z_1Z_2)},$$

$$\hat{T}(s_1,x_3;\omega) = -\frac{2Z_2(\rho_{f_1}c_{f_1}/\rho_{f_2}c_{f_2})(P_1P_4 - P_2P_3)}{(P_3 - P_1Z_2 - P_4Z_1 + P_2Z_1Z_2)} \times \exp(-\imath\omega s_3^{(2)} d), \tag{23}$$

with $Z_n=\rho_{f_n}/\sqrt{1/c_{f_n}^2 - s_1^2}$ (for $n=1$ or 2) and $k_1=\omega s_1$.

IV. VALIDATION OF THE METHOD

The aim of this section is to check that the Peano expansion of the matricant is well-adapted to study fluid-loaded waveguides. We take into account the fluid-structure interaction in different configurations of homogeneous plates comparing the results obtained from the numerical implementation of the Peano expansion of the matricant to results taken from literature.

TABLE I. Elastic properties of transversely isotropic plate (with $c_{23}=c_{22}-2c_{44}$).

ρ (g cm^{-3})	c_{11} (GPa)	$c_{22}=c_{33}$ (GPa)	$c_{12}=c_{13}$ (GPa)	c_{44} (GPa)	$c_{66}=c_{55}$ (GPa)
1.85	23.05	15.1	8.7	3.25	4.7

The numerical evaluation of P_1, P_2, P_3, and P_4 requires us to truncate the Peano series and to numerically calculate the integrals. Thus, the error can be estimated and controlled (Baron, 2005). We retained 70 terms in the series and evaluate the integrals over 100 points using Simpson's rule (fourth-order integration method). These choices ensure the convergence of the solution and the accuracy of the results for a reasonable computation-time (never exceeding few minutes on a desktop computer). Expressions (23) give the frequency spectrum (modulus and phase) of the reflection coefficient for different incidences (s_1 varies from zero-normal incidence to $1/c_{f_1}$ corresponding to the critical incidence in the fluid f_1).

A lot of works detailed the relationship between the poles and the zeros of the reflection coefficient and the leaky Lamb wave dispersion curves (Chimenti and Rokhlin, 1990; Deschamps and Poncelet, 2000). The results of Sec. IV A compare the dispersion curves obtained by seeking the poles of reflection coefficient (23) and the results taken from literature or from closed-form solution.

A. Validation for a homogeneous and isotropic or anisotropic fluid-loaded plate

The method is tested by plotting the dispersion curves (variation of the phase velocity versus frequency-thickness product) for an isotropic aluminum plate immersed in water. The data in the paper of Chimenti and Rokhlin (1990) are used. The results obtained (not shown) by the present method are in perfect agreement with the results presented by them (Chimenti and Rokhlin, 1990).

As mentioned by Chimenti and Rokhlin (1990), there are few differences between the zeros' loci and the poles' loci for a plate immersed in a fluid whose the mass density is lower than the plate mass density. As underlined by several authors, fluid-load does have just a weak influence on guided wave traveling in the plate immersed in water.

Taking into account the anisotropy does not change the scheme for the numerical solution of wave equation with the matricant. We consider a transverse isotropic plate immersed in water ($\rho_f=1$ g cm^{-3}, $c_f=1.485$ mm μs^{-1}) whose properties are reported in Table I. For that configuration, Nayfeh and Chimenti (1989) developed a method to obtain an analytical expression of the reflection coefficient. By using the data from this paper, the results obtained (see Fig. 1) with the present method are in perfect agreement with theirs. The curves presented in Figs. 1(a) and 1(b) are superimposed and need to be presented separately.

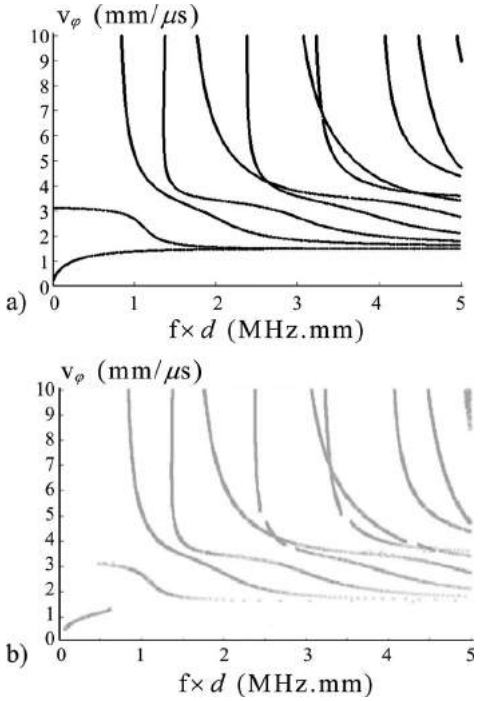

FIG. 1. Dispersion curves for a transversely isotropic plate immersed in water; comparison between (a) analytical results from Nayfeh and Chimenti (1989) and (b) results obtained via the Peano series expansion of the matricant.

B. Validation for an asymmetrically loaded homogeneous isotropic plate ($f_1 \neq f_2$)

The formalism presented here to solve the wave equation in an unidirectionally graded medium presents two main advantages: Without changing the scheme to obtain the numerical solution we can take into account (i) an asymmetric loading and (ii) the unidirectional continuous heterogeneity.

The mechanical behavior of the plate is different for symmetric and asymmetric loadings. For example, in the symmetric loading case, there is a unique critical frequency and a unique phase velocity value v_φ in the plate, which corresponds to the propagation velocity in the fluid ($v_\varphi = c_{f_1} = c_{f_2}$), for which the displacements and the stresses at the interfaces are quasi-null; whereas in the asymmetric loading ($f_1 = f_2$), there are two critical frequencies and two values of the phase velocity in the plate for which the structure does not respond (Dickey *et al.*, 1995). The validation is done on an isotropic aluminum plate with the following properties: $\rho = 2.79$ g cm^{-3}; the longitudinal and transverse wave velocities are, respectively, $v_L = 6.38$ mm μs^{-1} and $v_T = 3.10$ mm μs^{-1}. The characteristic properties of the fluid f_1 correspond to those of water (see Sec. IV A); the characteristic properties of the fluid f_2 correspond to glycerine: $\rho_{f_2} = 1.26$ g cm^{-3} and $c_{f_2} = 1.920$ mm μs^{-1}. This configuration is the same as the one studied by Franklin *et al.* (2001). The modulus of the reflection coefficient versus the incident angle is plotted in Fig. 2 for a fixed frequency-thickness product ($f \times d = 4.7$ MHz mm).

This figure shows the perfect agreement between our results and the ones presented by Franklin *et al.* (2001).

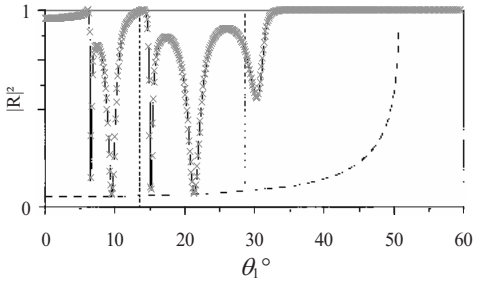

FIG. 2. Reflection coefficient modulus for an asymmetrically fluid-loaded aluminum plate (water and glycerine) versus incident angle: in dark lines results published in Franklin *et al.* (2001), and in gray crosses the reflection coefficient modulus calculated from Eq. (23). The vertical lines (dashed) represent the two critical angles for longitudinal waves and transverse waves. The dashed curve corresponds to the resonant amplitudes (Franklin *et al.*, 2001).

V. RELEVANCY OF THE METHOD FOR ULTRASOUND CHARACTERIZATION OF CORTICAL BONE

Cortical bone is a kind of hard tissue found at the edges of long bones and supports most of the load of the body. Several studies demonstrated the heterogeneous nature of the cortical bone, particularly they show evidence the gradual variation of the volumetric porosity (ratio between pores and total volume) along the cortical thickness. Yet, the porosity is intrinsically linked to the macroscopic mechanical behavior of the cortical bone (Baron *et al.*, 2007). Therefore, the continuous variation of porosity induces a continuous variation of material properties. Taking into account the gradient should prove itself to be essential in the context of diagnosis and therapeutic monitoring of osteoporosis. Indeed, the gradient characterization would allow assessing geometrical (cortex thickness) and material (elastic coefficients variation) information, which are fundamental parameters to evaluate the bone fragility. For several years, the quantitative ultrasonography (by axial and transverse transmissions) proved itself to be a hopeful alternative technique to evaluate the fracture risk (Marin *et al.*, 2006). However, the inter-individual and inter-site variations of bone mechanical properties make the standardization of the protocol of fracture risk evaluation by ultrasound very delicate.

The focus is set on a configuration closed to the axial transmission device for *in vivo* conditions. In this context, the relevancy of studying the head wave propagation has been demonstrated (Bossy *et al.*, 2004a, 2004b; Camus *et al.*, 2000). As a consequence all the reflection coefficients presented in this paper were calculated for an incident angle corresponding to the grazing-angle for longitudinal waves [critical angle of longitudinal wave propagation in the plate at the first interface ($x_3 = 0$)].

The surrounding media in the *in vivo* configuration of ultrasound characterization of cortical bone are the muscle for the upper fluid f_1 ($c_{f_1} = 1.54$ mm μs^{-1} and $\rho_{f_1} = 1.07$ g cm^{-3}) and the marrow for the lower fluid f_2 ($c_{f_2} = 1.45$ mm μs^{-1} and $\rho_{f_2} = 0.9$ g cm^{-3}) (Burlew *et al.*, 1980; Hill *et al.*, 1986). We are interested in the influence of the continuous gradient of the mechanical properties on the ultrasonic response in the configuration of *in vivo* cortical bone characterization.

A. Determination of a realistic range of variation of elastic bone properties

In order to define numerical values for a realistic value of the gradient of the different material properties, it is necessary to determine the limiting values reached by each elastic property. Our approach consists in considering *in vitro* measurements published in Dong and Guo, 2004 and performed in 18 samples. It is assumed that these limiting values for elastic properties are relevant for physiologic ranges of variations.

We assume that cortical bone is transversely isotropic. Transverse isotropy has been shown experimentally by different authors (Dong and Guo, 2004; Reilly and Burnstein, 1974; Rho, 1996) to be a realistic approximation of cortical bone degree of anisotropy.

Dong and Guo (2004) measured the homogenized bone properties by performing tensile and torsional tests with a mechanical testing system on 18 different human femoral bone specimens. The authors measured the values of the longitudinal and transverse Young's moduli (E_L and E_T, respectively) as well as the values of the longitudinal shear modulus G_L. From these measurements and by assuming constant values of Poisson's ratio, the values of the different components of the stiffness-tensor corresponding to the values of E_L, E_T, and G_L measured in Dong and Guo, 2004 were obtained following the relationships given in the Appendix.

The value of the longitudinal Poisson's ratio ν_L is taken equal to 0.37 for all computations because it corresponds to the average value found in Dong and Guo, 2004. The value of the transverse Poisson's ratio ν_T is taken equal to 0.45 following Eq. (A3) of the Appendix. The values of the stiffness coefficients corresponding to the mean values of the bone mechanical properties are referred to as "reference" set of parameters in what follows. The maximum and minimum values of the stiffness coefficients are obtained by considering, respectively, the maximum and minimum values of E_L and E_T within the range of variation measured in Dong and Guo, 2004, which is a simple way to obtain a realistic range of variation for the stiffness coefficients in cortical bone. Furthermore, the elastic properties deduced from the approach reported above were constrained to verify the thermodynamical stability conditions given in the Appendix by Eq. (A4).

We choose reference value of mass density ρ equal to 1.722 g cm^{-3}, following the value taken in Macocco *et al.*, 2006. In order to derive a realistic range of variation for mass density, we assume that the reference value is given by a porosity of 7%, which corresponds approximately to the mean porosity at the radius (Baron *et al.*, 2007). The porosity was assumed to vary between 3% and 15% (Bousson *et al.*, 2001; Dong and Guo, 2004) and a rule of mixture leads to the range of variation of mass density.

B. Modeling a gradient of material property

The impact of a controlled gradient vector $\boldsymbol{\delta}$ of any investigated material property S on the response of the structure studied is assessed. The scalar S corresponds to one of the stiffness coefficients c_{ij} of $\mathbb{C}$ or to mass density ρ. In each set of simulations, all the material properties are constant and equal to their reference value while S is subjected to the defined gradient.

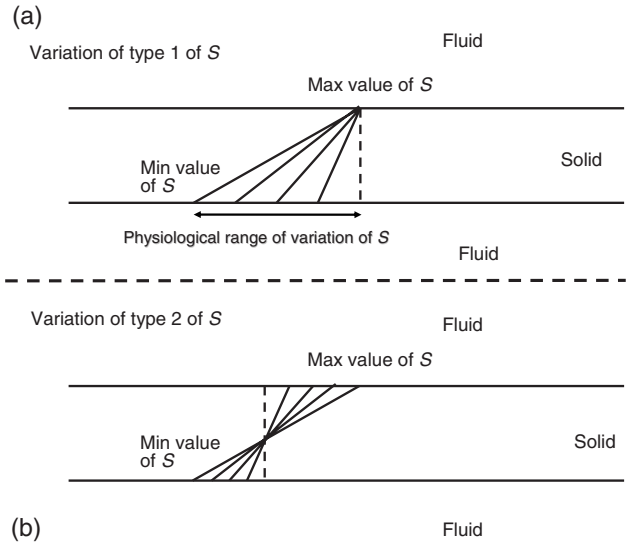

FIG. 3. Schematic representation of the two types of spatial variation considered for the material property S corresponding to the stiffness coefficient and to mass density. The solid lines in the solid layer indicate the spatial dependence of S. The dotted line in the solid layer indicates homogeneous material properties corresponding to the reference material properties. The variation of type 1 shown in (a) corresponds to a constant value at the bone-soft tissues' interface. The variation of type 2 shown in (b) corresponds to a constant value in the middle of the bone.

The gradient vector $\boldsymbol{\delta}=\text{grad}\, S=\delta \mathbf{x}_3$ is assumed to be independent of x_1 in all cases, where $\mathbf{x}_3$ is a unit vector along $\mathbf{x}_3$-axis and grad is the gradient operator acting on a scalar field. The quantity δ is always taken positive because the porosity is known to be higher in the endosteal part ($x_3=d$) than in the periosteal part ($x_3=0$) of the bone. Moreover, only the simple situation of affine spatial variations of S is considered, corresponding to a constant value of δ. This affine spatial variation of S is chosen because the actual physiological spatial dependence of S remains unknown. Two different affine spatial dependencies of the studied material property are considered and are illustrated in Fig. 3. Associated gradient δ will be referred to as type 1 or 2.

Type 1. The gradient of type 1 is such that the physical property S takes the same value S_M at the upper interface $x_3=0$ of the solid plate for all values of the gradient δ. The quantity $S(x_3)$ is therefore given by

$$S(x_3) = S_M + \delta \times x_3, \tag{24}$$

where S_M is given by the maximal value of the material property S considered. The maximal value δ_M of δ is chosen so that $S(d)$ is equal to S_m, where S_m is given by the minimal value of S. The gradient δ_M is given by

$$\delta_M = \frac{(S_m - S_M)}{d}. \tag{25}$$

Type 2. The gradient of type 2 is such that the physical property S takes the same value at the middle $x_3=d/2$ of the solid plate for all values of gradient δ. Furthermore, the

TABLE II. Mean value, maximum, and minimum values of the homogenized longitudinal and transversal Young moduli, of the four elastic constants and of mass density affecting the ultrasonic propagation in the framework of the model. These values are taken from Dong and Guo (2004).

Mechanical quantity	E_L (GPa)	E_T (GPa)	c_{11} (GPa)	c_{13} (GPa)	c_{33} (GPa)	$c_{55}=G_L$ (GPa)	ρ (g cm^{-3})
Mean value (reference)	16.6	9.5	23.1	8.7	15.1	4.7	1.722
Minimum	13.4	6.5	17.6	5.1	9.1	3.3	1.66
Maximum	20.6	12.8	29.6	15.9	25.9	5.5	1.753

mean value of the property S is identical for all δ. The quantity $S(x_3)$ is given by

$$S(x_3) = \frac{(S_m + S_M)}{2} + \delta \times \left(x_3 - \frac{d}{2} \right). \tag{26}$$

The maximal value of δ is also given by Eq. (25), so that all values of $S(x_3)$ are again always comprised between S_m and S_M. Again, the maximal value δ_M of δ is given by Eq. (25).

Gradient of type 2 leads for all magnitudes of δ to a constant value of the spatial average of the gradient.

For both types of spatial variations, five different values of δ regularly distributed between 0 and δ_M are arbitrarily considered in the thickness.

Table II recalls the maximum, minimum, and mean measured values of E_L, E_T, and G_L as given by Dong and Guo (2004). Table II also shows the maximum, minimum, and mean values of the four components (c_{11}, c_{13}, c_{33}, and c_{55}) of the stiffness-tensor $\mathbb{C}$ affecting wave propagation derived from Eq. (A3) of the Appendix.

In Table III, the minimal and maximal values of each variable corresponding to the realistic range of variation obtained (i) by considering the reference values of Table II and (ii) by verifying that the thermodynamical stability conditions are fulfilled. Values resulting from the stability conditions are marked with an asterisk.

In the simulations, the values of S_M and S_m are those reported in Table III.

C. Results and discussion

First of all, the method allows investigating the influence of the fluids on the ultrasonic response. In the case of the characterization of cortical bone, the two fluids f_1 and f_2 are different, which corresponds to an asymmetrical loading (see Sec. IV B): The fluid f_1 has been considered as muscle ($c_{f_1}=1540$ m s^{-1} and $\rho_{f_1}=1.07$ g cm^{-3}) and fluid f_2 as marrow ($c_{f_2}=1450$ m s^{-1} and $\rho_{f_2}=0.9$ g cm^{-3}). The properties of these two fluids are very close to those of water. The frequency spectrum of the reflection coefficient modulus has been plotted for the *in vivo* configuration and compared with the result obtained for a cortical bone plate immersed in water for the ten profiles of mechanical properties (figure not shown). For homogeneous plates as for linearly graded plates, the two curves are very close; however, the modulus of the reflection coefficient at null-frequency is not null and the minimum values are greater than for water but obtained for the same frequency-thickness products. That is why all the following results have been calculated for a cortical bone plate immersed in water.

The reflection coefficient calculated with the Peano series expansion of the matricant is sensitive to the variation of the properties gradient. As we consider that the osteoporosis entails a trabecularization of cortical bone from the endosteal side, the characterization of the gradient of the properties between the endosteal and periosteal regions may be an element of the diagnosis of the osteoporosis progress and of the therapeutic follow-up.

It is known that the gradient of the properties along the cortical thickness is due to the continuous variation of the porosity growing progressively from the periosteal to the endosteal region. From previous work, we know that the porosity influences all the stiffness coefficients (Baron *et al.*, 2007). The frequency spectrum of the reflection coefficient has been plotted for the ten profiles presented in Fig. 3 applied to all the stiffness coefficients implied (c_{11}, c_{13}, c_{33}, and c_{55}) and to the mass density ρ (see Table III). The reflection coefficients have been calculated at an incident angle corresponding to the grazing-angle (critical angle for the longitudinal waves in the bone plate). For the two types of gradients, differences appear between all the gradients and the homogenized plates (corresponding to the maximum value for type 1 and to the average value for type 2) particularly on the location of the extrema values of the reflection coefficient modulus (see Fig. 4).

The increase in the gradient of properties shifts the minimum and maximum values forward high frequency-thickness products. However, the results (see Fig. 4) put on evidence that the behavior of the reflection coefficient modulus is sensibly the same for frequency-thickness products be-

TABLE III. The minimal and maximal values of each variable corresponding to the realistic range of variation obtained (i) by considering the reference values of Table II and (ii) by verifying that the thermodynamical stability conditions are fulfilled. Values resulting from the stability conditions are marked with an asterisk.

Material property S	c_{11} (GPa)	c_{13} (GPa)	c_{33} (GPa)	$c_{55}=G_L$ (GPa)	ρ (g cm^{-3})
Realistic range $[S_m, S_M]$ (reference)	[17.6, 29.6]	[5.1, 11.1*]	[11.8*, 25.9]	[3.3, 5.5]	[1.66, 1.753]

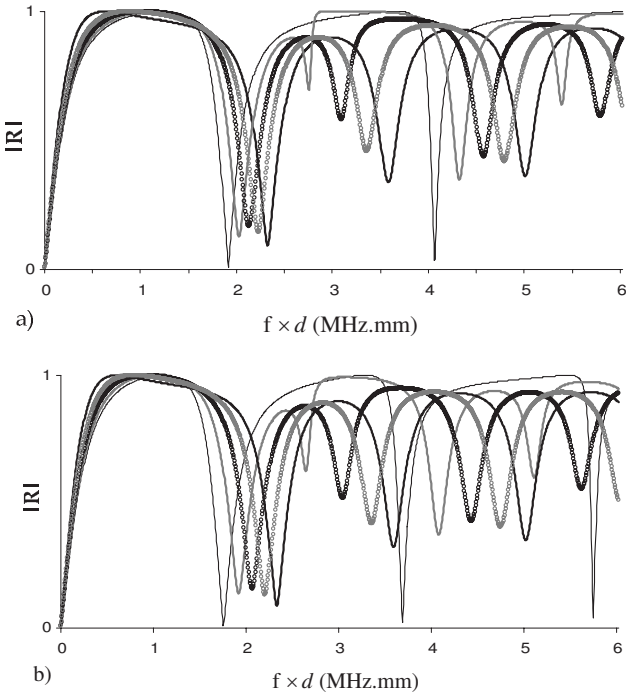

FIG. 4. Frequency spectrum of the reflection coefficient modulus for different properties' variations corresponding to (a) the five profiles of type 1 [Fig. 3(a)] and (b) the five profiles of type 2 [Fig. 3(b)].

tween 0 and 1.5 MHz mm. Beyond this value, the behavior is clearly different. At sufficiently high frequency, the wavelength is smaller and more sensitive to the affine variation of the material properties. It is noteworthy that for a heterogeneous waveguide, the minima of the reflection coefficient magnitude do not reach zero (except for null-frequency) but end at a finite value and the changes in phase (not shown) are not so rapid, which means that total transmission does not take place in this situation.

The influence of the variation of each parameter (stiffness coefficients) on the frequency spectrum of the reflection coefficient has been investigated. This analysis has been led for an incidence angle corresponding to the longitudinal wave critical angle in the plate at $x_3=0$. This incidence corresponds to the generation and the propagation of the head wave.

It appears that each of them has an impact on the reflection wave, but the leading term is c_{11}. The frequency spectrum of the reflection coefficient for a varying c_{11} in an affine way is very close to the frequency spectrum of the reflection coefficient obtained for the affine variation of all the material properties (c_{ij} and ρ) and is the most different to the results from homogenized plates (average value or maximum value) compared to the frequency spectrum calculated for the *one-parameter variation* of the other elastic parameters (c_{13}, c_{33}, and c_{55}, and ρ) (see Fig. 5). It is noteworthy that c_{11} is the stiffness coefficient associated with the axial direction and determining the speed of the head wave. So, it seems that the head wave would be the indicator of the c_{11} gradient. It is important to note that for homogenized plates (extremum value or average) the frequency spectrum of the reflection coefficient is really different from that of the plate with continuously varying properties. We infer that the approximation by a homogeneous plate of cortical bone and all the more so for the osteoporotic cortical bone (for which the gradient would be greater) may induce bad interpretation of the ultrasonic response.

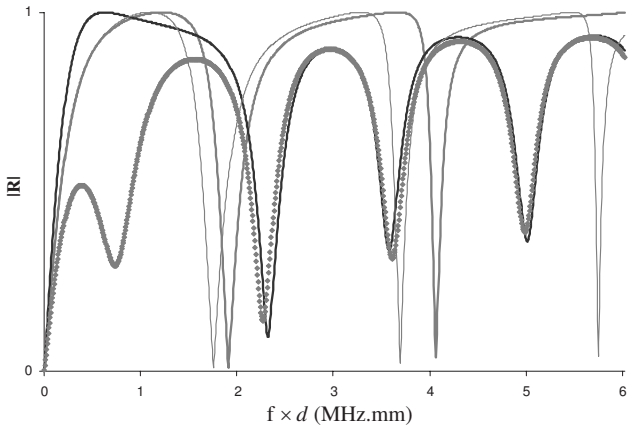

FIG. 5. Frequency spectrum of the reflection coefficient modulus for different properties' variations at grazing-incidence $\theta_1=\theta_c$: for a homogeneous plate whose properties are those at $x_3=0$ at $\theta_c=21.1°$ (thick gray line), for a homogeneous plate whose properties are the average of the properties through the plate at $\theta_c=23.6°$ (thin gray line), for a plate with all its properties linearly varying at $\theta_c=21.1°$ (black line), and for a plate with an affine variation of the c_{11} only at $\theta_c=21.1°$ (gray lozenges).

The authors do not know any results in literature about the measurement of the variation of the porosity within the cortical thickness. The assumption of an affine gradient is a first step; other gradients may be investigated and the method presented in this article would be applied in the same way for non-affine gradients (Shuvalov *et al.*, 2005).

VI. CONCLUSION AND PERSPECTIVES

Stroh's (1962) sextic plate formalism has been employed for analyzing the leaky Lamb waves in anisotropic heterogeneous plates immersed in fluids. This formalism and especially the polynomial form of the solution [see Eq. (15)] presents several analytical and numerical advantages. First, the low-frequency asymptotics are naturally assessed evaluating only two or three terms in the series (Shuvalov *et al.*, 2005). The information thus collected is of major interest in the analysis of the elastic behavior of waveguides (Baron *et al.*, 2008). Second, the polynomial form makes the numerical evaluation of the solution faster. Indeed, the polynomial coefficients are independent of the frequency, so they are calculated for a fixed slowness value and stored. When the frequency varies, there is no need to recalculate the polynomial coefficients, it comes to a polynomial evaluation whose coefficients are perfectly known, which is time-saving.

The Peano series of the matricant is a method that keeps the continuity of the profiles and so, the authenticity of the problem. One of the key points for methods based on multilayered media to deal with FGM is to relevantly discretize the properties' profiles. The choice of the discretization may lead to some errors especially in the evaluation of the resonances.

This elegant mathematical tool is also very adaptative to different physical problems. In the case studied—a fluid-loaded plane waveguide—the anisotropy, the heterogeneity (continuous or discontinuous variation of properties) and the asymmetric fluid-loading are taken into account without changing the resolution scheme.

Further work needs to be done to relate the results presented in this paper to dispersion curves and propagation of transient and heterogeneous waves in a fluid-loaded continuously heterogeneous waveguide.

Furthermore, from this study, the transient response of a fluid-loaded plate is considered. The frequency spectrum of the reflection coefficient is calculated for incidences between the normal and critical incidences for compression waves in the fluid f_1. Thus, the plate transfer function is calculated in the Fourier domain (x_1-wavenumber, frequency): $\hat{R}(k_1,x_3;\omega)$. A double inverse Fourier transform on (k_1,ω) is applied on $\hat{R}(k_1,x_3;\omega)$ to transform into the space-time domain; the temporal signals can be obtained at different points along the propagation $\mathbf{x}_3$-axis: $R(x_1,x_3;t)$.

Lastly, the formalism presented here is well-adapted to deal with wave propagation in anisotropic tubes with radial property gradients (Shuvalov, 2003). The wave equation keeps the same form as Eq. (12), the state-vector is expressed from the displacement and traction components in the cylindrical basis, and the matrix $\mathbf{Q}$ depends on the radial position r ($\mathbf{Q}=\mathbf{Q}(r)$). In cylindrical homogeneous structures, taking into account an anisotropy more important than transverse isotropy is fussy because there is no analytical solution to the "classical" wave equation (second-order differential equation). Stroh's (1962) formalism, upon which the Peano expansion of the matricant is based, is a promising alternative solution that allows considering altogether the geometry (cylinder), the anisotropy, and the heterogeneity (radial property gradients) of a structure.

APPENDIX: THERMODYNAMICS STABILITY CONDITIONS AND STIFFNESS COEFFICIENTS

Hooke's law is written under the form $\sigma_{ij}=C_{ijk\ell}\epsilon_{k\ell}$ for $(i,j,k,\ell=1,\ldots,3)$, where σ is the stress-tensor, ϵ is the strain-tensor, and $\mathbb{C}$ is the fourth-order stiffness-tensor. In the transversely isotropic case, with $(\mathbf{x}_2,\mathbf{x}_3)$ as isotropic plane, the stiffness-tensor is expressed as a stiffness matrix (using Voigt's notation)

$$\mathbb{C}=\begin{pmatrix} c_{11} & c_{13} & c_{13} & 0 & 0 & 0 \\ c_{13} & c_{33} & c_{23} & 0 & 0 & 0 \\ c_{13} & c_{23} & c_{33} & 0 & 0 & 0 \\ 0 & 0 & 0 & c_{44} & 0 & 0 \\ 0 & 0 & 0 & 0 & c_{55} & 0 \\ 0 & 0 & 0 & 0 & 0 & c_{55} \end{pmatrix}. \tag{A1}$$

We introduce the matrix $\mathbb{S}$, the inverse of the matrix $\mathbb{C}$. It is expressed by

$$\mathbb{S}=\begin{pmatrix} 1/E_L & -\nu_L/E_L & -\nu_L/E_L & 0 & 0 & 0 \\ -\nu_L/E_L & 1/E_T & -\nu_T/E_T & 0 & 0 & 0 \\ -\nu_L/E_L & -\nu_T/E_T & 1/E_L & 0 & 0 & 0 \\ 0 & 0 & 0 & 1/G_T & 0 & 0 \\ 0 & 0 & 0 & 0 & 1/G_L & 0 \\ 0 & 0 & 0 & 0 & 0 & 1/G_L \end{pmatrix}. \tag{A2}$$

with $E_{L,T}$, the longitudinal (L) and transverse (T) Young's moduli; $\nu_{L,T}$, the longitudinal (L) and transverse (T) Poisson's ratios; and $G_{L,T}$, the longitudinal (L) and transverse (T) shear moduli. By inverting Eq. (A1)and identifying it with Eq. (A2), we obtain the following relations:

$$E_L=\frac{c_{11}c_{33}-2c_{13}^2+c_{11}c_{23}}{c_{33}+c_{23}}, \quad \nu_L=\frac{c_{13}}{c_{33}+c_{23}},$$

$$E_T=\frac{c_{11}(c_{33}^2-c_{23}^2)+2c_{13}^2(c_{23}-c_{33})}{c_{11}c_{33}-c_{13}^2}, \quad \nu_T=\frac{c_{11}c_{23}-c_{13}^2}{c_{11}c_{33}-c_{13}^2},$$

$$G_T=c_{44}, \quad G_L=c_{55}. \tag{A3}$$

Knowing the stiffness coefficient values, we can verify if the thermodynamical stability conditions are satisfied as follows:

$$E_L>0, \quad E_T>0, \quad -1<\nu_T<1,$$

$$\frac{(1-\nu_T)}{2}\frac{E_L}{E_T}-\nu_L^2>0, \quad G_L>0. \tag{A4}$$

Baron, C. (**2005**). "Peano expansion of the matricant to study elastic wave propagation in continuously heterogeneous media," University Bordeaux 1 (in French).

Baron, C., Poncelet, O., Shuvalov, A., and Deschamps, M. (**2008**). "Propagation in continuous stratification environment," in *Materials and Acoustics Handbook*, edited by M. Bruneau and C. Potel (ISTE Ltd. and Wiley, London, UK), Chap. 6.

Baron, C., Talmant, M., and Laugier, P. (**2007**). "Effect of porosity on effective diagonal stiffness coefficients (c_{ii}) and anisotropy of cortical at 1 MHz: A finite-difference time domain study," J. Acoust. Soc. Am. **122**, 1810–1817.

Bossy, E., Talmant, M., and Laugier, P. (**2004a**). "Three-dimensional simulations of ultrasonic axial transmission velocity measurement on cortical bone models," J. Acoust. Soc. Am. **115**, 2314–2324.

Bossy, E., Talmant, M., Peyrin, F., Akrout, L., Cloetens, P., and Laugier, P. (**2004b**). "An *in vitro* study of the ultrasonic axial transmission technique at the radius: 1-MHz velocity measurements are sensitive to both mineralization and intracortical porosity," J. Bone Miner. Res. **19**, 1548–1556.

Bousson, V., Meunier, A., Bergot, C., Vicaut, E., Rocha, M. A., Morais, M. H., Laval-Jeantet, A. M., and Laredo, J. D. (**2001**). "Distribution of intracortical porosity in human midfemoral cortex by age and gender," J. Bone Miner. Res. **16**, 1308–1317.

Brekhovskikh, L. M. (**1980**). *Waves in Layered Media* (Academic, New York).

Burlew, M., Madsen, E., Zagzebski, J., Banjavic, R., and Sum, S. (**1980**). "A new ultrasound tissue-equivalent material," Radiology **134**, 517–520.

Camus, E., Talmant, M., Berger, G., and Laugier, P. (**2000**). "Analysis of the axial transmission technique for the assessment of skeletal status," J. Acoust. Soc. Am. **108**, 3058–3065.

Chimenti, D. E., and Nayfeh, A. H. (**1986**). "Anomalous ultrasonic dispersion in fluid-coupled, fibrous composite plates," Appl. Phys. Lett. **49**, 492–493.

Chimenti, D. E., and Nayfeh, A. H. (**1990**). "Ultrasonic reflection and guided waves in fluid-coupled composite laminates," J. Nondestruct. Eval. **9**, 51–69.
Chimenti, D. E., and Rokhlin, S. (**1990**). "Relationship between leaky Lamb modes and reflection coefficient zeroes for a fluid-coupled elastic layer," J. Acoust. Soc. Am. **88**, 1603–1611.
Deschamps, M., and Poncelet, O. (**2000**). "Transient Lamb waves: Comparison between theory and experiment," J. Acoust. Soc. Am. **107**, 3120–3129.
Dickey, J., Maidanik, G., and Uberall, H. (**1995**). "The splitting of dispersion curves for the fluid-loaded plate," J. Acoust. Soc. Am. **98**, 2365–2367.
Dong, X. N., and Guo, X. E. (**2004**). "The dependence of transversely isotropic elasticity of human femoral cortical bone on porosity," J. Biomech. **37**, 1281–1287.
Fiorito, R., Madigosky, W., and Überall, H. (**1979**). "Resonance theory of acoustic waves interacting with an elastic plate," J. Acoust. Soc. Am. **66**, 1857–1866.
Folds, D. L., and Loggins, C. D. (**1977**). "Transmission and reflection of ultrasonic waves in layered media," J. Acoust. Soc. Am. **62**, 1102–1109.
Franklin, H., Danila, E., and Conoir, J.-M. (**2001**). "S-matrix theory applied to acoustic scattering by asymmetrically fluid-loaded elastic isotropic plates," J. Acoust. Soc. Am. **110**, 243–253.
Gantmacher, F. (**1959**). *The Theory of Matrices* (Wiley, New York).
Haskell, N. A. (**1953**). "The dispersion of surface waves on multilayered media," Bull. Seismol. Soc. Am. **43**, 377–393.
Hill, C., Bamber, J., and Ter Haar, G. (**1986**). *Physical Principles of Medical Ultrasonics* (Wiley, New York).
Hosten, B., and Castaings, M. (**2003**). "Surface impedance matrices to model the propagation in multilayered media," Ultrasonics **41**, 501–507.
Kenneth, E. G. (**1982**). "A propagator matrix method for periodically stratified media," J. Acoust. Soc. Am. **73**, 137–142.
Lamb, H. (**1917**). "On waves in an elastic plate," Proc. R. Soc. London Ser. A **93**, 114–128.
Lévesque, D., and Piché, L. (**1992**). "A robust transfer matrix simulation for ultrasonic response of multilayered absorbing media," J. Acoust. Soc. Am. **92**, 452–467.
Macocco, K., Grimal, Q., Naili, S., and Soize, C. (**2006**). "Elastoacoustic model with uncertain mechanical properties for ultrasonic wave velocity prediction; application to cortical bone evaluation," J. Acoust. Soc. Am. **119**, 729–740.
Marin, F., Gonzales-Macias, J., Diez-Perez, A., Palma, S., and Delgado-Rodriguez, M. (**2006**). "Relationship between bone quantitative ultrasound and fractures: A meta-analysis," J. Bone Miner. Res. **21**, 1126–1135.
Nayfeh, A. H., and Chimenti, D. E. (**1988**). "Ultrasonic wave reflection from liquid-coupled orthotropic plates with application to fibrous composites," ASME J. Appl. Mech. **55**, 863–870.
Nayfeh, A. H., and Chimenti, D. E. (**1989**). "Free wave propagation in plates of general anisotropic media," ASME J. Appl. Mech. **56**, 881–886.
Peano, G. (**1888**). "Integration by series of linear differential equations (in French)," Math. Ann. **32**, 450–456.
Pease, M. (**1965**). *Methods of Matrix Algebra* (Academic, New York).
Pitts, L. E., Plona, T. J., and Mayer, W. G. (**1976**). "Theoretical similarities of Rayleigh and Lamb modes of vibration," J. Acoust. Soc. Am. **60**, 374–377.
Rayleigh, J. W. S. (**1885**). "On wave propagating along the plane surface of an elastic solid," Proc. London Math. Soc. **s1-17**, 4–11.
Reilly, D. T., and Burnstein, A. H. (**1974**). "The mechanical properties of cortical bone," J. Bone Jt. Surg., Am. Vol. **56**, 1001–1022.
Rho, J. Y. (**1996**). "An ultrasonic method for measuring the elastic properties of human tibial cortical and cancellous bone," Ultrasonics **34**, 777–783.
Rokhlin, S. I., and Wang, L. (**2002**). "Stable recursive algorithm for elastic wave propagation in layered anisotropic media: Stiffness matrix method," J. Acoust. Soc. Am. **112**, 822–834.
Rose, J. L. (**2002**). "A baseline and vision of ultrasonic guided wave inspection potential," J. Pressure Vessel Technol. **124**, 273–282.
Shuvalov, A. (**2003**). "A sextic formalism for three-dimensional elastodynamics of cylindrically anisotropic radially inhomogeneous materials," Proc. R. Soc. London, Ser. A **459**, 1611–1639.
Shuvalov, A., Poncelet, O., Deschamps, M., and Baron, C. (**2005**). "Long-wavelength dispersion of acoustic waves in transversely inhomogeneous anisotropic plates," Wave Motion **42**, 367–382.
Stroh, A. N. (**1962**). "Steady state problems in anisotropic elasticity," J. Math. Phys. **41**, 77–103.
Thomson, W. T. (**1950**). "Transmission of elastic waves through a stratified solid medium," J. Appl. Phys. **21**, 89–93.
Vlasie, V., and Rousseau, M. (**2004**). "Guided modes in a plane elastic layer with gradually continuous acoustic properties," NDT & E Int. **37**, 633–644.
Wang, L., and Rokhlin, S. I. (**2001**). "Stable reformulation of transfer matrix method for wave propagation in layered anisotropic media," Ultrasonics **39**, 413–424.
Worlton, H. (**1961**). "Experimental confirmation of Lamb waves at megacycle frequencies," J. Appl. Phys. **32**, 967–971.
Youssef, I., and El-Arabawi, H. (**2007**). "Picard iteration algorithm combined with Gauss-Seidel technique for initial value problems," Appl. Math. Comput. **190**, 345–355.

4.4 Ultrasonics 2011

Ultrasonics, 2011

Propagation of elastic waves in an anisotropic functionally graded hollow cylinder in vacuum.
C. Baron
Ultrasonics 51, 123-130.

Ultrasonics 51 (2011) 123–130

Contents lists available at ScienceDirect

Ultrasonics

journal homepage: www.elsevier.com/locate/ultras

Propagation of elastic waves in an anisotropic functionally graded hollow cylinder in vacuum

Cécile Baron *

UPMC Univ. Paris 06, UMR 7190, Institut Jean Le Rond d'Alembert, F-75005 Paris, France
CNRS, UMR 7190, Institut Jean Le Rond d'Alembert, F-75005 Paris, France

ARTICLE INFO

Article history:
Received 19 February 2010
Received in revised form 1 July 2010
Accepted 2 July 2010
Available online 7 August 2010

Keywords:
Elastic wave propagation
Radially graded tube
Stroh's formalism
Waveguide
In vitro bone characterization

ABSTRACT

As a non-destructive, non-invasive and non-ionizing evaluation technique for heterogeneous media, the ultrasonic method is of major interest in industrial applications but especially in biomedical fields. Among the unidirectionally heterogeneous media, the continuously varying media are a particular but widespread case in natural materials. The first studies on laterally varying media were carried out by geophysicists on the Ocean, the atmosphere or the Earth, but the teeth, the bone, the shells and the insects wings are also functionally graded media. Some of them can be modeled as planar structures but a lot of them are curved media and need to be modeled as cylinders instead of plates. The present paper investigates the influence of the tubular geometry of a waveguide on the propagation of elastic waves. In this paper, the studied structure is an anisotropic hollow cylinder with elastic properties (stiffness coefficients c_{ij} and mass density ρ) functionally varying in the radial direction. An original method is proposed to find the eigenmodes of this waveguide without using a multilayered model for the cylinder. This method is based on the sextic Stroh's formalism and an analytical solution, the matricant, explicitly expressed under the Peano series expansion form. This approach has already been validated for the study of an anisotropic laterally-graded plate (Baron et al., 2007; Baron and Naili, 2010) [6,5]. The dispersion curves obtained for the radially-graded cylinder are compared to the dispersion curves of a corresponding laterally-graded plate to evaluate the influence of the curvature.

Preliminary results are presented for a tube of bone in vacuum modelling the *in vitro* conditions of bone strength evaluation.

1. Introduction

The observation of natural media and particularly of living tissues is a great source of inspiration for scientists. As an example, they develop industrial Functionally Graded Materials (FGM) in the 80s which reproduce a characteristic observed in natural media such as wood, bone or shells. The continuous variation of the mechanical properties of these materials reveals interesting mechanical behavior particularly exploited in high-technology and biomedical applications [48,19,26]. As a consequence, the non-destructive characterization of FGM structures became a key issue: first, to better understand the natural mechanisms observed and second, to guide the conception of groundbreaking FGM. Surface and guided waves are significant information source in non-destructive testing and evaluation of complex structures. A lot of works detailed the behavior of the guided waves in isotropic or anisotropic plates [39,23,46,3]. Also, elastic wave propagation in cylindrical structures formed from material with lower anisotropy than orthotropy has been the subject of numerous theoretical and experimental investigations widely published [30,50,20]. For anisotropic material, the complexity of the problem relies on the fact that the boundary problem do not permit solution in cylindrical functions except in some particular configurations [29].

In this work, we solve the wave equation in an anisotropic waveguide with one-direction heterogeneity using a general method based on the sextic Stroh's formalism [44]. It takes into account the unidirectional continuous variation of the properties of the waveguide without using a multilayered model. It is based on the knowledge of an analytical solution of the wave equation, the matricant, explicitly expressed *via* the Peano series expansion [6]. The accuracy of the numerical evaluation of this solution and its validity domain are perfectly managed [4,49]. One of the advantages of knowing an analytical solution with respect to purely numerical methods is to control all the physical parameters and to interpret more easily the experimental data which result from the interaction and coupling of numerous physical phenomena.

In this paper, a sample of long bone is considered as an example of anisotropic functionally graded tube. The material is multiscale

* Address: UPMC Univ. Paris 06, UMR 7190, Institut Jean Le Rond d'Alembert, F-75005 Paris, France.
E-mail address: cecile.baron@upmc.fr

0041-624X/$ - see front matter © 2010 Elsevier B.V. All rights reserved.
doi:10.1016/j.ultras.2010.07.001

and the discrete variations of its microscopic properties (bone matrix elasticity, micro-architecture, etc.) [9,8,41] is assumed to induce continuous profiles of macroscopic properties in the radial direction [7,16,5]. Obviously, the mechanical behavior of bone depends on several parameters (microstructure, elasticity and geometry). The curvature is part of them and its influence remains unclear.

We first present the method and its setup for the cylindrical waveguide; this method has been validated by comparing our results to the dispersion curves obtained from classical schemes on homogeneous and functionally graded waveguides. Some advantages of the method are underlined: (i) general anisotropy may be taken into account for cylindrical structures; (ii) the influence of the property gradient on the mechanical behavior of the waveguide may be investigated; (iii) the influence of the curvature on the propagation of elastic waves may be evaluated.

2. Methods

We consider an elastic tube of thickness t placed in vacuum.

The radius r varies from a_0 to a_q, respectively, the inner and outer radius of the tube (Fig. 1). The elastic cylinder is supposed to be anisotropic and is liable to present continuously varying properties along its radius ($\mathbf{e}_r$-axis). These mechanical properties are represented by the stiffness tensor $\mathbb{C} = \mathbb{C}(r)$ and the mass density $\rho = \rho(r)$.

2.1. System equations

The momentum conservation equation associated with the constitutive law of linear elasticity (Hooke's law) gives the following equations:

$$\begin{cases} \operatorname{div}\boldsymbol{\sigma} = \rho\frac{\partial^2\mathbf{u}}{\partial t^2}, \\ \boldsymbol{\sigma} = \frac{1}{2}\mathbb{C}(\operatorname{grad}\mathbf{u} + \operatorname{grad}^T\mathbf{u}), \end{cases} \tag{1}$$

where $\mathbf{u}$ is the displacement vector and $\boldsymbol{\sigma}$ the stress tensor.

We are seeking the solutions of wave equation for displacement ($\mathbf{u}$) and radial traction-vector ($\boldsymbol{\sigma}_r = \boldsymbol{\sigma}.\mathbf{e}_r$) expressed in the cylindrical coordinates (r,θ,z) with the basis $\{\mathbf{e}_r,\mathbf{e}_\theta,\mathbf{e}_z\}$:

$$\begin{aligned} \mathbf{u}(r,\theta,z;t) &= \mathbf{U}^{(n)}(r)\exp\imath(n\theta + k_z z - \omega t), \\ \boldsymbol{\sigma}_r(r,\theta,z;t) &= \mathbf{T}^{(n)}(r)\exp\imath(n\theta + k_z z - \omega t); \end{aligned} \tag{2}$$

with k_z the axial wavenumber and n the circumferential wavenumber.

We distinguish two types of waves propagating in a cylindrical waveguide: the *circumferential waves* and the *axial waves*. The *circumferential waves* are the waves traveling in planes perpendicular to the axis direction. They correspond to $u_z(r) = 0$ $(\forall r)$, $k_z = 0$ and $n = k_\theta a_q$. The *axial waves* are the waves traveling along the axis direction, the circumferential wavenumber is an integer $n = 0,1,2,\ldots$. Among the *axial waves*, we distinguish three types of modes numbered with two parameters (n,m) representing the circumferential wavenumber and the order of the branches: longitudinal (L), flexural (F) and torsional (T) modes. The longitudinal modes are axially symmetric ($n = 0$), they are noted $L(0,m)$ and sometimes called the breathing modes [3]. For the two other types of modes, two classifications have been proposed in the literature. Meitzler [28] and Zemanek [50], following Gazis work [14], restricted the T-modes to axially symmetric circumferential fundamental modes $T(0,m)$ and the modes with non-zero n are considered as F-modes $F(n,m)$. An other way is proposed by Nishino and colleagues [34] who considered that the n-parameter of the T-modes is not limited to zero. Consequently they can associate "their" L- and F-modes to the Lamb waves (coupled bulk longitudinal and bulk shear-vertical waves) in the plate and the T-modes to the bulk horizontal-shear waves propagating in the plate. This classification may be relevant in the case of isotropic media but it becomes invalid for anisotropic media for which the flexural waves are longitudinal shear waves [14].

In this paper, only the *axial waves* are investigated and the usual classification of Gazis [14] is used.

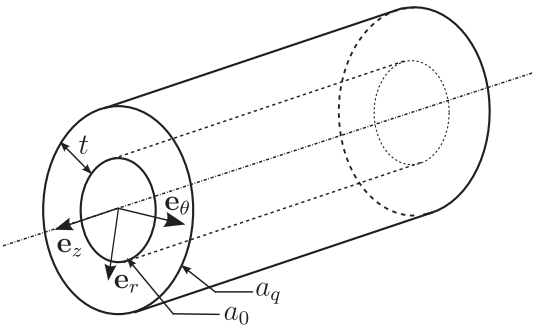

Fig. 1. Geometrical configuration of the waveguide.

2.2. A closed-form solution: the matricant

Introducing the expression (2) in Eq. (1), we obtain the wave equation under the form of a second-order differential equation with non-constant coefficients. In the general case, there is no analytical solution to the problem thus formulated. The most current methods to solve the wave equation in unidirectionally heterogeneous media are derived from the Thomson–Haskell method [45,18]. These methods are appropriate for multilayered structures [22,27,47,21]. But, for continuously varying media, these techniques mean to replace the continuous profiles of properties by step-wise functions. Thereby the studied problem becomes an approximate one, even before the resolution step; the accuracy of the solution as its validity domain are hard to evaluate. Moreover, the multilayered model of the functionally graded waveguide creates some "virtual" interfaces likely to induce artefacts. Lastly, for generally anisotropic cylinders, the solutions cannot been expressed analytically even for homogeneous layers [29,32,43].

In order to deal with the exact problem, that is to keep the continuity of the properties variation, the wave equation is written under the sextic Stroh's formalism [44] in the form of an ordinary differential equations system with non-constant coefficients for which an analytical solution exists: the matricant [4]. Another method relies on the Legendre's polynomial as explained and used in [25,11,13,12].

2.2.1. Hamiltonian form of the wave equation

In the Fourier domain, the wave equation may be written as:

$$\frac{d}{dr}\boldsymbol{\eta}(r) = \frac{1}{r}\mathbf{Q}(r)\boldsymbol{\eta}(r). \tag{3}$$

The components of the state-vector $\boldsymbol{\eta}(r)$ are the three components of the displacement and the three components of the stress traction in the cylindrical coordinates, and the matrix $\mathbf{Q}(r)$ contains all the information about the heterogeneity: it is expressed from stiffness coefficients of the waveguide in the cylindrical coordinates and from the two acoustical parameters: axial or circumferential wavenumbers (k_z, or n) and the angular frequency ω. The detailed expression of $\mathbf{Q}(r)$ is given in Appendix A for the case of a material with orthorhombic crystallographic symmetry but it can be expressed for any type of anisotropy [42].

2.2.2. Explicit solution: the Peano expansion of the matricant

The wave equation thus formulated has an analytical solution expressed between a reference point (r_0,θ,z) and some point of the cylinder (r,θ,z). This solution is called the matricant and is explicitly written under the form of the Peano series expansion:

$$\mathbf{M}(r,r_0)=\mathbf{I}+\int_{r_0}^{r}\mathbf{Q}(\xi)d\xi+\int_{r_0}^{r}\mathbf{Q}(\xi)\int_{r_0}^{\xi}\mathbf{Q}(\xi_1)d\xi_1 d\xi+\cdots, \tag{4}$$

where $\mathbf{I}$ is the identity matrix of dimension (6,6). If the matrix $\mathbf{Q}(r)$ is bounded in the study interval, these series is always convergent [4]. The components of the matrix $\mathbf{Q}$ are continuous in r and the study interval is bounded (thickness of the waveguide), consequently the hypothesis is always borne out. The matricant verifies the propagator property [4]:

$$\boldsymbol{\eta}(r)=\mathbf{M}(r,r_0)\boldsymbol{\eta}(r_0). \tag{5}$$

2.2.3. Free boundary conditions

The cylinder is supposed to be in vacuum, so the traction-vector $\boldsymbol{\sigma}_r$ defined in (2) is null at both interfaces. Using the propagator property of the matricant through the thickness of the cylinder, Eq. (5) is written as $\boldsymbol{\eta}(a_q)=\mathbf{M}(a_q,a_0)\boldsymbol{\eta}(a_0)$:

$$\begin{pmatrix}\mathbf{u}(r=a_q)\\ \mathbf{0}\end{pmatrix}=\begin{pmatrix}\mathbf{M}_1 & \mathbf{M}_2\\ \mathbf{M}_3 & \mathbf{M}_4\end{pmatrix}\begin{pmatrix}\mathbf{u}(r=a_0)\\ \mathbf{0}\end{pmatrix}. \tag{6}$$

Eq. (6) has non-trivial solutions for $\det\mathbf{M}_3=0$. As detailed in Appendix A for an orthotropic material and from Eq. (4), the components of $\mathbf{M}_3$ are bivariate polynomials in (k_z,ω). Consequently, to seek out the zeros of $\det\mathbf{M}_3$ corresponds to find the couples of values (k_z,ω) which describe the dispersion curves.

3. Results

To calculate the dispersion curves, we evaluate numerically the matricant $\mathbf{M}(a_q,a_0)$ from the expression (4). This step requires us to truncate the Peano series and to numerically calculate the integrals. Thus, the error can be estimated and controlled [4]. For the calculations in the plate we retained 70 terms in the series and evaluate the integrals over 100 points using the Simpson's rule (fourth-order integration method) and for the tube, we retained 33 terms in the series and evaluate the integrals over 30 points. These choices are not optimized but ensure the convergence of the solution and the accuracy of the results in the range of frequency-thickness products considered for a reasonable computation time (few dozen of minutes on a desktop computer).

3.1. Validation

We compare our results to results from the literature obtained on homogeneous tubes [30,34] (not shown). In the following part, the method is validated calculating the dispersion curves obtained for an isotropic FGM cylinder previously studied in the literature [17,11,13]. The properties of the tube (Young's modulus E, Poisson's ratio ν and mass density ρ) vary from silicon nitride properties at the inner interface ($r=a_0$) to the properties of stainless steel at the outer interface ($r=a_q$). The values of the properties for these two materials are reported in Table 1.

The dispersion curves are compared for an affine profile:

Table 1
Elastic properties of the materials at the two interfaces of the tube.

	E (GPa)	ν	ρ (kg/m^3)
Stainless steel (outer)	207.82	0.317	8166
Silicon nitride (inner)	322.4	0.24	2370

$$\begin{aligned}E(r)&=E_{out}+(E_{in}-E_{out})(r-a_0)/(a_q-a_0);\\ \nu(r)&=\nu_{out}+(\nu_{in}-\nu_{out})(r-a_0)/(a_q-a_0);\\ \rho(r)&=\rho_{out}+(\rho_{in}-\rho_{out})(r-a_0)/(a_q-a_0).\end{aligned} \tag{7}$$

In Fig. 2, the dispersion curves obtained for an isotropic FGM tube (Table 1) from two different schemes, Peano expansion of the matricant and Legendre polynomials, are in perfect agreement.

3.2. Influence of the ratio t/a_q

As mentioned in [37] and shown in [25], when the outer radius of the tube a_q is large compared to the wall thickness t, the longitudinal modes are very close to the Lamb modes obtained for a plate of the same thickness. Nishino and colleagues detailed the influence of the ratio t/a_q on the similarity of the modes of the cylindrical waveguide with the Lamb's waves [34]. The same trend is observed for the torsional modes as pointed in [34]: for small values of the ratio t/a_q (typically less than 0.5) they are very similar to horizontal-shear waves propagating in a plate of the same thickness. Considering the flexural waves, it is a little more delicate and sometimes cleverly sidestepped. In [25], the comparison is not convincing if superimposing the figures (Figs. 2–4 in [25]) and in Protopappas' paper [37], the comparison is made for particular flexural modes $F(1,2m+1)$ $(m=0,1,2)$.

Flexural modes are characterized by a three-dimensional polarization vector. As underlined by Rose [40], understanding the physical characteristics of flexural modes is necessary for advanced applications involving wave reflection from defects. For instance it can be difficult experimentally to generate pure longitudinal modes over a given frequency range. So, this point needs clarification.

3.2.1. Homogeneous isotropic tube

In this part, the results are inspired by Nishino's ones for a homogeneous isotropic aluminium tube ($C_L=6400$ m/s, $C_T=3040$ m/s, $\rho=2.7$ kg/m^3). Two configurations are represented: (a) $t/a_q=0.4<0.5$; (b) $t/a_q\approx 0.7>0.5$.

The results reported in Figs. 3 and 4 are in agreement with previous experimental and numerical studies above-cited. The dispersion curves obtained for the longitudinal and torsional modes are very similar to the plate modes for $t/a_q<0.5$ except at low frequency-thickness products ($ft<1$ MHz mm). When t/a_q increases the discrepancy becomes more and more significant in the whole range of frequency-thickness products.

As underlined before the case of flexural modes is more complex. We observe in Fig. 5 that for the first five modes, the branches $F(1,m)$ when m is even are similar to the Lamb's modes, whereas those $F(1,m)$ when m is odd are similar to the SH modes. For higher order modes, it seems that they are partly similar to Lamb's modes and partly similar to SH waves. These results are in accordance with the definition given by Gazis of longitudinal shear waves [14]. Furthermore, the influence of the ratio t/a_q remains identical to what it has been observed for longitudinal and torsional modes.

3.2.2. Heterogeneous anisotropic tube

The same trend is observed for anisotropic homogeneous structures (results not presented) and for anisotropic functionally graded ones. The anisotropic functionally graded structure studied in this paper has the mechanical properties of the cortical bone.

As the great majority of the biological tissue, the cortical bone is a complex medium. It is anisotropic, multi-components, heterogeneous. It can be modeled as a two-phase medium: the bone matrix and the pores full of marrow (assimilated to water). The characteristic size of the pores in the cortical bone is less than a few hundred micrometers. The classical range of frequency used in quantitative

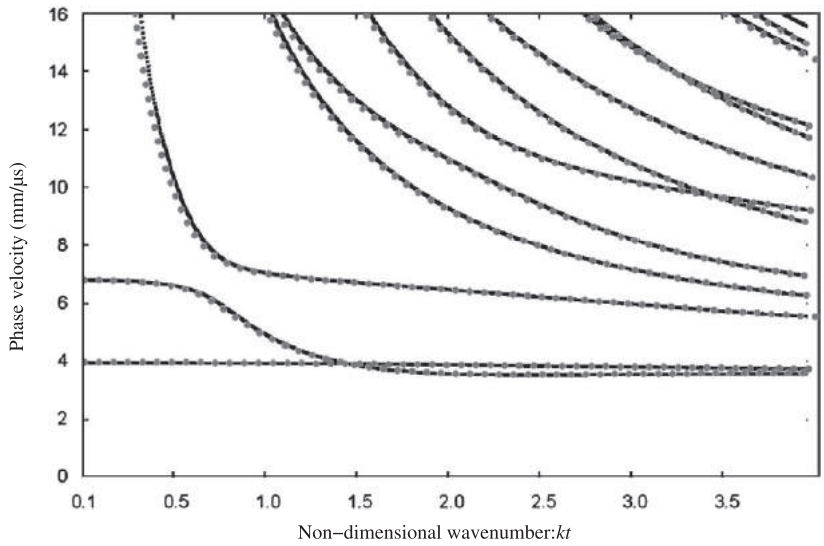

Fig. 2. The results obtained from the Stroh's formalism (grey points) compared with the results published in [11] (black points).

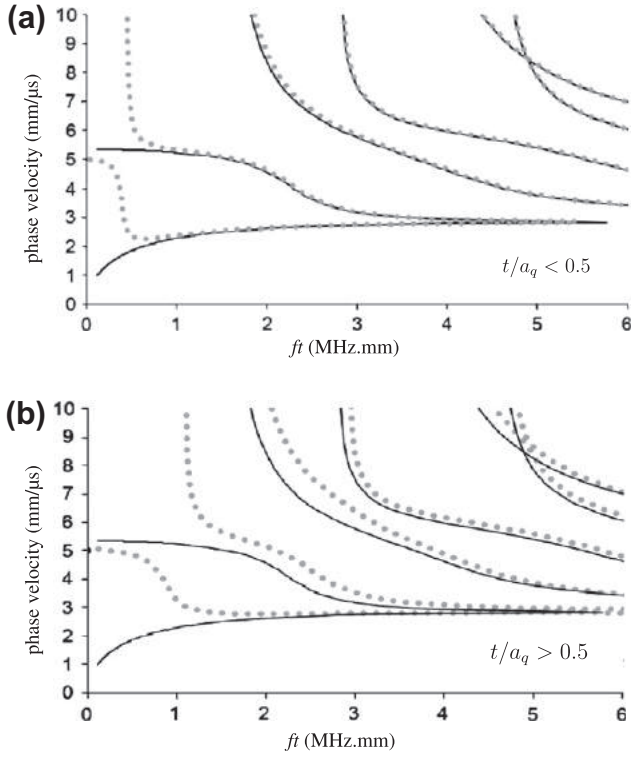

Fig. 3. Influence of the ratio t/a_q for a homogeneous isotropic aluminium tube. The Lamb's modes (black lines) are compared with the longitudinal modes $L(0,m)$ (grey points).

ultrasonography to evaluate bone fragility is [0.2; 2.5] MHz. For such frequencies, the wavelength of the ultrasonic waves is larger than the size of the pores and the waves propagate in an effective macroscopic medium whose properties obviously depend on the microscopic properties such as the porosity or the intrinsic material properties of the bone matrix. An increasing number of papers underlined the relevancy of taking into account these heterogeneities across the cortex to improve the ultrasonic method for cortical bone assessment [33,37,16]. It may be particularly relevant in the case of healing bone as proposed by Protopappas and colleagues [37,38]. In their papers, they pointed also the limitations of the Lamb wave theory when applied to real bones and underlined the relevance of taking into account the tubular geometry and the anisotropy of the long bones.

In our study, at the scale of the wavelength (few millimeters), the cortical bone may be viewed as a functionally graded material as its porosity increases continuously along the cortical thickness from the periosteal part (soft tissue side) to the endosteal one (marrow side). It is noteworthy that the intrinsic material properties of the bone matrix vary also across the cortical thickness [41] and contribute to the continuous gradient of macroscopic properties.

In a first approach, knowing the relationship between the porosity and the effective material properties [7] (neglecting the intrinsic material properties variation), the gradient of materials properties may be deduced from the gradient of porosity. To the best of our knowledge, we do not know exactly how the porosity varies across the cortical thickness and how it influences the macroscopic mechanical properties. Several studies brought some information on that point [9,8].

According to these results, one of the simplest realistic profile of properties to take into account seems to be the affine one.

As shown previously [5], the propagation of ultrasonic waves in the frequency range of clinical measurement is influenced by the gradient of properties encountered in cortical bone modeled as a plate. Therefore, we study the influence of the curvature on the dispersion curves for a transversely isotropic bone material with linearly varying mechanical properties along its radius. A particular attention was paid to assign realistic values to the properties of bone, for this reason we use the data published in [16,5]. The properties profile tested is an affine function:

$$C(r) = C_m + (C_M - C_m)(r - a_0)/(a - q - a_0); \tag{8}$$

the values of C_m and C_M are reported in Table 2.

The dispersion curves of the longitudinal $L(0,m)$, torsional $T(0,m)$ and flexural $F(1,m)$ modes calculated for a radially graded tube of thickness t are compared with the dispersion curves calculated for a plate of the same thickness (Lamb and Shear Horizontal modes). All the results are obtained from the Peano expansion of the matricant (4).

In Figs. 6–8, we can remark the same trend as observed in Figs. 3–5. The dispersion curves of the longitudinal modes L are very similar to Lamb's modes for ratios $t/a_q < 0.5$ except for low frequency-thickness products ($ft < 0.3$ MHz mm) (Fig. 6). Note that

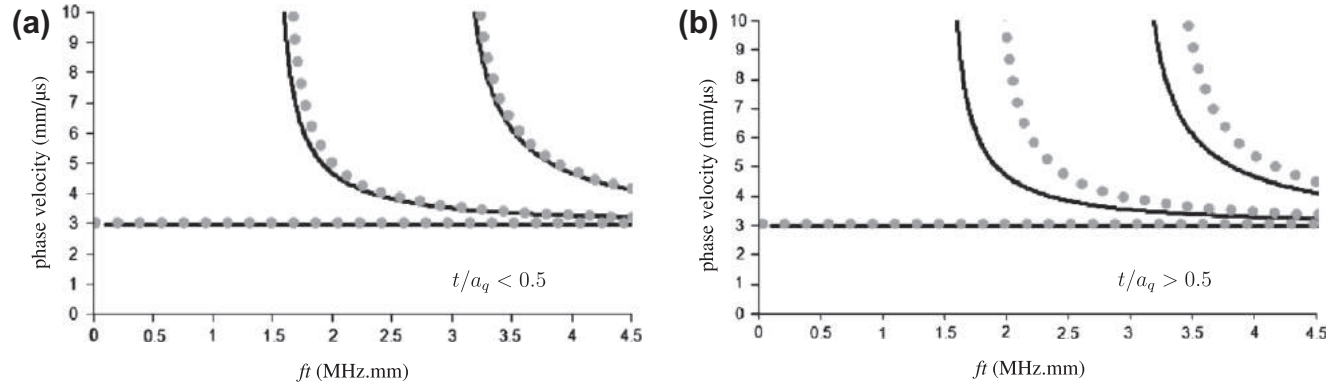

Fig. 4. Influence of the ratio t/a_q for a homogeneous isotropic aluminium tube. The SH modes (black lines) are compared with the torsional modes $T(0,m)$ (grey points).

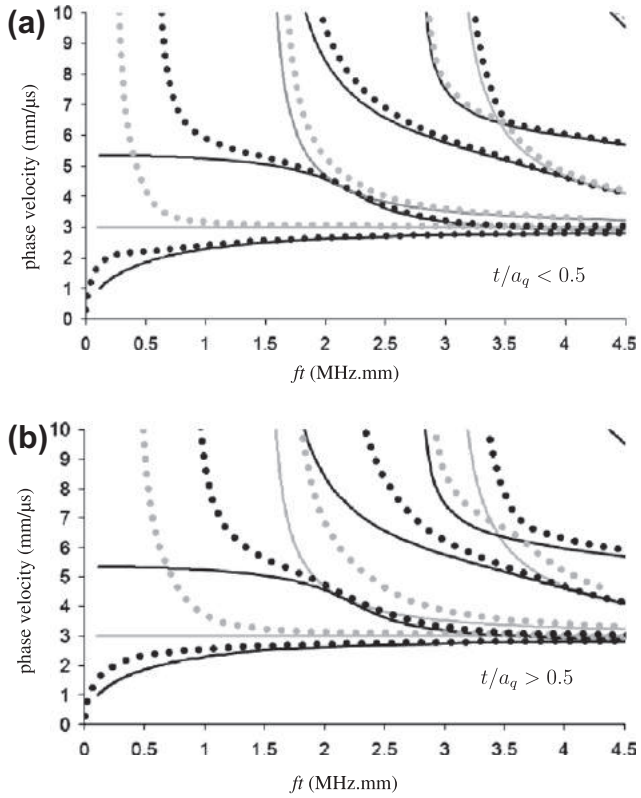

Fig. 5. Influence of the ratio t/a_q for a homogeneous isotropic aluminium tube. The SH modes (grey lines) and Lamb's modes (black lines) are compared with the flexural modes $F(1,2m)$ (grey points) and $F(1,2m-1)$ (black points) with $m = 1,2,3,4$.

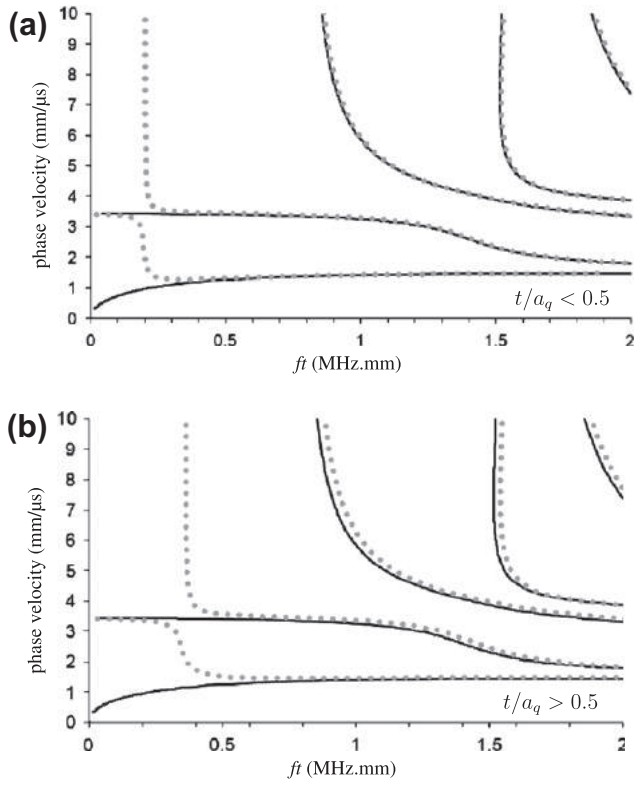

Fig. 6. Influence of the ratio t/a_q for a tube with bone properties (Table 2). The Lamb's modes (black lines) are compared with the longitudinal modes (grey circles).

the range is smaller than for the isotropic aluminium tube. The differences become significant when the ratio t/a_q increases. We can also compare the dispersion curves of the torsional modes T to the SH modes in a plate of the same thickness (Fig. 7). They are represented in Fig. 7 for the same range [0–2 MHz mm]. Again, the dispersion curves are very similar for low ratios and the difference increases with t/a_q. Concerning the flexural waves, the anisotropy makes the comparison between tube modes and plate modes more difficult. Again, in Fig. 8 we observe the coupling between longitudinal and shear waves expressed in the dispersion curves of the flexural modes. The dependence on t/a_q remains the same.

4. Discussion and perspectives

The non-destructive evaluation of cylindrical anisotropic waveguide remains a key issue, particularly for generally anisotropic

Table 2
The minimal and maximal values $[C_m, C_M]$ of each variable corresponding to the realistic range of variation taken from [5] with $c_{12} = c_{11} - 2c_{66}$. Remember that the correspondence between space directions and index notation is $1 \leftrightarrow r$; $2 \leftrightarrow \theta$; $3 \leftrightarrow z$.

$c_{11} = c_{22}$ (GPa)	$c_{13} = c_{23}$ (GPa)	c_{33} (GPa)	$c_{44} = c_{55}$ (GPa)	c_{66}	ρ (g cm^{-3})
[11.8,25.9]	[5.1,11.1]	[17.6,29.6]	[3.3,5.5]	[2.2,4.4]	[1.66,1.753]

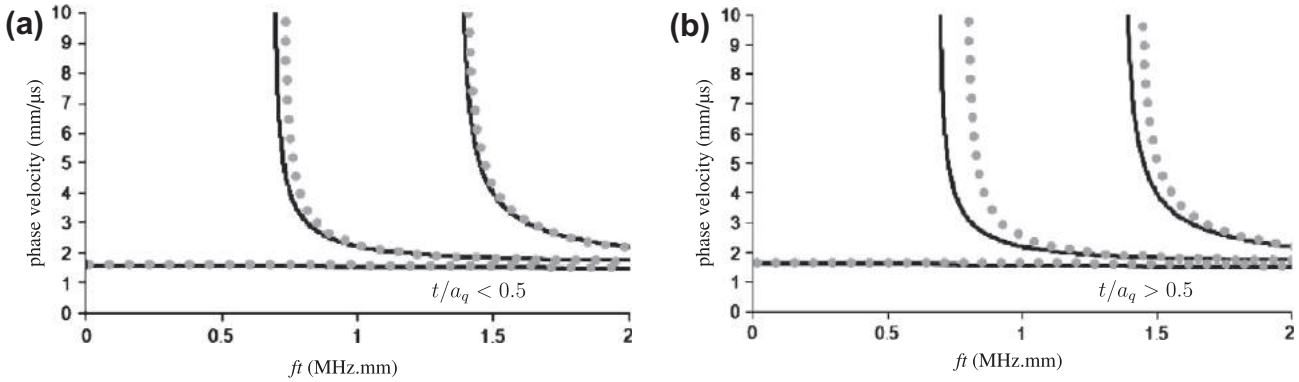

Fig. 7. Influence of the ratio t/a_q for a tube with bone properties (Table 2). The SH modes (black lines) are compared with the torsional modes (grey circles).

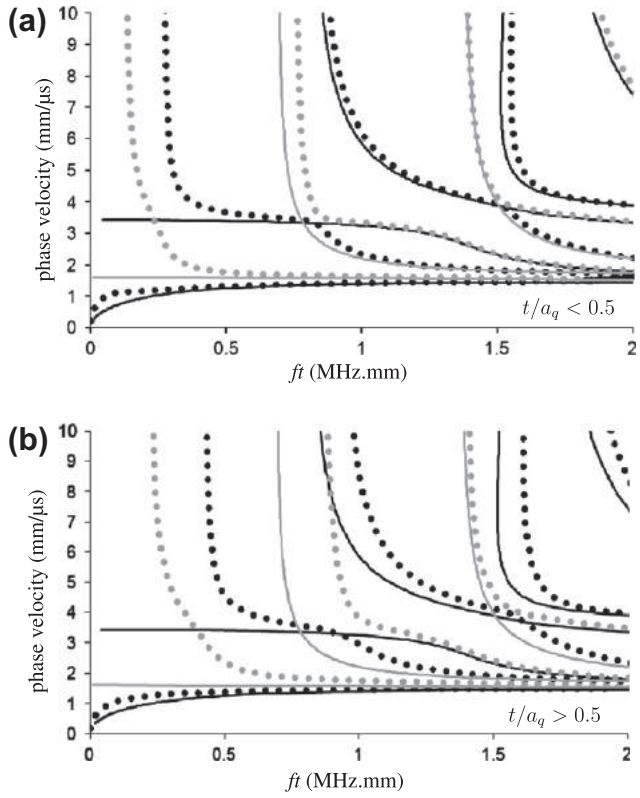

Fig. 8. Influence of the ratio t/a_q for a tube with bone properties (Table 2). The SH modes (grey lines) and Lamb's modes (black lines) are compared with the flexural modes $F(1,2m)$ (grey points) and $F(1,2m-1)$ (black points) with $m = 1,2,3,4$.

materials. The method proposed in the present paper allows to solve the wave equation in an anisotropic tube with radially varying properties. From these results dealing with the direct problem, further work is needed to develop inversion techniques. There are many industrial applications: super heat resistant materials, "smart structures", powder metallurgy and ceramics or the graded-index plastic optical fibers for communications. Among these domains, the improvement of evaluation of biological tissues such as bone and the development of biomimetic materials for bone implants are booming subjects.

4.1. The bone evaluation in prospect

The characterization of bone strength remains a major issue particularly in the context of osteoporosis diagnosis known as a public health problem. Nowadays it is established that bone fragility does not depend only on bone density but also on geometry, microstructure and elasticity of bone [33,15]. Consequently, a lot of works investigate this way in order to provide relevant criteria of bone strength evaluation. The work presented in this paper is altogether part of that perspective. One of the point is to improve the models used to inverse the experimental data. The goal is to select the relevant characteristic parameters which influence the clinical ultrasonic response and to relate them to the bone fragility. In this study, we take into account the anisotropy of the cortical bone, its tubular geometry and its heterogeneity and we evaluate the influence of the curvature on the ultrasound response representative of the mechanical behavior of the bone.

As a preliminary study on the influence of the curvature on *in vitro* ultrasound characterization of bone, the results presented are promising. But, obviously there are a lot of weaknesses in this study.

First, one of the limitations is the choice of the elastic properties values and their variation across the cortical thickness. These values are different from some data given in other papers [24,2,35,7] but remain in a realistic range deduced from experimental measurements [10] and thermodynamical conditions. Moreover they take into account the known anisotropy of cortical bone. Concerning the linear variation of the elastic properties (stiffness coefficients and mass density), it is a basic model which provides a first insight into the effect of multiscale heterogeneity of long bone. A recent study [16], Haiat and colleagues inputed the same values and the same profiles of properties in their simulations and obtained a good agreement between their results and former studies. Nevertheless, experimental data are needed to better define the way the microscopic properties (properties and intrinsic bone matrix properties) vary across the cortical thickness and contribute to the gradient of macroscopic elastic properties.

Second, the dispersion curves are obtained for a free-stress tube. Consequently, another limitation of this work is the absence of surrounding media which obviously influence the clinical measurements and has to be included in a relevant mechanical model [5,31]. The presence of fluids inside and outside the tube induces significant changes: the appearance of extra fluid modes and some differences in the shape of the tube modes in terms of attenuation and, phase and group velocities [36,1,31]. Moreover the behavior of the fluid-loaded structure depends on the viscosity of the fluids [1]. Further work is needed to consider the effect of soft tissue and marrow modelling the bone as a fluid-loaded tube. The boundary conditions may be taken into account in the same way as we did for the plate [5]. The reflection and transmission coefficients for a fluid-loaded anisotropic tube with radially varying properties will be calculated following the same steps as detailed for the plate. Nevertheless, the present work may provide an interesting tool to give support to *in vitro* studies.

5. Conclusion

In the context of non-destructive evaluation of complex media, the method presented here reveals several advantages to solve the wave equation in graded anisotropic waveguide. First, the formalism used allows to take into account a general anisotropy of the material even in the case of cylindrical geometry. Second, the Peano expansion of the matricant is one of the only method which provides an analytical solution of the exact problem in a functionally graded medium, that is to say without modelling the waveguide as a multilayered medium. Consequently, the accuracy and validity range are managed. Third, the computation time is a few dozen minutes for the structures studied in this paper. Using this method, it has been demonstrated that the trend revealed in the case of isotropic, homogeneous tubes is confirmed in the case of anisotropic heterogeneous tubes: for thickness to outer radius ratios less than 0.5, the plate model seems to be efficient except at low frequency-thickness products. In the particular context of ultrasonic evaluation of bone, further work is needed to analyse the relevance of the anisotropic heterogeneous tube model. A study will begin to compare different types of properties profiles and gain an insight into the parameters of the profiles which influence predominantly the ultrasonic response. Anyway, using the Stroh's formalism, one of the point of this method is the possibility of taking into account the anisotropy of the bone tube which has been proven to widely influence the wave propagation. Furthermore, this study gives some clues on the interaction between the ultrasonic waves and a realistic model of long bone under *in vitro* conditions (tubular geometry, radial heterogeneity and anisotropy): the guided modes are more sensitive to the curvature at low frequency-thickness products (at low frequencies and/or for thin bones). Whereas, the guided waves are more sensitive to the variation of properties at higher frequency-thickness products (at high frequencies and/or for thick bones). Now, this gradient may provide a multiparametric evaluation of the bone fragility by assessing pieces of information on the geometry, the structure and the material at a time and may reveal itself a relevant parameter in the diagnosis an the therapeutic following of the osteoporosis.

But a question remains: are the ultrasounds sensitive to this gradient? an experimental study is insistently needed to gain insight on that point.

Appendix A

Expression of the vector $\boldsymbol{\eta}(r)$ and of the matrix $\mathbf{Q}(r)$ for a material with orthorhombic crystallographic symmetry (nine independent stiffness coefficients). The symbol $\hat{\cdot}$ represents the quantities in the Fourier domain.

$\boldsymbol{\eta}(r) = (\,\hat{u}_r(r),\ \hat{u}_\theta(r),\ \hat{u}_z(r),\ \imath r\hat{\sigma}_{rr}(r),\ \imath r\hat{\sigma}_{r\theta}(r),\ \imath r\hat{\sigma}_{rz}(r)\,)^T$,

and

$$\mathbf{Q}(r) = \frac{1}{r}\begin{pmatrix} -\frac{c_{12}}{c_{11}} & -\imath n\frac{c_{12}}{c_{11}} & & & & \\ -\imath n & 1 & & & & \\ -\imath k_z r & 0 & & & & \\ \imath(\gamma_{12} - r^2\rho\omega^2) & -n\gamma_{12} & & & & \\ n\gamma_{12} & \imath n^2\gamma_{12} + \imath r^2\left(k_z^2 c_{44} - \rho\omega^2\right) & & & & \\ k_z r\gamma_{23} & \imath n k_z r(\gamma_{23} + c_{44}) & & & & \end{pmatrix}$$

$$\begin{pmatrix} -\imath k_z r\frac{c_{13}}{c_{11}} & -\frac{\imath}{c_{11}} & 0 & 0 \\ 0 & 0 & -\frac{\imath}{c_{66}} & 0 \\ 0 & 0 & 0 & \frac{\imath}{c_{55}} \\ -k_z r\gamma_{23} & \frac{c_{12}}{c_{11}} & -\imath n & -\imath k_z r \\ \imath n k_z r(\gamma_{123} + c_{44}) & -\imath n\frac{c_{12}}{c_{11}} & -1 & 0 \\ \imath n^2 c_{44} + \imath r^2\left(k_z^2\gamma_{13} - \rho\omega^2\right) & -\imath k_z r\frac{c_{13}}{c_{11}} & 0 & 0 \end{pmatrix}$$

with

$$\gamma_{12} = c_{22} - \frac{c_{12}^2}{c_{11}};\ \gamma_{13} = c_{33} - \frac{c_{13}^2}{c_{11}};\ \gamma_{23} = c_{23} - \frac{c_{12}c_{13}}{c_{11}}.$$

References

[1] C. Aristegui, M. Lowe, P. Cauley, Guided waves in fluid-filled pipes surrounded by different fluids, Ultrasonics 39 (2001) 367–375.
[2] R.B. Ashman, A continuous wave measurement of the elastic properties of cortical bone, Journal of Biomechanics 17 (1984) 349–361.
[3] B.A. Auld, Acoustic Fields and Waves in Solids, Wiley Interscience, New York, 1973.
[4] C. Baron, Le dTveloppement en sTrie de Peano du matricant pour l'Ttude de la propagation d'ondes en milieux continvment variables – Peano expansion of the matricant to study elastic wave propagation in continuously heterogeneous media. Ph.D. thesis, UniversitT Bordeaux 1, France, 2005.
[5] C. Baron, S. Baron and Naili, Propagation of elastic waves in a fluid-loaded anisotropic functionally graded waveguide: application to ultrasound characterization, Journal of Acoustical Society of America 127 (2010) 1307–1317.
[6] C. Baron, A. Shuvalov, O. Poncelet, Impact of localized inhomogeneity on the surface-wave velocity and bulk-wave reflection in solids, Ultrasonics 46 (2007) 1–12.
[7] C. Baron, M. Talmant, P. Laugier, Effect of porosity on effective diagonal stiffness coefficients (c_{ii}) and anisotropy of cortical at 1 MHz: a finite-difference time domain study, Journal of Acoustical Society of America 122 (2007) 1810–1817.
[8] S. Bensamoun, J.-M. Gherbezza, J.-F. de Belleval, M.-C. Ho Ba Tho, Transmission scanning acoustic imaging of human cortical bone and relation with the microstructure, Clinical Biomechanics 19 (2004) 639–647.
[9] V. Bousson, A. Meunier, C. Bergot, E. Vicaut, M.A. Rocha, M.H. Morais, A.-M. Laval-Jeantet, J.-D. Laredo, Distribution of intracortical porosity in human midfemoral cortex by age and gender, Journal of Bone and Mineral Research 16 (2001) 1308–1317.
[10] X.N. Dong, X.E. Guo, The dependence of transversely isotropic elasticity of human femoral cortical bone on porosity, Journal of Biomechanics 37 (2004) 1281–1287.
[11] L. Elmaimouni, J.E. Lefebvre, T. Gryba, V. Zhang, Polynomial method applied to acoustic waves in inhomogeneous cylinders, in: IEEE Ultrasonics Symposium, 2003.
[12] L. Elmaimouni, J.E. Lefebvre, A. Raherison, F.E. Ratolojanahary, Acoustical guided waves in inhomogeneous cylindrical materials, Ferroelectrics 372 (2008) 115–123.
[13] L. Elmaimouni, J.E. Lefebvre, V. Zhang, T. Gryba, Guided waves in radially graded cylinders: a polynomial approach, NDT & E International 38 (2005) 344–353.
[14] D.C. Gazis, Three-dimensional investigation of the propagation of waves in hollow circular cylinders. I. Analytical foundation, Journal of Acoustical Society of America 31 (1959) 568–573.
[15] J.F. Griffith, H.K. Genant, Bone mass and architecture determination: state of the art, Best Practice & Research Clinical Endocrinology & Metabolism 22 (2008) 737–764.
[16] G. Haiat, S. Naili, Q. Grimal, M. Talmant, Influence of a gradient of material properties on ultrasonic wave propagation in cortical bone: application to axial transmission, Journal of Acoustical Society of America 125 (2009) 4043–4052.
[17] X. Han, G.R. Liu, Z.C. Xi, K.Y. Lam, Characteristics of waves in a functionally graded cylinder, International Journal for Numerical Methods in Engineering 53 (2002) 653–676.
[18] N.A. Haskell, The dispersion of surface waves on multilayered media, Bulletin of the Seismological Society of America 43 (1953) 377–393.
[19] H. Hedia, N. Mahmoud, Design optimization of functionally graded dental implant, Bio-Medical Materials and Engineering 14 (2004) 133–143.
[20] F. Honarvar, E. Enjilela, A. Sinclair, S. Mirnezami, Wave propagation in transversely isotropic cylinders, International Journal of Solids and Structures 44 (2007) 5236–5246.
[21] B. Hosten, M. Castaings, Surface impedance matrices to model the propagation in multilayered media, Ultrasonics 41 (2003) 501–507.
[22] E.G. Kenneth, A propagator matrix method for periodically stratified media, Journal of Acoustical Society of America 73 (1) (1982) 137–142.
[23] H. Lamb, On waves in an elastic plate, Proceedings of the Royal Society of London A 93 (1917) 114–128.
[24] S.B. Lang, Ultrasonic method for measuring elastic coefficients of bone and results on fresh and dried bovine bones, in: IEEE Transactions on Biomedical Engineering, vol. 17, 1970.
[25] F. Lefebvre, Y. Deblock, P. Campistron, D. Ahite, J.J. Fabre, Development of a new ultrasonic technique for bone and biomaterials in vitro characterization, Journal of Biomedical Material Research, Part B 63 (2002) 441–446.
[26] D. Lin, Q. Li, W. Li, S. Zhou, M. Swain, Design optimization of functionally graded dental implant for bone remodeling, Composites: Part B 40 (2009) 668–675.
[27] D. LTvesque, L. PichT, A robust transfer matrix simulation for ultrasonic response of multilayered absorbing media, Journal of Acoustical Society of America 92 (1992) 452–467.

[28] A.H. Meitzler, Mode coupling occurring in the propagation of elastic pulses in wires, Journal of the Acoustical Society of America 33 (1961) 435–445.
[29] I. Mirsky, Axisymmetric vibrations of orthotropic cylinders, Journal of the Acoustical Society of America 36 (1964) 2106–2112.
[30] I. Mirsky, Wave propagation in transversely isotropic circular cylinders, part I: theory, Journal of the Acoustical Society of America 37 (1965) 1016–1026.
[31] P. Moilanen, M. Talmant, V. Kilappa, P.H.F. Nicholson, S. Cheng, J. Timonen, P. Laugier, Modeling the impact of soft tissue on axial transmission measurements of ultrasonic guided waves in human radius, Journal of the Acoustical Society of America 124 (2008) 2364–2373.
[32] R. Nelson, S. Dong, R. Kalkra, Vibrations and waves in laminated orthotropic circular cylinders, Journal of Sound and Vibration 18 (1971) 429–444.
[33] P.H.F. Nicholson, P. Moilanen, T. KSrkkSinen, J. Timonen, S. Cheng, Guided ultrasonic waves in long bones: modelling, experiment and *in vivo* application, Physiological Measurement 23 (2002) 755–768.
[34] H. Nishino, S. Takashina, F. Uchida, M. Takemoto, K. Ono, Modal analysis of hollow cylindrical guided waves and applications, Japanese Journal of Applied Physics 30 (1) (2001) 364–370.
[35] M. Pithioux, P. Lasaygues, P. Chabrand, An alternative ultrasonic method for measuring the elastic properties of cortical bone, Journal of Biomechanics 35 (2002) 961–968.
[36] T. Plona, B. Sinha, S. Kostek, S.-K. Chang, Axisymmetric wave propagation in fluid-loaded cylindrical shells. II: theory versus experiment, Journal of Acoustical Society of America 92 (1992) 1144–1155.
[37] V. Protopappas, D. Fotiadis, K. Malizos, Guided ultrasound wave propagation in intact and healing long bone, Ultrasound in Medicine and Biology 32 (2006) 693–708.
[38] V. Protopappas, I.C. Kourtis, L.C. Kourtis, K. Malizos, C.V. Massalas, D. Fotiadis, Three-dimensional finite element modeling of guided ultrasound wave propagation in intact and healing long bones, Journal of the Acoustical Society of America 121 (2007) 3907–3921.
[39] J.W.S. Rayleigh, On wave propagating along the plane surface of an elastic solid, Proceedings of the London Mathematical Society 7 (1885) 4–11.
[40] J.L. Rose, Ultrasonic Waves in Solid Media, Cambridge University Press, Cambridge, 1999.
[41] A. Saned, K. Raum, I. Leguerney, P. Laugier, Spatial distribution of anisotropic acoustic impedance assessed by time-resolved 50-MHz scanning acoustic microscopy and its relation to porosity in human cortical bone, Bone 43 (2008) 187–194.
[42] A. Shuvalov, A sextic formalism for three-dimensional elastodynamics of cylindrically anisotropic radially inhomogeneous materials, Proceedings of the Royal Society of London A 459 (2003) 1611–1639.
[43] K. Soldatos, Y. Jianqiao, Wave propagation in anisotropic laminated hollow cylinders of infinite extent, Journal of the Acoustical Society of America 96 (1994) 3744–3752.
[44] A.N. Stroh, Steady state problems in anisotropic elasticity, Journal of Mathematics and Physics 41 (1962) 77–103.
[45] W.T. Thomson, Transmission of elastic waves through a stratified solid medium, Journal of Applied Physics 21 (1950) 89–93.
[46] I.A. Viktorov, Rayleigh and Lamb Waves, Plenum Press, New York, 1970.
[47] L. Wang, S.I. Rokhlin, Stable reformulation of transfer matrix method for wave propagation in layered anisotropic media, Ultrasonics 39 (2001) 413–424.
[48] F. Watari, A. Yokoyama, M. Omori, T. Hirai, H. Kondo, M. Uo, T. Kawasaki, Biocompatibility of materials and development to functionally graded implant for bio-medical application, Composites Science and Technology 64 (2004) 893–908.
[49] I. Youssef, H. El-Arabawi, Picard iteration algorithm combined with Gauss–Seidel technique for initial value problems, Applied Mathematics and Computation 190 (2007) 345–355.
[50] J.J. Zemanek, An experimental and theoretical investigation of elastic wave propagation in a cylinder, Journal of the Acoustical Society of America 51 (1972) 265–283.

4.5 UMB 2012

Ultrasound in Medicine and Biology, 2012

Using the gradient of human cortical bone properties to determine age-related bone changes via ultrasonic guided waves.
C. Baron.
UMB 38, 972-981.

Ultrasound in Med. & Biol., Vol. 38, No. 6, pp. 972–981, 2012

0301-5629/$ - see front matter

doi:10.1016/j.ultrasmedbio.2012.02.024

● *Original Contribution*

USING THE GRADIENT OF HUMAN CORTICAL BONE PROPERTIES TO DETERMINE AGE-RELATED BONE CHANGES *VIA* ULTRASONIC GUIDED WAVES

CÉCILE BARON
Aix-Marseille Univ, Institute of Movement Sciences, Marseille, France

(*Received* 9 *November* 2011; *revised* 1 *February* 2012; *in final form* 23 *February* 2012)

Abstract—Bone fragility depends not only on bone mass but also on bone quality (structure and material). To accurately evaluate fracture risk or propose therapeutic treatment, clinicians need a criterion, which reflects the determinants of bone strength: geometry, structure and material. In human long bone, the changes due to aging, accentuated by osteoporosis are often revealed through the trabecularization of cortical bone, *i.e.*, increased porosity of endosteal bone inducing a thinning of the cortex. Consequently, the intracortical porosity gradient corresponding to the spatial variation in porosity across the cortical thickness is representative of loss of mass, changes in geometry (thinning) and variations in structure (porosity). This article examines the gradient of material properties and its age-related evolution as a relevant parameter to assess bone geometry, structure and material. By applying a homogenization process, cortical bone can be considered as an anisotropic functionally graded material with variations in material properties. A semi-analytical method based on the sextic Stroh formalism is proposed to solve the wave equation in an anisotropic functionally graded waveguide for two geometries, a plate and a tube, without using a multilayered model to represent the structure. This method provides an analytical solution called the matricant and explicitly expressed under the Peano series expansion form. Our findings indicate that ultrasonic guided waves are sensitive to the age-related evolution of realistic gradients in human bone properties across the cortical thickness and have their place in a multimodal clinical protocol. (E-mail: cecile.baron@univ-amu.fr) © **2012 World Federation for Ultrasound in Medicine & Biology.**

Key Words: **Cortical bone, Porosity gradient, Elastic wave propagation, Stroh formalism, Waveguide.**

INTRODUCTION

It is now widely accepted that bone strength relies on two main factors: bone density and bone quality. Thus, accurate information is needed on the quantity of bone, the way it is organized and the mechanical quality of its constituent materials (elastic properties) to accurately evaluate fracture risk, to optimize treatment (time and dosage) and to reduce adverse effects. Nowadays, bone densitometry as determined by dual-energy X-ray absorptiometry (DXA) is the gold standard technique used to diagnose osteoporosis and to decide on treatment. It provides a value for bone mineral density (BMD), which is compared with that of a reference population to assess whether the patient is "normal," presents with osteopenia or presents with osteoporosis.

One of the fundamental challenges in bone characterization is to identify the relevant parameters, which have to be correlated to the pathology and accessible through clinical measurements. Moreover, as with all technological developments for biomedical applications, it is essential to respect certain criteria: techniques should be nondestructive, noninvasive and nonradiating. Quantitative ultrasound techniques are good candidates on all these conditions. Yet, they continue to struggle for acceptance against the gold standard of DXA analysis, partly because no single physical parameter has been identified to represent the "structure, geometry, material" triangle. For a long time now, it has been recognized that bone mass alone (bone mineral density) is insufficient to predict risk of fracture (Faulkner 2000; Robbins et al. 2005). It has been reported that BMD alone explains less than half the risk of hip fractures (Marshall et al. 1996). Several studies have revealed cases where the effect of BMD on risk of fracture is atypical. Postmenopausal Chinese women, for example, have significantly

Address correspondence to: Cécile Baron, Institute of Movement Sciences UMR 7287 CNRS/AMU 163, Avenue de Luminy, 13288 Marseille Cedex 09, France. E-mail: cecile.baron@univ-amu.fr

lower hip bone mineral density than white women and are classified at higher risk but in fact they have fewer fractures (Tobias et al. 1994; Xiaoge et al. 2000).

It would appear, then, that bone quantity alone is not sufficient to evaluate bone fragility and that bone geometry and quality are key factors which significantly affect bone strength (Augat et al. 1996; Ammann and Rizzoli, 2003; Moilanen et al. 2007; Gregory and Aspden 2008).

Moreover, even though BMD combines cortical and trabecular bone mass, the majority of what is measured by DXA is trabecular bone. As a consequence, osteoporosis treatments focus primarily on trabecular bone. Yet, while both bone compartments contribute to bone strength (Manske et al. 2009), several recent studies point out that cortical bone is a critical component in determining fracture resistance at the femoral neck (Augat and Schorlemmer, 2006; Holzer et al. 2009; Treece et al. 2010).

At the same time, as imaging techniques become more and more accurate, a newly visible characteristic of bone is emerging: intracortical porosity changes gradually across the thickness of long bones (Bousson et al. 2001; Tatarinov et al. 2005; Haïat et al. 2009; Grimal et al. 2011). When homogenization methods are applied to cortical bone, it can be viewed as a functionally graded material at mesoscopic scale.

Among the changes in cortical bone due to aging, there is a joint process accentuated by osteoporosis: trabecularization of the endosteal part leading to thinning of the cortex. Therefore, the gradient (spatial variation) of intracortical porosity is a parameter representative of increased variation in porosity across a reduced thickness and should be relevant to evaluate the combined effect of thinning and trabecularization. This gradient of intracortical porosity induces gradients of material properties (mass density and stiffness coefficients). Thus, characterizing the gradient of the bone properties across the cortical thickness, will provide information on structure (porosity), geometry (thickness) and material (stiffness).

In this study, we consider the diaphysis of long bone, in particular cortical bone. We model cortical bone as a one-phase material with varying mechanical properties (mass density and stiffness coefficients). Modeling how porosity changes across the cortical thickness and translating this variation in a microscopic property to mesoscopic level are complex tasks. We base ourselves on two studies (Bousson et al. 2000; Grimal et al. 2011) and define a mesoscopic functionally graded material (FGM) model. A semi-analytical method is proposed to solve the wave equation in an FGM waveguide. This method, based on the Stroh formalism, allows us to avoid a multilayered media approximation and to consider a cylindrical geometry in association with an anisotropic material. According to numerous experimental studies (Reilly and Burnstein 1974; Dong and Guo 2004; Lakshmanan et al. 2007), human cortical bone is assumed to be a transversely isotropic material. Here cortical bone is represented by a transversely isotropic plate or tube in vacuum. The dispersion curves of the guided waves are explored to evaluate the sensitivity of these waves to a realistic variation in intracortical porosity.

MATERIALS AND METHODS

Cortical bone as an anisotropic functionally graded material waveguide

The model takes into account the anisotropy and the heterogeneity of cortical bone: it is considered as transversely isotropic with linearly varying material properties. Moreover, two geometries are investigated for long bone modeled as a plate or as a tube with realistic dimensions.

Functionally graded material properties

Here, every attempt was made to model realistic variation in porosity across the cortical thickness. Based on previous work reported on femoral cortical bone samples from skeletons (Bousson et al. 2000, 2001), we focus on a solely female population (86 subjects) aged from 11 to 96. We use these authors' 3-point measurement of porosity (periosteal, midcortical and endosteal regions) to infer the evolution of porosity across the cortical thickness.

Then, the evolution of intracortical porosity (microscopic scale) is translated into a variation in the elastic properties of the bone at the mesoscopic level by using the regression models (size of the mesodomain $L = 0.5$ mm) proposed by Grimal and colleagues (Grimal et al. 2011). Thereby, the Young's and shear moduli and the Poisson ratios are expressed as a function of porosity.

Porosity varies with position across the thickness of the bone and, consequently, the Young's and shear moduli and Poisson ratios are also dependent on the spatial variable across the thickness (x - variable for the plate and r - variable for the tube), except for ν_{TL}, which is assumed to be constant at 0.3.

Then, we deduce the five independent stiffness coefficients as five spatially-dependent functions from the following equations:

$$c_{11} = \frac{E_T(1-\nu_{TL}\nu_{LT})}{\Delta}; \quad c_{12} = \frac{E_T(\nu_{TT}+\nu_{TL}\nu_{LT})}{\Delta};$$
$$c_{13} = \frac{E_T(\nu_{LT}+\nu_{TT}\nu_{LT})}{\Delta}; \quad c_{33} = \frac{E_L(1-\nu_{TT}\nu_{TT})}{\Delta}; \qquad (1)$$
$$c_{44} = G_{LT};$$

with $\Delta = \nu_{TT}^2 + 2\nu_{LT}\nu_{TL} + 2\nu_{LT}\nu_{TL}\nu_{TT}$.

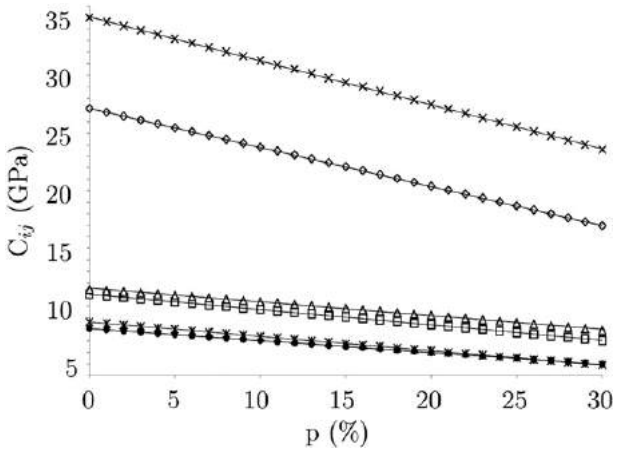

Fig. 1. Variation in stiffness coefficients over porosity: $c_{11} = c_{22}(\diamond)$, $c_{12}(\square)$, $c_{13} = c_{23}(\Delta)$, $c_{33}(\times)$, $c_{44} = c_{55}(*)$, $c_{66}(\bullet)$.

Note the correspondence $1 \rightarrow T; 2 \rightarrow T; 3 \rightarrow L$ where L and T are *longitudinal* and *transverse,* respectively.

The degree of porosity (from 0% to 30%) does not disturb the crystallographic symmetry of the material at the mesoscopic scale (Baron et al. 2007): the thermodynamic conditions are still valid.

Figure 1 shows that the stiffness coefficients can be supposed to linearly vary according to porosity across the cortical thickness for each age group. A linear regression provides an affine function representing the evolution of the stiffness coefficients across the cortical thickness. Thus, the elastic properties vary from a maximum value in the periosteal region to a minimum value in the endosteal region (Table 1).

Table 1. Elastic properties of cortical bone at the periosteal boundary (per.) and at the endosteal boundary (end.)

	c_{11} (GPa)	c_{12} (GPa)	c_{13} (GPa)	c_{33} (GPa)	c_{44} (GPa)	c_{66} (GPa)	ρ (g/cm^3)
[10–19]							
per.	26.33	10.73	11.25	34.17	8.30	7.80	1.88
end.	25.05	10.22	10.80	32.72	7.83	7.41	1.84
[20–29]							
per.	26.30	10.72	11.23	34.13	8.29	7.79	1.88
end.	24.61	10.05	10.64	32.22	7.67	7.28	1.83
[30–39]							
per.	26.10	10.64	11.16	33.90	8.22	7.73	1.87
end.	24.40	9.97	10.57	31.99	7.60	7.22	1.83
[40–49]							
per.	25.08	10.23	10.81	32.76	7.84	7.42	1.85
end.	22.91	9.38	10.06	30.32	7.05	6.76	1.79
[50–59]							
per.	25.08	10.23	10.81	32.76	7.84	7.42	1.85
end.	22.06	9.04	9.76	29.36	6.74	6.51	1.77
[60–69]							
per.	25.69	10.48	11.02	33.44	8.07	7.61	1.86
end.	22.03	9.03	9.75	29.32	6.73	6.49	1.76
[70–79]							
per.	25.05	10.22	10.80	32.72	7.83	7.41	1.84
end.	20.09	8.27	9.08	27.15	6.02	5.91	1.71
[80–99]							
per.	25.15	10.26	10.83	32.83	7.87	7.44	1.85
end.	18.06	7.47	8.37	24.86	5.28	5.29	1.66

A classical mixture law is used to obtain mass density as a function of spatial variable ξ, where $\xi = x$ for the plate and $\xi = r$ for the tube. We assume that the pores are filled with water, which is considered to be a perfect fluid:

$$\rho(\xi) = \rho_{\text{bone}}(1 - p(\xi)) + \rho_{\text{water}} p(\xi); \tag{2}$$

with p the porosity, $\rho_{\text{bone}} = 1.9$ g/cm^3 and $\rho_{\text{water}} = 1$ g/cm^3.

Choice of waveguide geometry

It was essential to set realistic parameters for the geometry of the model. For a first approximation, long bone can be modeled as a plate, ignoring the curvature effect on guided wave propagation (Lefebvre et al. 2002; Bossy et al. 2004; Protopappas et al. 2006; Baron 2011). However, a more realistic shape for long bone is a tube (Protopappas et al. 2007) and here both geometries were investigated. For the plate, the set of parameters was reduced to the thickness, taken as decreasing with age (Bousson et al. 2001) (Table 2). For the tube, one of the parameters known to influence guided wave propagation is the ratio of thickness over outer radius (Nishino et al. 2001; Baron 2011). Here too, thickness was taken from (Bousson et al. 2001). Previous findings (Carter et al. 1996; Feik et al. 2005) have established that the outer diameter remains the same after 30 years; in this study, it is fixed at 24 mm and the thinning of the cortical wall with age is represented by an increase in the inner diameter to reach the thickness measured by Bousson and colleagues (Bousson et al. 2001).

Ultrasonic guided waves

We consider an elastic waveguide (plate or tube) of thickness t placed in vacuum. The coordinate systems

Table 2. Age-related regional evolution in intracortical porosity and gradient

	t (mm)	p% per. (%)	p% mid. (%)	p% end. (%)	*grad* (%/mm)
[10–19]	3.804	2.4	3.7	6.2	0.999
[20–29]	4.166	2.5	3.75	7.5	1.200
[30–39]	4.368	3.1	4.4	8.1	1.145
[40–49]	4.354	6.1	7.4	12.5	1.470
[50–59]	3.762	6.1	8	15	2.366
[60–69]	3.104	4.3	11.5	15.1	3.479
[70–79]	3.46	6.2	11.3	20.8	4.220
[80–99]	2.502	5.9	17.5	26.8	8.353

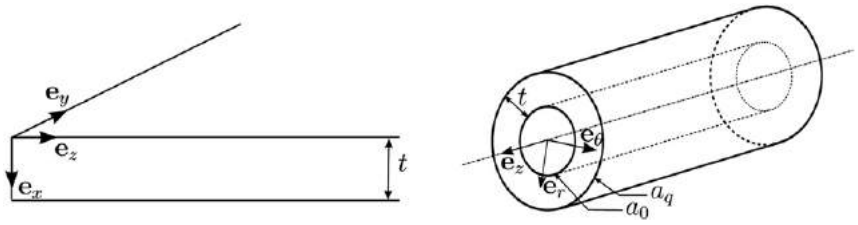

Fig. 2. Geometrical configuration of the waveguides.

(x, y, z) for the plate and (r, θ, z) for the tube are defined with the z-axis corresponding to the axis of the long bone and x and r representing the spatial variables along the cortical thickness.

The variable x describes the thickness of the plate from 0 to t. The radius of the tube r varies from a_0 to a_q, the inner and outer radius of the tube (Fig. 2), respectively. To simplify the notation, we use the variable ξ where $\xi = x, r$.

The elastic waveguide is considered to be anisotropic and is liable to present continuously varying properties across its thickness ($\mathbf{e}_x$-axis or $\mathbf{e}_r$-axis). These mechanical properties are represented by the stiffness tensor $\mathrm{C} = \mathrm{C}(\xi)$ and the mass density $\rho = \rho(\xi)$.

System equations

The momentum conservation equation associated with the constitutive law of linear elasticity (Hooke's law) gives the following equations:

$$\begin{cases} \operatorname{div} \boldsymbol{\sigma} = \rho \dfrac{\partial^2 \mathbf{u}}{\partial t^2}, \\ \boldsymbol{\sigma} = \dfrac{1}{2}\, \mathbb{C}\, (\operatorname{grad} \mathbf{u} + \operatorname{grad}^T \mathbf{u}), \end{cases} \tag{3}$$

where $\mathbf{u}$ is the displacement vector and $\boldsymbol{\sigma}$ the stress tensor.

- For the plate

We assume that the structure is two-dimensional (2-D) and that the guided waves travel in the plane $y = 0$; in the following, this coordinate is implicit and is omitted in the mathematical expressions. Solutions are sought for the vectors of displacement ($\mathbf{u}$) and traction ($\boldsymbol{\sigma}_x = \boldsymbol{\sigma} \,.\, \mathbf{e}_x$) expressed in the Cartesian coordinates (x, z) with the basis $\{\mathbf{e}_x, \mathbf{e}_z\}$:

$$\begin{aligned} \mathbf{u}(x, z; t) &= \mathbf{U}(\mathrm{x}) \exp \imath(k_z z - \omega t), \\ \boldsymbol{\sigma}_x(x, z; t) &= \mathbf{T}(x) \exp \imath(k_z z - \omega t); \end{aligned} \tag{4}$$

with k_z the axial wavenumber. The modes propagating in such a structure are called Lamb modes. We distinguish two types of Lamb modes: symmetrical (S-modes) and anti-symmetrical branches (A-modes) (Lamb 1917).

- For the tube

We seek to solve the wave equation for displacement vector ($\mathbf{u}$) and radial traction vector ($\boldsymbol{\sigma}_r = \boldsymbol{\sigma}.\mathbf{e}_r$) expressed in the cylindrical coordinates (r, θ, z) with the basis $\{\mathbf{e}_r, \mathbf{e}_\theta, \mathbf{e}_z\}$:

$$\begin{aligned} \mathbf{u}(r, \theta, z; t) &= \mathbf{U}^{(n)}(r) \exp \imath(n\theta + k_z z - \omega t), \\ \boldsymbol{\sigma}_r(r, \theta, z; t) &= \mathbf{T}^{(n)}(r) \exp \imath(n\theta + k_z z - \omega t); \end{aligned} \tag{5}$$

with k_z the axial wavenumber and n the circumferential wavenumber.

We distinguish two types of waves propagating in a cylindrical waveguide: *circumferential waves* and *axial waves*. *Circumferential waves* are waves traveling in planes perpendicular to the axis direction. They correspond to $u_z(r) = 0\ (\forall r)$, $k_z = 0$ and $n = k_\theta\, a_q$. *Axial waves* are waves traveling along the axis direction, the circumferential wavenumber is an integer $n = 0, 1, 2, \ldots$. Among the *axial waves*, we distinguish three types of modes numbered with two parameters (n, m) representing the circumferential wavenumber and the order of the branches: longitudinal (L), flexural (F) and torsional (T) modes. The longitudinal and torsional modes are axially symmetric ($n = 0$) and denoted $L(0, m)$ and $T(0, m)$. The flexural modes are non-axially symmetric ($n \geq 1$) and are denoted $F(n, m)$ (Gazis 1959). In this article, we focus on longitudinal and first flexural modes ($n = 1$).

A closed-form solution: the matricant

Introducing the expression (4) for the plate or (5) for the tube into the equation (3), we obtain the wave equation in the form of a second-order differential equation with nonconstant coefficients. In the general case, there is no analytical solution to the problem thus formulated. Most current methods of solving the wave equation in unidirectionally heterogeneous media are derived from the Thomson-Haskell method (Thomson 1950; Haskell 1953). These methods are appropriate for multilayered structures (Kenneth 1982; Lévesque and Piché 1992; Wang and Rokhlin 2001; Hosten and Castaings 2003). However, for continuously varying media, these techniques replace the continuous profiles of properties by step-wise functions, thereby making

the problem approximate, even before the resolution step. The accuracy of the solution, like its validity domain, are thus hard to evaluate. Moreover, a multilayered model of functionally graded waveguides creates "virtual" interfaces likely to induce artifacts. Lastly, for generally anisotropic cylinders, the solutions cannot be expressed analytically, even for homogeneous layers (Mirsky 1964; Nelson et al. 1971; Soldatos and Jianqiao 1994).

To solve the exact problem, that is, to maintain the continuity of the variation in properties, and to take into account the anisotropy of cylindrical waveguides, we write the wave equation under the sextic Stroh formalism (Stroh 1962) in the form of an ordinary differential equations system with nonconstant coefficients for which an analytical solution exists: the matricant (Pease 1965; Baron 2005).

Hamiltonian form of the wave equation. In the Fourier domain, the wave equation can be written as:

- For the plate

$$\frac{d}{dx}\boldsymbol{\eta}(x) = \mathbf{Q}(x)\boldsymbol{\eta}(x); \tag{6}$$

- For the tube

$$\frac{d}{dr}\boldsymbol{\eta}(r) = \frac{1}{r}\mathbf{Q}(r)\boldsymbol{\eta}(r). \tag{7}$$

The components of the state-vector $\boldsymbol{\eta}(\xi)$ are the components of the displacement vector $\mathbf{u}$ and the components of the traction vector $\boldsymbol{\sigma}_\xi$. As for the matrix $\mathbf{Q}(\xi)$, it contains all the information about heterogeneity: it is expressed from the stiffness coefficients of the waveguide in the appropriate system of coordinates (Cartesian for the plate and cylindrical for the tube) and from two acoustical parameters (wavenumbers, angular frequency, horizontal slowness). Detailed expressions of $\mathbf{Q}(\xi)$ are given in Appendix A for the case of a material with hexagonal crystallographic symmetry; but it can be expressed for any type of anisotropy (Shuvalov 2003).

Explicit solution: the Peano expansion of the matricant. The wave equation, thus, formulated has an analytical solution expressed between a reference point ξ_0 and some point along the cortical thickness direction ξ. This solution is called the matricant and is explicitly written in the form of the Peano series expansion:

$$\mathbf{M}(\xi,\xi_0) = \mathbf{I} + \int_{\xi_0}^{\xi} \mathbf{Q}(\varsigma)d\varsigma + \int_{\xi_0}^{\xi} \mathbf{Q}(\varsigma)\int_{\xi_0}^{\varsigma} \mathbf{Q}(\varsigma_1)d\varsigma_1 d\varsigma + \ldots, \tag{8}$$

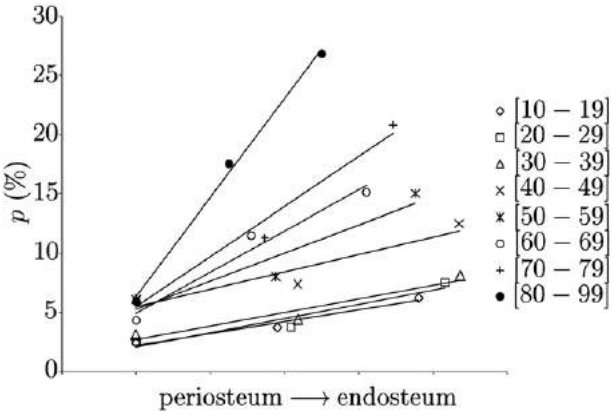

Fig. 3. Variation in porosity across the cortical thickness: linear regression for each age range ($R^2 \geq 0.9$).

where $\mathbf{I}$ is the identity matrix of dimension $(6,6)$. If the matrix $\mathbf{Q}(\xi)$ is bounded in the study interval, these series are always convergent (Baron 2005). The components of the matrix $\mathbf{Q}$ are continuous in ξ and the study interval is bounded (thickness of the waveguide), consequently the hypothesis is always borne out. The matricant verifies the propagator property (Baron 2005):

$$\boldsymbol{\eta}(\xi) = \mathbf{M}(\xi,\xi_0)\boldsymbol{\eta}(\xi_0). \tag{9}$$

Free boundary conditions. The waveguide is considered to be in vacuum, so the traction vector $\boldsymbol{\sigma}_\xi$ defined in (4 and 5) is null at both interfaces. Using the propagator property of the matricant through the thickness of the structure, eqn (7) is written as $\boldsymbol{\eta}(\xi_0 + t) = \mathbf{M}(\xi_0 + t, \xi_0)\boldsymbol{\eta}(\xi_0)$ with $\xi_0 = 0$ for the plate and $\xi_0 = a_0$ for the tube. Factorizing the matricant $\mathbf{M}(\xi_0 + t, \xi_0)$ under four block matrices of dimension $(3,3)$, eqn (7) becomes:

$$\begin{pmatrix} \mathbf{u}(\xi = \xi_0 + t) \\ 0 \end{pmatrix} = \begin{pmatrix} \mathbf{M}_1 & \mathbf{M}_2 \\ \mathbf{M}_3 & \mathbf{M}_4 \end{pmatrix} \begin{pmatrix} \mathbf{u}(\xi = \xi_0) \\ 0 \end{pmatrix}. \tag{10}$$

Equation (10) has non-trivial solutions for $\det \mathbf{M}_3 = 0$. As detailed in Appendix A for a transversely isotropic material and from eqn (8), the components of $\mathbf{M}_3$ are bivariate polynomials in (s_z, ω) or (k_z, ω). Consequently, seeking the zeros of $\det \mathbf{M}_3$ amounts to seeking the pairs of values (s_z, ω) or (k_z, ω), which describe the dispersion curves of guided waves propagating in a plate or a tube respectively.

RESULTS

Gradient of porosity

The variation in porosity across the cortical thickness and its age-related evolution are presented in Table 2. Figure 3 shows that a linear profile is a good

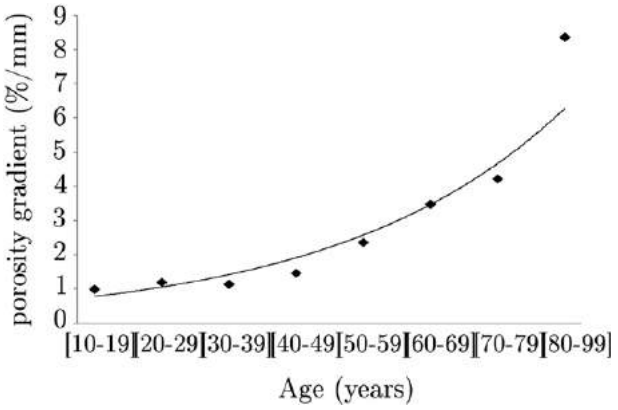

Fig. 4. Age-related evolution of the porosity gradient: exponential regression ($R^2 = 0.93$).

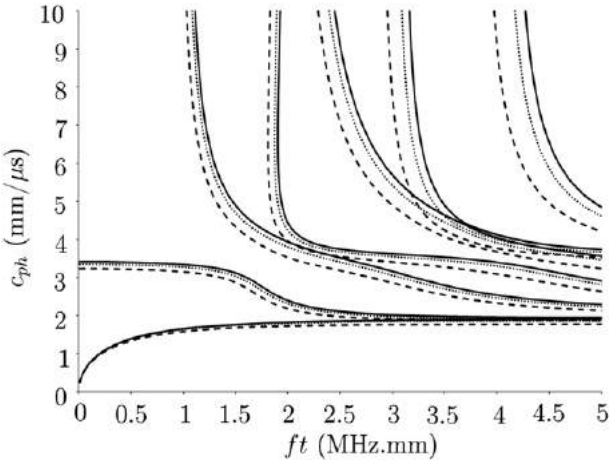

Fig. 5. Dispersion curves of Lamb modes propagating in a transversely isotropic plate, for three age ranges: [30–39] straight line, [60–69] dots and [80–99] dotted line.

approximation to model porosity changes. For every age range, $p\% = a\,\xi + b$, where ξ is the spatial variable along the cortical thickness, $(a, b) \in \Re^2$.

The porosity gradient (%/mm) is deduced from an estimation of the slope a for each age class (Table 2).

Figure 3 clearly shows that porosity sharply increases with age in the endosteal region, whereas it remains fairly stable in the periosteal region. Moreover, cortical thickness greatly decreases with age, from adulthood to old age. These two processes identified by Bousson (Bousson et al. 2000, 2001) are linked under the name trabecularization of the endosteal region.

The age-related evolution of the porosity gradient represented on Figure 4 reveals an inverse trend compared with the evolution of BMD (Melton III et al. 2000): it remains almost constant up to the 4th decade and then it increases with advancing age. The regression is exponential, similar to the evolution of the risk of fracture with age reported in the literature (Hui et al. 1988; De Laet et al. 1997; Kanis et al. 2008).

Sensitivity of guided waves to the gradient of material properties

The effect of a realistic intracortical porosity gradient on guided wave propagation was investigated to determine how sensitive the guided waves are to the age-related evolution of long bone strength; in particular, whether they are sensitive both to thinning of the cortex and to increased endosteal porosity during aging. We compared the ultrasonic guided waves' interaction with three planar waveguides and three tubular waveguides modeling the diaphysis of the femur at three different age ranges: [30–39], [60–69] and [80–99] (Bousson et al. 2001). Waveguides dimensions are reported in Table 3. The dispersion curves are plotted as functions of the frequency-thickness product in the usual range for the study of ultrasonic waves in long bones (Bossy et al. 2004; Muller et al. 2005; Tatarinov et al. 2005; Protopappas et al. 2006). For guided waves in long bones, the typical frequency range is between 50 kHz to 350 MHz (Moilanen et al. 2008) to generate wavelengths greater than the cortical thickness (Bossy et al. 2004). Consequently, the frequency-thickness product to be considered is roughly [0.2, 1.5] MHz.mm for [30–39], [0.15, 1.1] MHz.mm for [60–69] and [0.125, 0.875] MHz.mm for [80–99].

Table 3. Geometry of the waveguides for three age ranges

	Thickness (plate or tube)	Tube dimensions		
	t (mm)	a_0 (mm)	a_q (mm)	t/a_q
[30–39]	4.368	7.64	12	0.36
[60–69]	3.104	8.9	12	0.26
[80–99]	2.502	9.5	12	0.21

The dispersion curves of Lamb modes propagating in plates show measurable differences throughout aging (Fig. 5). The discrepancy between the dispersion spectra obtained for each age range grows with the frequency-thickness product. For example, at 1 MHz.mm, the phase velocity of the S_0 mode for the [80–99] age group is 6% lower than for the [30–39] age group, the phase velocity of the A_2 mode for the [60–69] age group is 5% higher than for the [80–99] age group and 10% lower than for the [30–39] age group. All these differences correspond to several thousand meters per second, which are experimentally measurable quantities.

The same trends can be seen from the dispersion curves of the longitudinal and flexural modes propagating in the tubes (Fig. 6). The cut-off frequencies of all the modes are distinct for the three age ranges considered (Table 4).

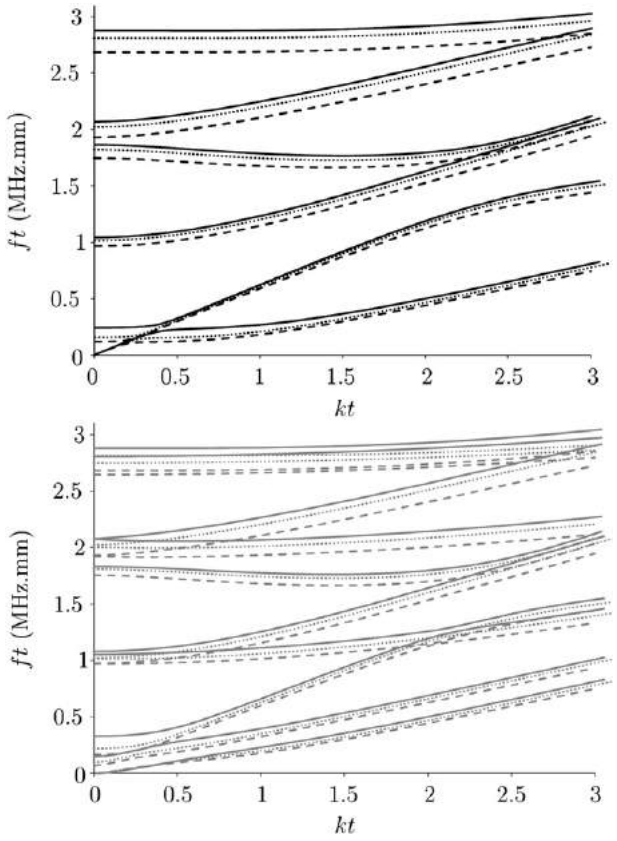

Fig. 6. Dispersion curves of the eight first longitudinal modes (in black) and the ten first flexural (in grey) modes propagating in a transversely isotropic tube, for three age ranges: [30–39] straight line, [60–69] dots and [80–99] dotted line.

The phase velocities are also significantly different: for instance, the discrepancy between the $F\,(1,3)$-mode phase velocity for [80–99] and the $F\,(1,3)$-mode phase velocity for [30–39] is about 420 m/s.

One of the critical parameters of long bone strength is cortical thickness. To evaluate cortical thickness, Moilanen and his team showed the relevance of considering the $F\,(1,1)$ mode instead of the A_0 mode (Moilanen et al. 2007). This is confirmed by our results on the group velocity of these two modes calculated for the three age ranges (Fig. 7).

It is clearly shown that around the frequency of 200 kHz used by Moilanen and colleagues, the group velocity of A_0 mode is consistently different from the group velocity of the $F\,(1,1)$ mode and it appears that the group velocity of the $F\,(1,1)$ mode is very sensitive to the porosity gradient in the frequency range considered.

Table 4. Variations in cut-off frequencies for longitudinal and flexural modes with aging

	L(0,2)	L(0,3)	F(1,2)	F(1,3)	F(1,4)	F(1,5)
$\Delta f_{30/60}$ (kHz)	4.9	88.3	2.9	4.5	87.2	80.8
$\Delta f_{60/80}$ (kHz)	3.4	60.3	2.2	4	60.1	59.7
$\Delta f_{30/80}$ (kHz)	8.3	148.6	5.1	8.4	147.3	140.5

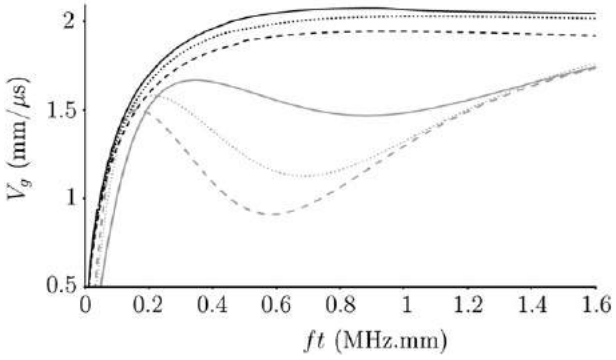

Fig. 7. Group velocity of A_0 mode (in black) and $F\,(1,1)$ mode (in grey) propagating in a transversely isotropic plate and tube respectively, for three age ranges: [30–39] straight line, [60–69] dots and [80–99] dotted line.

DISCUSSION

The Stroh formalism used in this study has several advantages. First, it allows ultrasound propagation to be investigated in a continuously varying medium (FGM) instead of approximating it by a multilayered medium, thus, avoiding potential round-off errors and artifacts that cannot be estimated. It provides an exact solution to the exact problem and the degree of round-off error is manageable (Baron 2005). Furthermore, this formalism is numerically stable and is applicable to planar and tubular geometries whatever the degree of anisotropy of the material. The conventional methods used to solve the wave equation are unable to deal with cylindrical coordinates coupled with general anisotropy. The Stroh formalism is one of the only ways to provide an analytical solution (Peano expansion of the matricant) to the wave equation in a cylindrical structure whatever the anisotropy of the material (Shuvalov 2003). Moreover, fluid-loading of the waveguide here can be treated as in the case of the plate (Baron and Naili 2010). The advantages of this formalism in the context of bone characterization are clear, since long bone can be realistically modeled as an FGM orthotropic tube surrounded by blood and full of marrow. In addition, because this method takes into account actual variations in material properties of long bones, it could prove useful as a reference to validate models which do not allow for the gradient of material properties, confirming the range of validity (frequency domain, thickness range, order of the modes) of the results yielded by such simplified models.

Bone fragility has long been known to be related to the quantity of material (bone density), its quality

(stiffness) and its organization (geometry and microarchitecture). An accurate evaluation of fracture risk has to assess these three parameters together. As cortical bone ages, endosteal trabecularization induces thinning of the cortex. Thus, the spatial variation in porosity across the cortical thickness revealed during aging can be taken as the "missing" parameter to represent bone quality. This is confirmed by Figure 4, which illustrates an evolution in porosity gradient with age similar to the evolution in risk of fracture reported in the literature for the vertebra (Cooper et al. 1992) and for the hip (De Laet et al. 1997). As previously pointed out, the gradient of material properties (density and stiffness coefficients) reflects the spatial distribution of the quantity and quality of bone across the cortical thickness. Looking at the dispersion curves obtained here for the plate and for the tube, this discrepancy between the different age ranges appears to be experimentally measurable. Thus, this study indicates that the gradient of homogenized material properties can be evaluated from measured ultrasound velocities.

Solving the inverse problem, however, will be tricky, and further work will be required before this can be achieved. An accurate evaluation of the various factors influencing bone strength would require a wider range of measurements (other ultrasound frequencies, other imaging modalities).

Our work demonstrates the sensitivity of guided waves to realistic variations in the intrinsic properties of human cortical bone: porosity, density, stiffness, as revealed by the gradient in material properties. Nevertheless, it remains difficult to establish a reliable criterion to apply in a clinical protocol. Careful consideration needs to be given to choosing appropriate anatomical sites for ultrasonic evaluation. To avoid too much ultrasound absorption, the most suitable sites are the phalanx, the radius and the tibia (Njeh et al. 2001). These sites are long bones for which the question of the influence of the curvature on wave propagation needs to be addressed (Baron 2011). The choice of geometric model (plate or tube) is particularly important in pediatrics since the thickness over outer radius ratio (t/a_q) of growing bone is greater than 0.5. Thus, ultrasound evaluation is a promising alternative technique in pediatrics.

Our model could usefully be extended. Several realistic characteristics can easily be added to the formalism we use. First, how soft tissue affects wave propagation can be modeled by fluid-loading, as examined in a recent paper (Baron and Naili 2010). Second, the gradual variation in the intrinsic properties of the bone matrix described in Lakshmanan et al. (2007) can be included in the homogenization step and would contribute to the mesoscopic gradient of bone properties.

Furthermore, it would be relevant to consider not only the variation in "global" intracortical porosity (the ratio of the volume of pores over the total volume) but also the distribution of pore sizes and of the number of pores across the cortical thickness. In Bousson et al. (2001), it was noted that increased endosteal porosity arises from an increase in the size of pores rather than from an increase in the number of pores; this difference in the organization of the microstructure may affect the mechanical behavior of the bone.

CONCLUSION

The gradient of material properties appears here to be relevant to evaluating age-related changes in cortical bone, particularly in the context of osteoporosis and therapeutic follow-up. This article describes an original method applied to bone characterization able to take into account the heterogeneity (porosity gradient) and the anisotropy (orthotropy) of the material as well as the tubular geometry of the structure, even under *in vivo* conditions (soft tissue).

Ultrasound evaluation appears to be a good candidate to characterize long bone (structure, geometry and material); however, the potential of *in vivo* techniques that take into account the influence of soft tissue and marrow needs to be further explored.

The results we obtained are promising but the method should be extended, in particular, with a view to solving the inverse problem. An *in vitro* experimental program would validate the feasibility of the ultrasound measurements on bone samples of different ages. It could also evaluate the relevance of using an *in vivo* characterization of the gradient of properties across the cortical thickness to determine bone strength and the risk of fracture.

REFERENCES

Ammann P, Rizzoli R. Bone strength and its determinants. Osteoporos Int 2003;14(Suppl. 3):S13–S18.

Augat P, Reeb H, Claes LE. Prediction of fracture load at different skeletal sites by geometric properties of the cortical shell. J Bone Miner Res 1996;11:1356–1363.

Augat P, Schorlemmer S. The role of cortical bone and its microstructure in bone strength. Age Ageing 2006;35(Suppl. 2):ii27–ii31.

Baron C. Le développement en série de Peano du matricant pour l'étude de la propagation d'ondes en milieux continûment variables–Peano expansion of the matricant to study elastic wave propagation in continuously heterogeneous media. Ph.D. thesis, Université Bordeaux 1, France, 2005.

Baron C. Propagation of elastic waves in an anisotropic functionally graded hollow cylinder in vacuum. Ultrasonics 2011;51:123–130.

Baron C, Naili S. Propagation of elastic waves in a fluid-loaded anisotropic functionally graded waveguide: Application to ultrasound characterization. J Acoust Soc Am 2010;127:1307–1317.

Baron C, Talmant M, Laugier P. Effect of porosity on effective diagonal stiffness coefficients (c_{ii}) and anisotropy of cortical at 1 MHz: A finite-difference time domain study. J Acoust Soc Am 2007; 122:1810–1817.

Bossy E, Talmant M, Laugier P. Three-dimensional simulations of ultrasonic axial transmission velocity measurement on cortical models. J Acoust Soc Am 2004;115:2314–2324.

Bousson V, Bergot C, Meunier A, Parlier-Cuau C, Laval-Jeantet AM, Laredo JD. CT of the middiaphyseal femur: Cortical bone mineral density end relation to porosity. Radiology 2000;217:179–187.

Bousson V, Meunier A, Bergot C, Vicaut E, Rocha MA, Morais MH, Laval-Jeantet AM, Laredo JD. Distribution of intracortical porosity in human midfemoral cortex by age and gender. J Bone Mineral Res 2001;16:1308–1317.

Carter DR, Van Der Meulen MCH, Beaupré GS. Mechanical factors in bone growth and development. Bone 1996;18:5S–10S.

Cooper C, Atkinson EJ, Michael O'Fallon W, Melton JL. Incidence of clinically diagnosed vertebral fractures: A population-based study in Rochester, Minnesota, 1985–1989. J Bone Miner Res 1992;87:221–227.

De Laet CE, van Hout BA, Burger H, Hofman A, Pols HA. Bone density and risk of hip fracture in men and women: Cross-sectional analysis. Br Med J 1997;315:221–225.

Dong XN, Guo XE. The dependence of transversely isotropic elasticity of human femoral cortical bone on porosity. J Biomech 2004;37: 1281–1287.

Faulkner KG. Bone matters: Are density increases necessary to reduce fracture risk? J Bone Miner Res 2000;15:183–187.

Feik SA, Thomas DL, Clement JG. Age trends in remodeling of the femoral midshaft differ between the sexes. J Orthopaed Res 2005; 14:590–597.

Gazis DC. Three-dimensional investigation of the propagation of waves in hollow circular cylinders. i. Analytical foundation. J Acoust Soc Am 1959;31:568–573.

Gregory JS, Aspden RM. Femoral geometry as a risk factor for osteoporotic hip fracture in men and women. Med Eng Phys 2008;30: 1275–1286.

Grimal G, Raum K, Gerisch A, Laugier P. A determination of the minimum sizes of representative volume elements for the prediction of cortical bone elastic properties. Biomech Modeling Mechanobiol 2011;OnLineFirst™:1–13.

Haïat G, Naili S, Grimal Q, Talmant M. Influence of a gradient of material properties on ultrasonic wave propagation in cortical bone: Application to axial transmission. J Acoust Soc Am 2009;125: 4043–4052.

Haskell NA. The dispersion of surface waves on multilayered media. Bull Seismol Soc Am 1953;43:377–393.

Holzer G, von Skrbensky G, Holzer LA, Pichl W. Hip fractures and the contribution of cortical versus trabecular bone to femoral neck strength. J Bone Miner Res 2009;243:468–474.

Hosten B, Castaings M. Surface impedance matrices to model the propagation in multilayered media. Ultrasonics 2003;41:501–507.

Hui SL, Slemenda CW, Johnston CJ. Age and bone mass as predictors of fracture in a prospective study. J Clin Invest 1988;80:1804–1809.

Kanis JA, Johnell O, Oden A, Johansson H, McCloskey A. FRAXZ and the assessment of fracture probability in men and women from the UK. Osteoporos Int 2008;19:385–397.

Kenneth EG. A propagator matrix method for periodically stratified media. J Acoust Soc Am 1982;731:137–142.

Lakshmanan S, Bodi A, Raum K. Assessment of anisotropic tissue elasticity of cortical bone from high-resolution, angular acoustic measurements. IEEE Trans Ultrason Ferroelectr Freq Control 2007;54:1560–1570.

Lamb H. On waves in an elastic plate. Proc R Soc Lond A 1917;93: 114–128.

Lefebvre F, Deblock Y, Campistron P, Ahite D, Fabre JJ. Development of a new ultrasonic technique for bone and biomaterials in vitro characterization. J Biomed Mater Res Part B 2002;63:441–446.

Lévesque D, Piché L. A robust transfer matrix simulation for ultrasonic response of multilayered absorbing media. J Acoust Soc Am 1992; 92:452–467.

Manske SL, Liu-Ambrose T, Cooper DML, Kontulainen S, Guy P, Forster BB, McKay HA. Cortical and trabecular bone in the femoral neck both contribute to proximal femur failure load prediction. Osteoporos Int 2009;203:445–453.

Marshall D, Johnell O, Wedel H. Meta-analysis of how well measures of bone mineral density predict occurrence of osteoporotic fractures. Br Med J 1996;312:1254–1259.

Melton III LJ, Khosla S, Atkinson EJ, O'Connor MK, O'Fallon WM, Riggs BL. Cross-sectional versus longitudinal evaluation of bone loss in men and women. Osteoporos Int 2000;11:592–599.

Mirsky I. Axisymmetric vibrations of orthotropic cylinders. J Acoust Soc Am 1964;36:2106–2112.

Moilanen P, Nicholson PHF, Kilappa V, Cheng S, Timonen J. Assessment of the cortical thickness using ultrasonic guided waves: Modeling and *in vitro* study. Ultrasound Med Biol 2007;33:254–262.

Moilanen P, Talmant M, Kilappa V, Nicholson PHF, Cheng S, Timonen J, Laugier P. Modeling the impact of soft tissue on axial transmission measurements of ultrasonic guided waves in human radius. J Acoust Soc Am 2008;124:2364–2373.

Muller M, Moilanen P, Bossy E, Nicholson PHF, Kilappa V, Timonen J, Talmant M, Cheng S, Laugier P. Comparison of three ultrasonic axial transmission methods for bone assessment. Ultrasound Med Biol 2005;31:633–642.

Nelson R, Dong S, Kalkra R. Vibrations and waves in laminated orthotropic circular cylinders. J Sound Vibration 1971;18:429–444.

Nishino H, Takashina S, Uchida F, Takemoto M, Ono K. Modal analysis of hollow cylindrical guided waves and applications. Jpn J Appl Phys 2001;301:364–370.

Njeh C, Saeed I, Grigorian M, Kendler D, Fan B, Shepherd J, McClung M, Drake W, Genant H. Assessment of bone status using speed of sound at multiple sites. Ultrasound Med Biol 2001;27: 1337–1345.

Pease MC. Methods of matrix algebra. New York: Academic Press; 1965.

Protopappas V, Fotiadis D, Malizos K. Guided ultrasound wave propagation in intact and healing long bone. Ultrasound Med Biol 2006; 32:693–708.

Protopappas V, Kourtis IC, Kourtis LC, Malizos K, Massalas CV, Fotiadis D. Three-dimensional finite element modeling of guided ultrasound wave propagation in intact and healing long bones. J Acoust Soc Am 2007;121:3907–3921.

Reilly DT, Burnstein AH. The mechanical properties of cortical bone. J Bone Joint Surg Am 1974;56:1001–1022.

Robbins JA, Schott AM, Garnero P, Delmas PD, Hans D, Meunier PJ. Risk factors for hip fracture in women with high BMD: EPIDOS study. Osteoporos Int 2005;16:149–154.

Shuvalov A. A sextic formalism for three-dimensional elastodynamics of cylindrically anisotropic radially inhomogeneous materials. Proc R Soc Lond A 2003;459:1611–1639.

Soldatos K, Jianqiao Y. Wave propagation in anisotropic laminated hollow cylinders of infinite extent. J Acoust Soc Am 1994;96: 3744–3752.

Stroh AN. Steady state problems in anisotropic elasticity. J Math Phys 1962;41:77–103.

Tatarinov A, Sarvazyan N, Sarvazyan A. Use of multiple acoustic wave modes for assessment of long bones: Model study. Ultrasonics 2005; 438:672–680.

Thomson WT. Transmission of elastic waves through a stratified solid medium. J Appl Phys 1950;21:89–93.

Tobias JH, Cook DG, Chambers TJ, Dalzell N. A comparison of bone mineral density between caucasian, Asian and Afro-Caribbean women. Clin Sci 1994;87:587–591.

Treece G, Gee A, Mayhew P, Poole K. High resolution cortical bone thickness measurement from clinical CT data. Med Image Anal 2010;143:276–290.

Wang L, Rokhlin SI. Stable reformulation of transfer matrix method for wave propagation in layered anisotropic media. Ultrasonics 2001; 39:413–424.

Xiaoge D, Eryuan L, Xianping W, Zhiguang Z, Gan H, Zaijing J, Xiaoli P, Hongzhuan T, Hanwen W. Bone mineral density differences at the femoral neck and Ward's triangle: A comparison study on the reference data between Chinese and Caucasian women. Calcif Tissue Int 2000;67:195–198.

APPENDIX A

$$\frac{d}{dx}\boldsymbol{\eta}(x) = \imath\omega\mathbf{Q}(x)\boldsymbol{\eta}(x), \tag{A.1}$$

Plate/tube

Formalism for plate.

$$\frac{d}{dx}\begin{pmatrix} \imath\omega\widehat{u}_x \\ \imath\omega\widehat{u}_z \\ \widehat{\sigma}_{xx} \\ \widehat{\sigma}_{xz} \end{pmatrix} = \imath\omega\begin{pmatrix} 0 & -c_{13}(x)/c_{11}(x)s_z & 1/c_{11}(x) & 0 \\ s_3 & 0 & 0 & 1/c_{55}(x) \\ \rho(x) & 0 & 0 & -s_z \\ 0 & \rho(x1) - s_z^2\zeta(x) & -c_{13}(x)/c_{11}(x)s_z & 0 \end{pmatrix}\begin{pmatrix} \imath\omega\widehat{u}_x \\ \imath\omega\widehat{u}_z \\ \widehat{\sigma}_{xx} \\ \widehat{\sigma}_{xz} \end{pmatrix}, \tag{A.2}$$

$$\mathbf{Q}(r) = \frac{1}{r}\begin{pmatrix} -\dfrac{c_{12}}{c_{11}} & -\imath n\dfrac{c_{12}}{c_{11}} & -\imath k_z r\dfrac{c_{13}}{c_{11}} & -\dfrac{1}{c_{11}} & 0 & 0 \\ -\imath n & 1 & 0 & 0 & -\dfrac{1}{c_{66}} & 0 \\ -\imath k_z r & 0 & 0 & 0 & 0 & \dfrac{1}{c_{44}} \\ \imath(\gamma_{12} - r^2\rho\omega^2) & -n\gamma_{12} & -k_z r\gamma_{23} & \dfrac{c_{12}}{c_{11}} & -\imath n & -\imath k_z r \\ n\gamma_{12} & \imath n^2\gamma_{12} + \imath r^2\left(k_z^2 c_{44} - \rho\omega^2\right) & \imath n k_z r(\gamma_{123} + c_{44}) & -\imath n\dfrac{c_{12}}{c_{11}} & -1 & 0 \\ k_z r\gamma_{23} & \imath n k_z r(\gamma_{23} + c_{44}) & \imath n^2 c_{44} + \imath r^2\left(k_z^2\gamma_{13} - \rho\omega^2\right) & -\imath k_z r\dfrac{c_{13}}{c_{11}} & 0 & 0 \end{pmatrix}$$

with the relations:

$$\zeta(x) = c_{33}(x) - \frac{c_{13}^2(x)}{c_{11}(x)}, \quad k_z = \omega s_z, \tag{A.3}$$

where s_z is the **z**-component of the slowness.

Formalism for tube. Expression of the vector $\boldsymbol{\eta}(r)$ and of the matrix $\mathbf{Q}(r)$ for a material with hexagonal crystallographic symmetry (5 independent stiffness coefficients). The symbol $\hat{\cdot}$ represents the quantities in the Fourier domain.

$$\boldsymbol{\eta}(r) = (\hat{u}_r(r), \hat{u}_\theta(r), \hat{u}_z(r), \imath r\hat{\sigma}_{rr}(r), \imath r\hat{\sigma}_{r\theta}(r), \imath r\hat{\sigma}_{rz}(r))^T,$$

and

with $c_{66} = (c_{11} - c_{12})/2$ and

$$\gamma_{12} = c_{11} - \frac{c_{12}^2}{c_{11}}; \quad \gamma_{13} = c_{33} - \frac{c_{13}^2}{c_{11}}; \quad \gamma_{23} = c_{13} - \frac{c_{12}c_{13}}{c_{11}}.$$

4.6 JMBBM 2015

Journal of the Mechanical Behavior of Biomedical Materials, 2015

Analyzing the anisotropic Hooke's law for children's cortical bone.
E. Lefèvre, P. Lasaygues, C. Baron, C. Payan, F. Launay, H. Follet, M. Pithioux. JMBBM 49, 370-377.

JOURNAL OF THE MECHANICAL BEHAVIOR OF BIOMEDICAL MATERIALS 49 (2015) 370–377

Available online at www.sciencedirect.com

ScienceDirect

www.elsevier.com/locate/jmbbm

Research Paper

Analyzing the anisotropic Hooke's law for children's cortical bone

Emmanuelle Lefèvre[a,e,*], *Philippe Lasaygues*[b], *Cécile Baron*[a,e], *Cédric Payan*[b], *Franck Launay*[a,d], *Hélène Follet*[c,1], *Martine Pithioux*[a,e,1]

[a]*Aix-Marseille Université, CNRS, ISM UMR 7287, 13288 Marseille cedex 09, France*
[b]*Laboratory of Mechanics and Acoustics, UPR CNRS 7051, Aix-Marseille University, Centrale Marseille, 13009 Marseille, France*
[c]*INSERM, UMR 1033, University of Lyon, 69372 Lyon cedex 08, France*
[d]*APHM, La Timone, Service de pédiatrie orthopédique, 13385 Marseille cedex 5, France*
[e]*APHM, Hôpital Sainte-Marguerite, Institute for Locomotion, 13009, Marseille, France*

ARTICLE INFO

Article history:
Received 16 March 2015
Received in revised form
13 May 2015
Accepted 17 May 2015
Available online 19 June 2015

Keywords:
Ultrasonic wave velocities
Stiffness coefficients
Pediatrics
Cortical bone
Anisotropy

ABSTRACT

Child cortical bone tissue is rarely studied because of the difficulty of obtaining samples. Yet the preparation and ultrasonic characterization of the small samples available, while challenging, is one of the most promising ways of obtaining information on the mechanical behavior of non-pathological children's bone. We investigated children's cortical bone obtained from chirurgical waste. 22 fibula or femur samples from 21 children (1–18 years old, mean age: 9.7±5.8 years old) were compared to 16 fibula samples from 16 elderly patients (50–95 years old, mean age: 76.2±13.5 years old). Stiffness coefficients were evaluated *via* an ultrasonic method and anisotropy ratios were calculated as the ratio of C_{33}/C_{11}, C_{33}/C_{22} and C_{11}/C_{22}. Stiffness coefficients were highly correlated with age in children ($R>0.56$, $p<0.01$). No significant difference was found between C_{11} and C_{22} for either adult or child bone ($p>0.5$), nor between C_{44} and C_{55} ($p>0.5$). We observe a transverse isotropy with $C_{33}>C_{22}=C_{11}>C_{44}=C_{55}>C_{66}$. For both groups, we found no correlation between age and anisotropy ratios. This study offers the first complete analysis of stiffness coefficients in the three orthogonal bone axes in children, giving some indication of how bone anisotropy is related to age. Future perspectives include studying the effect of the structure and composition of bone on its mechanical behavior.

1. Introduction

Bone is a hierarchical and organized structure with properties varying by successive stages from juvenile to mature state. Numerous studies have aimed to determine the mechanical properties of cortical bone tissue collected from adult human subjects (Bensamoun et al., 2004; Choi et al., 1990; Cuppone et al., 2004; Grimal et al., 2009; Ho Ba Tho et al., 1991; Keller

*Corresponding author at: Aix-Marseille Université, CNRS, ISM UMR 7287, 13288 Marseille cedex 09, France.
E-mail address: emmanuelle.lefevre@univ-amu.fr (E. Lefèvre).
[1]equal contribution.

http://dx.doi.org/10.1016/j.jmbbm.2015.05.013
1751-6161/

et al., 1990; Lotz et al., 1991; Reilly et al., 1974; Reilly and Burstein, 1975; Smith and Smith, 1976; Zioupos and Currey, 1998). Ultrasonic waves have frequently been used in the measurement of the elastic properties of adult bone *in vitro* (Ashman et al., 1984; Yoon and Katz, 1976; Rho, 1996; Espinoza Orías et al., 2009; Rudy et al., 2011; Baumann et al., 2012; Bernard et al., 2013). A method based on the measurement of both longitudinal and shear ultrasonic bulk wave velocities (BWV) allows the determination of numerous stiffness coefficients of the elasticity tensor C_{ijkl}, on a single specimen (Ashman et al., 1984; Rho, 1996; Espinoza Orías et al., 2009; Rudy et al., 2011; Baumann et al., 2012; Lang, 1969). Cortical bone is an anisotropic medium due to its highly oriented, mineralized collagen fibril structure, and the literature on adults contains different assumptions regarding the type of anisotropy of the cortical bone structure. Some authors (Haïat et al., 2009; Neil Dong and Edward Guo, 2004; Rho, 1996; Yoon and Katz, 1976) assume that human cortical bone can be considered as transverse isotropic (five independent elastic coefficients), meaning that bone elastic properties are similar in the transverse directions (radial and tangential) but are different in the axial direction. Others have made the more general assumption of orthotropy (Ashman et al., 1984; Hoffmeister et al., 2000; Rho, 1996) (with three perpendicular planes of symmetry), where nine elastic coefficients are needed to fully characterize the medium.

Little reference data is available on young bone mechanical behavior, especially on children's cortical bone. Several papers study mechanical properties of children's bone by uniaxial bending (Currey and Butler, 1975; Jans et al., 1998; Davis et al., 2012; Agnew et al., 2013; Berteau et al., 2013; Albert et al., 2013a, 2013b, 2014), compression (McPherson et al., 2007; Ohman et al., 2011) or ultrasonic characterization (Berteau et al., 2012, 2013). Some even study mechanical properties at the tissue level by nanoindentation (Fan et al., 2006; Weber et al., 2006; Albert et al., 2013a,2013b; Imbert et al., 2014). However, most of these studies were conducted on only a few samples, because of the scarcity of specimens for laboratory testing. Moreover, the representativeness of these samples is questionable, since they are largely associated with child pathologies. Due to the limited number of samples available, papers have up to now focused on mechanical properties in only one axis, generally the axial direction. The notion of anisotropy, particularly transverse isotropy or orthotropy, has rarely been investigated. Only one study on this subject reports orthotropy in children's bone before ossification (McPherson and Kriewall, 1980). In our study, children's bone samples were recovered from small chirurgical bone waste, with exclusion criteria; the only way to obtain non-pathologic bone samples from children. Yet this adds a difficulty: the specimens have been cut into very small cubes (~2 mm), smaller than those used in a previous study which tested 5 mm samples on Resonant Ultrasound Spectroscopy (RUS) and obtained promising results (Bernard et al., 2013).

Here, we report measurements of ultrasonic wave velocities (compressional and shear) in the three orthogonal bone axes (axial, radial and tangential) to obtain the diagonal elements of the stiffness matrix (C_{11}, C_{22}, *etc.*). To our knowledge, this study is the first to provide numerous stiffness coefficients on non-pathologic pediatric cortical bone. The major aim of the study was to obtain stiffness coefficients of children's cortical bone samples, and to analyze the anisotropic Hooke's law enabling us to explore the anisotropic behavior of child cortical bone. Values from children were compared with those from elderly adult cortical bone samples to evaluate how stiffness evolves with age. To achieve this objective, we required an experimental protocol specifically for measuring ultrasonic parameters with very small samples, both compressional and shear; the protocol needed to be reproducible and robust.

2. Methods

2.1. Sample preparation

15 fibula and 7 femur samples from 21 children (1–18 years old, mean age: 9.7±5.8 years old) were extracted from chirurgical waste during lower limb lengthening surgery performed in Marseille, France. Samples were extracted from the lower 1/3 of the bone. The selected population was composed of walking children not on drugs disturbing their bone metabolism.

16 fibula samples from 16 elderly patients (50–95 years old, mean age: 76.2±13.5 years old) were extracted from the same anatomic location, but from cadavers at Inserm U1033 and UMR-T 9406 Ifsttar/UCBL (Lyon, France) bone bank.

The fresh material was frozen and stored, the child bone at −80 °C (to lessen the impact of collagen degradation, which will be analyzed in a future study) and the adult bone at −20 °C. The samples were slowly thawed and then cut with a water-cooled low-speed diamond saw (Buehler Isomet 4000, Buehler, Lake Bluff, IL, USA) into cubic parallelepipeds (dimensions: $2 \times 2 \times 2 mm^3$; mean= 1.96±0.56 mm). The faces of the specimens were oriented according to the radial (axis 1), tangential (axis 2) and axial (axis 3) directions defined by the anatomic shape of the bone diaphysis (Fig. 1).

The greatest challenge here was the very small size of the chirurgical waste bone (less than 1 cm in the axial axis), the radial thickness of the sample being imposed by the cortical thickness taken. The second difficulty was cutting samples this

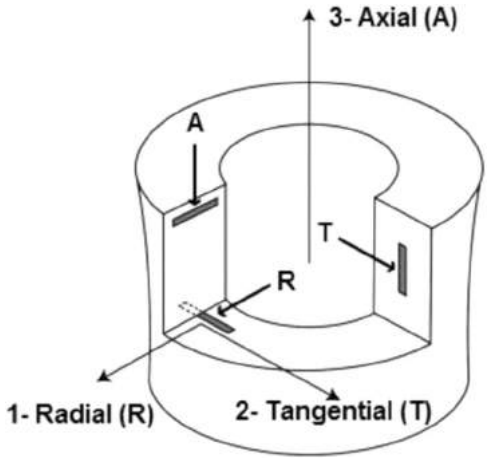

Fig. 1 – Sketch showing orientation of cortical bone samples prepared to study bone anisotropy. Figure adapted from (Reilly et al., 1974).

small with parallel faces. This necessitated an enhanced mounting protocol for the cutting. The mass density (ρ g/cm^3) was measured with a micrometric balance equipped with a density kit (Voyager 610, Ohaus Corporation, FlorhamPark, NJ, USA, measurement uncertainty of 0.001 g/cm^3) and the dimensions were measured with a digital caliper (Absolute digimatik solar, Mitutoyo, Kanagawa, Japan, measurement error of 0.03 mm).

2.2. Theoretical approach

In this study, we considered cortical human bone as an elastic unlimited medium (the wavelength is smaller than the transverse dimension of the sample). Human bones are generally considered to be orthotropic (Ashman et al., 1984; Yoon and Katz, 1976).

For generally anisotropic media, Hooke's law is written as follows:

$$\sigma_{ij} = C_{ijkl}\,\varepsilon_{kl} \text{ where } i,j,k,l \in \{1,2,3\} \quad (1)$$

In Eq. (1), σ_{ij} denotes the ij component of the stress tensor, ε_{kl} represents the components of the strain infinitesimal tensor and C_{ijkl} is the stiffness tensor. Assuming orthotropic behavior of the bone requires nine independent elastic coefficients of the stiffness tensor which can be expressed in Voigt notation as follows:

$$C_{IJ} = \begin{bmatrix} C_{11} & C_{12} & C_{13} & 0 & 0 & 0 \\ C_{21} & C_{22} & C_{23} & 0 & 0 & 0 \\ C_{31} & C_{32} & C_{33} & 0 & 0 & 0 \\ 0 & 0 & 0 & C_{44} & 0 & 0 \\ 0 & 0 & 0 & 0 & C_{55} & 0 \\ 0 & 0 & 0 & 0 & 0 & C_{66} \end{bmatrix} \quad (2)$$

We calculated the velocities of pure compressional and shear waves propagating along the three principal axes, which gave us the diagonal elements of the stiffness matrix. The relationships between the velocities and elastic coefficients of the material are:

$$\begin{aligned} C_{11} &= \rho V_{11}^2 \\ C_{22} &= \rho V_{22}^2 \\ C_{33} &= \rho V_{33}^2 \\ C_{44} &= \rho V_{23}^2 = \rho V_{32}^2 \\ C_{55} &= \rho V_{13}^2 = \rho V_{31}^2 \\ C_{66} &= \rho V_{12}^2 = \rho V_{21}^2 \end{aligned} \quad (3)$$

V_{ii}: velocity of a compressional wave propagating in the i direction, with particle motion in the i direction;

V_{ij}: velocity of a shear wave propagating in the i direction, with particle motion in the j direction;

Anisotropy was measured as the ratio of elastic constants in the axial/radial (C_{33}/C_{11}), in the axial/tangential (C_{33}/C_{22}) and in the radial/tangential (C_{11}/C_{22}) anatomic specimen axes (Rudy et al., 2011; Baumann et al., 2012).

2.3. Ultrasonic measurements

To find the diagonal elements of the stiffness matrix, the velocities of compressional and shear waves need to be determined. Two mountings, one for compressional waves and the other for shear waves, were used. For both compressional and shear waves, we assumed a non-dispersive medium and we determined the wave velocity propagating in the x_i direction using a comparison method:

$$V_{ij} = \frac{l_{sample\_i}}{-\Delta t + \frac{l_{ref}}{V_{ref}}}$$

- V_{ij} : compressional ($i=j$) or shear ($i \neq j$) wave velocity;
- l_{sample_i} : thickness of the sample in direction x_i;
- Δt: time delay between the first arriving signal traveling in the reference medium and the first arriving signal propagating through the bone sample;
- l_{ref}: distance between the two transducers in the reference medium;
- V_{ref}: ultrasonic wave velocity in the reference medium.

2.3.1. Compressional wave velocity measurement

The ultrasonic bench consisted of two transducers (VP1093, center frequency 5 MHz, CTS Valpey Corporation, Hopkinton, MA) facing each other with their axes aligned and operating in transmission mode. The whole device was immersed in water. First, a reference measurement was made in water without samples (V_{ref}). The bone sample to be tested was then placed over a gelatin block (agar) to keep it aligned between the transducers (Fig. 2).

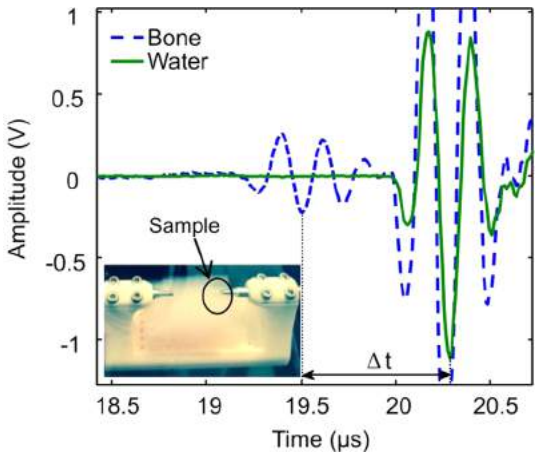

Fig. 2 – Picture of the experimental set-up (left), and example of a reference signal (water) and ultrasonic wave through the bone sample.

The entire protocol was validated on bovine bone samples. We obtained $V_{11}=3375\pm65$ m/s, $V_{22}=3637\pm91$ m/s and $V_{33}=3999\pm31$ m/s, in agreement with the literature (Lees et al., 1979; Lipson and Katz, 1984; Lasaygues and Pithioux, 2002).

2.3.2. Shear wave velocity measurement

Measurements were made with two transverse wave transducers (Panametrics V156, 5 MHz, Inc., Waltham, MA) facing each other with their axes aligned and operating in transmission mode. First, a reference measurement was made in a 5 mm thick aluminum sample. The bone samples to be tested were then placed in contact between the transducers (Fig. 3).

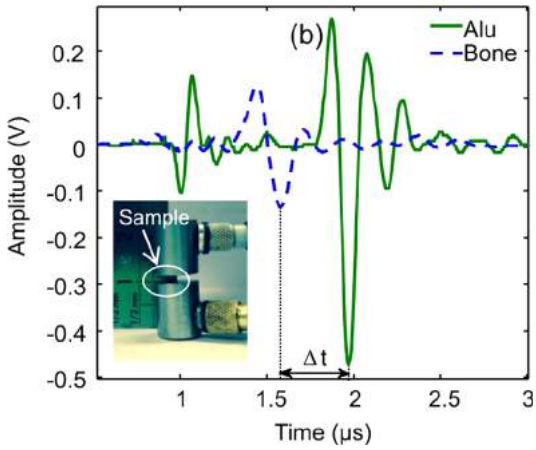

Fig. 3 – Picture of the experimental set-up (left), and example of a reference signal (aluminum sample) and ultrasonic wave through the bone sample.

2.4. *Statistical analysis*

Statistical analysis was performed using the SPSS program (SPSS Statistics 22, IBM, USA). The Shapiro–Wilk test was used to evaluate the normality of the distribution. A Pearson correlation was performed for normal distribution and a Spearman correlation was performed for non-normal distribution. The significance level is $p<0.05$. The Wilcoxon rank-sum test was used to determine the difference between coefficients.

3. Results

Raw data are presented. All the values of ultrasonic wave velocities are presented in Table 1, with mean and standard deviation for each group. The relationships established above between the velocities and the stiffness coefficients of the material gave the C_{ii} coefficients summarized in Table 2. The mean values of elastic coefficients from our study are also compared with values from the literature (Table 2).

The elastic coefficients for adult fibulae are quite similar to those from the literature for femur and tibiae evaluated with ultrasonic methods (Ashman et al., 1984; Hoffmeister et al., 2000). Values from the children's bone, especially the femur, are lower than those from the adults. Due to the mean age gap of the two groups (resp. 12.9±3.3 years.o for fibula and 3.6±5.3 y.o for femur), we cannot compare fibula and femur values in these children. A significant correlation was found in the children's bone between all the stiffness coefficients and age ($R>0.56$, $p<0.01$). Moreover, the stiffness coefficients are all correlated ($R>0.55$, $p<0.01$). In the elderly adult bone, we only found a negative correlation between C_{33} and age ($R=-0.63$, $p<0.01$).

No significant difference was found between C_{11} and C_{22} and between C_{44} and C_{55}, for either adult or child bone ($p>0.5$), which confirms transverse isotropy with $C_{33}>C_{22}=C_{11}>C_{44}=C_{55}>C_{66}$. In both groups, we found no correlation between age and anisotropy ratios.

Fig. 4 shows the evolution of stiffness coefficients with age, revealing that stiffness coefficients increase in growing bone. Moreover, the effect of main direction is observed, with the axial stiffness coefficient (C_{33}) 1/3 above radial and tangential values (respectively C_{11} and C_{22}).

Fig. 5 illustrates the evolution of the axial stiffness coefficient (C_{33}) with age. Depending on age range, the linear interpolation slope changes from positive to negative. A Spearman correlation was found between age and C_{33}; in the children's bone, we obtained a positive value ($R=0.694$, $p<0.01$) whereas in the elderly adult bone, we obtained a negative value ($R=-0.634$, $p=0.08$).

Fig. 6 represents the evolution of anisotropy ratios with age. In both groups, we found no correlation between age and anisotropy ratios.

4. Discussion

The first aim of the study was to determine and to compare stiffness coefficients in children's and elderly adults' cortical bone samples. The method we used is based on measuring both compressional and shear ultrasonic bulk wave velocities (BWV) propagating along various directions of a bone specimen (Lang, 1969). While this method is widely used, it has major drawbacks related to specimen size and geometry. With a range frequency of 1–2.5 MHz, the specimen must typically be larger than a few millimeters (~5 mm). This is because measured wave velocities must be linked to bulk waves, which propagate when the wavelength is smaller than the dimension of the specimen (Ashman et al., 1984). In this study, samples were machined from fibulae whose cortical thickness was below 3 mm. By improving the cutting process so as to avoid any lack of parallelism, we finally obtained specimens of approximately $2\times2\times2$ mm^3. For both compressional and shear wave velocity measurements, we used a frequency of 5 MHz to achieve a wavelength greater than the typical size of bone tissue heterogeneities (<a few hundred microns) and smaller than the specimen dimensions. Another limitation of this study was that only elastic constants for the main diagonal of the stiffness tensor could be evaluated. It takes one or several 45° oblique cuts to retrieve all non-diagonal terms of the stiffness tensor, which was not technically possible with our specimen size. This prevented conversion of the elastic stiffness coefficients into engineering coefficients (Young's moduli, shear moduli and Poisson's ratios).

The longitudinal stiffness coefficients (C_{11}, C_{22} and C_{33}) generally found for adult cortical bone with the ultrasonic method range between 16.8 GPa and 31.7 GPa (Ashman et al., 1984; Bernard et al., 2013; Espinoza Orías et al., 2009; Hoffmeister et al., 2000). However, these values were for femur or tibia bone; to our knowledge, no value for the fibula is available. These results on adult fibulae therefore contribute a new batch of data and allow us to compare adults' and children's values for the same bone from the same anatomic location. The results on children's bone enrich the literature concerning the mechanical properties of children's bone. Our findings show that stiffness coefficients increase with age up to puberty, when they appear to reach adult values (Fig. 4). The evolution of C_{33} with age shows a linear regression by age group, positive in the children and negative in the adults (Fig. 5). This trend is similar to the evolution of the bone

Table 1 – Ultrasonic wave velocities (compressional and shear) for all directions.

Samples	Age (years)	Mass density (kg/m$^{3)}$	V_{11} (m/s)	V_{22} (m/s)	V_{33} (m/s)	V_{31} (m/s)	V_{32} (m/s)	V_{13} (m/s)	V_{12} (m/s)	V_{23} (m/s)	V_{21} (m/s)
fibula 1	6	1873	2924	2912	3632	1506	1553	1446	1279	1535	1340
fibula 2*	10	1864	2972	2537	3596	1603	1701	1525	1306	1598	1378
fibula 3	10	1398	2406	2449	2920	1309	1347	1435	1339	1248	1460
fibula 4	10	1768	3170	3137	3994	1621	1608	1628	1354	1613	1379
fibula 5	10	1690	3181	2836	3358	1462	1409	1459	1361	1501	1202
fibula 6	12	1735	3033	3069	3873	1615	1591	1549	1355	1547	1431
fibula 7	13	1664	3053	3155	3491	1351	1514	1471	1319	1526	1243
fibula 8	14	1598	3194	2728	3320	1314	1348	1462	1165	1280	1199
fibula 9	14	1790	3228	3031	3964	1520	1616	1352	1478	1444	1269
fibula 10	15	1848	2985	3183	3918	1608	1599	1628	1369	1664	1295
fibula 11	15	1798	3099	3166	3666	1548	1551	1540	1347	1584	1365
fibula 12	16	1882	3199	3100	4057	1662	1612	1737	1436	1557	1329
fibula 13	17	1617	3455	3566	4012	1525	1616	1583	1364	1666	1396
fibula 14	18	1764	3071	3103	3918	1641	1684	1489	1440	1651	1351
Mean	**12.9**	**1734**	**2930**	**2903**	**1466**	**1507**	**1475**	**1324**	**1500**	**1303**	**1466**
SD	**3.3**	**182**	**292**	**279**	**132**	**121**	**120**	**99**	**116**	**89**	**132**
femur 1	1	1498	2491	2532	2960	1307	1362	1343	1272	1440	1383
femur 2	1	1712	2791	2798	3146	1287	1494	1404	1113	1464	1224
femur 3	1	1365	2515	2616	3206	1314	1319	1217	1209	1393	1250
femur 4	1	1873	2751	2858	3132	1403	1479	1314	1213	1505	1255
femur 5	1	1688	2678	2654	3287	1398	1383	1375	1220	1400	1154
femur 6	5	1798	2892	2658	3642	1298	1341	1477	1475	1378	1147
femur 7	15	2197	2439	2883	3613	1500	1520	1552	1397	1503	1315
Mean	**3.57**	**1733**	**2651**	**2714**	**3284**	**1358**	**1414**	**1383**	**1271**	**1440**	**1247**
SD	**5.26**	**268**	**172**	**133**	**255**	**79**	**81**	**109**	**124**	**52**	**84**
Adult 1	67	1748	4258	3190	3382	1599	1707	1645	1385	1618	1399
Adult 2	80	1761	4028	3390	3556	1586	1626	1636	1454	1621	1431
Adult 3	95	1623	3862	2672	3465	1728	1684	1676	1298	1545	1344
Adult 4	68	1664	4402	3367	3514	1727	1732	1679	1426	1705	1421
Adult 5	87	1573	3770	2755	2195	2218	1680	1464	1238	1550	1507
Adult 6	83	1798	3818	3412	3169	1575	1658	1690	1386	1600	1412
Adult 7	78	1647	3965	3248	2442	1699	1564	1684	1609	1579	1490
Adult 8	73	1831	3819	3051	2014	1840	1667	1598	1234	1675	1532
Adult 9	73	1855	4011	3332	3375	1660	1627	1661	1394	1662	1404
Adult 10	77	2230	3830	3020	3128	1473	1492	1728	1788	1476	1359
Adult 11	89	1577	3867	3299	3280	1620	1637	1582	1374	1679	1346
Adult 12	50	1775	4071	3414	3508	1645	1713	1714	1398	1691	1381
Adult 13	76	1882	4192	3016	3447	1529	1720	1665	1464	1669	1497
Adult 14	56	1914	4093	3206	3454	1583	1693	1472	1439	1718	1635
Adult 15	91	1498	3906	3166	3068	1368	1602	1617	1434	1559	1328
Adult 16	57	1623	4015	3250	3191	1504	1675	1653	1502	1575	1398
Mean	**76.2**	**1750**	**3174**	**3137**	**3994**	**1647**	**1655**	**1635**	**1426**	**1620**	**1430**
SD	**13.5**	**177**	**223**	**486**	**178**	**189**	**63**	**76**	**134**	**69**	**82**

* Mean value of two fibulae samples from the same child.

Table 2 – Average stiffness coefficients (SD).

	Children ($n=14$)	Children ($n=7$)	Adults ($n=16$)	Hoffmeister et al. (2000)	Ashman et al. (1984)
	fibula (GPa)	femur (GPa)	fibula (GPa)	tibia (GPa)	femur (GPa)
C_{11}	16.5 (2.70)	12.2 (2.42)	17.7 (2.89)	19.5 (2.0)	18.0 (1.60)
C_{22}	15.8 (3.24)	12.9 (3.15)	17.7 (5.27)	20.1 (1.9)	20.2 (1.79)
C_{33}	24.0 (5.15)	19.0 (5.50)	28.0 (3.71)	30.9 (2.1)	27.6 (1.74)
C_{44}	4.17 (0.800)	3.57 (0.833)	4.69 (0.518)	5.72 (0.49)	6.23 (0.479)
C_{55}	4.05 (0.746)	3.31 (0.921)	4.72 (0.579)	5.17 (0.57)	5.61 (0.398)
C_{66}	3.13 (0.373)	2.77 (0.656)	3.60 (0.690)	4.05 (0.54)	4.52 (0.371)

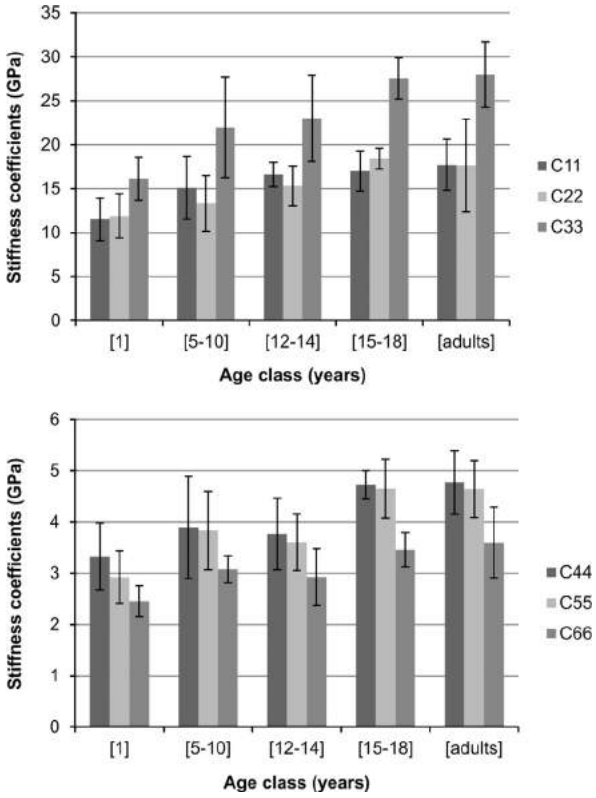

Fig. 4 – Comparison of the mean (± standard deviation) of the stiffness coefficients with age class.

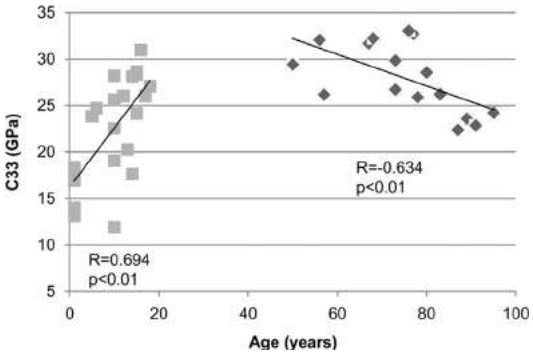

Fig. 5 – Axial stiffness coefficient measured on children's bone samples (squares) and elderly adults' bone samples (diamonds).

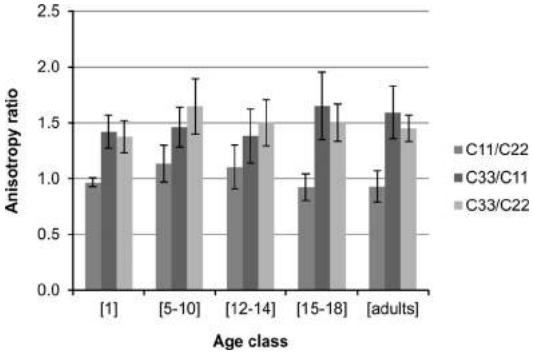

Fig. 6 – Representation of the mean (± standard deviation) of anisotropy ratios by age class.

mineral density with age (Bonjour, 1998; Boot et al., 2010). An *in vivo* study by Drozdzowska and Pluskiewicz (2003) assessed the speed of sound (SOS) at the hand phalanx in a population of people aged from 7 to 80. The authors conclude that the SOS increases linearly to a maximum reached at around 25–30 years old, after which values decrease more slowly up to the age of 80. These data differ from ours because the *in vivo* approach introduces the effect of soft tissue and bone geometry. Moreover, the study was performed on the hand phalanx, which is not mechanically stressed. Nevertheless, even with the gap in age coverage between our studies (our population being children of 1–18 and adults of 50–95), our *in vitro* results exhibit the same trend as their *in vivo* study.

The second aim of this study was to analyze the anisotropic behavior of our samples. The results for all specimens show transverse isotropy for both adult and child bone, and both fibula and femur, at the location tested. Several studies point to the fact that ultrasonic wave velocity measurement relies on anatomical location. It has been suggested that ultrasonic wave velocity depends on the circumferential location (Bensamoun et al., 2004; Rho, 1996). Rudy et al. (2011) showed that anisotropy depends on the location along the bone: their tissue specimens, pooled from multiple donors, exhibited orthotropy at all locations along the femoral diaphysis and transverse isotropy at mid-diaphysis. In this study, samples were extracted from the lower 1/3 of the bone, which does not explain the transverse isotropy.

Anisotropy in cortical bone can be explained by multiple factors. Bone material properties depend on microscopic-scale components such as hydroxyapatite crystals and collagen (Hasegawa et al., 1994; Burr, 2002; Currey, 2003; Follet, 2004; Boivin et al., 2008), and their layout, as confirmed experimentally in a study showing that ultrasonic velocity is influenced by changes in organic matrix (Mehta et al., 1998). Katz et al. (1984) argued that orthotropic *versus* transversely isotropic symmetry was dependent on whether the tissue exhibited a predominately laminar or Haversian microstructure, respectively. According to Baumann et al. (2012), transverse isotropy is governed primarily by apatite crystal orientations while orthotropy is governed primarily by intracortical porosity. While our study did not investigate any of these factors, further exploration would enrich our knowledge of the anisotropy of bone.

In conclusion, this study contributes a new set of ultrasonic wave velocities and elasticity values for children's cortical bone, providing insights into the evolution of stiffness coefficients with age. Moreover, it offers the first complete analysis of stiffness coefficients in the three orthogonal bone axes in children, giving some indication of how bone anisotropy is related to age. Future perspectives include studying the effect of the structure and composition of bone on its mechanical behavior.

Acknowledgments

This research is supported by the French National Research Agency (ANR MALICE Program, under Grant no. BS09-032). We thank the Timone Hospital surgery team and the donors or their legal guardians who gave informed written consent to

providing their tissues for investigation, in accordance with the French Code of Public Health (Code de la Santé Publique Française) and approved by the Committee for the Protection of Persons. This work has benefited from the help of Marine LOUBET for the setting up of experiments. We thank Marjorie SWEETKO for English language revision.

REFERENCES

Agnew, A.M., Moorhouse, K., Kang, Y.-S., Donnelly, B.R., Pfefferle, K., Manning, A.X., Litsky, A.S., Herriott, R., Abdel-Rasoul, M., Bolte, J.H., 2013. The response of pediatric ribs to quasi-static loading: mechanical properties and microstructure. Ann. Biomed. Eng. 41, 2501–2514, http://dx.doi.org/10.1007/s10439-013-0875-6.

Albert, C.I., Jameson, J., Harris, G., 2013a. Design and validation of bending test method for characterization of miniature pediatric cortical bone specimens. Proc. Inst. Mech. Eng. 227, 105–113.

Albert, C., Jameson, J., Smith, P., Harris, G., 2014. Reduced diaphyseal strength associated with high intracortical vascular porosity within long bones of children with osteogenesis imperfecta. Bone 66, 121–130, http://dx.doi.org/10.1016/j.bone.2014.05.022.

Albert, C., Jameson, J., Toth, J.M., Smith, P., Harris, G., 2013b. Bone properties by nanoindentation in mild and severe osteogenesis imperfecta. Clin. Biomech. 28, 110–116, http://dx.doi.org/10.1016/j.clinbiomech.2012.10.003.

Ashman, R.B., Cowin, S.C., Van Buskirk, W.C., Rice, J.C., 1984. A continuous wave technique for the measurement of the elastic properties of cortical bone. J. Biomech. 17, 349–361, http://dx.doi.org/10.1016/0021-9290(84)90029-0.

Baumann, A.P., Deuerling, J.M., Rudy, D.J., Niebur, G.L., Roeder, R. K., 2012. The relative influence of apatite crystal orientations and intracortical porosity on the elastic anisotropy of human cortical bone. J. Biomech. 45, 2743–2749, http://dx.doi.org/10.1016/j.jbiomech.2012.09.011.

Bensamoun, S., Ho Ba Tho, M.-C., Luu, S., Gherbezza, J.-M., de Belleval, J.-F, 2004. Spatial distribution of acoustic and elastic properties of human femoral cortical bone. J. Biomech 37, 503–510, http://dx.doi.org/10.1016/j.jbiomech.2003.09.013.

Bernard, S., Grimal, Q., Laugier, P., 2013. Accurate measurement of cortical bone elasticity tensor with resonant ultrasound spectroscopy. J. Mech. Behav. Biomed. Mater. http://dxdoi.org/10.1016/j.jmbbm.2012.09.017.

Berteau, J.-P., Baron, C., Pithioux, M., Launay, F., Chabrand, P., Lasaygues, P., 2013. *In vitro* ultrasonic and mechanic characterization of the modulus of elasticity of children cortical bone. Ultrasonics http://dxdoi.org/10.1016/j.ultras.2013.09.014.

Berteau, J.-P., Pithioux, M., Follet, H., Guivier-Curien, C., Lasaygues, P., Chabrand, P., 2012. Computed tomography, histological and ultrasonic measurements of adolescent scoliotic rib hump geometrical and material properties. J. Biomech. 45, 2467–2471, http://dx.doi.org/10.1016/j.jbiomech.2012.07.002.

Boivin, G., Bala, Y., Doublier, A., Farlay, D., Ste-Marie, L.G., Meunier, P.J., Delmas, P.D., 2008. The role of mineralization and organic matrix in the microhardness of bone tissue from controls and osteoporotic patients. Bone 43, 532–538, http://dx.doi.org/10.1016/j.bone.2008.05.024.

Bonjour, J.P., 1998. Delayed puberty and peak bone mass. Eur. J. Endocrinol. 139, 257–259, http://dx.doi.org/10.1530/eje.0.1390257.

Boot, A.M., de Ridder, M.A.J., van der Sluis, I.M., van Slobbe, I., Krenning, E.P., Keizer-Schrama, S.M.P.F., de, M., 2010. Peak bone mineral density, lean body mass and fractures. Bone 46, 336–341, http://dx.doi.org/10.1016/j.bone.2009.10.003.

Burr, D.B., 2002. The contribution of the organic matrix to bone's material properties. Bone 31, 8–11.

Choi, K., Kuhn, J.L., Ciarelli, M.J., Goldstein, S.A., 1990. The elastic moduli of human subchondral, trabecular, and cortical bone tissue and the size-dependency of cortical bone modulus. J. Biomech. 23, 1103–1113.

Cuppone, M., Seedhom, B.B., Berry, E., Ostell, A.E., 2004. The longitudinal Young's modulus of cortical bone in the midshaft of human femur and its correlation with CT scanning data. Calcif. Tissue Int. 74, 302–309, http://dx.doi.org/10.1007/s00223-002-2123-1.

Currey, J.D., 2003. Role of collagen and other organics in the mechanical properties of bone. Osteoporos. Int. 14, 29–36, http://dx.doi.org/10.1007/s00198-003-1470-8.

Currey, J.D., Butler, G., 1975. The mechanical properties of bone tissue in children. J. Bone Jt. Surg. Am. 57, 810–814.

Davis, M.T., Loyd, A.M., Shen, H.H., Mulroy, M.H., Nightingale, R. W., Myers, B.S., Bass, C.D., 2012. The mechanical and morphological properties of 6 year-old cranial bone. J. Biomech 45, 2493–2498, http://dx.doi.org/10.1016/j.jbiomech.2012.07.001.

Drozdzowska, B., Pluskiewicz, W., 2003. Skeletal status in males aged 7–80 years assessed by quantitative ultrasound at the hand phalanges. Osteoporos. Int. 14, 295–300, http://dx.doi.org/10.1007/s00198-002-1355-2.

Espinoza Orías, A.A., Deuerling, J.M., Landrigan, M.D., Renaud, J. E., Roeder, R.K., 2009. Anatomic variation in the elastic anisotropy of cortical bone tissue in the human femur. J. Mech. Behav. Biomed. Mater. 2, 255–263, http://dx.doi.org/10.1016/j.jmbbm.2008.08.005.

Fan, Z., Smith, P.A., Eckstein, E.C., Harris, G.F., 2006. Mechanical properties of OI type III bone tissue measured by nanoindentation. J. Biomed. Mater. Res. A 79A, 71–77, http://dx.doi.org/10.1002/jbm.a.30713.

Follet, H., 2004. The degree of mineralization is a determinant of bone strength: a study on human calcanei. Bone 34783–789 http://dxdoi.org/10.1016/j.bone.2003.12.012.

Grimal, Q., Haupert, S., Mitton, D., Vastel, L., Laugier, P., 2009. Assessment of cortical bone elasticity and strength: mechanical testing and ultrasound provide complementary data. Med. Eng. Phys. 31, 1140–1147, http://dx.doi.org/10.1016/j.medengphy.2009.07.011.

Haïat, G., Naili, S., Grimal, Q., Talmant, M., Desceliers, C., Soize, C., 2009. Influence of a gradient of material properties on ultrasonic wave propagation in cortical bone: application to axial transmission. J. Acoust. Soc. Am. 125, 4043–4052, http://dx.doi.org/10.1121/1.3117445.

Hasegawa, K., Turner, C.H., Burr, D.B., 1994. Contribution of collagen and mineral to the elastic anisotropy of bone. Calcif. Tissue Int. 55, 381–386, http://dx.doi.org/10.1007/BF00299319.

Ho Ba Tho, M.-C., Rho, J.Y., Ashman, R.B., 1991. Atlas of mechanical properties of human cortical and cancellous bone. J. Biomech. 25, 669.

Hoffmeister, B.K., Smith, S.R., Handley, S.M., Rho, J.Y., 2000. Anisotropy of Young's modulus of human tibial cortical bone. Med. Biol. Eng. Comput. 38, 333–338.

Imbert, L., Aurégan, J.-C., Pernelle, K., Hoc, T., 2014. Mechanical and mineral properties of osteogenesis imperfecta human bones at the tissue level. Bone 65, 18–24, http://dx.doi.org/10.1016/j.bone.2014.04.030.

Jans, G., Van Audekercke, R., Sloten, J.V., Gobin, R., Van der Perre, G., Mommaerts, M.Y., 1998. P020 Bending properties of cranial bone segments of new-born children. J. Biomech. 31 (Supplement 1), S65, http://dx.doi.org/10.1016/S0021-9290(98)80132-2.

Katz, J.L., Yoon, H.S., Lipson, S., Maharidge, R., Meunier, A., Christel, P., 1984. The effects of remodeling on the elastic properties of bone. Calcif. Tissue Int. 36 (Suppl 1), S31–S36.

Keller, T.S., Mao, Z., Spengler, D.M., 1990. Young's modulus, bending strength, and tissue physical properties of human compact bone. J. Orthop. Res. 8, 592–603, http://dx.doi.org/10.1002/jor.1100080416.

Lang, S.B., 1969. Elastic coefficients of animal bone. Science 165, 287–288.

Lasaygues, P., Pithioux, M., 2002. Ultrasonic characterization of orthotropic elastic bovine bones. Ultrasonics 39, 567–573, http://dx.doi.org/10.1016/S0041-624X(02)00261-5.

Lees, S., Heeley, J.D., Cleary, P.F., 1979. A study of some properties of a sample of bovine cortical bone using ultrasound. Calcif. Tissue Int. 29, 107–117.

Lipson, S.F., Katz, J.L., 1984. The relationship between elastic properties and microstructure of bovine cortical bone. J. Biomech. 17, 231–240.

Lotz, J.C., Gerhart, T.N., Hayes, W.C., 1991. Mechanical properties of metaphyseal bone in the proximal femur. J. Biomech. 24, 317–329, http://dx.doi.org/10.1016/0021-9290(91)90350-V.

McPherson, G.K., Kriewall, T.J., 1980. Fetal head molding: an investigation utilizing a finite element model of the fetal parietal bone. J. Biomech. 13, 17–26, http://dx.doi.org/10.1016/0021-9290(80)90004-4.

McPherson, S.B.I., Copley, L.A.B., Niemann, J.J., Lankachandra, K., Williams, J.L., 2007. Biomechanical evaluation of fetal calf skull as a model for testing halo-pin designs for use in children. J. Biomech. 40, 1137–1144, http://dx.doi.org/10.1016/j.jbiomech.2006.05.003.

Mehta, S.S., Oz, O.K., Antich, P.P., 1998. Bone elasticity and ultrasound velocity are affected by subtle changes in the organic matrix. J. Bone Miner. Res. 13, 114–121, http://dx.doi.org/10.1359/jbmr.1998.13.1.114.

Neil Dong, X., Edward Guo, X., 2004. The dependence of transversely isotropic elasticity of human femoral cortical bone on porosity. J. Biomech. 37, 1281–1287, http://dx.doi.org/10.1016/j.jbiomech.2003.12.011.

Ohman, C., Baleani, M., Pani, C., Taddei, F., Alberghini, M., Viceconti, M., Manfrini, M., 2011. Compressive behaviour of child and adult cortical bone. Bone 49, 769–776, http://dx.doi.org/10.1016/j.bone.2011.06.035.

Reilly, D.T., Burstein, A.H., 1975. The elastic and ultimate properties of compact bone tissue. J. Biomech. 8, 393–405, http://dx.doi.org/10.1016/0021-9290(75)90075-5.

Reilly, D.T., Burstein, A.H., Frankel, V.H., 1974. The elastic modulus for bone. J. Biomech. 7, 271–275, http://dx.doi.org/10.1016/0021-9290(74)90018-9.

Rho, J.-Y., 1996. An ultrasonic method for measuring the elastic properties of human tibial cortical and cancellous bone. Ultrasonics 34, 777–783, http://dx.doi.org/10.1016/S0041-624X(96)00078-9.

Rudy, D.J., Deuerling, J.M., Espinoza Orías, A.A., Roeder, R.K., 2011. Anatomic variation in the elastic inhomogeneity and anisotropy of human femoral cortical bone tissue is consistent across multiple donors. J. Biomech. 44, 1817–1820, http://dx.doi.org/10.1016/j.jbiomech.2011.04.009.

Smith, C.B., Smith, D.A., 1976. Relations between age, mineral density and mechanical properties of human femoral compacta. Acta Orthop. 47, 496–502.

Weber, M., Roschger, P., Fratzl-Zelman, N., Schöberl, T., Rauch, F., Glorieux, F.H., Fratzl, P., Klaushofer, K., 2006. Pamidronate does not adversely affect bone intrinsic material properties in children with osteogenesis imperfecta. Bone 39, 616–622, http://dx.doi.org/10.1016/j.bone.2006.02.071.

Yoon, H.S., Katz, L.J., 1976. Ultrasonic wave propagation in human cortical bone—II. Measurements of elastic properties and microhardness. J. Biomech. 9, 459–464, http://dx.doi.org/10.1016/0021-9290(76)90089-0.

Zioupos, P., Currey, J.., 1998. Changes in the stiffness, strength, and toughness of human cortical bone with age. Bone 22, 57–66, http://dx.doi.org/10.1016/S8756-3282(97)00228-7.

4.7 JMBBM 2016

Journal of the Mechanical Behavior of Biomedical Materials, 2016

Pore Network Microarchitecture Influences Human Cortical Bone Elasticity During Growth and Aging.
Y. Bala, E. Lefèvre, J-P. Roux, C. Baron, P. Lasaygues, M. Pithioux, V.Kaftandjian, H. Follet.
JMBBM 63, 164-173.

JOURNAL OF THE MECHANICAL BEHAVIOR OF BIOMEDICAL MATERIALS 63 (2016) 164–173

Available online at www.sciencedirect.com

ScienceDirect

www.elsevier.com/locate/jmbbm

Research Paper

Pore network microarchitecture influences human cortical bone elasticity during growth and aging

Yohann Bala[a,b,*], Emmanuelle Lefèvre[c,d], Jean-Paul Roux[b], Cécile Baron[c,d], Philippe Lasaygues[e], Martine Pithioux[c,d], Valérie Kaftandjian[a], Hélène Follet[b]

[a]Laboratoire Vibrations Acoustique, INSA Lyon, Campus LyonTech la Doua, 69621 Villeurbanne Cedex, France
[b]INSERM UMR 1033, Université de Lyon, 69372 Lyon Cedex 08, France
[c]Aix-Marseille University, CNRS, ISM UMR 7287, 13009 Marseille, France
[d]APHM, Institute for Locomotion, Sainte-Marguerite Hospital, 13009 Marseille, France
[e]Laboratory of Mechanics and Acoustics, UPR CNRS 7051, Aix-Marseille University, Centrale Marseille, 13009 Marseille, France

ARTICLE INFO

Article history:
Received 15 October 2015
Received in revised form
11 May 2016
Accepted 12 May 2016
Available online 22 June 2016

Keywords:
Aging
Bone microarchitecture
Bone microstructure
Cortical porosity
Growth

ABSTRACT

Cortical porosity is a major determinant of bone strength. Haversian and Volkmann's canals are'seen' as pores in 2D cross-section but fashion a dynamic network of interconnected channels in 3D, a quantifiable footprint of intracortical remodeling. Given the changes in bone remodeling across life, we hypothesized that the 3D microarchitecture of the cortical pore network influences its stiffness during growth and ageing.

Cubes of cortical bone of 2 mm side-length were harvested in the distal 1/3 of the fibula in 13 growing children (mean age ± SD: 13 ± 4 yrs) and 16 adults (age: 75 ± 13 yrs). The cubes were imaged using desktop micro-CT (8.14 μm isotropic voxel size). Pores were segmented as a solid to assess pore volume fraction, number, diameter, separation, connectivity and structure model index. Elastic coefficients were derived from measurements of ultrasonic bulk compression and shear wave velocities and apparent mass density.

The pore volume fraction did not significantly differ between children and adults but originates from different microarchitectural patterns. Compared to children, adults had 42% ($p=0.033$) higher pore number that were more connected (Connective Density: +205%, $p=0.001$) with a 18% ($p=0.007$) lower pore separation. After accounting for the contribution of pore volume fraction, axial elasticity in traction-compression mode was significantly correlated with better connectivity in growing children and with pore separation among adults.

The changes in intracortical remodeling across life alter the distribution, size and connectedness of the channels from which cortical void fraction originates. These alterations in pore network microarchitecture participate in changes in compressive and shear mechanical behavior, partly in a porosity-independent manner. The assessment of pore volume fraction (i.e., porosity) provides only a limited understanding of the role of cortical void volume fraction in its mechanical properties.

*Corresponding author at: INSERM UMR_S 1033, 7-11 Rue Guillaume Paradin, 69372 Lyon Cedex 08, France.
E-mail address: yohannbala@gmail.com (Y. Bala).

http://dx.doi.org/10.1016/j.jmbbm.2016.05.018
1751-6161/

1. Introduction

Human cortical bone displays a multiscale porous architecture originating from optimization to contradictory needs. Bone has to be stiff and strong to resist loading but light to allow mobility (Bala et al., 2015; Seeman and Delmas, 2006). During last decade, cortical porosity has emerged as a major predictor of bone strength (Baron et al., 2007; McCalden et al., 1993) and fragility fracture (Bala et al., 2014b, 2015; Bjornerem et al., 2013). The cortical void volume fraction contributes to bone mechanical behavior because the apparent density (inverse of porosity) is inversely proportional to the 7th power of its stiffness (Schaffler and Burr, 1988).

Cortical bone void volume originates from Haversian and Volkmann's canals that contain bone vasculature and innervation. While these canals are 'seen' as pores in cross-section images (Chappard et al., 2013; Thomas et al., 2006), they form a three dimensional network of interconnected canals (Chappard et al., 2013; Cooper et al., 2007). The structure of this porous network is not static; the number of canals, their diameter, and their connectedness are the quantifiable footprints of the bone remodeling activity and balance (Cooper et al., 2007).

During growth, the skeleton adapts its size, shape and material properties to be of sufficient strength to support the evolving physical activity (Currey and Butler, 1975; Jee and Frost, 1992; Loro et al., 2000; Palacio-Mancheno et al., 2014; Parfitt et al., 2000). Histomorphometric studies highlighted that this adaptation was made possible through changes in modeling and remodeling activity and its balance at both the tissue and the Bone Multicellular Unit (BMU) level (Parfitt et al., 2000; Rauch et al., 2007). For instance, from 2 to 20 years, the thickening of the cortex is determined by a net positive balance at the tissue level between endocortical resorption and periosteal formation (Rauch et al., 2007). In this age range, intracortical remodeling activation frequency decreases and displays a ~5% positive balance at BMU level reducing intracortical porosity and participating to bone consolidation (Parfitt, 1994b, Parfitt et al., 2000).

During young adulthood, remodeling is slow and in steady-state at the tissue-level - the number of Bone Multicellular Units (BMU) resorbing bone equals the number of BMU refilling cavities excavated earlier at other locations. At the level of the BMU, remodeling is balanced – each BMU resorbs and deposits similar volumes of bone matrix. At this stage there is little or no bone loss or structural decay in cortical bone (Bala et al., 2014a; Compston, 2011). After midlife in women and later in men, a rapid extent of remodeling surfaces at the tissue level coupled to a ~5% negative balance at the BMU level, increases pore number and diameter resulting in an overall higher cortical void volume fraction and permanent bone loss (Bjornerem et al., 2011; Lips et al., 1978; Qiu et al., 2010; Recker et al., 2004; Vedi et al., 1983). This has been repeatedly observed using 2D histomorphometry (Lips et al., 1978; Rauch et al., 2007; Schnitzler, 2015; Schnitzler and Mesquita, 2013; Schnitzler et al., 2009; Zebaze et al., 2010). However, the structural changes in pore network 3D microarchitecture beyond these alterations in the void volume fraction are not known.

Recent studies suggest that porosity achieved during growth may influence intracortical remodeling and structural decay later in life (Bala et al., 2014b; Bjornerem et al., 2013; Bui et al., 2013; Loro et al., 2000; Seeman, 2008). Haversian and Volkmann's canal density, size and connectivity in young adult defines indeed the extent of surfaces available for unbalanced remodeling to be initiated upon at the onset of age-related perturbation at the BMU level (Bui et al., 2013). However, porosity is only regarded as a single value describing void volume fraction and may not be sufficient to predict entirely the influence of microstructure on cortical bone fragility (Chappard et al., 2013; Yeni et al., 1997; Yeni and Norman, 2000). There is most likely a contribution of age-related structural changes in pore network microarchitecture but these parameters, especially in growing bone, are rarely investigated.

Given the age related-changes in bone remodeling activity and balance across life, we hypothesized that cortical bone void volume fraction originates from canals networks with different microarchitectures in growing children and adults. This study also aimed to evaluate comprehensively the impact of the canal network microarchitecture on cortical bone elasticity. We tested these hypotheses in human cortical bone samples collected in the distal fibula of growing children and ageing adults. Pore number, diameter, connectivity and other morphological parameters of the cortical void volume were quantified using micro-CT. These variables were compared to the elasticity assessed in the same samples using ultrasonic bulk wave velocities in the three principal directions of bone. Understanding the contribution of pore volume fraction and pore network microarchitecture to bone mechanical properties during growth and ageing may help in finding early predictors of bone fragility.

2. Material and methods

2.1. Specimens

Bone samples were collected in the distal 1/3 of the fibula in 13 children (9 males and 4 females, mean age±SD: 13.2±3.5 years, range: 6–18 years) during corrective surgery after a fracture at the growth plate or equinovarus of the foot ($n=2$). Equinovarus of the foot is apparently not associated with alterations in bone remodeling parameters (Rauch et al., 2007). Surgeries were performed at the Timone Hospital (Marseille, France). All children were ambulatory prior to surgery and none received medications known to affect bone remodeling. In accordance with the French code of public health and after approbation of the study by the committee for the protection of persons, informed consents were obtained from children's legal guardians. In addition, bone samples were harvested in the distal 1/3 of the fibula from 16 human donors (7 males and 9 females, mean age±SD: 75.0±12.9 years, range: 50–91 years). Autopsies were performed between 2010 and 2012 under the guidance of the INSERM UMR-S 1033 (Lyon, France) and the IFSTTAR UMR-T 9406 (Bron, France) in order to build a bone sample bank. Samples were maintained frozen at −20 °C wrapped in Phosphate Buffer Saline soaked gauze. Twenty-nine 2x2x2

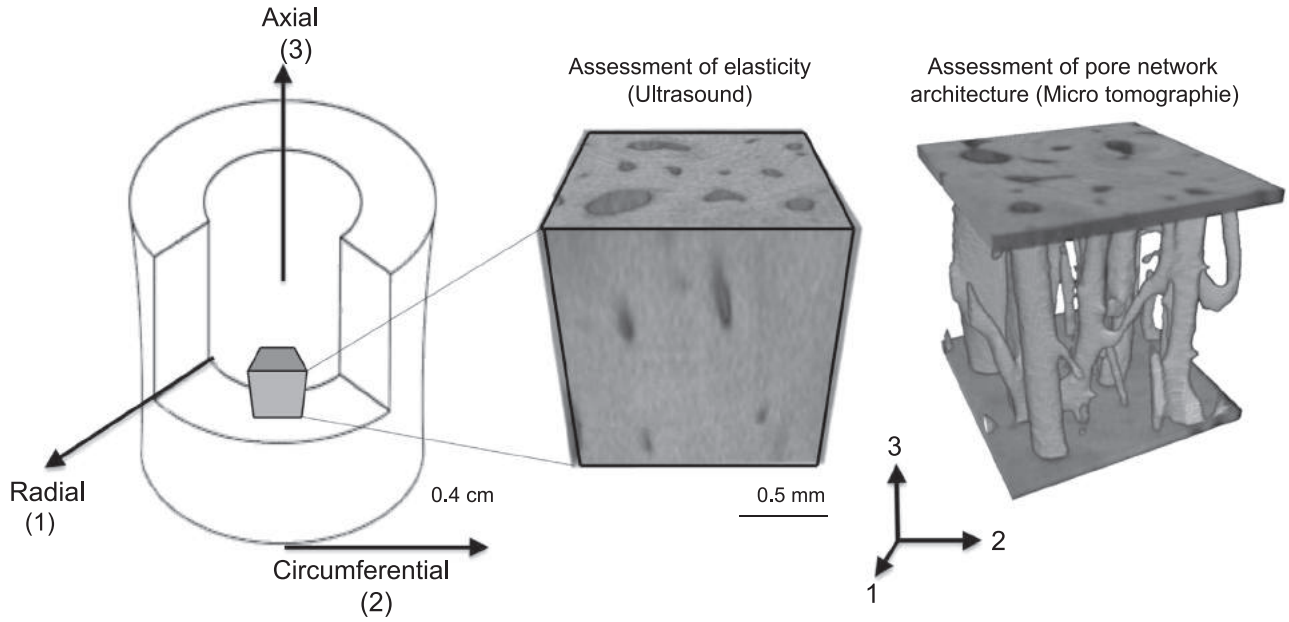

Fig. 1 – From left to right, bone cubical samples were cored from the distal fibula and oriented according to the radial (1), circumferential (2) and axial (3) axes for assessment of the elastic coefficients by ultrasound and pore network architecture using micro-CT.

mm cubic samples were extracted from the cortex using a water-cooled low speed diamond saw (Buehler Isomet 4000, Buehler, Lake Bluff, IL, USA). All cubes included the periosteal region and the 2 mm thickness permitted to avoid the highly 'trabecularized' endosteal region in samples from elderly. The regions of coring were matched by the quadrant and the fraction of bone length between children and adults. Cubes faces were identified according to the radial (axis 1), tangential (axis 2) and axial (axis 3) orientations in the fibula (Fig. 1).

2.2. *Image acquisitions*

The cubic samples were imaged using a desktop micro-CT system (Skyscan 1174, Bruker, Kontich, Belgium). Scanning was done with the bone specimen immerged in distilled water in a 6 mm inner diameter plastic tube and held in place thanks to gauze. Sample axial axis (i.e., Haversian canals' principal orientation) was aligned to the rotation axis of the sample holder. Scans were performed with a field of view of 1024 × 1024 pixels a source voltage 50 kV, current 800 μA, rotation step 0.6° over a 360° rotation and a 0.5 mm-thick aluminium filter for beam hardening reduction. An isotropic voxel size of 8.14 μm was used with an exposure time of 4 seconds, 2 frames averaging leading to a total scan time of 82 minutes for each sample. The images were reconstructed using a filtered back-projection algorithm (NRecon software, V 1.6.9, Skyscan NV, Kontich, Belgium). For each cube, a stack of 210 sections was reconstructed.

2.3. *Morphometric analysis*

From the stack of contiguous reconstructed images, the volumes of interest were selected for morphometric analysis using a semi-automated method (CTAnalyser Software V 1.14.4, Skyscan NV, Kontich, Belgium). For each specimen, the external borders were contoured by the operator and then automatically interpolated over the axial axis defining the volume of interest (VOI). Within the tissue volume (TV, mm^3), the porosity (void volumes) was segmented as a solid and the mineralized bone as a background by using global thresholding. Calibration was performed using a phantom of hydroxyapatite rods, a cut-off of 0.79 g/cm^3 was chosen after observation of several reconstructed images from samples spreading the whole age-range. The following morphometric variables were calculated: the pore volume fraction (Po.V/TV, %), the pore surface to pore volume ratio (Po.S/Po.V, 1/mm). Pore diameter (Po.Dm, μm) corresponding to the average diameter of the pores and pore separation (Po.Sp, μm) corresponding to the average separation between pores were both calculated using a sphere-fitting algorithm (Hildebrand and Ruegsegger, 1997; Ulrich et al., 1999). As an index of heterogeneity in the intra-individual distribution of pore size and separation, the standard deviation of Po.Dm and Po.Sp are reported as Po.Dm.SD and Po.Sp.SD both expressed in μm. The pore number (Po.N, 1/mm) was calculated as: Po.N=1/(Po.Sp+Po.Dm). Connectivity (ConnD, $1/mm^3$) was evaluated by the Euler characteristic according to the method detailed by Odgaard (1997) and normalized by the TV. We also assessed the pore pattern factor (Po.Pf in analogy with the trabecular pattern factor, 1/mm) calculated as the ratio of volumes and surfaces before and after dilation. Lower Po.Pf indicates higher concavity i.e., better-connected pore network.

2.4. *Ultrasound based measurement of bone elasticity*

Bone elasticity was determined using a well-established method based on the measurements of ultrasonic bulk compression and shear wave velocities and sample apparent mass density (Espinoza Orias et al., 2009; Granke et al., 2011). This method provides measurements of the elastic properties in the

Table 1 – Values of microstructural parameters of the pore network and elastic coefficients. *P*-values for group comparison were obtained using Man–Whitney's *U* test. Bold font denotes *p*-values ≤ 0.05.

	Children (5–18 yrs) Mean (SD)	Adults (50–91 yrs) Mean (SD)	P-Value
Po.V/TV (%)	10.3 (6.5)	15.9 (10.3)	0.151
Po.S/Po.V (1/mm)	40.5 (15.9)	37.7 (13.4)	0.628
Po.N (1/mm)	0.69 (0.28)	0.98 (0.29)	**0.033**
Po.Dm (μm)	139 (62)	144 (69)	0.626
Po.Dm.SD (μm)	67 (39)	67 (41)	0.953
Po.Sp (μm)	397 (58)	325 (62)	**0.007**
Po.Sp.SD (μm)	125 (22)	100 (20)	**0.010**
ConnD ($1/mm^3$)	6.6 (5.5)	20.1 (15)	**0.001**
Structure Model Index	3.2 (0.6)	2.8 (0.2)	**0.002**
Po.Pf (1/mm)	0.021 (0.007)	0.017 (0.006)	0.076
Elastic coefficients (Gpa)			
C11	16.1 (2.5)	17.9 (3.6)	**0.021**
C22	15.3 (2.5)	17.9 (6.15)	**0.045**
C33	23.6 (4.4)	28.8 (5.1)	**0.011**
C44	4.1 (0.8)	4.8 (0.6)	**0.017**
C55	4.0 (0.9)	4.9 (1.1)	**0.019**
C66	3.0 (0.4)	3.6 (1.0)	**0.017**

three principal directions of a same bone material volume. The apparent mass density (ρ, g/cm^3) was measured with a micrometric balance equipped with a density kit (Voyager 610, Ohaus Corporation, FlorhamPark, NJ, USA, measurement uncertainty of 0.001 g/cm^3) and the dimensions were measured with a digital caliper (Absolute digimatik solar, Mitutoyo, Kanagawa, Japan, measurement error of 0.03 mm). Taking into account average values of mass densities, determined during the experiments, equal to 1700 kg/m^3, we obtain a relative error of 0.06%. For Time-Of-Flight measurements, uncertainties are of around 0.02 μs, given by the laboratory test apparatus/electroacoustic device (Eurosonic, Vitrolles, France). Given the apparent density ρ, the diagonal terms $C_{ij\ (1 \leq i \leq 6)}$ of the elastic tensor are calculated from:

$$C_{ii} = \rho.v_{ii}^2 (i = 1, 2, 3)$$

$$C_{44} = \rho.v_{23}^2 = \rho.v_{32}^2$$

$$C_{55} = \rho.v_{13}^2 = \rho.v_{31}^2$$

$$C_{66} = \rho.v_{12}^2 = \rho.v_{21}^2$$

where the longitudinal elastic coefficients C_{11}, C_{22}, and C_{33} represent the stiffness in traction-compression mode, C_{44}, C_{55}, C_{66} represent the shear stiffness coefficients (Fig. 1). Velocity v_{ij} denotes velocity of a wave propagating in the i direction, with particle motion in the j direction. For compressional waves, $i=j$, and for shear waves, $i \neq j$. Compressional and shear waves velocities were measured using a pulse transmission method with a pair of 5 MHz transducers (VP1093, CTS Valpey Corporation, Hopkinton, MA, USA for compressional waves and Panametrics V156, Inc., Waltham, MA, USA for shear waves). The received signal was post-processed with a custom MatLab program (The Mathworks Inc., Natick, MA, USA) (Lefevre et al., 2015). Repeated measurements on a set of same samples revealed a good reproducibility for the stiffness with coefficient of variation ranging between 0.8% and 2.5% depending on the coefficients.

2.5. Statistics

Data are reported as mean ± SD unless otherwise stated. As our population is composed of growing children and ageing adults, all analyses were performed separately in the two groups and not on the pooled population. Statistical analyses were performed using SPPS 20.0 (IBM, Amonk, NY, USA). Normality was tested using Shapiro-Wilk procedure. Most of the variables were not normally distributed, non-parametric test were consequently used. Differences between groups were tested using Mann-Whitney U test. Bivariates correlations between morphometric variables and age were tested by the Spearman's rank correlation test (r'). Correlations between morphometric variables and elastic coefficients were calculated with or without accounting for the contribution of the pore volume fraction. A two-tailed significance level of 0.05 was used.

3. Results

3.1. Pore volume fraction originates from different microarchitectures in children and adults

The pore volume fraction (Po.V/TV) did not significantly differ between growing children and adults but originated from different microarchitectural pattern (Table 1). Relative to children, adults had a higher pore number (Po.N: +42%) and connectivity density (ConnD: +205%), a lower pore separation (Po.Sp: −18%) and intra-individual distribution of separation (Po.Sp.SD: −20%). In accordance with a higher ConnD in adults, Pore pattern factor tended to be lower in adults compared to children but the difference did not reach significance level (Po.Pf: −19%, $p=0.076$) (Table 1).

Table 2 presents the correlation coefficients obtained between the age and the parameters of the pore network microarchitecture. Among growing children, increasing age was negatively correlated with Po.V/TV. This decrease in the pore volume fraction was associated with a decrease in Po.N, Po.Dm and an increase in Po.Sp. Between 5 and 18 years old there was also a positive correlation between age and the specific surface of the pore (Po.S/Po.V). As expected, among adults, increasing age between 50 and 91 years old was correlated with higher Po.V/TV. This increase in pore volume fraction was associated with an increasing Po.N and a decreasing Po.Sp (Fig. 2).

3.2. Pore network microarchitecture contributes to cortical bone elasticity

Despite the differences in pore network microarchitecture, cortical bone from both children and adults were both transversely isotropic (with $C_{33} > C_{11} = C_{22}$ and $C_{44} = C_{55} > C_{66}$). However, relative to children all elastic coefficients were higher in adults (+11%, +17% and +22% for C_{11}, C_{22} and C_{33}, respectively,

and +17%, +23% and +20% for C_{44}, C_{55} and C_{66}, respectively) (Table 1).

Among growing children, increasing age was associated with increasing elastic coefficients in traction-compression. In adult group, increasing age was associated with lower elastic coefficients in traction-compression mode. Correlation between age and shear elastic coefficients did not reach statistical significance in both groups (except for C_{44} in adult group, $r' = -0.70$) (Table 2).

Table 3 reports the correlation coefficients obtained between the elastic coefficients and the parameters of the pore network microarchitecture. Among the children samples, the C_{33} elastic coefficient (i.e., axial traction-compression) was negatively correlated with Po.V/TV, Po.N and Po.Dm (r' from −0.46 to −0.82) and positively Po.S/Po.V, Po.Sp and Po.Pf (r' from 0.48 to 0.88). Similar results were obtained with C_{66} (transverse shear). The positive correlation between C_{33} and Po.Pf remained significant after adjustment for Po.V/TV (r'-adjusted=0.52, p=0.020). In the adult group, C_{33} was negatively correlated with Po.V/TV ($r' = -0.63$) and Po.N ($r' = -0.59$) and positively with Po.Sp ($r' = 0.71$) and Po.Sp.SD ($r' = 0.72$). No correlation was observed between C_{66} and pore network microarchitecture. When accounting for the contribution of Po.V/TV, the correlation between C_{33} and Po.Sp and Po.Sp.SD remained significant (r'-adjusted=0.56, p=0.007 and r'-adjusted=0.70, p=0.001, respectively).

Table 2 – Spearman correlation coefficients (r′) obtained between variables of the pore network architecture, elastic coefficients and age among children and adults group. Bold font denotes p-values ≤0.05.

	Children (5–18 yrs)		Adults (50–91 yrs)	
	r′	*p*-value	r′	*p*-value
Po.V / TV (%)	−0.53	**0.043**	0.50	**0.047**
Po.S / Po.V (1/mm)	0.51	**0.048**	−0.19	0.471
Po.N (1/mm)	−0.57	**0.027**	0.53	**0.035**
Po.Dm (μm)	−0.50	**0.048**	0.17	0.524
Po.Dm.SD (μm)	−0.41	0.083	0.23	0.395
Po.Sp (μm)	0.50	**0.049**	−0.77	**0.001**
Po.Sp.SD (μm)	0.58	**0.029**	−0.78	**0.001**
ConnD (1/mm^3)	−0.33	0.232	0.23	0.389
Structure Model Index	−0.15	0.590	−0.23	0.436
Po.Pf (1/mm)	0.62	**0.013**	−0.60	**0.009**
Elastic coefficients (Gpa)				
C11	0.53	**0.022**	−0.41	0.057
C22	0.67	**0.003**	−0.46	**0.038**
C33	0.44	**0.050**	−0.55	**0.014**
C44	0.15	0.292	−0.70	**0.001**
C55	0.17	0.273	−0.22	0.210
C66	0.29	0.151	−0.22	0.207

4. Discussion

To our knowledge, the present study is the first to evaluate the 3D-microarchitecture of the pore network in both children and adults in appendicular skeleton. In site- and size-matched samples of compact-appearing cortex, we report that cortical porosity originates from different canal network microarchitectures in growing children and adults. Growth was associated with a decrease in cortical void volume fraction due to a decrease in pore diameter, pore number and pore connectivity. On the opposite, in adults, ageing was associated with an increase in void volume fraction related to an increase in pore number and pore connectivity, not in pore size. Within the limitations of a small sample size that may results in low statistical power to detect statistical significance for some differences, our data support that elastic properties are influenced by pore network microarchitecture even after accounting for void volume fraction contribution, suggesting an independent contribution.

4.1. *Pore network microarchitecture during growth*

During growth, long bones increase in width by periosteal apposition (modeling formation) and endocortical resorption (modeling resorption) and in length by endochondral ossification (Cadet et al., 2003; Enlow, 1962; Rauch, 2012). At the same time, bone also undergoes Haversian remodeling to adapt to the mechanical environment and to face the increasing need in calcium (Parfitt, 1994b; Parfitt et al., 2000). Our knowledge of growth-related changes in cortical

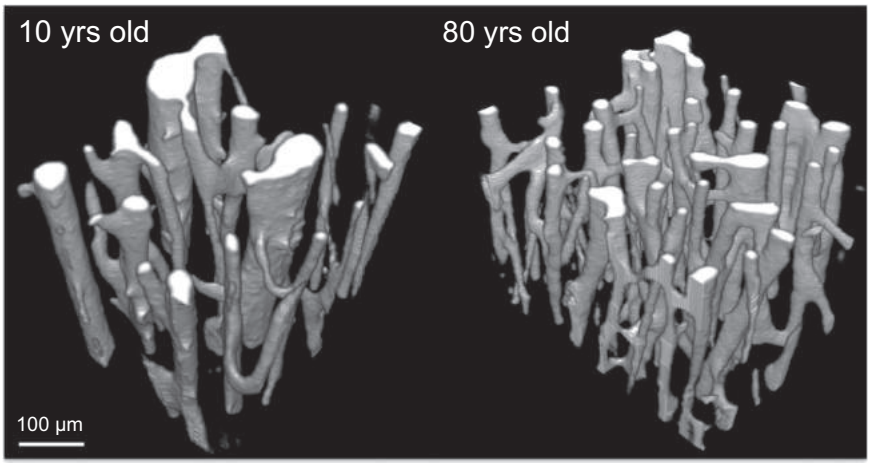

Fig. 2 – 3D reconstructions of the pore network imaged in cube of cortical bone cored in the distal part of the fibula in females.

Table 3 – Spearman correlation coefficients (r) obtained between the different variables describing the pore network microarchitecture and the elastic coefficients obtained by ultrasound in children/adults. * $p<0.05$, ** $p<0.001$, *** $p<0.0001$. a: significant correlation after controlling for the contribution of the void volume fraction (Po.V/TV).

	Elastic coefficients (GPa)											
	C11		C22		C33		C44		C55		C66	
	Children	Adults	Children	Adults	Children	Adults	Children	Adults	Children	Adults	Children	Adults
Po.V/TV (%)	−0.52*	−0.64*	−0.52*	−0.71**	−0.80***	−0.63*	−0.52*	−0.72**	−0.56*	−0.08	−0.65*	−0.13
Po.S/Po.V (1/mm)	0.40	0.69*	0.41	0.66*	0.70*	0.38	0.52*	0.56*	0.50*	0.01	0.64*	0.08
Po.N (1/mm)	−0.80*** [1]	−0.21	−0.72**,[1]	−0.36	−0.82***	−0.59*	−0.55*	−0.67*	−0.60*	−0.25	−0.61*	−0.12
Po.Dm (μm)	−0.23	−0.67*	−0.17	−0.61*	−0.46*	−0.30	−0.55*	−0.64*	−0.30	−0.15	−0.56*	−0.13
Po.Dm.SD (μm)	−0.35	−0.70*,[1]	−0.11	−0.63*	−0.10	−0.41	−0.16	−0.72**	0.02	−0.13	−0.48	−0.16
Po.Sp (μm)	0.62*,[1]	0.32	0.51*	0.50*	0.48*	0.71**,[1]	−0.05	0.70**	0.09	0.14	0.22	0.24
Po.Sp.SD (μm)	0.35	0.24	0.28	0.54*	0.07	0.72**,[1]	−0.55*	0.76**,[1]	−0.32	0.15	0.03	0.41
ConnD ($1/mm^3$)	−0.05	−0.31	−0.38	−0.59*,[1]	−0.39	−0.17	−0.06	−0.20	−0.22	0.37	−0.13	−0.07
Po.Pf (1/mm)	0.61*	0.71**	0.63*,[1]	0.67*	0.88***,[1]	0.49	0.50*	0.63*	0.62*,[1]	0.06	0.69*	−0.10

* $p<0.05$,
** $p<0.001$,
*** $p<0.0001$
[1] $p<0.05$ after controlling for the contribution of Po.V/TV

porosity has been nurtured by histomorphometric studies performed in iliac crest samples limiting comparison with present results. Most of these studies reported a high porosity in children principally originating from large asymmetrical drifting osteons (Schnitzler and Mesquita, 2013). In this set up, bone resorption not only progresses in the cutting cone forming a round and narrow canal in the matrix, but also toward the endosteal surface. In these units, the onset of bone formation appears to be delayed forming canals up to 30 times larger than common cutting cones (Robling and Stout, 1999; Schnitzler and Mesquita, 2013). Later when growth slowdowns, these asymmetrical osteons are replaced through remodeling by smaller symmetrical concentric osteons (Parfitt, 1994a; Schnitzler, 2015; Schnitzler and Mesquita, 2013).

We propose that the age-related decrease in void volume fraction we observed might also be due to the replacement of large drifting osteons by smaller symmetrical osteons. Our bone samples were not evaluated by histomorphometry. However, in the context of this study, we collected fibula samples from a 6 years old and 16 years old boys and imaged them using microradiography (Montagner et al., 2015). The resulting images supported our statement and suggested a transition from large asymmetric drifting osteons to smaller symmetric osteons during growth at the fibula (Fig. 3). Growth has been associated with an age-dependent decrease in remodeling frequency. Rauch et al. indeed highlighted a fall in the percentage of active osteons from ~70% at 5 years old to ~20% at 20 years old (Rauch et al., 2007). These mechanisms contract the remodeling space consolidating bones (Parfitt et al., 2000; Schnitzler et al., 2009).

In the present study, the consolidation of the cortical bone (*i.e.*, suggested by an increase in C_{33}) was not only associated with the decrease in porosity but also with an increase in the pore pattern factor. This suggests that in growing children, the age-related decrease in pore network connectivity also increases stiffness in axial direction. However, as observed for most of the variables describing pore network microarchitecture, correlations were stronger with the elastic coefficients corresponding to the tension-compression mode than in shear. This may indicate that shear elasticity is more sensitive to different parameters of cortical structure other than porosity or material properties. Indeed, several *ex vivo* studies show alterations of bone tissue structure and composition at the micro- and nano-scale during growth. Akkus et al. suggested that the remaining fraction of primary lamellar bone continues to mature as they observed an increase in mineral particles size and an improvement in its crystallinity between 17 and 25 years (Akkus et al., 2003). Saito et al., described also age-related changes in average collagen enzymatic cross-linking profile with a transition from the immature forms to mature ones (Saito and Marumo, 2010). All these parameters of bone quality are known determinants of bone mechanical behavior in human adults and in animal models (see (Bala and Seeman, 2015; Ural and Vashishth, 2014) for reviews). Finally, it has been shown in rats cortical bone that Young's and shear moduli derived from ultrasounds were not determined by the same physicochemical properties. For instance, shearing was influenced by crystal size while elasticity was principally determined by apparent density (Kohles and Martinez, 2000). Taken together, these results suggest that cortical shear and tensile-compressive stiffness may not be similarly sensitive to growth-related changes in microstructure and material composition.

4.2. *Pore network microarchitecture during aging*

We observed an increasing void volume fraction with age. In our experimental set up, higher pore number, not higher pore diameter, accounted for the most of the higher void volume fraction in older subjects. While this is consistent with some earlier works by Kerley (1965) for instance , this seems in contradiction with the repeated observation that most of the age-related increase in porosity can be explained by an increase in pore area, not in pore number (Cooper et al.,

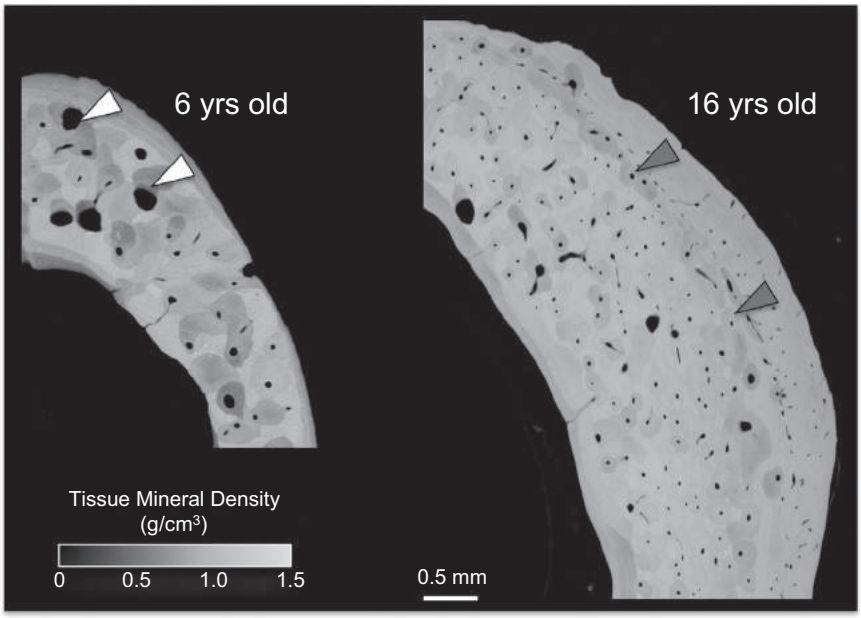

Fig. 3 – Microradiographs of fibula cortical bone cored in the same quadrant from a 6 years old (left panel) and a 16 years old (right panel) boy. White arrows highlight large asymmetric drifting osteons, dark grey arrows highlight smaller symmetric osteons.

2007; Perilli et al., 2015; Thomas et al., 2006). This apparent discrepancy may be explained by the variability in the localization of the VOIs analyzed among the studies. Indeed, the age-related changes in void volume fraction are highly heterogeneous in the bone cross-section and through the thickness of the cortex (Keshawarz and Recker, 1984; Perilli et al., 2015; Zebaze et al., 2010). A recent study by Perilli et al. reported in human subtrochanteric cortical bone that both higher pore number and size accounted for higher void volume fraction in older subject in medial and lateral regions. In the anterior region, the pore diameter, not the pore number, was higher in older subjects compared to the younger ones (Perilli et al., 2015). Across the cortical thickness, with increasing age, bone remodeling becomes particularly vigorous in the inner part of the cortex, the closest to the medullary cavity (Zebaze et al., 2013; Zebaze et al., 2010). In this region, pores not only enlarge focally because of the negative balance, but also coalesce resulting in giant pores and most likely in a local decrease in pore number. This creates a gradient in pore size from the periosteum to the endosteum (Bell et al., 1999; Bell et al., 2001; Chappard et al., 2013; Zebaze et al., 2010).

In the current study, we extruded small cubical samples of compact-appearing cortex excluding the cortico-trabecular junction with its giant pores. In our VOIs, we propose that age related increase in porosity principally originates from an increase in pore number, modestly from an increase in pore size. Indeed, the negative bone balance at the BMU level responsible for canals enlargement is only ~5%; 95% of the bone removed by osteoclasts is refilled representing a deficit of a few microns in regard of the osteonal wall width - a difference unlikely to be detectable using an 8.14 μm voxel size (Qiu et al., 2010). An increase in the number of canals in these confined VOIs suggests an excavation of new canals. This increase in pore number perhaps originates from remodeling initiated upon surfaces of existing BMUs and their branching (Maggiano et al., 2016) or within osteocytes lacunae (Perilli et al., 2015). Indeed, many studies suggest that osteocytes are key regulators of osteoclasts and osteoblasts activities but also may be able to locally remodel the perilacunar bone matrix (Atkins and Findlay, 2012; Bonewald, 2011; Qing et al., 2012; Teti and Zallone, 2009). However, knowing whether new canals can emerge from, or under the control of osteocytes activity needs further research. In addition to increasing the cortical void volume fraction, the excavation of new canals incidentally decreased the average separation between them and that correlated with a lower axial elasticity in traction-compression mode.

It is well documented that the age-related increase in porosity originating from alterations in intracortical remodeling is detrimental for bone strength (Bala et al., 2015; Granke et al., 2011; McCalden et al., 1993). At the tissue level (i.e., mesoscale), variations in cortical porosity explained from 62 to 98% of the variation in compression-tension and shear elastic coefficients (Dong and Guo, 2004; Granke et al., 2011). At the organ level (i.e., macroscale), variations in porosity, explained the majority of the variation in long bones mechanical properties in several human and animal models (Baron et al., 2007; Bousson et al., 2006; Granke et al., 2011; Yeni et al., 1997). However, in these studies, porosity was only regarded as a fraction of void volume and therefore did not provide information about the role of pore network microarchitecture in bone mechanical behavior.

In our population, we noticed that in elderly men and women, changes in pore separation and pore separation intra-individual distribution were correlated with axial tensile-compressive elasticity after accounting for void volume fraction. This new result suggests that for a given porosity, the way this void is fashioned in the bone volume affects significantly bone elasticity. In addition, our results

also displayed that shear elastic coefficients C_{55} and C_{66} were less sensitive to porosity and pore network microarchitecture among adults than observed among growing children. As bone anisotropy is influenced by material properties and structural properties (including osteonal morphology), this could reflect that bone anisotropy may emerge from relatively different structural and compositional variables across life.

Indeed, during growth and ageing the changes in cortical remodeling activity, balance and their consequences on pore network architecture are very distinct. However, with bone tissue age as well as individual's age, matrix properties also vary affecting tissue stiffness. During the last decade, the study of the so-called bone quality or we should say bone qualities has revealed that bone matrix stiffness was also a function of bone mineralization, bone mineral characteristics (crystallinity, maturity, carbonation), arrangement, maturity and cross-linking profile of bone collagen fibrils, all these properties varying with age of both the tissue and the individual (Bala and Seeman, 2015; Malo et al., 2013). The fact that the age-related changes in elastic coefficients are likely multifactorial, with changing in both cortical structure and matrix properties are likely to be the reason why the relationships between some pore network architecture and elastic coefficients were opposite in the present study (e.g., for Po.Sp.SD). Consequently, our understanding of the biomechanical impacts of changes in void volume fraction during pathology or treatments is only a partial improvement in the prediction of bone elasticity using bone imaging and computational modeling of the cortex may need to further consider pore network microarchitecture and regional heterogeneity (Granke et al., 2011; Hellmich et al., 2004). Studying the relative contributions of structural and material properties in age-related changes in mechanical properties will be the very objective of our future studies.

4.3. *Strengths and limitations*

A strength of the study was the use of a high-resolution imaging modality combined with relevant image processing in assessing bone microstructure *in vitro*. In addition, assessments were performed in site-matched samples of a long bone in growing children and adults. This study is the first to offer an analysis of the 3D microarchitecture of the pore network in growing children in a long bone. Indeed, our knowledge of growth-related changes in cortical porosity comes from histologic studies in iliac crest samples, an irregular and non-load-bearing bone site that rarely fractures (Rauch et al., 2007; Schnitzler, 2015; Schnitzler and Mesquita, 2013; Schnitzler et al., 2009). In addition, elasticity has been evaluated based on the assessment of ultrasonic bulk wave velocities. While this method has been largely used for investigation of bone mechanical properties, it is non-ionizing, non-destructive and provides both axial and one of the few with Resonant Ultrasond Spectroscopy to allow the assessment of shear elastic properties in the three principal directions of bone (Ashman et al., 1984; Espinoza Orias et al., 2009; Granke et al., 2011; Bernard et al., 2013; Remilleux et al., 2015). In addition for such small dimensions, direct mechanical testing are complicated to realize and interpret.

The first limitation of our study was the sample size that precluded the analysis of the sex- and pubertal stage-related differences in the trends we reported with age in both children and adults groups. Bone microarchitecture is known to vary with age with different chronologies in male and female during bone growth or aging (Chen et al., 2010; Khosla et al., 2006; Wang et al., 2010). The trends described in the current paper are coherent with the known age-related changes in bone remodeling and its balance at the BMU level, though. Second, our analyses were performed on VOIs of relatively small size (cubes of 2mm-sides) and consequently were blind to the porosity gradient along the cortical thickness that appears due to the trabecularization of the cortex with ageing. Therefore, it may remain complicated to generalize those results to what happen in different ROIs. However, despite limited to the compact-appearing cortex, our results are relevant in regard of bone strength because the VOIs were the farthest from the neutral axis, i.e., where the effect of bone porosity on strength is at maximum in a bone submitted to bending (Burr, 2010). Third, we used a polychromatic cone-beam micro-CT device, incidentally submitted to beam-hardening. However due to the small size of our specimens and the use of an aluminum filter that reduces beam hardening artefact, no correction was necessary. Fourth, it has been observed that most of the architectural parameters are inter-correlated (Chappard et al., 2013) and may result in multicollinearity. Unfortunately, using non parametric statistics it was not possible to statistically evaluate for potential collinearity among variables. Finally, while pediatric samples were included in our study based on the literature's definition of 'reference' for this very population (Rauch et al., 2007), we acknowledge that they were cored following orthopedic issues and results need to be interpreted with cautious.

5. Conclusion

In conclusion, within the limitation of a small sample size, we infer that during both growth and ageing, changes in pore network microarchitecture, that reflects activity and balance of remodeling upon canals surfaces, contributes to cortical bone stiffness. Alterations in this microarchitecture may impact cortical bone mechanical properties independently of the changes in the void volume fraction. While cortical porosity is a strong determinant of bone elasticity, further considering how this void volume fraction is fashioned will improve our ability to predict the changes in strength associated with pathologies and treatments.

Disclosures

The authors declare no competing financial interests. Yohann Bala, Emmanuelle Lefèvre, Jean-Paul Roux, Cécile Baron, Philippe Lasaygue, Martine Pithioux, Valérie Kaftandjian and Hélène Follet declare that they have no conflict of interest related to this work.

Acknowledgement

This research is supported by the French National Research Agency (ANR MALICE Program, under Grant no. BS09-032). We are grateful to Prof. Franck Launay's team, the donors and their legual guardians who consented us to use their samples for investigation. We also acknowledge the technical support of Marine Loubet, Sebastien Rizzo and Florian Montagner.

REFERENCES

Akkus, O., Polyakova-Akkus, A., Adar, F., Schaffler, M.B., 2003. Aging of microstructural compartments in human compact bone. J. Bone Miner. Res. 18, 1012–1019.

Ashman, R.B., Cowin, S.C., Van Buskirk, W.C., Rice, J.C., 1984. A continuous wave technique for the measurement of the elastic properties of cortical bone. J. Biomech. 17, 349–361.

Atkins, G.J., Findlay, D.M., 2012. Osteocyte regulation of bone mineral: a little give and take. Osteoporos. Int. 23, 2067–2079.

Bala, Y., Bui, Q.M., Wang, X., Iuliano, S., Wang, Q., Ghasem-Zadeh, A., Rozental, T.D., Bouxsein, M.L., Zebaze, R., Seeman, E., 2015. Trabecular and cortical microstructure and frgaility of the distal radius in women. J. Bone Miner. Res. 30, 621–629.

Bala, Y., Chapurlat, R., Cheung, A.M., Felsenberg, D., Laroche, M., Morris, E., Reeve, J., Thomas, T., Zanchetta, J., Bock, O., Ghasem-Zadeh, A., Djoumessi, R.M., Seeman, E., Rizzoli, R., 2014a. Risedronate slows or partly reverses cortical and trabecular microarchitectural deterioration in postmenopausal women. J. Bone Miner. Res. 29, 380–388.

Bala, Y., Seeman, E., 2015. Bone's Material Constituents and their Contribution to Bone Strength in Health, Disease, and Treatment. Calcif. Tissue Int.

Bala, Y., Zebaze, R., Ghasem-Zadeh, A., Atkinson, E.J., Iuliano, S., Peterson, J.M., Amin, S., Bjornerem, A., Melton 3rd, L.J., Johansson, H., Kanis, J.A., Khosla, S., Seeman, E., 2014b. Cortical porosity identifies women with osteopenia at increased risk for forearm fractures. J. Bone Miner. Res. 29, 1356–1362.

Baron, C., Talmant, M., Laugier, P., 2007. Effect of porosity on effective diagonal stiffness coefficients (cii) and elastic anisotropy of cortical bone at 1 MHz: a finite-difference time domain study. J. Acoust. Soc. Am. 122, 1810.

Bell, K.L., Loveridge, N., Power, J., Garrahan, N., Meggitt, B.F., Reeve, J., 1999. Regional differences in cortical porosity in the fractured femoral neck. Bone 24, 57–64.

Bell, K.L., Loveridge, N., Reeve, J., Thomas, C.D., Feik, S.A., Clement, J.G., 2001. Super-osteons (remodeling clusters) in the cortex of the femoral shaft: influence of age and gender. Anat. Rec. 264, 378–386.

Bernard, S., Grimal, Q., Laugier, P., 2013. Accurate measurement of cortical bone elasticity tensor with resonant ultrasound spectroscopy. J. Mech. Behav. Biomed. Mater. 18, 12–19.

Bjornerem, A., Bui, Q.M., Ghasem-Zadeh, A., Hopper, J.L., Zebaze, R., Seeman, E., 2013. Fracture risk and height: An association partly accounted for by cortical porosity of relatively thinner cortices. J. Bone Miner. Res. 28, 2017–2026.

Bjornerem, A., Ghasem-Zadeh, A., Bui, M., Wang, X., Rantzau, C., Nguyen, T.V., Hopper, J.L., Zebaze, R., Seeman, E., 2011. Remodeling markers are associated with larger intracortical surface area but smaller trabecular surface area: a twin study. Bone 49, 1125–1130.

Bonewald, L.F., 2011. The amazing osteocyte. J Bone Miner. Res. 26, 229–238.

Bousson, V., Le Bras, A., Roqueplan, F., Kang, Y., Mitton, D., Kolta, S., Bergot, C., Skalli, W., Vicaut, E., Kalender, W., Engelke, K., Laredo, J.D., 2006. Volumetric quantitative computed tomography of the proximal femur: relationships linking geometric and densitometric variables to bone strength. Role for compact bone. Osteoporos. Int. 17, 855–864.

Bui, M., Bjornerem, A., Ghasem-Zadeh, A., Dite, G.S., Hopper, J.L., Seeman, E., 2013. Architecture of cortical bone determines in part its remodelling and structural decay. Bone 55, 353–358.

Burr, D.B., 2010. Cortical bone: a target for fracture prevention?. Lancet 375, 1672–1673.

Cadet, E.R., Gafni, R.I., McCarthy, E.F., McCray, D.R., Bacher, J.D., Barnes, K.M., Baron, J., 2003. Mechanisms responsible for longitudinal growth of the cortex: coalescence of trabecular bone into cortical bone. J. Bone Jt. Surg. Am. 85-A, 1739–1748.

Chappard, C., Bensalah, S., Olivier, C., Gouttenoire, P.J., Marchadier, A., Benhamou, C., Peyrin, F., 2013. 3D characterization of pores in the cortical bone of human femur in the elderly at different locations as determined by synchrotron micro-computed tomography images. Osteoporos. Int. 24, 1023–1033.

Chen, H., Zhou, X., Shoumura, S., Emura, S., Bunai, Y., 2010. Age- and gender-dependent changes in three-dimensional microstructure of cortical and trabecular bone at the human femoral neck. Osteoporos. Int. 21, 627–636.

Compston, J., 2011. Age-related changes in bone remodelling and structure in men: histomorphometric studies. J. Osteoporos. 2011, 108324.

Cooper, D.M., Thomas, C.D., Clement, J.G., Turinsky, A.L., Sensen, C.W., Hallgrimsson, B., 2007. Age-dependent change in the 3D structure of cortical porosity at the human femoral midshaft. Bone 40, 957–965.

Currey, J.D., Butler, G., 1975. The mechanical properties of bone tissue in children. J. Bone Jt. Surg. Am. 57, 810–814.

Dong, X.N., Guo, X.E., 2004. The dependence of transversely isotropic elasticity of human femoral cortical bone on porosity. J. Biomech. 37, 1281–1287.

Enlow, D.H., 1962. Functions of the Haversian system. Am. J. Anat. 110, 269–305.

Espinoza Orias, A.A., Deuerling, J.M., Landrigan, M.D., Renaud, J. E., Roeder, R.K., 2009. Anatomic variation in the elastic anisotropy of cortical bone tissue in the human femur. J. Mech. Behav. Biomed. Mater. 2, 255–263.

Granke, M., Grimal, Q., Saied, A., Nauleau, P., Peyrin, F., Laugier, P., 2011. Change in porosity is the major determinant of the variation of cortical bone elasticity at the millimeter scale in aged women. Bone 49, 1020–1026.

Hellmich, C., Ulm, F.J., Dormieux, L., 2004. Can the diverse elastic properties of trabecular and cortical bone be attributed to only a few tissue-independent phase properties and their interactions? Arguments from a multiscale approach. Biomech. Model. Mechanobiol. 2, 219–238.

Hildebrand, T., Ruegsegger, P., 1997. A new method for the model-independent assessment of thickness in three-dimensional images. J. Microsc. 185, 67–75.

Jee, W.S., Frost, H.M., 1992. Skeletal adaptations during growth. Triangle; Sandoz J. Med. Sci. 31, 77–88.

Kerley, E.R., 1965. The microscopic determination of age in human bone. Am. J. Phys. Anthropol. 23, 149–164.

Keshawarz, N.M., Recker, R.R., 1984. Expansion of the medullary cavity at the expense of cortex in postmenopausal osteoporosis. Metab. Bone Dis. Relat. Res. 5, 223–228.

Khosla, S., Riggs, B.L., Atkinson, E.J., Oberg, A.L., McDaniel, L.J., Holets, M., Peterson, J.M., Melton 3rd, L.J., 2006. Effects of sex and age on bone microstructure at the ultradistal radius: a population-based noninvasive in vivo assessment. J. Bone Miner. Res. 21, 124–131.

Kohles, S.S., Martinez, D.A., 2000. Elastic and physicochemical relationships within cortical bone. J. Biomed. Mater. Res. 49, 479–488.

Lefevre, E., Lasaygues, P., Baron, C., Payan, C., Launay, F., Follet, H., Pithioux, M., 2015. Analyzing the anisotropic Hooke's law for the children's cortical bone. J. Mech. Behav. Biomed. Mater. DOI: j.jmbbm.2015.05.013.

Lips, P., Courpron, P., Meunier, P.J., 1978. Mean wall thickness of trabecular bone packets in the human iliac crest: changes with age. Calcif. Tissue Res. 26, 13–17.

Loro, M.L., Sayre, J., Roe, T.F., Goran, M.I., Kaufman, F.R., Gilsanz, V., 2000. Early identification of children predisposed to low peak bone mass and osteoporosis later in life. J. Clin. Endocrinol. Metab. 85, 3908–3918.

Maggiano, I.S., Maggiano, C.M., Clement, J.G., Thomas, C.D.L., Carter, Y., Cooper, D.M.L., 2016. Three-dimensional reconstruction of Haversian systems in human cortical bone using synchrotron radiation-based micro-CT: morphology and quantification of branching and transverse connections across age. J. Anat.http://dxdoi.org/10.1111/joa.12430.

Malo, M.K.H., Rohrbach, D., Isaksson, H., Töyräs, J., Jurvelin, J.S., Tamminen, I.S., Kröger, H., Raum, K., 2013. Longitudinal elastic properties and porosity of cortical bone tissue vary with age in human proximal femur. Bone 53, 451–458.

McCalden, R.W., McGeough, J.A., Barker, M.B., Court-Brown, C.M., 1993. Age-related changes in the tensile properties of cortical bone. The relative importance of changes in porosity, mineralization, and microstructure. J. Bone Jt. Surg. Am. 75, 1193–1205.

Montagner, F., Kaftandjian, V., Farlay, D., Brau, D., Boivin, G., Follet, H., 2015. Validation of a novel microradiography device for characterization of bone mineralization. J. X-ray Sci. Technol. 23, 201–211.

Odgaard, A., 1997. Three-dimensional methods for quantification of cancellous bone architecture. Bone 20, 315–328.

Palacio-Mancheno, P.E., Larriera, A.I., Doty, S.B., Cardoso, L., Fritton, S.P., 2014. 3D assessment of cortical bone porosity and tissue mineral density using high-resolution microCT: effects of resolution and threshold method. J. Bone Miner. Res. 29, 142–150.

Parfitt, A.M., 1994a. Osteonal and hemi-osteonal remodeling: the spatial and temporal framework for signal traffic in adult human bone. J. Cell. Biochem. 55, 273–286.

Parfitt, A.M., 1994b. The two faces of growth: benefits and risks to bone integrity. Osteoporos. Int. 4, 382–398.

Parfitt, A.M., Travers, R., Rauch, F., Glorieux, F.H., 2000. Structural and cellular changes during bone growth in healthy children. Bone 27, 487–494.

Perilli, E., Bala, Y., Zebaze, R., Reynolds, K.J., Seeman, E., 2015. Regional heterogeneity in the configuration of the intracortical canals of the femoral shaft. Calcif. Tissue Int. Epub Ahead of Print.

Qing, H., Ardeshirpour, L., Pajevic, P.D., Dusevich, V., Jahn, K., Kato, S., Wysolmerski, J., Bonewald, L.F., 2012. Demonstration of osteocytic perilacunar/canalicular remodeling in mice during lactation. J. Bone Miner. Res. 27, 1018–1029.

Qiu, S., Rao, D.S., Palnitkar, S., Parfitt, A.M., 2010. Dependence of bone yield (volume of bone formed per unit of cement surface area) on resorption cavity size during osteonal remodeling in human rib: implications for osteoblast function and the pathogenesis of age-related bone loss. J. Bone Miner. Res. 25, 423–430.

Rauch, F., 2012. The dynamics of bone structure development during pubertal growth. J. Musculoskelet. Neuronal Interact. 12, 1–6.

Rauch, F., Travers, R., Glorieux, F.H., 2007. Intracortical remodeling during human bone development–a histomorphometric study. Bone 40, 274–280.

Recker, R., Lappe, J., Davies, K.M., Heaney, R., 2004. Bone remodeling increases substantially in the years after menopause and remains increased in older osteoporosis patients. J. Bone Miner. Res. 19, 1628–1633.

Remilleux, M.C., Ulrich, T.J., Payan, C., Rivière, J., Lake, C.R., Le Bas, P.Y., 2015. Resonant ultrasound spectroscopy for materials with high damping and samples of arbitrary geometry. J. Geophys. Res. Solid Earth 120, 4898–4916.

Robling, A.G., Stout, S.D., 1999. Morphology of the drifting osteon. Cells Tissues Organs 164, 192–204.

Saito, M., Marumo, K., 2010. Collagen cross-links as a determinant of bone quality: a possible explanation for bone fragility in aging, osteoporosis, and diabetes mellitus. Osteoporos. Int. 21, 195–214.

Schaffler, M.B., Burr, D.B., 1988. Stiffness of compact bone: effects of porosity and density. J. Biomech. 21, 13–16.

Schnitzler, C.M., 2015. Childhood cortical porosity is related to microstructural properties of the bone-muscle junction. J. Bone Miner. Res. 30, 144–155.

Schnitzler, C.M., Mesquita, J.M., 2013. Cortical porosity in children is determined by age-dependent osteonal morphology. Bone 55, 476–486.

Schnitzler, C.M., Mesquita, J.M., Pettifor, J.M., 2009. Cortical bone development in black and white South African children: iliac crest histomorphometry. Bone 44, 603–611.

Seeman, E., 2008. Structural basis of growth-related gain and age-related loss of bone strength. Rheumatol. Oxf. J. 47 (Suppl. 4) iv2-8.

Seeman, E., Delmas, P.D., 2006. Bone quality–the material and structural basis of bone strength and fragility. New Engl. J Med. 354, 2250–2261.

Teti, A., Zallone, A., 2009. Do osteocytes contribute to bone mineral homeostasis? Osteocytic osteolysis revisited. Bone 44, 11–16.

Thomas, C.D., Feik, S.A., Clement, J.G., 2006. Increase in pore area, and not pore density, is the main determinant in the development of porosity in human cortical bone. J. Anat. 209, 219–230.

Ulrich, D., van Rietbergen, B., Laib, A., Ruegsegger, P., 1999. The ability of three-dimensional structural indices to reflect mechanical aspects of trabecular bone. Bone 25, 55–60.

Ural, A., Vashishth, D., 2014. Hierarchical perspective of bone toughness-from molecules to fracture. Int. Mater. Rev. 59, 245–263.

Vedi, S., Compston, J.E., Webb, A., Tighe, J.R., 1983. Histomorphometric analysis of dynamic parameters of trabecular bone formation in the iliac crest of normal British subjects. Metab. Bone Dis. Relat. Res. 5, 69–74.

Wang, Q., Wang, X.F., Iuliano-Burns, S., Ghasem-Zadeh, A., Zebaze, R., Seeman, E., 2010. Rapid growth produces transient cortical weakness: a risk factor for metaphyseal fractures during puberty. J. Bone Miner. Res. 25, 1521–1526.

Yeni, Y.N., Brown, C.U., Wang, Z., Norman, T.L., 1997. The influence of bone morphology on fracture toughness of the human femur and tibia. Bone 21, 453–459.

Yeni, Y.N., Norman, T.L., 2000. Fracture toughness of human femoral neck: effect of microstructure, composition, and age. Bone 26, 499–504.

Zebaze, R., Ghasem-Zadeh, A., M'bala, A., Seeman, E., 2013. A new method of segmentation of compact-appearing, transitional and trabecular compartments and quantificatino of cortical porosity from high resolution peripheral quantitative computed tomographic images. Bone 54, 8–20.

Zebaze, R.M., Ghasem-Zadeh, A., Bohte, A., Iuliano-Burns, S., Mirams, M., Price, R.I., Mackie, E.J., Seeman, E., 2010. Intracortical remodelling and porosity in the distal radius and post-mortem femurs of women: a cross-sectional study. Lancet 375, 1729–1736.